Microwave Activation of Drug Release.

Jónasson, Sævar Þór

Publication date:
2014

Document Version
Publisher's PDF, also known as Version of record

Technical University of Denmark

Sævar Þór Jónasson

Microwave Activation of Drug Release

PhD thesis, September 2014

DTU Electrical Engineering
Department of Electrical Engineering

The work presented in this thesis was carried out at the Department of Electrical Engineering in partial fulfillment of the requirements for the PhD degree at the Technical University of Denmark.

Supervisors:

Tom Keinicke Johansen, Associate Professor, PhD,
Vitaliy Zhurbenko, Assistant Professor, PhD,
Department of Electrical Engineering,
Technical University of Denmark

www.elektro.dtu.dk

Preface

This thesis is submitted as a part of the requirements to achieve the PhD degree at the Department of Electrical Engineering, Technical University of Danmark. The PhD study was carried out from November 1st, 2009 to March 31st, 2013, with the exception of September 14th 2012 to November 26th 2012. From January 1st 2011 to June 30st 2011 I had an external research stay at the Department of Biomedical Engineering, Reykjavik University under the supervision of Prof. Ceon Ramon. Financial support for the PhD Study was provided by the Villum Kann Rasmussen Fonden as a part of the NAMEC (NAno MEChanical sensors and actuator, http://www.namec.dtu.dk/) consortium, consisting of members from DTU-Elektro, DTU-Nanotech, DTU-Mathematics and KU-Pharma. Associate Professor Tom Keinicke Johansen acted as the main project supervisor and Assistant Professor Vitaliy Zhurbenko as the co-supervisor.

Acknowledgements

I would like to begin by thanking my former supervisor, Prof. Viktor Krozer for encouraging me and giving me the opportunity of persuing a PhD at the Technical University of Denmark within a field of my special interest. Secondly, I would like to thank my supervisors Associate Prof. Tom Keinicke Johansen and Assistant Prof. Vitaliy Zhurbenko for being there when I needed it. PhD students Brian Sveistrup Jensen and Carlos Cilla Hernandez should receive special gratitude for our many scientific and non-scientific discussions.

I would like to thank DTU Elektro's mechanical workshop for all their assistance on the mechanical parts and technician Bo Brændstrup for his support. I express my gratitude to Associate Prof. Sergey Pivnenko for all his antenna measurements for me and researcher Tonny Rubæk for his assistance in COMSOL and LabView. Associate Prof. Samel Arslanagic also deserves thanks for his assistance. Special thanks goes out to Prof. Ceon Ramon and Associate Prof. Haraldur Auðunsson for their hospitality during my external stay.

I thank my whole family, my parents Jónas and Edda, my sister Erla and my brother Arnór for understanding my situation and my limited time during this work.

This work is in its entirety dedicated to my son Isaac Jónas Sævarsson who is always in my heart and on my mind.

Technical University of Denmark
Kgs. Lyngby, Denmark
September, 2014

Sævar Þór Jónasson

Abstract

Due to current limitations in control of pharmaceutical drug release in the body along with increasing medicine use, methods of externally-controlled drug release are of high interest. In this thesis, the use of microwaves is proposed as a technique with the purpose of externally activating pharmaceutical drug capsules, in order to release drugs at a pre-determined location at a pre-determined time. The concept is, to use an array of transmitting sources that add together in phase to produce a constructive interference at a certain focus point inside the human body. To this end, an experimental setup, called the microwave activation system has been developed and tested on a body phantom that emulates the human torso. The system presented in this thesis, operates unobtrusively, i.e. without physically interfering with the target (patient). The torso phantom is a simple dual-layered cylindrical structure that contains fat and muscle tissue mimicking media. The core of the system consists of a single submerged antenna, four external antennas, four transmitters and four receivers, all designed to operate within the ISM-band around 2.45 GHz with a bandwidth of 100 MHz.

The wave behaviour inside the phantom is of interest for disclosing essential information about the limitations of the concept, the phantom and the system. For these purposes, a twofold operation of the microwave activation system was performed, which are reciprocal of each other.

In the first operation phase, named *mapping*, microwaves were transmitted from within the phantom and were received externally to the phantom. With this setup, the amplitudes and phases of the transmitted signal were measured as the submerged source was moved around, inside the phantom. The measurement results reveal a significant influence of the so-called creeping waves, on the measured signal. If the submerged source was at a certain offset from the centre of the phantom, the receiver furthest away from the submerged source, measured the contribution from the creeping waves instead of the contribution from the direct path. These creeping waves (diffracted waves) originated from the face of the phantom from which the submerged source was closest. Most of the power of the transmitted wave, exits at that face and followed the curvature of the phantom, on both sides, and was ultimately received on the other side of the phantom, by the receiver farthest away from the submerged source.

In the second operation phase of the microwave activation system, named *focusing*, four transmitters, external to the phantom, transmitted microwaves at the phantom. The phases and amplitudes of each of the transmitters were controlled to provide a constructive interference at a pre-determined focus point. Focusing microwaves inside the torso phantom was partly accomplished close to the centre of the phantom. Outside a certain radius from the centre, the effect of creeping waves is believed to be responsible for the limitations of focusing. An experiment was performed to verify the presence of creeping waves.

Due to the inherent high wave attenuation in biological tissues, such as muscles at microwave frequencies, sensitive receiving structures are suggested to be integrated on a drug capsule. The capsules are meant to contain the pharmaceutical drugs and the receiving structure is presented to efficiently utilize the available power, to be present at the focusing location. Split-ring resonators are proposed to be integrated on the lid of the capsules which concentrate their acquired power to high-amplitude electric fields across the gaps of the split-ring resonators, at the resonance frequency. An optimal conductivity for the lossy dielectric lid of the capsule is suggested in this work. The specific conductivity property of the lid that the split-ring resonators are suggested to be integrated on is, to ensure maximum temperature increase in the lid. The temperature increase is proposed to be used to melt an adhesive layer, between the container and its lid, consequently releasing the drug. Experiments were performed to determine the optimal orientation of the split-ring resonators, in respect to the polarization of the exciting wave.

Resumé

På grund af nuværende begrænsninger vedrørende kontrol af frigivelse af lægemiddelstoffer i kroppen, samtidig med et stigende medicinforbrug, er metoder til ekstern kontrolleret frigivelse af lægemiddelstoffer af stor interesse. I denne afhandling foreslås brug af mikrobølger som en teknik til ekstern aktivering af frigivelsen af lægemiddel på et forudbestemt sted til et forudbestemt tidspunkt. Konceptet går ud på at benytte et array af sendere som addere i fase for at producere konstruktiv interferens ved et bestemt fokuspunkt inden i den menneskelige krop. Til dette formål er en eksperimental opstilling, kaldet mikrobølgeaktiveringssystemet, blevet udviklet og testet på et fantom der efterligner den menneskelige torso. Systemet som præsenteres i denne afhandling virker diskret, altså uden at indvirke fysisk på målet (patienten). Fantomet er en simpel dobbelt-lagdelt cylindrisk struktur som indeholder et medium der efterligner fedt og muskelvæv. Kernen af systemet består af en enkelt nedsænket antenne, fire eksterne antenner, fire sendere og fire modtagere, alle designet til at virke indenfor ISM-båndet omkring 2.45 GHz med en båndbredde på 100 MHz.

Opførelsen af bølgerne inden i fantomet er af interesse for at afsløre essentiel information omkring begrænsninger af konceptet, fantomet og systemet. Til dette formål anvendes mikrobølgeaktiveringssystemet på to forskellige måder som er reciprokke af hinanden.

I den første fase, kaldet *mapping*, transmitteres mikrobølger fra inden i fantomet og modtages eksternt udenfor fantomet. Med denne opstilling måles amplituden og fasen af det transmitteret signal mens den nedsænket kilde bevæges rundt inden i fantomet. Måleresultaterne afslører en betydende indflydelse fra såkaldte overfladebølger. Hvis den nedsænket kilde er ved et bestemt offset fra centrum af fantomet vil modtageren placeret længst væk fra kilden måle bidraget fra overfladebølger i stedet for bidraget fra den direkte vej. Disse overfladebølger har deres udspring fra overfladen af fantomet tættest på den nedsænket kilde. Størstedelen af effekten i den transmitterede bølge eksistere på denne overflade og følger fantomets facon rundt på begge sider og vil til sidst ultimativt blive modtaget på den anden side af fantomet af modtageren længst fra den nedsænket kilde.

I den anden fase, kaldet *fokusering*, transmitterer fire sendere udenfor fantomet mikrobølger ind i mod fantomet. Fasen og amplituden af hver transmitter kontrolleres individuelt for at give konstruktiv interferens ved et forudbestemt fokuspunkt. Fokuseringen af mikrobølger kan delvis opnås tæt på centrum af fantomet. Udenfor en bestemt radius fra centrum menes effekten fra overfladebølger at være ansvarlig for en begrænsning i fokusering. Et eksperiment er udført for at verificere tilstedeværelsen af disse overfladebølger.

På grund af den store dæmpning af bølger i biologisk væv, så som muskler, ved mikrobølge frekvenser er der forslået at følsomme modtagestrukturer kan integreres oven på en kapsel. Kapslen er tiltænkt at indeholde lægemiddelet og modtagerstrukturen er indført for at bedst muligt at udnytte effekten til rådighed i fokuspunktet. Det foreslås at integrerede split-ringsstrukturer placeres på låget af kapslen hvorved et elektrisk felt med høj amplitude koncentreres i mellemrummet af split-ringsstrukturen ved dennes resonansfrekvens. Som en del af dette arbejde er en optimal konduktivitet for det tabsrige dielektriske låg af kapslen bestemt. Egenskaberne fra lågets specifikke konduktivitets er valgt for at sikre maksimal temperaturstigning i låget. Det foreslås at benytte temperaturstigningen til at smelte et adhesivt lag mellem containeren indeholdende lægemiddelet og låget for at efterfølgende at frigive medicinen. Eksperimenter er udført for at bestemme den optimale orientering af split-ringsstrukturen i forhold til den indfaldende bølge.

Acronyms and Abbreviations

ADC	Analog to Digital Converter
ADS	Advanced Design System
ATC	American Technologcy Ceramics
BPF	Band-Pass Filter
CW	Continous Wave
CST	Computer Simulation Technology
DAC	Digital to Analog Converter
DGBE	Diethylene Glycol Butyl Ether
DTU	Danish: Danmarks Tekniske Universitet (The Technical University of Denmark)
EMI	Electromagnetic Interference
ESA	European Space Agency
FFT	Fast Fourier Transform
GND	Ground
HPA	High Power Amplifier
IF	Intermidiate Frequency
LDMOS	Laterally Diffused Metal Oxide Semiconductor
LNA	Low Noise Amplifier
LO	Local Oscillator
LPF	Low-Pass Filter
MCU	Microcontroller Unit
MTMM	Muscle Tissue Mimicking Media
NAMEC	NAnoMechanical sensors and actuators (Project collaboration between Technical University of Denmark and Copenhagen University)
NI	National Instruments (Corp.)
PA	Power Amplifier
PCB	Printed Circuit Board
PLL	Phase Locked Loop
PW	Pulsed Wave
RF	Radio Frequency
RX-i	Receiver Number i
SMA	SubMiniature version A connector
SPI	Serial Peripheral Interface
SRR	Split-Ring Resonator
TEM	Transverse Electromagnetic
TX-i	Transmitter Number i
VA	Variable Attenuator
VGA	Variable Gain Amplifier
VPS	Variable Phase Shifter

Patents

Below is listed the patent that resulted from the PhD study.

[PAT1] Sævar Þór Jónasson, "Ingestible Capsule for Remote Controlled Release of a Substance," *European Patent Office*, Patent Application No. 12187095.0, Filing Date: 3rd October 2012.

Publications

Below are listed the papers that have resulted from the PhD study period.

[CP1] Sævar Þór Jónasson, Brian Sveistrup Jensen and Tom Keinicke Johansen, "Study of Split-Ring Resonators for use on a Pharmaceutical Drug Capsule for Microwave Activated Drug Release," In Proc. *EuMC 2012 Amsterdam*, Oct. 2012.

[CP2] Sævar Þór Jónasson, Tom Keinicke Johansen and Vitaliy Zhurbenko, "Design and Characterization of a Low-Viscous Muscle Tissue Mimicking Media at the ISM-band (2.4-2.48 GHz) for Easy Antenna Displacement in In Vitro Measurements," In Proc. *APMC 2012 Kaohsiung*, Dec. 2012.

[CP3] Sævar Þór Jónasson, Vitaliy Zhurbenko and Tom Keinicke Johansen, "Microwave Assisted Drug Delivery," *Accepted, URSI General Assembly and Scientific Symposium*, Aug. 2014.

[CP4] Brian Sveistrup Jensen, Sævar Þór Jónasson, Thomas Jensen and Tom Keinicke Johansen, "Vital Signs Detection Radar using Low Intermediate-Frequency Architecture and Single-Sideband Transmission," *EuRAD 2012 Amsterdam*, Oct. 2012.

[CP5] Carlos Cilla Hernández, Sævar Þór Jónasson and Jesper Hanberg , "Bondwire array modeling for the design of hybrid high power amplifiers above C-band," *APMC 2012 Kaohsiung*, Dec. 2012.

[CP6] Chenhui Jiang, Tom Keinicke Johansen, Sævar Þór Jónasson, Lei Yan and Anja Boisen, "Cantilever-Based Microwave Biosensors: Analysis, Designs and Optimizations," In Proc. *27th Annual Review of Progress in Applied Computational Electromagnetics, Virginia, USA*, 2011.

Contents

Chapter 1

Introduction

1.1 Project Description

The description of the PhD project proposal, as defined by DTU-Elektro, sets the guidelines for the research in this thesis. The PhD-student shall follow these guidelines, which are described below.

The purpose of the PhD project is to develop a microwave system and all its components for application in bio-sensing and drug delivery. The development will include microwave component development, system architecture design, proof-of-principle demonstrator and electromagnetic modeling of microwave-body interaction. In particular the following tasks shall be pursued during the project:

- System architecture- and antenna design for constructive interference of microwaves within a human body-like phantom, based on EM simulations.
- Determination of the field strength and estimation of the local heating inside biological materials.
- Study of pulsed versus continuous-wave microwave operation for local heating.
- Development of the antenna and signal generation hardware, including the phase control for focusing.
- System assembly and proof-of-principle testing on simplified phantoms.

1.2 Motivation

In the year 2008, 48% of the people in the United States took at least one prescription drug in a single month. The prescription drug use had increased by 4% compared to 1998 [1]. With this increasing intake of drugs, a more efficient and controllable way of delivering the drugs is of great interest.

Oral delivery of pharmaceuticals is the preferred method compared to intravenous injection because of less costs and higher patient compliance due to self-administration. However the traditional oral delivery of therapeutics face several challenges such as low drug permeability (not to be confused with electromagnetic permeability) through the gastrointestinal epithelium (one of four basic tissue types) [2,3] and degradation of the active pharmaceutical components in the stomach [4].

Inherently the problem with current drug delivery systems, e.g. in the form of pills is the limited external control of when the drug is broken down and absorbed by the body. Typically, the drug release is controlled by the intestinal pH gradient and is therefore released over a large segment of the intestine. The drugs are coated with special protective coatings which dissolve at a certain pH value. The time and the location for the drug release are therefore difficult to control. For certain diseases such as schizophrenia and diabetes, dosing must be stable and reliable [5].

Pharmaceutical drugs taken orally are normally designed to release the drug in the small intestine because there, the drugs typically exhibit maximal absorption [6]. The small intestines are usually less than 3 cm in diameter [7, pp. 272].

A number of techniques have been proposed in the literature to externally control the drug delivery. These include, but are not limited to, the use of ultrasound [8], light waves [9], magnetic fields [10] and radio waves below 100 MHz [11]. Drug delivery modules consisting of a receiving inductor, control circuitry chip and a drug delivery chip have also been proposed [12]. These techniques have different disadvantages. Magnetic fields are e.g. difficult to focus and have short ranges. The focal point area of electromagnetic waves is directly related to the wavelength and at RF frequencies e.g. below 100 MHz, the focal point is decades of centimeters across. Light waves are limited to only surface excitation and ultrasound sources are typically placed on the skin's surface. Drug delivery modules that include control circuitry and numerous different components tend to be complex.

The alternative method that is proposed in this work is, to use microwaves to focus electromagnetic energy inside the human body to get localized high-amplitude electric fields (E-fields). The prototype developed for this purpose is called *microwave activation system* for an easy reference of the prototype system, even though drug activation has not been accomplished. The use of microwaves with sufficiently small wavelength could possibly focus energy at small volumes inside the body and not only limited to the

surface. Microwaves do have their challenges in biological media, where one of the most limiting factors is the inherent attenuation of the electromagnetic (EM) waves propagating in tissues with high water content, especially muscle tissues.

In order to efficiently utilize the received power despite this limitation caused by tissues of high water content, specially designed micro-containers (also referred to as capsules) for pharmaceutical drugs is proposed in this work, to exploit the high-amplitude E-fields. The containers consist, among other, of resonance circuits that are able to concentrate their received power to localized areas on the capsule. This in turn, heats up parts of the containers' lid for the drug to be released.

Hyperthermia systems have been around for decades and their purpose is typically to heat up cancerous tissues in cancer treatment [13–36]. Non-invasive hyperthermia systems are similar to the microwave activation system in the way that electromagnetic waves are to be transmitted into a human body and therefore many of the same principles apply in the microwave activation system as in non-invasive hyperthermia systems.

Non-invasive hyperthermia systems are meant to heat up cancerous tissues inside the body, which can result in prolonged exposure time of the person to electromagnetic waves due to the body's natural temperature regulating abilities. Due to the heat, blood flow increases in the heated tissue which can improve the effectiveness of chemo- and radiation therapy. The microwave activation system's function also is to radiate electromagnetic waves into the human body, which inevitably causes some temperature increase. The main difference between known non-invasive hyperthermia systems and the microwave activation system is that, the microwave activation system is to operate in the far-field of the transmitting antennas whereas the patient is typically situated in the near-field of hyperthermia applicators. The proposed micro-containers are specifically designed to respond to microwaves at a certain frequency that induce high-intensity E-fields with the help of the receiving structure, which again induces localized heating in the containers. By the use of these containers, the idea is to try and avoid prolong heating of the body's tissues while inducing enough heat in the containers themselves to release the drug. No other external activation systems for drug release based on microwaves are currently known to the author.

The idea of the microwave activation system is to provide a method of releasing drugs inside the body, unobtrusively, i.e. without disturbing, or attaching sources to the prospective patients. The idea is illustrated in Figure 1.1 where a person is lying on a bed, sleeping after having ingested numerous capsules that contain pharmaceutical drugs. At a certain time, and at a pre-determined location inside the human body, the microwave activation system is to focus electromagnetic energy that should open and release the medical drug from some of the capsules.

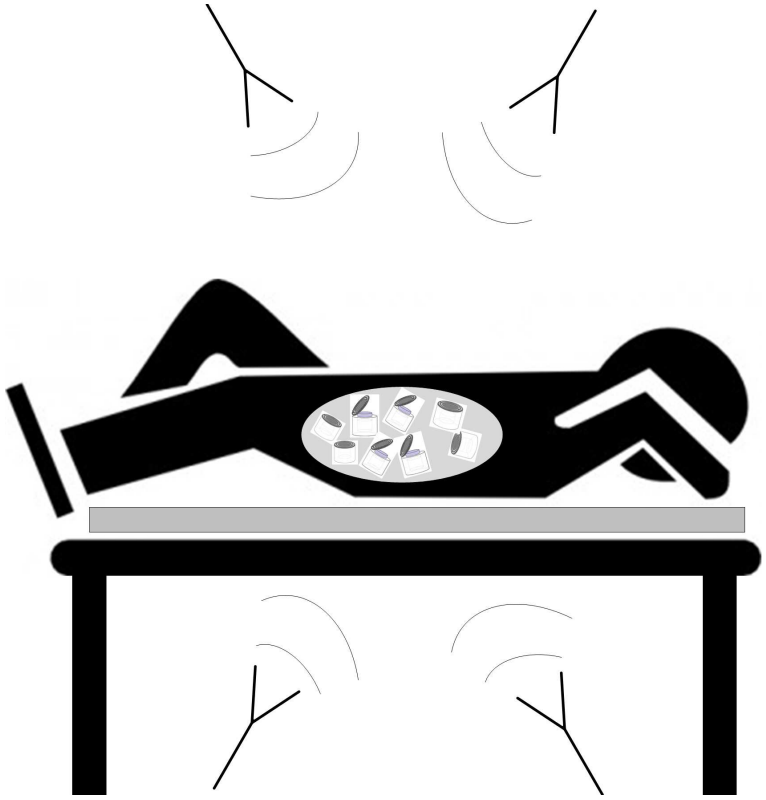

Figure 1.1: A person sleeping after ingesting drug capsules that are being activated by four external microwave applicators and drug is released.

1.3 Thesis Overview

The approach to this work was primarily practical, as the main purpose was to develop and build an experimental microwave system which consists of numerous microwave and several non-microwave modules. This work was started off by reviewing previous research on related topics such as hyperthermia and wireless body area networks to find out what has been examined before. The findings of the literature survey form, among other, the basis for the design considerations in later chapters where the system is developed on both block- and module-level.

A fundamental theoretical description of electromagnetic (EM) properties of biological media is considered essential to the understanding of a wave behaviour in such media and is therefore presented in this thesis, as the first topic after the literature survey. Wave transmission and reflection at interfaces between two media, where at least one of the two media has the properties of a biological media is included as a part of the fundamental theoretical description.

In order to appropriately model human interaction with EM waves, human tissue-like media must be fabricated for simulation purposes. The development of a suitable muscle tissue mimicking media is presented right after the description of EM properties of biological media due to its close relation. Since no suitable media recipe that imitates muscle tissue seemed to exist in the literature, it was of high importance to develop such a recipe in order to properly mimic human muscle tissue.

After the presentation of previous work in the literature, the theoretical description of biological media properties and the creation of a mixture that imitates muscle tissue, the system development is considered. The microwave activation system that has the purpose of transmitting EM waves into a phantom was first designed at a block-level. There, e.g. the operating frequency was chosen along with considerations on continuous wave vs. pulsed wave transmission. After the block-level design, the development of each individual block (module) of the system was performed. The chapter on module design and fabrication describes an extensive work done on numerous microwave modules. The design, fabrication and verification of each module is described in a relatively short manner since they are many and because several of these modules are designed using standard engineering techniques. Although some modules are described in a short manner, design and practical fabrication effort is not reflected in the length of the description. The most laborious work was done on the development of an antenna that has the ability to operate submerged in a muscle tissue mimicking medium and maintain omnidirectional field distribution and it is therefore described in a more detailed manner.

When the development of the system had been finished, two kind of experimental setups were measured on. First, the wave transmission from inside a phantom and outwards was measured. The result from this setup provides information on the wave propagation as measured by the receivers, while changing the source's location inside the phantom. Secondly is a setup where several sources transmit simultaneously from the far-field of the phantom and radiate at the phantom in order to try and accomplish a focus point inside the phantom. The wave behaviour encountered during these measurements is then discussed and more experiments to verify the explanations given in the discussion, were performed.

As with any practical system, imperfections will to greater or less extent affect the functionality of the system. Therefore, some of the essential performance-reduction factors are discussed after the measurement results. These factors are important to keep in mind while interpreting the measurements results.

Heating up a volume inside the body with microwaves as suggested in the PhD project proposal was quickly found to be very challenging. The idea of having a sensitive receiving structure attached to the drug-container that reacts to EM fields which activates the drug release was therefore additionally

conceived. There was an encouragement to file a patent application for the idea, which was done and is currently in a PCT patent application stage at the European Patent Office. The concept of the receiving structure is described at the end of this thesis in more details with simulation results.

A more detailed overview of the topic for each chapter is given below.

Chapter 2 presents a literature survey of prior research on the interaction of microwaves with the human body. Attention is primarily directed at the field of hyperthermia and the field of wireless body area networks.

Chapter 3 begins with introducing the theory of biological tissues as lossy media. The behaviour of plane waves at the interfaces between two lossless media as well as between a lossless and a lossy media, such as an air - fat interface, is then examined. Attention is directed at the Brewster angle and wave attenuation in biological media at oblique incident angles for maximizing power transfer into tissue.

The development of a suitable muscle tissue mimicking media is presented in **Chapter 4**. A basic recipe is given, including only two ingredients. An improved and a more complex recipe with three ingredients is furthermore given.

In **Chapter 5** an overview of the microwave activation system is given. The principle of operation is explained and the human torso phantom is presented. The phantom is useful in verifying the functionality of the system as well as to give an indication of the wave behaviour inside and around an actual human torso that, would be exposed to the microwave activation system' waves. Various critical design-choices are discussed such as the evaluation of the differences between continuous and pulsed waves. At the end of the chapter, designs are given for the *mapping* and the *focusing* operations. These two cases describe a process of exiting EM waves from within the phantom as well as exiting EM waves from the outside of the phantom, respectively.

Chapter 6 presents the development of the individual modules that the microwave activation system consists of. These include an antenna that is specially developed for being submerged in a muscle tissue mimicking media, stacked patch antennas with extended bandwidth and controllable transmitters and receivers. Other microwave components such as a power amplifier that ensures correct local oscillator drive and a 4-way power divider that has a very good phase balance are also considered. Then the digital part is covered which includes microcontroller boards, digital control, data acquisition and the user interface for the PC.

In **Chapter 7** the measurement results from the *mapping* operation are presented. The behaviour of EM waves, which were transmitted from within the phantom and received externally to the phantom, are discussed and explanations about their behaviour are proposed.

Chapter 8 shows measurement results from the *focusing* operation. Four external antennas were used to transmit EM waves towards a human torso phantom from a distance of about 0.7 m, arranged evenly around the phantom. An internal antenna, located inside the phantom was moved around in the phantom for amplitude measurements. Results from focusing of microwaves inside the human torso phantom are presented.

Creeping waves are explained in **Chapter 9** and their effect on focusing is discussed along with simulations that are carried out on a human voxel model. An experiment was performed to verify their presence.

Chapter 10 discusses several factors that need to be kept in mind while operating the microwave activation system and during interpretation of the measured data. Some of these factors can result in performance-reduction of the overall system if not taken care of.

Chapter 11 deals with the development of a micro-container (capsule) that is to hold pharmaceutical drugs until released. The capsule is proposed to be equipped with a resonance circuit that, when mounted on a media with specific EM properties, heats up a certain part of the capsule and releases the drug. Experiments were performed to determine what influence the orientation of the capsule has on its abilities to be excited by EM waves and by extension, release the medical drugs.

Chapter 12 summarizes the conclusions of the work that is presented here.

Chapter 2

Literature Survey

This chapter describes existing work on the influence of electromagnetic waves in and around a human body for medical or communication purposes. To the best of the author's knowledge, no previous work exists on using electromagnetic waves in the microwave region for external drug activation purposes. The topics that are considered are hyperthermia in cancer treatment and the use of wireless body area network. Both of these topics deal with electromagnetic waves inside the human body or close to the surface of the body.

2.1 Hyperthermia

Hyperthermia has been shown to be effective, especially when combined chemo- and radio-therapy, in the treatment against cancer [37, 38]. As previously noted, non-invasive hyperthermia systems are used to heat up cancerous tissues in the body without penetrating the body. Hyperthermia utilized various frequencies such as 40 MHz [13], 60 MHz [15], 100 MHz [14], 140 MHz [16, 17], 433 MHz [18–22], 520 MHz [23], 630 MHz [24], 915 MHz [25–32] and 2.45 GHz [33–36].

Phased arrays have been the most popular setups for non-invasive hyperthermia systems due to the ability of focusing [13, 13, 14, 16–18, 20, 22, 25–27, 31, 33, 36, 39–48]. In order to measure the E-fields inside or on the surface of phantoms and as a feedback signal for adaptive array, typically an non-perturbing E-field probe have been used. [14, 49, 50].

High power transmitters have been used with phased arrays to increase the temperature up to 6°C for up to several hours. Power levels of 35W [31], 40W [16], 100W [26, 27], 150W [18, 22], 175W [51], 300W [25], 500W [14, 20] and 860W [52] have been shown in the literature. Several of the systems make use of a water bolus, which typically contain de-ionized water to couple the electromagnetic energy into the patient and therefore avoid large reflections [14, 20, 22, 27, 29, 34, 41, 53].

Several attempts have been made to measure the effects of the phased array non-invasive hyperthermia systems in regards to temperature distribution mapping. The most precise technique is claimed to be MRI (Magnetic Resonance Imaging) [54, 55]. However other methods have also been presented for this purpose such as presented in [51, 56] or [57] for phantoms. A non-perturbing temperature probe is presented in [58] which can be used, with negligible disturbance of the E-field.

Various types of applicators have been presented in the literature for non-invasive hyperthermia systems. These include dipole antennas [14, 17, 21, 35, 42], end-loaded dipole antennas [16], square applicators [25], inductive current sheet applicators [59], microstrip spiral antennas [27], microstrip patch antennas [41,59], parabolic reflectors [60], helical radiators [13], waveguide antennas [34, 59, 61] and metal-plate lens applicators that are found to radiate 2 times deeper than a regular waveguide antenna [20].

There is a fine line when irradiating tissues between heating it, without damaging the tissue and causing a definite injury. Research has shown that when heating tissue to 43.5°C for 40 minutes, no injury is presented but when heated for 60 minutes, major damage occurs [62]. By heating to high temperatures, prolonged heating time can be avoided [63]. Time can be decreased by a factor of two for every single degree increase in temperature [26].

Variations in physical parameters [64, 65] such as e.g. fat thickness can have big influence on the appearance of hot spots in the fat layer and the muscle layer underneath [24, 53].

Both single antenna array ring structures or multiple ring structures have been presented in the literature. In general, the ability to focus and avoid hot spots, which appear at least above 250 MHz [66], are improved with more than one ring [48]. With increasing number of radiators, power optimization gets improved [17, 18, 45, 67]. By implementing adaptive nulling techniques, hot spots in healthy tissues can be reduced significantly [52, 55, 68]. Reports also exist of the possibility of using broadband signals to focus electromagnetic waves and reduce hot spots [23, 69], although mostly for low loss breast tissue.

2.2 Wireless Body Area Network

Wireless body area network (WBAN) consist of a number of wireless devices that communicate with each other and are either wearable or implantable in the human body. This can, e.g. be a single wireless sensor inside the body that communicates to an outside network such as a local area network, or a number of sensors on the body communicating with each other. The term wireless body-centric communications describes the communication method between modules located in and around the body.

There are three scenarios for wireless body-centric communications, where the two most relevant will be covered below:

- Off-body, where a device located on a body communicates with one or more devices located off-body (not covered here).
- On-body, where a number of devices located on the body communicate with each other.
- In-body, where some (or all) of the devices are implanted in the body, rather than worn (e.g. pace-makers).

Over the last few years, the interest of WBANs has grown significantly and common applications of WBANs are within medicine, military, sports and multimedia. Writings by T.G. Zimmerman at IBM gave the field of personal area networks or, the more common, body area networks a lift into the current form [70,71]. Today, sensors are often placed in shoes of runners that can communicate with their mobile devices which makes a complete recording of the pace, distance, time elapsed and calories burned during the workout [72]. Wrist watches can record heart-rate while receiving GPS signals from satellites for accurate positioning [73]. For diagnosing sleeping disorders, a compact device is attached on the body to measure among other EEG, ECG and EMG signals and transmits the signals in real time over Bluetooth to a tablet or a personal computer to be diagnosed [74].

Sensor modules are often simply connected to a standard off-the-shelf wireless module for transmitting and receiving the necessary data without giving too much considerations to propagation paths or the influence of the body on the antenna. These standard wireless modules typically support widespread technologies such as Bluetooth, WLAN or Zigbee and are used for simplicity and to ensure reliable data transfer [75,76]. Bluetooth, WLAN and Zigbee operate in the license-free band between 2.4 and 2.5 GHz. Furthermore, Zigbee also operates at 868 MHz and 915 MHz bands [77]. A recently allocated band, the so-called MICS (Medical Implant Communication System) band, operating between 402 and 405 MHz is mainly aimed at communication between medical implants and external transceivers. This band is, however, limited to maximum EIRP of -16 dBm since the frequency band is shared with the METAIDS meteorological system [78].

The power consumptions of the sensors and wireless devices is one of the biggest concern in WBANs. The size and weight of the unit is at a large part determined by the battery required to supply current to the circuits. The running time of the unit is also determined by the battery size, since it is directly related to the power consumption. For these reasons, it can be essential to reduce power consumption as much as possible. The efficiency of the transmit and receive antenna as well as the ability to predict the propagation behaviour from or on the body are of high importance, especially when determining wave propagation path and attenuation of a system.

2.2.1 On-Body Communication

Transmitting from one place on the surface of the body to another place on the surface of the body is called on-body communication. Transmission paths can e.g. be direct line of sight or, the transmitter and the receiver can be on opposite sides of the body. For the line-of-sight case the propagation is simpler than when the path is a curved path, a reflecting path or a combination of both. The human body essentially acts as a wave guiding structure [79] which allows for curved paths. An example of this is in hearing aids where a person has one hearing aid in each ear and one device transmits data to the other hearing aid to obtain stereo sound effect in both ears [80]. Propagation model for the human head can e.g. be found in [81] whereas a conventional dual-slope model can be obtained to provide an on-body propagation model for the human body as a function of distance in [82].

A challenging part of any on-body system is the antenna design. An antenna placed on the skin of a person can experience detuning in resonance frequency and change in gain pattern [77, 83]. The electromagnetic properties of the skin varies from person to person and things such as increased perspiration can change the conductivity of the skin and therefore the antenna properties. Some on-body antennas [84, 85] show decreased efficiency of between 40% and 90% when placed on a phantom simulating muscle tissue [86]. Specialized antennas have been manufactured to excite creeping waves specifically for transmission along the curvature of the body in [87]. According to [88], in order to match the characteristics of the creeping waves, the on-body antennas must be vertically polarized with an end-fire pattern along the body surface.

2.2.2 In-Body Communication

Transmitting from a source inside the body and outwards to an external receiver and vice versa is known as in-body communication. Inductive coupling is the most commonly used technique for communicating with implanted devices, due to its simplicity and deep penetration into the human body owing to the non-magnetic properties of the body. Inductive coupling has typically very short range which requires the external transceiver to be touching the person [78]. A longer communication range can be achieved by operating at higher frequencies since that gives rise to propagating electromagnetic waves. This also improves the bandwidth and therefore higher bitrates can be realized.

The propagation behaviour of electromagnetic waves inside the human body is complicated to model due to the numerous different tissue types and variations in the human form between every individual. There have, however, been advances in this area over the last decade or so.

The creation of a propagation model for wireless body area networks started with [89] for small dipole antennas inside the body which have been further developed, e.g. in [90] where simulations and measurements are compared for a homogeneous phantom. Propagation models using heterogeneous models have since been introduced [91, 92]. Experiments with propagation models outside the body have also been presented [93]

A general limitation of transmitting data from within the human body is the signal to noise ratio (SNR) at the receiver's end. Faster data-rates call for wider bandwidth which often mean higher operating frequencies and with higher frequencies, power attenuation increases in human tissues, thus reducing the received signal power. More advanced modulation schemes than the classical QPSK (Quadrature Phase-Shift Keying) and FSK (Frequency-Shift Keying) are not considered practical in the case of medical implants as they require more data processing capabilities and are more power consuming. QPSK and FSK, however, require positive SNR in order to operate satisfactory [78]. Selection of the operating frequency not only determines the power attenuation in tissue due to tissue conductivity's frequency dependence, but it also determines the free-space path loss. This path loss is one of the largest single loss factors of the propagating wave between an implanted source and a transceiver external to the body and ultimately greatly influences the SNR. Beside selecting the optimal frequency, by increasing the transmitting power, the gains of the transmitting and receiving antennas as well as increasing the receiver's sensitivity are measures of increasing the SNR. The most effective and perhaps simple action could however be, to simply bring the transmitter and the receiver physically closer to each other, if possible.

Variations in implant situations can have high impact on propagation models. For example, when dealing with propagation models of implants in moving patients, transmitting to a stationary receiver at a distance from the patient, additional margin, due to fading, should be taken into a consideration to account for reflections in the patient's room [78, 94]. When dealing with an implant in a patient's stomach, there is a difference in whether the patient has recently eaten or not that has to be accounted for. Wave attenuation is shown to be greater and steeper if a radiator is placed inside an empty stomach (radiator surrounded with air) compared to a full stomach [95, 96]. When examining the effect of varying frequency close to the implanted source, revealing results appear. In [95] a drop in the E-field of approximately 90 dB, relative to the source, is seen within 7 centimetres from the source, almost independent of the frequency. This is suggested to be due to the quasi-static E-field's dependence on distance rather than frequency. Also it is noted that generally the average received signal decreases logarithmically with distance as expected.

2.3 Discussion

The objective of this work is to examine the possibility of using microwaves for external activation of drug release. The project description from Chapter 1 provides the guidelines for this work and must be followed. Beside these guidelines, I imposed a requirement as well which is that, the system shall operate in the far-field. Ultimately, the idea is that drug release inside the body can be activated externally for the convenience of the patient. This includes, but is not limited to, release of medicine during the night while the patient is sleeping. For this reason, only an unobtrusive system is considered as a possibility in this work. Even though this requirement poses a significant challenge to transmit sufficient power into the human body, it also simplifies wave propagation analysis.

Hyperthermia systems are treatment systems where patients are typically placed in the near-field of the applicators. This reduces the effect of path loss which is inevitable in systems that operate in the far-field. The power levels of hyperthermia systems are not applicable in the microwave activation system as the objective is not to heat tissue and maintain high temperatures over a period of time, rather it is to excite a receiving structure on a drug capsule.

Several hyperthermia systems utilize water bolus that is placed at the surface of the patient's skin. The transmitting antennas are typically submerged in this water bolus. This is done because from theory predictions and previous research, large wave reflections at air - skin interface have been observed. A theoretical analysis is performed on wave propagation at interfaces typical for the human body in Chapter 3, where a method of maximum transmission of power into the body is also suggested.

According to the literature, the number of antennas and the number of ring structures around the patient improves the ability to focus and reduces hot spots outside the focus point. However, a certain degree of simplicity had to be maintained and therefore four sources were considered sufficient to provide a proof-of-principle setup.

The operating frequency of the microwave activation system was chosen to be around 2.45 GHz. A number of phased-array hyperthermia systems have been reported to operate at this frequency, some specially designed for deep-seated tumour irradiation. Smaller wavelength of the operating system ensures narrower focus point, but the losses also increase with higher frequency and therefore it was a matter of compromise. The choice of operating frequency was ultimately decided based on the practicality of the availability of microwave components since for an entire system, numerous different components were required. A discussion on the choice of operating frequency is covered in further detail in Chapter 5.

As presented above, inductive coupling is the most commonly used technique for communicating with implanted devices which is rarely operated at

microwave frequencies. The literature of wireless body area networks largely covers only standard wireless modules such as Bluetooth, WLAN and Zigbee and generally not much consideration is given to the actual microwave part. There are, however, several reported cases where the propagation behaviour of EM waves inside the human body has been modelled, both for homogeneous and heterogeneous phantoms. The homogeneous model predicts approximately 5 dB power attenuation for every centimeter in muscle.

Chapter 3

Electromagnetic Properties of Biological Media

In this chapter, the electromagnetic properties of lossy media such as biological tissues are examined. Also the transmission and the reflection at boundaries of air and fat are studied for determining the power transfer into a body or a phantom.

3.1 Lossy Biological Media

Losses in media such as biological tissues are a consequence of a finite and non-zero conductivity. The conductivity typically contains both static and frequency dependent components that result in a current flow when an E-field is applied.

$$\nabla \times \mathbf{H} = \mathbf{J_c} + \mathbf{J_d}, \tag{3.1}$$

is one of Maxwell's equations and shows the relation between the magnetic field intensity, $\boldsymbol{H}$ and the two current densities in a source-free lossy dielectric media. $\boldsymbol{J_c}$ is the conduction current density which represents flow of electrons and holes and $\boldsymbol{J_d}$ is the displacement current density. The relation between the conduction current and the electric field intensity, $\boldsymbol{E}$, is

$$\mathbf{J_c} = \sigma_s \mathbf{E}, \tag{3.2}$$

where σ_s is the static conductivity (DC-conductivity) in [S/m]. Similarly for the displacement current and the electric flux density, $\boldsymbol{D}$, the relation is

$$\mathbf{J_d} = j\omega \mathbf{D}, \tag{3.3}$$

where ω is the angular frequency and can be represented by the frequency, f, $\omega = 2\pi f$.

The electric flux density and the electric field intensity are linked through the complex permittivity, $\dot{\epsilon}$ with:

$$\mathbf{D} = \dot{\epsilon}\mathbf{E}. \tag{3.4}$$

The complex permittivity has, as the name indicates, a real part and an imaginary part and is represented by

$$\dot{\epsilon} = \epsilon' - j\epsilon'' = \epsilon_0(\epsilon_r' - j\epsilon_r''), \tag{3.5}$$

where ϵ_0 is the permittivity of vacuum ($8.854 \cdot 10^{-12}$ F/m), ϵ_r' is the real part (often referred to as the relative dielectric constant) and ϵ_r'' is the imaginary part of the relative permittivity.

The magnitude of the real part is directly related to the medium's ability to store E-field whereas the imaginary part represents the losses in the medium as a result of an oscillating E-field.

By inserting (3.2) through (3.5) into (3.1) the result is

$$\nabla \times \mathbf{H} = \sigma_s\mathbf{E} + j\omega(\epsilon' - j\epsilon'')\mathbf{E} \tag{3.6}$$

$$= (\sigma_s + \omega\epsilon'')\mathbf{E} + j\omega\epsilon'\mathbf{E} \tag{3.7}$$

$$= \sigma_e\mathbf{E} + j\omega\epsilon'\mathbf{E}, \tag{3.8}$$

where σ_e is the effective conductivity and is given by

$$\sigma_e = \sigma_s + \omega\epsilon''. \tag{3.9}$$

The effective conductivity is frequency dependent and includes both losses due to conduction current as well as losses due to displacement current. The effective conductivity is used throughout this work and will be interchangeably referred to as the effective conductivity or simply the conductivity. Materials that often are nearly lossless at DC, such as deionized water that has $\sigma_s = 0.0001$ S/m [97] become lossy at microwave frequencies. At 2.45 GHz e.g., the conductivity is $\sigma_e = 1.35$ S/m for deionized water and the losses are almost solely due to the displacement current.

Table 3.1 lists examples of relative permittivity and conductivity values for some typical biological tissues at 2.45 GHz [98, 99].

The complex propagation constant γ is composed of α and β and their relationship is

$$\gamma = \alpha + j\beta. \tag{3.10}$$

The propagation constant describes the phase change and attenuation of a travelling wave in a lossy medium.

Table 3.1: Typical relative permittivity and effective conductivity for biological tissues at 2.45 GHz.

Tissue	ϵ_r'	σ_e [S/m]
Fat	5.28	0.10
Bone	15.0	0.60
Skin	38.0	1.46
Brain	42.5	1.51
Muscle	53.6	1.81

Wave attenuation in media is dependent on σ_e and ϵ_r' and is represented using the attenuation constant by [100, pp. 139]

$$\alpha = \omega\sqrt{\mu\epsilon'}\left\{\frac{1}{2}\left[\sqrt{1+\left(\frac{\sigma_e}{\omega\epsilon'}\right)^2}-1\right]\right\}^{\frac{1}{2}}, \tag{3.11}$$

where μ is the permeability. All parameters are that of the media. The permeability of biological tissue is approximately the same as that of vacuum and can therefore be directly replaced by $\mu_0 = 4\pi \cdot 10^{-7}$ H/m [101, pp. 33]. In a lossless media σ_e is zero and therefore α becomes zero as well. The phase constant, β, is similarly [100, pp. 139]

$$\beta = \omega\sqrt{\mu\epsilon'}\left\{\frac{1}{2}\left[\sqrt{1+\left(\frac{\sigma_e}{\omega\epsilon'}\right)^2}+1\right]\right\}^{\frac{1}{2}}. \tag{3.12}$$

Table 3.2 shows α and β of skin, fat and muscle at 2.45 GHz, based on ϵ_r' and σ_e from Table 3.1. As can be seen, the attenuation in every cm of muscle is very close to the attenuation in a cm of skin, or approximately 4 dB, which can be found by multiplying α with 0.08686 [97].

Table 3.2: Typical attenuation constants and phase constants for biological tissues at 2.45 GHz along with the wavelength in the tissue.

Tissue	α [Np/m]	α_{dB} [dB/cm]	β [rad/m]	λ [cm]
Muscle	46.24	4.01	378.67	1.7
Fat	15.29	1.33	169.55	5.3
Skin	44.31	3.85	319.57	2.0

3.2 Transmission and Reflection at Interfaces

Radiating electromagnetic waves at a human torso for the purpose of having power penetrating into a tissue efficiently, requires considerations about wave behaviour at interfaces between two media. Attention is directed at the air-fat interface which analogous to the experimental setup to be presented in Chapter 5. This kind of interface can cause large reflections, thus low penetration of power.

Electromagnetic waves that are traveling from air (media 1) across an air-fat interface are partially reflected at the interface and the rest is transmitted into the fat (media 2). The levels of the reflected and the transmitted waves depend upon the respective permittivities and conductivities as well as the polarization and the incidence angle of the field. This will be further explained in the next sections.

3.2.1 Lossless - Lossless Interface

Biological tissues such as muscle and skin can be considered as a intermediate conductive media, on the low conductive end. A good dielectric is a media that fulfils $(\sigma/\omega\epsilon') \ll 1$ and a good conductor as a media that fulfils $(\sigma/\omega\epsilon') \gg 1$ [100, pp. 74-75].

At 2.45 GHz, muscle has $e'_r = 53.6$ and $\sigma = 1.81$ S/m [98] which gives $(\sigma/\omega\epsilon') = 0.25$. Disputably, 0.25 is not *much* less than 1 and therefore muscle is categorized here as a intermediate conductive media. Fat is in general slightly lossy, with $(\sigma/\omega\epsilon') = 0.14$ and can be categorized as either a intermediate conductive media or as a good dielectric. In this section, lossless fat is defined as a medium that has similar permittivity to fat but with zero conductivity. The simplification of a lossless fat in this section is for illustrating the transmission and reflection behaviour at a air-fat boundary in approximate manner.

In Figure 3.1, two media with a planar interface are shown for two polarization cases. Media 1 (air) has the permittivity ϵ_1 and permeability μ_1 and media 2 (fat) has correspondingly ϵ_2 and μ_2. The conductivities σ_1, σ_2 are 0 S/m as both media are considered lossless for now.

If there is an incident uniform TEM (transverse electromagnetic) wave travelling from air into a fat at an incident angle, θ_i, in respect to the normal to the planar interface of the two media, part of the wave gets reflected while the rest is transmitted into the lossless fat. The plane of the interface lies in the x-y plane and the normal vector out of media 2, $\hat{n}$, is in the negative z direction.

The incident wave can be split into a linearly polarized perpendicular component and a parallel component, as shown in Figure 3.1(a) and 3.1(b), respectively. A perpendicular polarized wave has the E-field vector perpendicular to the plane created by the direction vector of the incident wave,

$\hat{k^i}$, and the unit vector $\hat{n}$. This E-field vector points towards the viewer. A parallel polarized wave has the E-field vector in the plane formed by $\hat{k^i}$ and the unit vector $\hat{n}$. This E-field vector lies in the plane of the figure. These two polarizing cases can be treated separately.

From Snell's laws of reflection and refraction for lossless media we have

$$\sin\theta_i = \sin\theta_r, \tag{3.13}$$

$$\sqrt{\epsilon'_{r1}}\ \sin\theta_i = \sqrt{\epsilon'_{r2}}\ \sin\theta_t, \tag{3.14}$$

respectively, where θ_i is the incident angle, θ_r is the reflected angle and θ_t the transmitted angle as illustrated in Figure 3.1. The reflected and the transmitted angles can be found from Snell's law, if the angle of incidence and the media's electromagnetic properties are known.

Besides the directions of the travelling waves in air and fat, the reflection and the transmission coefficients at the boundary, is of interest.

From [100, pp. 179-180] we have for a perpendicular polarized wave at the boundary

$$\Gamma_\perp = \frac{E^r_\perp}{E^i_\perp} = \frac{\eta_2\cos\theta_i - \eta_1\cos\theta_t}{\eta_2\cos\theta_i + \eta_1\cos\theta_t}, \tag{3.15}$$

$$T_\perp = \frac{E^t_\perp}{E^i_\perp} = \frac{2\eta_2\cos\theta_i}{\eta_2\cos\theta_i + \eta_1\cos\theta_t}, \tag{3.16}$$

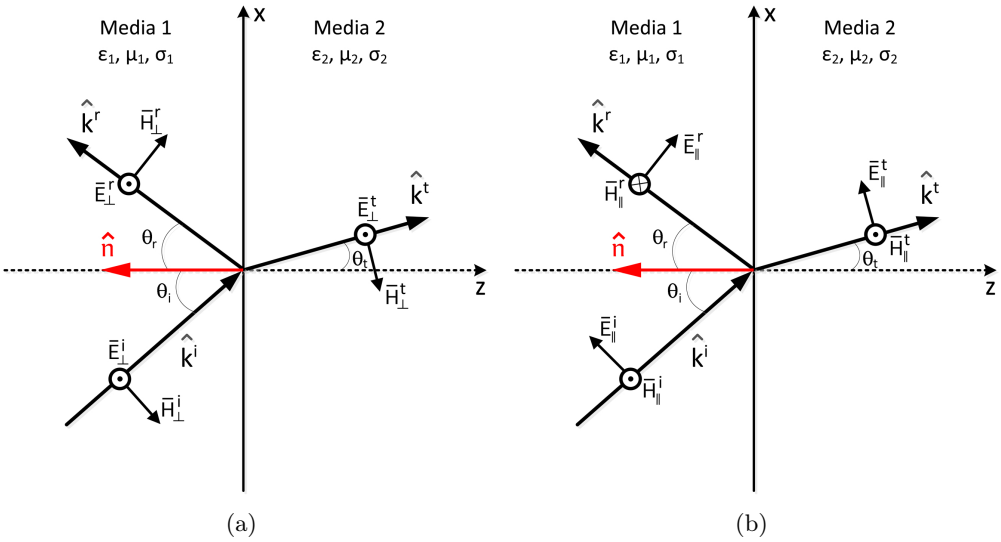

Figure 3.1: Incident, reflected and transmitted wave at the interface of two media. In (a) is a perpendicular polarized wave and in (b) is a parallel polarized wave.

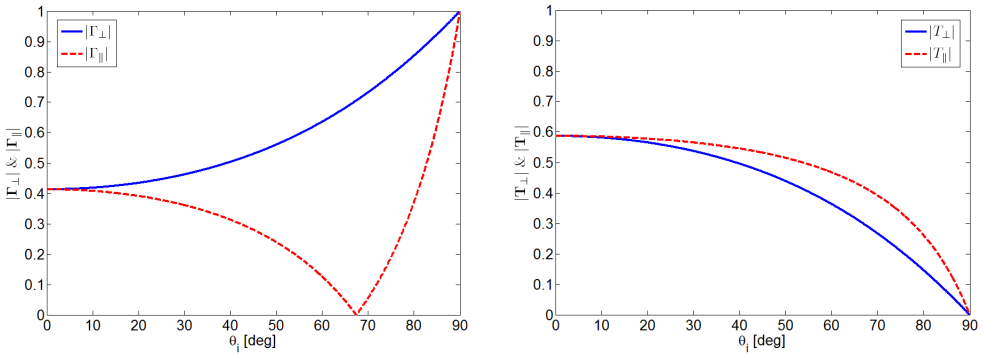

(a) (b)

Figure 3.2: The perpendicular and parallel reflection and transmission coefficients at boundary of media with $\epsilon'_{r1} = 1$ (air) and $\epsilon'_{r2} = 5.8$ (lossless fat). The magnitude of the reflection coefficient is shown in (a) and the magnitude of the transmission coefficient is shown in (b).

where $\Gamma_\perp$ is the perpendicular reflection coefficient, $T_\perp$ is the perpendicular transmission coefficient, $E^i_\perp$, $E^r_\perp$, $E^t_\perp$ are the perpendicular incident, reflected and transmitted E-field amplitudes respectively. $\eta_1 = \sqrt{\mu_1/\epsilon_1}$ and $\eta_2 = \sqrt{\mu_2/\epsilon_2}$ are the wave impedances in media 1 and media 2, respectively.

For the parallel polarized wave at the boundary we have similarly

$$\Gamma_\parallel = \frac{E^r_\parallel}{E^i_\parallel} = \frac{-\eta_1 \cos\theta_i + \eta_2 \cos\theta_t}{\eta_1 \cos\theta_i + \eta_2 \cos\theta_t}, \tag{3.17}$$

$$T_\parallel = \frac{E^t_\parallel}{E^i_\parallel} = \frac{2\eta_2 \cos\theta_i}{\eta_1 \cos\theta_i + \eta_2 \cos\theta_t}, \tag{3.18}$$

where $\Gamma_\parallel$ is the parallel reflection coefficient, $T_\parallel$ is the parallel transmission coefficient, $E^i_\parallel$, $E^r_\parallel$, $E^t_\parallel$ are the parallel incident, reflected and transmitted E-field amplitudes respectively.

The magnitudes of the perpendicular and parallel reflection and transmission coefficients are plotted in Figure 3.2 as a function of the incident angle. In Figure 3.2(a) the reflection coefficients from (3.15) and (3.17) are illustrated for a boundary with media 1 having $\epsilon'_{r1} = 1$ (approximately same as air) and $\epsilon'_{r2} = 5.8$ (similar to fat) as a function of the incident angle. In Figure 3.2(b) the corresponding transmission coefficients from (3.16) and (3.18) are displayed.

For the parallel polarization there is an noteworthy behaviour, at the so-called Brewster angle at around 67° where the reflection coefficient goes towards zero. Contrary to what one might expect, the corresponding parallel transmission coefficient does not approach 1 at the Brewster angle as is shown in Figure 3.2(b). In order to see how much energy flows into the lossless fat

in the parallel case, the power transmission coefficient, $T_{\parallel}^{PWR}$, is found. The time-averaged power densities for the incident, reflected and transmitted plane waves are

$$\vec{S}^i = \frac{1}{2}\Re\left\{\vec{E}^i \times \vec{H}^{i*}\right\} = \frac{1}{2\eta_1}\left|E^i\right|^2 \hat{k}^i, \tag{3.19}$$

$$\vec{S}^r = \frac{1}{2}\Re\left\{\vec{E}^r \times \vec{H}^{r*}\right\} = \frac{1}{2\eta_1}\left|E^r\right|^2 \hat{k}^r, \tag{3.20}$$

$$\vec{S}^t = \frac{1}{2}\Re\left\{\vec{E}^t \times \vec{H}^{t*}\right\} = \frac{1}{2\eta_2}\left|E^t\right|^2 \hat{k}^t, \tag{3.21}$$

respectively. The energy that is incident on a unit area of the interface of the two media is the normal component of the power density vector. This also applies to the energies propagating away from the interface, the reflected and transmitted power densities. This results in

$$\hat{n}\cdot\vec{S}^i = -\frac{1}{2\eta_1}\left|E^i\right|^2 \cos\theta_i, \tag{3.22}$$

$$\hat{n}\cdot\vec{S}^r = \frac{1}{2\eta_1}\left|E^r\right|^2 \cos\theta_r, \tag{3.23}$$

$$\hat{n}\cdot\vec{S}^t = -\frac{1}{2\eta_2}\left|E^t\right|^2 \cos\theta_t, \tag{3.24}$$

where the minus signs of the incident and transmitted waves are due to the fact that their respective $\hat{k}$ vectors are in the opposite direction to the vector normal to media 2, $\hat{n}$.

The power transmission coefficient, $T_{\parallel}^{PWR}$ can now be found as

$$T_{\parallel}^{PWR} = \frac{\hat{n}\cdot\vec{S}^t}{\hat{n}\cdot\vec{S}^i} = \frac{\eta_1\left|E_{\parallel}^t\right|^2\cos\theta_t}{\eta_2\left|E_{\parallel}^i\right|^2\cos\theta_i} = \sqrt{\frac{\epsilon'_{r2}}{\epsilon'_{r1}}}\frac{\cos\theta_t}{\cos\theta_i}\left|T_{\parallel}\right|^2, \tag{3.25}$$

as well as the power reflection coefficient

$$\Gamma_{\parallel}^{PWR} = \frac{\hat{n}\cdot\vec{S}^r}{\hat{n}\cdot\vec{S}^i} = \frac{\eta_1\left|E_{\parallel}^r\right|^2\cos\theta_r}{\eta_1\left|E_{\parallel}^i\right|^2\cos\theta_i} = \left|\Gamma_{\parallel}\right|^2, \tag{3.26}$$

since from Snell's law of reflection, (3.13), $\theta_i = \theta_r$.

Figure 3.3 illustrates the parallel power transmission and reflection coefficients as a function of the incidence angle at the boundary of two media having $\epsilon'_{r1} = 1$ and $\epsilon'_{r2} = 5.8$, as before.

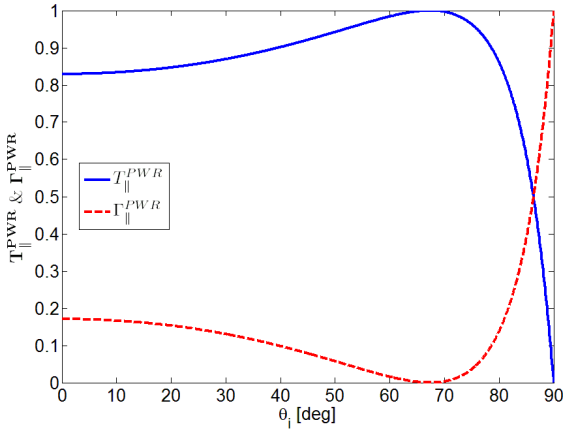

Figure 3.3: The power transmission and reflection coefficients as a function of the incidence angle.

At the Brewster angle [100, pp. 187],

$$\theta_B = \tan^{-1}\left(\sqrt{\frac{\epsilon'_{r2}}{\epsilon'_{r1}}}\right), \tag{3.27}$$

all the energy flows into media 2 and nothing is reflected, as can be seen from Figure 3.3.

3.2.2 Lossless - Lossy Interface

Now, the case when media 1 is air ($\sigma = 0$) as before and media 2 is a lossy fat (typical fat), is considered [100]. Regardless of the polarization, the E-field in fat can be described as

$$\vec{E}_t = \vec{E}_2 e^{-(\alpha_2 + j\beta_2)(x\sin\theta_t + z\cos\theta_t)}, \tag{3.28}$$

where $(\alpha_2 + j\beta_2)$ is the complex propagation constant from (3.10) and $\vec{E}_2$ is the E-field intensity vector in the fat, holding information about the amplitude and the polarization of the wave. θ_t is the angle that the wave is expected to make with the normal of the interface, out of media 1 as shown in Figure 3.1. $(x\sin\theta_t + z\cos\theta_t)$ describes the direction of propagation in the fat.

Snell's law of refraction for lossy media can be written as

$$\gamma_1 \sin\theta_i = \gamma_2 \sin\theta_t \Longleftrightarrow \sin\theta_t = \frac{j\beta_1}{\alpha_2 + j\beta_2}\sin\theta_i. \tag{3.29}$$

Using $\cos^2\theta_t + \sin^2\theta_t = 1$, we can write

$$\cos\theta_t = \sqrt{1 - \left(\frac{j\beta_1}{\alpha_2 + j\beta_2}\right)^2 sin^2\theta_i} = s(\cos\zeta + j\sin\zeta), \tag{3.30}$$

where $s(\cos\zeta + j\sin\zeta)$ is a vector in the complex plane since θ_t is clearly a complex angle, indicating a non-uniform wave. Inserting (3.30) and (3.29) into (3.28), $\vec{E}_t$ can now be written as

$$\vec{E}_t = \vec{E}_2 e^{-(\alpha_2 + j\beta_2)\left(x\frac{j\beta_1}{\alpha_2+j\beta_2}\sin\theta_i + zs(\cos\zeta + j\sin\zeta)\right)}. \tag{3.31}$$

The $\frac{j\beta_1}{\alpha_2+j\beta_2}$ term from (3.30) can be rewritten as

$$\frac{j\beta_1}{\alpha_2 + j\beta_2} \cdot \frac{\alpha_2 - j\beta_2}{\alpha_2 - j\beta_2} = \overbrace{\frac{\beta_1\beta_2}{\alpha_2^2 + \beta_2^2}}^{a} + j\overbrace{\frac{\beta_1\alpha_2}{\alpha_2^2 + \beta_2^2}}^{b}, \tag{3.32}$$

where a represents the real part and b the imaginary part. (3.30) can now be rewritten as

$$\cos\theta_t = \sqrt{1 - \left(a^2 + j2ab - b^2\right) sin^2\theta_i}, \tag{3.33}$$

and combining $s(\cos\zeta + j\sin\zeta)$ from (3.30) and (3.33), $\cos^2\theta_t$ becomes

$$\cos^2\theta_t = s^2(\cos\zeta + j\sin\zeta)^2 \tag{3.34}$$

$$= s^2\overbrace{(\cos^2\zeta - \sin^2\zeta)}^{\cos 2\zeta} + js^2\overbrace{2(\cos\zeta\sin\zeta)}^{\sin 2\zeta} \tag{3.35}$$

$$= 1 - a^2\sin^2\theta_i + b^2\sin^2\theta_i - j2ab\sin^2\theta_i. \tag{3.36}$$

From (3.35) and (3.36) the real parts must be equal, thus

$$s^2\cos 2\zeta = 1 - (a^2 - b^2)\sin^2\theta_i, \tag{3.37}$$

and the imaginary parts as well

$$s^2\sin 2\zeta = -2ab\sin^2\theta_i. \tag{3.38}$$

An effort to simplify the argument in the exponential of (3.31) yields

$$\begin{aligned} &-(\alpha_2 + j\beta_2)\left(x\frac{j\beta_1}{\alpha_2 + j\beta_2}\sin\theta_i + zs(\cos\zeta + j\sin\zeta)\right) \\ &= -x(a\alpha_2 - b\beta_2)\sin\theta_i - jx(b\alpha_2 + a\beta_2)\sin\theta_i \\ &\quad - z\overbrace{s(\alpha_2\cos\zeta - \beta_2\sin\zeta)}^{\alpha_{2e}} - jz\overbrace{s(\alpha_2\sin\zeta + \beta_2\cos\zeta)}^{q}, \end{aligned} \tag{3.39}$$

where we define $s(\alpha_2 \cos\zeta - \beta_2 \sin\zeta)$ as the effective attenuation constant, α_{2e} and $s(\alpha_2 \sin\zeta + \beta_2 \cos\zeta)$ as q, for ease of reference.

Examining the $(a\alpha_2 - b\beta_2)$ factor from (3.39) closer results in

$$(a\alpha_2 - b\beta_2) = \frac{\beta_1\beta_2}{\alpha_2^2 + \beta_2^2}\alpha_2 - \frac{\beta_1\alpha_2}{\alpha_2^2 + \beta_2^2}\beta_2 = 0. \tag{3.40}$$

Likewise, the $(b\alpha_2 + a\beta_2)$ factor can be replaced by β_1 since

$$a = \frac{b\beta_2}{\alpha_2}, \tag{3.41}$$

and

$$b = \frac{\beta_1\alpha_2}{\alpha_2^2 + \beta_2^2} \Longleftrightarrow \beta_1 = b\alpha_2 + \frac{b\beta_2^2}{\alpha_2}, \tag{3.42}$$

which results in

$$\beta_1 = b\alpha_2 + a\beta_2. \tag{3.43}$$

Using the results from (3.39), (3.40) and (3.43), (3.31) can be written as

$$\vec{E}_t = \vec{E}_2 e^{-z\alpha_{2e}} \cdot e^{-j(x\beta_1 \sin\theta_i + zq)}. \tag{3.44}$$

The first thing to notice about the result in (3.44) is that the transmitted wave is indeed a non-uniform wave since the planes of constant amplitude and planes of constant phases do not coincide. It is noteworthy that the wave is only attenuated in the z-direction, regardless of the angle of incidence. In principle, it means that when the resulting wave is travelling in some direction in the x-z plane, as is the case here, only the travel in z-direction will cause attenuation. The magnitude of the attenuation is, however, dependent on the angle of incident. The resulting angle of transmission and the effective phase constant are

$$\psi_t = \tan^{-1}\left(\frac{\beta_1 \sin\theta_i}{q}\right), \tag{3.45}$$

$$\beta_{2e} = \sqrt{(\beta_1 \sin\theta_i)^2 + q^2}, \tag{3.46}$$

respectively.

In order to see the effect which the conductivity has on the properties of the transmitted wave in a typical (lossy) fat tissue, let's consider $\sigma_2 = 0.48$ S/m whereas $\sigma_1 = 0$ S/m as before. As derived above, the angle of transmission is altered by the introduction of losses in fat. Figure 3.4(a) shows a comparison in transmission angle of the lossless fat from Section 3.2.1 and the lossy fat presented above. The introduction of losses in fat results in a smaller transmission angle. In fact, as the conductivity increases,

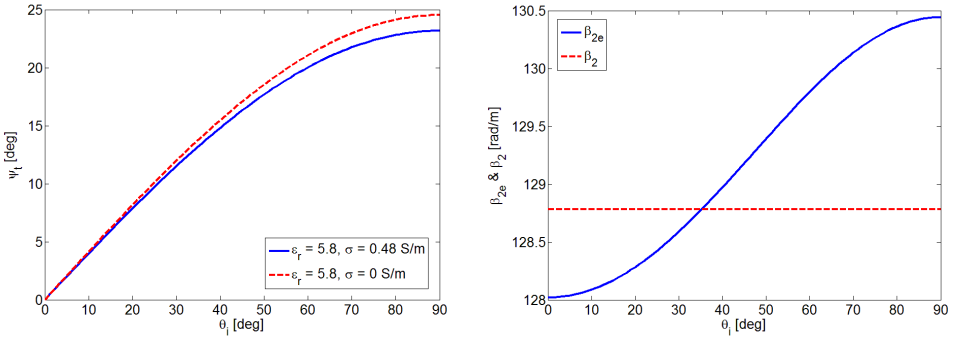

(a) (b)

Figure 3.4: In (a) the angle of transmission for lossless and intermediate conductive media is shown. In (b) the phase constant of media 2 along with the effective phase constant of a travelling wave in lossy media at an oblique angle is shown.

the transmission angle approaches 0, since there can not exist a tangential E-field in a perfect electrical conductor. Figure 3.4(b) illustrates how the conductivity slightly alters the behaviour of the phase constant in fat which becomes dependent on the incident angle in the lossy fat. This is also true for the effective attenuation constant, α_{2e}.

As will become evident later in this work, the ϵ'_{r2} and σ_2 values representing fat, actually are the measured values for a media that emulates the electromagnetic properties of fat in the microwave activation system (discussed in Appendix B).

3.2.3 Maximum Power Transfer into Tissue

The utilization of the Brewster angle is proposed for maximizing the power transfer into a tissue such as skin or fat. By using the Brewster angle, a minimum reflection and maximum transmission into tissue can be accomplished. Even though the case presented in Section 3.2.1 is for the lossless-lossless interface, a maximum in the transmission is still obtained at an air-fat interface which is an lossless-lossy interface. The Brewster angle is in the case of a lossy medium not an angle of full transmission. However, a biological tissue is merely an intermediate conductive media, or even low conductive media, which brings the maximum of transmission close to a full transmission (above 98%), as can be seen in Figure 3.5. The parameters in this simulation for the lossy fat are still the same as before, i.e., $\epsilon'_{r2} = 5.8$ and $\sigma_2 = 0.48$ S/m. For comparison, see Figure 3.3 for the lossless fat.

At an incident angle of approximately 69°, the resulting transmission angle becomes approximately 22° as was illustrated in Figure 3.4(a) and more than 98% of the power is transmitted into the fat.

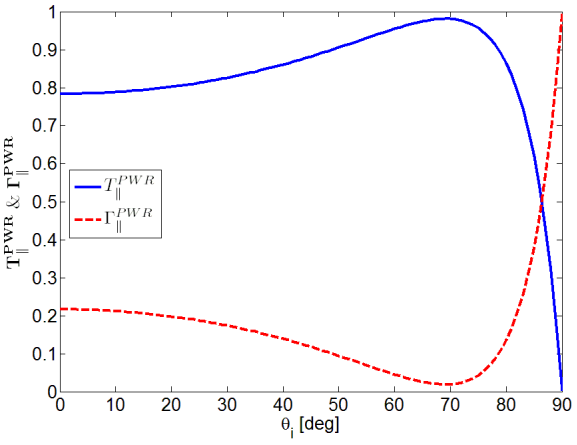

Figure 3.5: The power transmission and reflection coefficients as a function of the incidence angle when media 2 has $\epsilon_r' = 5.8$ and $\sigma = 0.48$ S/m.

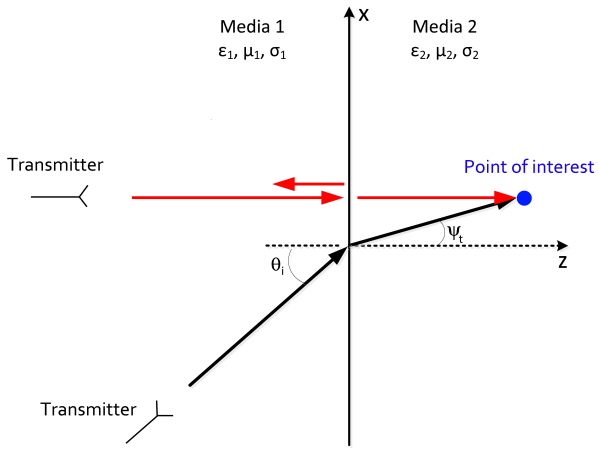

Figure 3.6: Transmission into a lossy media normal to the media and at the Brewster angle.

Two cases are compared in Figure 3.6. The first case is when a transmitter is normal to the interface and the second case is when a transmitter is oriented at an angle equal to the Brewster angle. As was illustrated in Figure 3.5 the Brewster angle provides a better power transfer than the normal, or 98% compared to 78%. This might not seem as a big difference but, if the dielectric properties of skin are taken instead of fat, the power transfer at the Brewster angle would be above 99% and only 47% at normal incidence.

The theory about the transmitted wave when the incident wave is at an oblique angle at an air-fat interface, presented in Section 3.2.2 which ultimately resulted in (3.44) stated that there only is an attenuation in the

z-direction. This fact is noteworthy since, at the Brewster angle, the transmitted wave travels farther in media 2 than the normal incident wave would, to reach the same point. The attenuations of the two waves in the Brewster case and the normal case are therefore the same at the *point of interest*, despite the additional travelling distance of the transmitted wave in the Brewster case.

The path loss, which is not accounted for, in this geometrical optic representation of the travelling waves, has to be taken into consideration since additional travelling distance would mean increased path loss. This could be solved simply by having the transmitter closer to the target, in the Brewster case.

This utilization of the Brewster angle for maximum power transfer can be further examined for multiple-layered media with increased complexity. The transmitted uniform plane wave at an oblique angle, travelling from a lossless to a lossy media becomes non-uniform as discussed above. Additional layers of lossy media would require solving for non-uniform waves at both sides of the boundaries of the two lossy media. In those cases it is easier to deal with modified propagation constants ($\hat{\alpha_{2e}}$ and $\hat{\beta_{2e}}$) than it is to deal with complex angles. It can be stated though, generally that, when travelling from a conductive media to a media with a similar or more conductivity, the modified propagation constants approach that of the intrinsic media propagation constants [102] as would be the case when travelling from fat to muscle. This is only true for their absolute values and not necessarily their direction.

Chapter 4

Muscle Tissue Mimicking Media Development

4.1 Introduction

For experimental setups of the interaction of microwaves and biological tissue, phantoms are traditionally used as the equivalent of a biological tissue. Phantoms are designed to have similar electromagnetic properties as a human, within a specific frequency range. Depending on the complexity of a phantom, it can consist of one or more different tissue mimicking media.

Several different types of phantom recipes have been proposed through the years such as [103–110]. Phantoms are often made from solid materials and high viscous gels that are optically non-transparent. These kinds of phantoms are preferred when they have to take a certain form, such as a leg or a head because they do not easily lose their original shape with time and can be cast in the required form. These kind of phantoms, however, cannot accommodate for free movements of measurement probes inside the media. One of the most important tissue type to mimic accurately is the muscle as it is one of the main cause of EM wave attenuation in the body and also it constitutes a large part of the human body.

4.2 Reference Medium

The most utilized muscle tissue mimicking media recipe for 2.45 GHz was presented by Chou *et al.* [103] and was therefore a possible candidate for this work. Its viscous properties were, however, undocumented and unknown. The recipe was followed and the resulting electromagnetic properties measured.

The mixture was fabricated from deionized water, household salt (NaCl), polyethylene powder ($<$20 μm diameter) and TX-151. When mixing together, the salt was first dissolved in the water, a drop of dishwashing liquid

was added to reduce the surface tension of the polyethylene powder in water, which was then added and stirred to get it all wet. Finally the TX-151 was gradually added while stirring, and the stirring was continued until the media started to get thick (like a thick sauce). The TX-151 is a gelling medium and helps making the mixture homogeneous, as the polyethylene powder would otherwise float on top of the water. Ten to twenty minutes after finishing mixing, the mixture had moved from a thick sauce-like texture and became a gel-like medium.

In Figure 4.1(a) a photo of a fabricated mixture following the recipe from [103] is shown. The mixture was mixed in a thin plastic cup and after half an hour, the plastic cup was removed. The blue colour comes from the colour of the polyethylene powder and illustrates that the media is optically non-transparent. The photo shows the viscous behaviour of the mixture as it holds its form and furthermore, holds up a coin.

4.2.1 Dielectric Measurement Procedure

Agilent's 85070E dielectric probe kit was used for measuring the dielectric properties of the muscle tissue mimicking media. This kit contains among other a slim coaxial probe, a small metallic plate for calibration, coaxial cable to be connected to a vector network analyzer (VNA) and USB key to activate the license of the measurement software. The slim coaxial probe was connected to a VNA through the coaxial cable, and a PC with a USB-to-GPIB converter connected to the VNA. Calibration of the slim probe of the dielectric kit was done by terminating the open end using air, de-ionized water at a known temperature and a metallic plate with a thin conductive flexible cover that acted as a short. There was a slight variation between each calibration, mostly due to the imperfect connection between the slim probe and the metallic plate. For verifying the calibration, ϵ_r' and σ of ethanol were measured because ethanol is a well documented medium in regards to electromagnetic properties over a wide frequency range. For comparison, a well-known Debye model based on previous measurements, [111], of ethanol was employed. The resulting comparison can be found in Appendix A.

Measurements of a medium was performed by dipping the open end of the slim probe into the medium to be measured. There was medium at least 5 mm radially from the centre of the tip of the probe in all directions for the measurements to fulfil the specification of the probe kit [112]. When the slim probe was dipped into a liquid, a small air bubble could form at the tip of the probe if not careful. This would result in a inaccurate measurement data and was checked before every measurement.

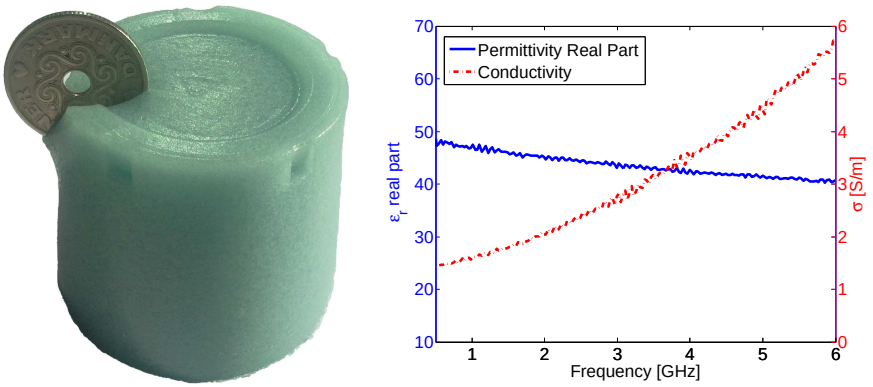

(a) (b)

Figure 4.1: In (a) a photo of fabricated muscle mimicking gel for 2.45 GHz from [103]. In (b) the real part of the relative permittivity and the conductivity are shown.

4.2.2 Measurement Results

Figure 4.1(b) shows measurement results of the real part of the permittivity and the conductivity of the medium. At 2.45 GHz, the real part of permittivity was measured to be 44.4 and the conductivity was 2.31 S/m. The parameters aimed for, in [103], are $\epsilon_r' = 47.0$ and $\sigma = 2.17$ S/m and the measured values were therefore within 6.5% of the proposed design values. The deviation from the aimed values was party due to the small mixture (in total 200 g) and the limitation to measure the weight accurately below ± 0.5 g, especially since the NaCl is the controlling factor for the conductivity while at the same time only accounts for 1.051 % of the total weight.

As a result from experimentally preparing the medium described above, it was clear that it could be cast with a measuring probe or an antenna inside and its electromagnetic properties were measured to be close of the design values. It was, however, not possible to move, e.g. an antenna around inside such medium while maintaining the medium's homogeneity, therefore it was unsuitable for the current application.

4.3 Design and Verification

Since the gel-like medium described above was too viscous and not transparent, a low-viscous, optically transparent muscle tissue mimicking media (MTMM) was developed to make it possible to easily move an antenna inside the medium.

A muscle tissue mimicking medium is presented using diethylene glycol butyl ether (DGBE) and de-ionized water for a phantom at 2.45 GHz. The DGBE was in liquid form at room temperature, and the resulting MTMM

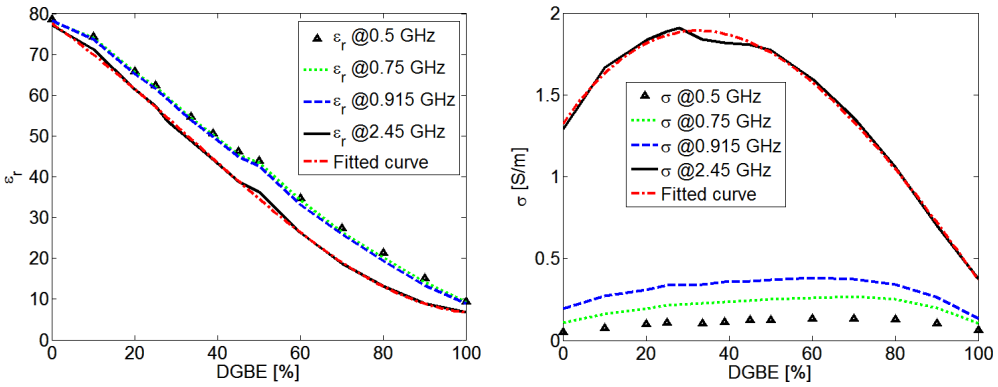

(a) (b)

Figure 4.2: In (a) is the measured relative permittivity of DGBE as a function of the weight-ratio of the total mixture for several frequencies, typical for biological systems. In (b) is the measured conductivity of DGBE as a function of the weight-ratio of the total mixture. The fitted curves are only valid for 2.45 GHz.

became a low-viscous liquid, with similar viscosity as water when mixed together. The recipe is summed up in Table 4.1. The MTMM was optically transparent and had the benefit that the two materials blended easily together. The DGBE has been used to mimic the EM behaviour of skin, [104], and human head [113], along with polyethylene glycol mono [4-(1,1,3,3-tetramethylbutyl) phenyl ether] (Triton X-100), at 2.45 GHz with success. Additionally NaCl was also used for the human head phantom to increase its conductivity.

Figure 4.2 shows measurement results of the proposed MTMM that consists of DGBE and de-ionized water. Figure 4.2(a) shows the real part of the relative permittivity of the MTMM and in Figure 4.2(b) the conductivity of the MTMM is shown, as function of the weight-ratio of DGBE in the DGBE-H_2O mixture. The parameters are displayed at several frequencies, typical for biological systems; 0.5 GHz, 0.75 GHz, 0.915 GHz, and 2.45 GHz. As can be seen, the relative variation of the relative permittivity over frequency of the mixture is very small compared to the relative variation of the conductivity for the same liquid. The conductivity is low for lower frequencies which is an advantage since it is generally easier to increase conductivity rather than decreasing it, e.g. by adding NaCl.

In 1996, Gabriel *et al.* [98, 114–116] presented a compilation of dielectric properties of body tissues where most results from the existing literature were combined along with measurements and models of the data. These results are typically used as reference for most work done today within the field of tissue mimicking media. The reference values of relative permittivity and conductivity for muscle tissue at 2.45 GHz are 53.6 and 1.81 S/m. In

Table 4.1: Simple muscle tissue mimicking media recipe at 2.45 GHz.

De-ionized water	DGBE
72%	28%

the abdominal region both transverse and parallel muscle groups can be found. There are a slight permittivity and conductivity differences between those muscle types, and the values of 53.6 and 1.81 S/m are the average of the two. From Figure 4.2, the closest permittivity of 53.5 is acquired when DGBE is 28% of the mixture. This results in a conductivity of 1.91 S/m. The deviations of the measured MTMM, compared to the reference, [114], are shown by

$$Error_{\epsilon_r} = \frac{|\epsilon_{rmeas} - \epsilon_{rref}|}{\epsilon_{rref}} < 0.19\%, \tag{4.1}$$

$$Error_{\sigma} = \frac{|\sigma_{meas} - \sigma_{ref}|}{\sigma_{ref}} < 5.53\%. \tag{4.2}$$

Along with the measurements in Figure 4.2, two 3rd order least-squares fitting polynomials, as shown in (4.3), are fitted to the 2.45 GHz measurements for both the relative permittivity and the conductivity, using MATLAB's curve fitting function, *polyfit*, that fits the data best in a least-squares sense. The parameters for each of the curves are presented in Table 4.2.

$$p(x) = p_1x^3 + p_2x^2 + p_3x + p_4, \tag{4.3}$$

where *p(x)* is the polynomial as a function of the variable x which, in the present case, is the weight-ratio of DGBE in the mixture.

Table 4.2: Parameters of the polynomial fitted curve at 2.45 GHz.

Parameter	Polynomial for ϵ_r	Polynomial for σ
p_1	$6.18363728 \cdot 10^{-5}$	$2.04026154 \cdot 10^{-6}$
p_2	$-6.25630329 \cdot 10^{-3}$	$-6.70726099 \cdot 10^{-4}$
p_3	$-7.00787624 \cdot 10^{-1}$	$3.71651344 \cdot 10^{-2}$
p_4	$7.75912484 \cdot 10^{1}$	$1.32226342 \cdot 10^{0}$

The polynomial presented can be used for creating a recipe for a new tissue mimicking media, emulating other parts of the body. As an example, the grey matter of the brain has a relative permittivity and a conductivity of 48.91 and 1.808 S/m respectively [114]. By composing two polynomials (one for the permittivity and one for the conductivity), a permittivity value

Table 4.3: Improved muscle tissue mimicking media recipe at 2.45 GHz.

De-ionized water	DGBE	Triton X-100
72%	23%	5%

of 48.96 can be found which corresponds to a DGBE ratio of 34%. This DGBE ratio results in a conductivity of 1.891 S/m and is within 4.7% of the reference values for the grey matter.

The degrees of freedom in a medium with only two ingredients, limit the range of relative permittivity and conductivity that can be simultaneously accomplished. Adding another medium, such as Triton X-100 adds another degree of freedom and makes it possible to fine-tune the muscle tissue mimicking media. Triton X-100 has both lower permittivity and lower conductivity than DGBE, but the relative difference in conductivity is larger than for the permittivity and can therefore be used to reduce the conductivity deviation from (4.2).

Figure 4.3(a) and Figure 4.3(b) show the relative permittivity and conductivity, respectively, for the DGBE-H_2O recipe (First DGBE recipe) presented in Table 4.1 along with an optimized recipe, proposed in Table 4.3. A 4-Cole-Cole model of muscle tissue, [114], is also depicted in Figure 4.3 as reference. The new ϵ_r' and σ, for the improved media, are measured to be 53.67 and 1.797 S/m respectively at 2.45 GHz which means that the deviation from the reference is less than 1%, i.e. 0.13% for the permittivity and 0.72% for the conductivity. The ISM band of 2.4 - 2.4835 is confined between the two blue dotted lines. Figures 4.3(c) and 4.3(d) show the same measurement as in Figures 4.3(a) and 4.3(b), respectively, but here the graphs are zoomed in, restricted to the frequencies between 2 and 3 GHz.

4.4 Discussion

The muscle tissue mimicking media that is the most used in the literature by Chou *et al.* [103] was prepared in order to determine its viscosity and to compare the measured electric parameters to that of the literature. The formula was found to be too viscous to be able to freely move an antenna around in it. A new recipe with DGBE and de-ionized water was proposed and its electrical parameters were measured to be within 6% of the design values. By adding another ingredient, Triton X-100, another degree of freedom resulted in a muscle tissue mimicking media that had electrical properties within 1% of the design values. The necessity of improving the mimicking media within 1%, from 6%, is arguable and depends upon the application and the strictness of the requirements at hand. Regardless of the require-

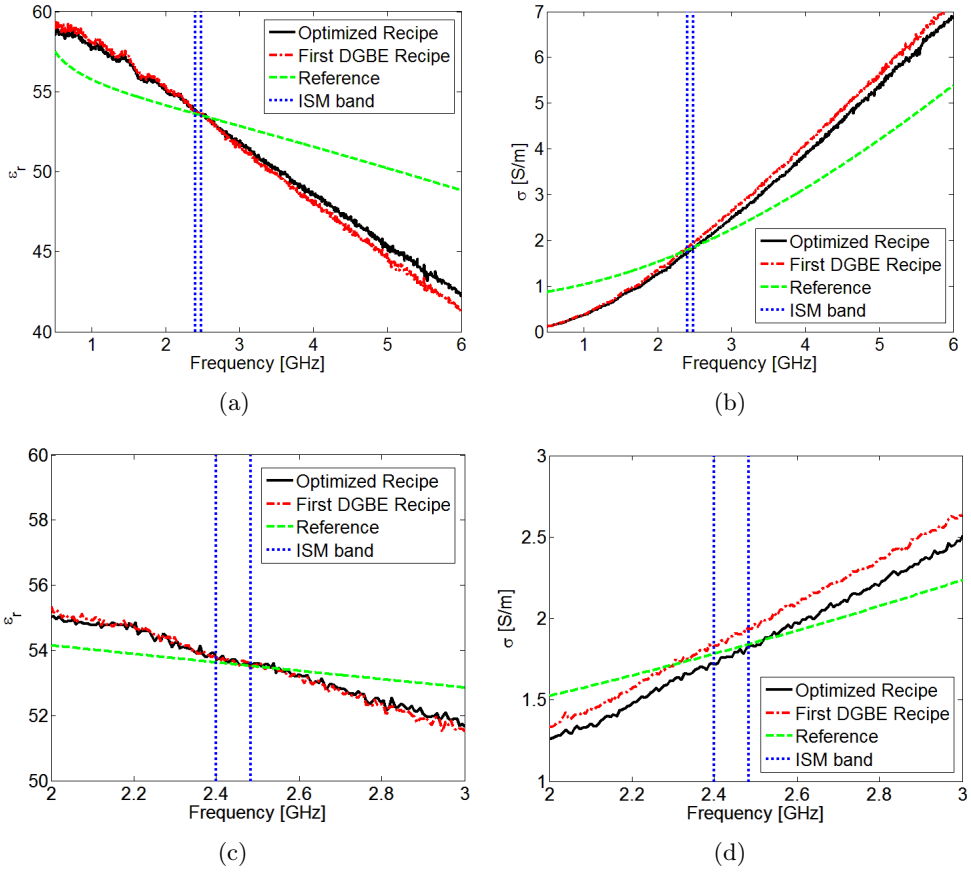

Figure 4.3: Figures 4.3(a) through 4.3(d) show measurements of the DGBE-H_2O and DGBE-Triton X-100-H_2O mixtures along with the reference. (a) shows the relative permittivity over wide frequency range, while (b) shows the conductivity over wide frequency range. (c) and (d) show zoomed views of (a) and (b), respectively.

ments, however, two slightly different low-viscous muscle tissue mimicking media that are very close to the design values from the literature have been presented for 2.45 GHz.

Chapter 5

Microwave Activation System - Overview

5.1 Introduction

Constructive interference of electromagnetic waves were proposed in Chapter 1 as the method to be utilized in the microwave activation system. Multiple superimposed waves that are in phase, add together creating a focus point. There are a number of critical design-choices to be made in a system that is to radiate electromagnetic waves inside the human body. These include operating frequency, number and location of antennas, pulsed vs. continuous wave, power level and flexibility of the system.

Generally with increasing frequency, attenuation in biological tissues increases and makes it more challenging to penetrate deeper into the body. With higher frequency, due to its smaller wavelength it is, however, possible to focus onto smaller volumes. Components such as antennas can be made smaller and that impacts the overall size of the system as well as the far-field region.

The most similar systems that focus electromagnetic waves inside the human body are non-invasive electromagnetic hyperthermia systems. These systems are able to illuminate the surface or the sub-surface of a body part in order to heat up a specific volume. The heat is usually applied to regions in the body that contain a cancerous tissue for the purpose of increasing chemo- and radiation therapy's effectiveness. Hyperthermia systems have been made, utilizing various frequencies, typically within any of the ISM bands between 40 MHz and 2.45 GHz.

The two most often used frequencies within hyperthermia throughout the years have been 433 MHz and 915 MHz. There have been several publications regarding selection of the optimal frequency for penetrating deep into biological tissue. The suggested frequencies are among others 1.5 GHz [117] and 1 GHz [118]. Practical matters such as the size of the radiating an-

tennas, availability of components at the operating frequency and cost also affect the choice of frequency. Typically the physical size of the antenna needs to be around one half the operating wavelength. Antennas that are smaller than that tend to have reduced efficiency. In general, with increasing frequency the focus point inside the tissue becomes smaller. The half-power spot size at the focal depth is around 3/4 of the wavelength in diameter [43]. The conductivity of biological tissue also increases with higher frequencies, as was shown in Section 4, resulting in higher power loss. A trade-off therefore has to be made when selecting the operating frequency. As stated in Chapter 2, the operating frequency of the current microwave activation systems is chosen to be 2.45 GHz mainly because the required components are readily available. The fact that the antennas can be relatively small sized and the predicted focus area is smaller than it would be at lower frequencies are also good qualities. Limited existing research on the topic, at 2.45 GHz also makes it interesting to examine and perhaps supplement to the existing research, if possible. The system is designed to cover a bandwidth of 100 MHz, i.e. from 2.4 to 2.5 GHz to cover the ISM band and more importantly, to allow for manufacturing deviations.

The process of typical medication such as orally ingested pills as described in Chapter 1, has its difficulties. The introduction to a microwave activation system for drug release is to offer an alternative solution to standard drug delivery mechanisms. The goal is to deliver drugs without presenting a restrain to a person. That means that strapping a person with a belt of antennas or having a person lie in a specially made bench where bags of water are placed on the person could be avoided. A drug delivery system of that kind would almost defeat the purpose of its existence if a person needs to strap on a belt every time they need a dose of medicine, instead of just taking a pill or having an injection.

Having an unobtrusive microwave activation system inherently causes several issues. One of the issues is the power coupling from air to the tissue. Air has a relative permittivity close to 1 and coupling into a tissue that has a relative permittivity of 38 - 53, depending on the type of tissue, causes a high reflection at the boundary. As was presented in Section 3.2.3, the reflected power of a normal incident plane wave is approximately 53% (-3.3 dB) of the incident power, making less than half of the transmitted power enter into the tissue. It is however worth mentioning that a reflection loss of 3.3 dB is equivalent to losses that would occur in less than 0.9 cm of extra muscle thickness. Variation of muscle mass between individuals can easily be beyond 0.9 cm, hence the reflection loss is not a dominant factor.

Another important issue is the path loss that occurs in travelling waves. The path loss decreases the power density with distance from the radiating antenna. The farther the radiating antennas are from the target, the less power is radiated onto the target.

5.2 Operating Principle

The experimental setup for microwave activation consists of four antennas, a simple dual-layered cylindrical phantom, a single antenna operating inside the phantom, four transmitters, four receivers, two frequency synthesizers, a driver amplifier, three power dividers along with a PC and data acquisition hardware. The outer layer of the phantom represents fat layer of a human and the inner layer represents a muscle layer.

The principle of operation for the experimental setup is twofold. First, an antenna that is operating inside of a phantom (internal antenna) is connected to a single transmitter and radiates EM waves from within the phantom and outwards. Receivers are connected to four external antennas. The absolute and relative amplitudes and phases, respectively, at the locations of the external antennas are measured and collected using the data acquisition hardware along with the PC. This is referred to as *mapping*.

In the second part of operation, each of the four external antennas are connected to their own transmitter. Their relative amplitudes and phases are set to obtain constructive interference and hence a focus point. The internal antenna are used, connected to a single receiver, measuring the total amplitude received. This is referred to as *focusing*.

Focusing in this case can be considered the reciprocal of the mapping since the phantom media, as well as real biological tissues, are linear, isotropic and, with certain approximation, time-invariant media. For the experimental setup for microwave activation, Lorentz's reciprocity principle can be utilized, since the system fulfils the requirement for a reciprocal system [100, pp. 323]. The Lorentz's reciprocity principle can be written, when the fields are observed in the far field and the sources are in the same medium, as follows

$$\iiint_V (\vec{E_1} \cdot \vec{J_2} - \vec{H_1} \cdot \vec{M_2}) dv' = \iiint_V (\vec{E_2} \cdot \vec{J_1} - \vec{H_2} \cdot \vec{M_1}) dv', \tag{5.1}$$

where $\vec{J}$ and $\vec{M}$ are electric and magnetic sources, respectively. $\vec{E_1}$ and $\vec{H_1}$ are the electric and magnetic field intensities, respectively, that are generated by $\vec{J_1}$ and $\vec{M_1}$. Similarly, $\vec{E_2}$ and $\vec{H_2}$ are generated by $\vec{J_2}$ and $\vec{M_2}$. Assuming that we have no magnetic sources we get

$$\iiint_V (\vec{E_1} \cdot \vec{J_2}) dv' = \iiint_V (\vec{E_2} \cdot \vec{J_1}) dv'. \tag{5.2}$$

This form of reduced Lorentz's reciprocity theorem (5.2) states is that if e.g. a current density at location 1 generates an E-field at location 2, another equal current source which is at location 2, will generate the same E-field at location 1.

This essentially means that the forward transmission coefficient S_{21} has to be equal to the reverse transmission coefficient S_{12} for a system where

one radiator (port 1) is situated inside a medium such as a muscle tissue mimicking media and another radiator (port 2) is situated external to this medium, e.g. in air. If this is extended to 4 external radiators (port 2-5) instead of just one, $S_{21} = S_{12}$, $S_{31} = S_{13}$, $S_{41} = S_{14}$ and $S_{51} = S_{15}$ applies. From this follows that focusing can be considered as a so-called reverse excitation of mapping and the idea is shown in Figure 5.1.

The process of mapping measures the amplitudes and phases that could possibly be used for setting up the focusing. Furthermore, mapping reveals the behaviour of EM waves travelling from within the phantom and outwards, as a function of the location of the internal antenna in respect to the four external antennas. This can give a good indication of the behaviour in the reverse case, namely EM waves travelling from outside and into the phantom.

Figure 5.2 illustrates a simplified drawing of the structure of the microwave activation system, including the phantom and the external antennas. The four external antenna-mounts are fixed to wooden arms, which are mounted on a circular wooden disc, 65 cm from the edge of the phantom. This wooden disc has a circular extruded cut at its centre where the cylindrical phantom is fixed. The phantom is dual-layered and has a lid on top of the cylinders, where the internal antenna mount is placed. Both the external and internal antenna mounts (in black) are made from polyacetate which is specified to have $\epsilon_r' = 3.7$ and $\tan\delta = 0.006$ @ 1 MHz (the EM properties of polyacetate at microwave frequencies could not be found in the literature).

5.3 Human Torso Phantom Structure

Ever since the beginning of studying electromagnetic fields in biological tissues, phantoms have been developed. Phantoms are compositions of materials that emulate behaviour of electromagnetic fields in biological tissues such as human muscle, skin or fat, instead of using actual human tissue. In the microwave activation system, a phantom is used to emulate the human torso where the drug release is expected to happen.

A drawing of the phantom structure and its lid with the antenna mount is shown in Figure 5.3(a) along with a photo of the setup in Figure 5.3(b). The inner cylinder is white whereas the outer cylinder and the lid is transparent.

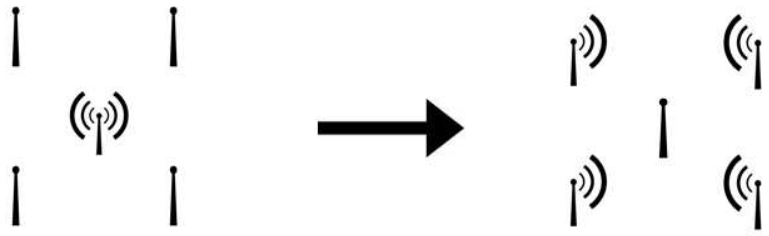

Figure 5.1: Reverse excitation of a reciprocal system.

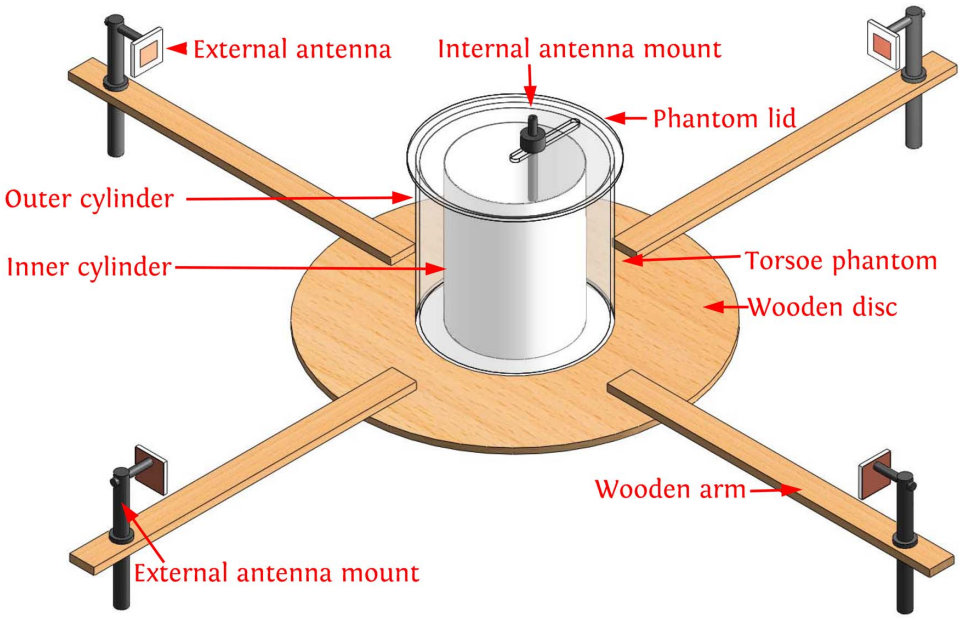

Figure 5.2: Drawing of the structure of the microwave activation system.

The inner cylinder is to contain the muscle tissue mimicking media described in Chapter 4 while the outer cylinder is to contain fat tissue mimicking media described in Appendix B. The fat mimicking media consists of pure glycerin that is used because of simplicity and convenience, since glycerin was readily available at the university and it has electrical properties that are acceptable for fat tissue. The transceiving antenna is to be placed in the muscle tissue mimicking media and therefore the importance of a accurate equivalent medium for muscle is of higher importance than for fat.

The inner cylinder's dimensions are shown in Table 5.1. The inner cylinder is actually not a true cylinder as it has a slight conical slope (the top

Table 5.1: Dimensional and electrical parameters of the phantom.

Parameter	Inner Cylinder	Outer Cylinder
Material	Polypropylene	Polymethylmethacrylate
Inner Radius	14.1 cm	19.1 cm
Outer Radius	14.25 cm	19.9 cm
Height	37.0 cm	39.0 cm
ϵ_r'	2.26 [119]	2.61 [119]
tanδ	0.00008 @ 9.4 GHz [119]	0.008 @ 11 GHz [119]

(a) (b)

Figure 5.3: Drawing and a photograph of the phantom structure, with the internal antenna mount.

radius is 14.8 cm and bottom radius is 12.9 cm) and therefore the radius is taken approximately at the middle of its height. It will still be referred to as the inner cylinder hereafter regardless. The electrical parameters of the inner cylinder are shown in Table 5.1. The outer cylinder's dimensions and electrical parameters are also shown in Table 5.1. The outer cylinder is made of polymethylmethacrylate (PMMA) which is also known as acrylic glass or Plexiglas.

A disadvantage to a liquid phantom media is that a watertight container with finite thickness has to be used for each liquid and that causes fictitious separation at the boundaries between the two media as well as at the boundary between the fat mimicking media and air. Another challenge is to find or create containers that have the "right" proportionate size (diameter) in respect to each other. The thickness of the fat mimicking layer in the microwave activation system, 4.85 cm, is e.g. thicker than the average thickness of the abdominal cavity of 2 cm [120] and is limited by the available containers. The inner cylinder can, however, be moved closer towards the edge of the outer cylinder making the fat mimicking layer thinner on one side and thicker on another. Unless otherwise stated, the outer and inner cylinders are considered concentric and therefore the phantom is symmetrical in the vertical plane, going through the centre of the cylinders.

The internal antenna is mounted on a PMMA lid on top of the outer PMMA cylinder. The structure is such that, the lid can rotate in a full circle, as well as there is a slot for the antenna to move back and forward from the centre and outwards. In this way, the antenna can be continuously moved all around, inside the cylinder, to provide measurements at multiple locations. It is also possible to move the antenna up and down if needed. The internal antenna mount is made of polyacetate, the same as for the external

antenna mounts.

A doughnut shape piece of polystyrene is cut out and placed in between the two cylinders in order to hold the inner cylinder in a semi-fixed position in respect to the outer one. The polystyrene is placed above the fat mimicking media, occupying space that only occupied air before. As polystyrene is very close to air's permittivity, it does not influence the phantom. The polystyrene is not shown in the figures.

A disadvantage of using glycerin as the fat layer in the dual-layered phantom is that, the density of glycerin is higher than the density of the muscle tissue mimicking media. The inner cylinder is not completely fixed to the outer cylinder which means that inner cylinder floats, unless the volume of the glycerin is lowered a bit below the muscle media.

Figure 5.3 shows the phantom with a circular cross-section. The maximum power transfer into the phantom at the Brewster angle, as discussed in Section 3.2.3, can be possible for (maximum) two locations on the phantom from every single transmitter. In a near proximity of these locations, the power transfer will be higher than the normal incident case. A pre-destorting lens could perhaps be designed to obtain more locations of maximum power transfer and is a task for a future research. To utilize the maximum power transfer method in the experimental setup for focusing is complex and will not be covered in further details in this work. Although it will not be utilized in this work, the method was found to be interesting and I had not come across the combination of Brewster angle and oblique angle transmissions into lossy media in the literature, even though it might (probably) already have been published.

5.4 Continuous Wave vs. Pulsed Wave

When it comes to evaluating whether a continuous wave (CW) system or a pulsed wave (PW) system is best suited for microwave activation of drug release, several factors have to be considered such as safety, simplicity and functionality.

Human biophysical reactions to microwaves are mostly documented to be a thermo-physiological response. Experimental studies are in conflict when it comes to the comparison of the biophysical response of CW compared to PW, when the time-average radiated power is the same, or similar. In [121] and [122] e.g. no conclusive difference was found when applying PW compared to CW. However significant decrease in arterial blood pressures in rats have been reported [123] when radiated with PW and auditory effect such as clicking, buzzing and hissing noises are a known response to high peak E-field PW [124]. No conclusions can be made, currently, about the relative safety of using PW compared to CW. There seems however, to be a tendency throughout the literature, that either PW and CW causes similar

responses in tissue or, that PW causes more negative effects than CW, rather than vice versa.

A pulse can be represented as a Fourier transformation including multiple frequencies. As was presented in Section 4, the dielectric properties of biological tissues vary over frequency, making them frequency dispersive. This results in different phase velocities for waves of different frequencies as can be seen through

$$v_p = \omega/\beta, \tag{5.3}$$

where β is the same as presented in Equation 3.12. Lets consider two waves travelling in a muscle tissue, one at 2.45 GHz and the other at 4.9 GHz. The phase velocity for the 2.45 GHz would be $0.4065 \cdot 10^8$ m/s and $0.4183 \cdot 10^8$ m/s for 4.9 GHz. Without any losses in the muscle, the phase velocities would be approximately 1% higher than the presented values, indicating the relative insignificance of losses, to phase velocity in biological tissue. However, the relative permittivities of 53.6 and 50.3 at 2.45 GHz and 4.9 GHz, respectively, are responsible for the phase velocities being approximately 13-14% of the speed of light.

For biological tissues the most dominating factor in controlling dispersion is therefore the variation in relative permittivity with frequency. The losses in the tissues, even though they grow very fast with increasing frequency, have little influence on the dispersion. This is true as long as $(\sigma/\omega\epsilon')^2 << 1$ is fulfilled, which is typically the case for biological tissues at microwave frequencies below 6 GHz (e.g. $(\sigma/\omega\epsilon')^2 = 0.06$ for muscle tissue at 2.45 GHz). The dispersive effects described above can cause pulses to distort when travelling in the human body.

Analysis of pulses done in [125] indicates that, a PW does not penetrate deeper in tissues than CW signals having frequency equal to or lower than the fundamental frequency of the PW since higher harmonics of the fundamental frequency are attenuated more. The narrower the pulse is, the more attenuation occurs [64].

When it comes to simplicity, the CW system has the advantage. A pulsed system requires e.g. a pulse generator and all the circuits need to be relatively wideband. The CW system can on the contrary, be narrowband, therefore relaxing the requirements towards components and circuit designs.

All things considered, the CW approach is selected for the microwave activation system for drug release.

5.5 System-Level Block Diagram - *Mapping*

The system block design is carried out keeping in mind that, preferably the same equipment is to be used for both mapping and focusing, and therefore the link budgets for both setups are realized simultaneously. When determining the receiver architecture, the limitation of real components is

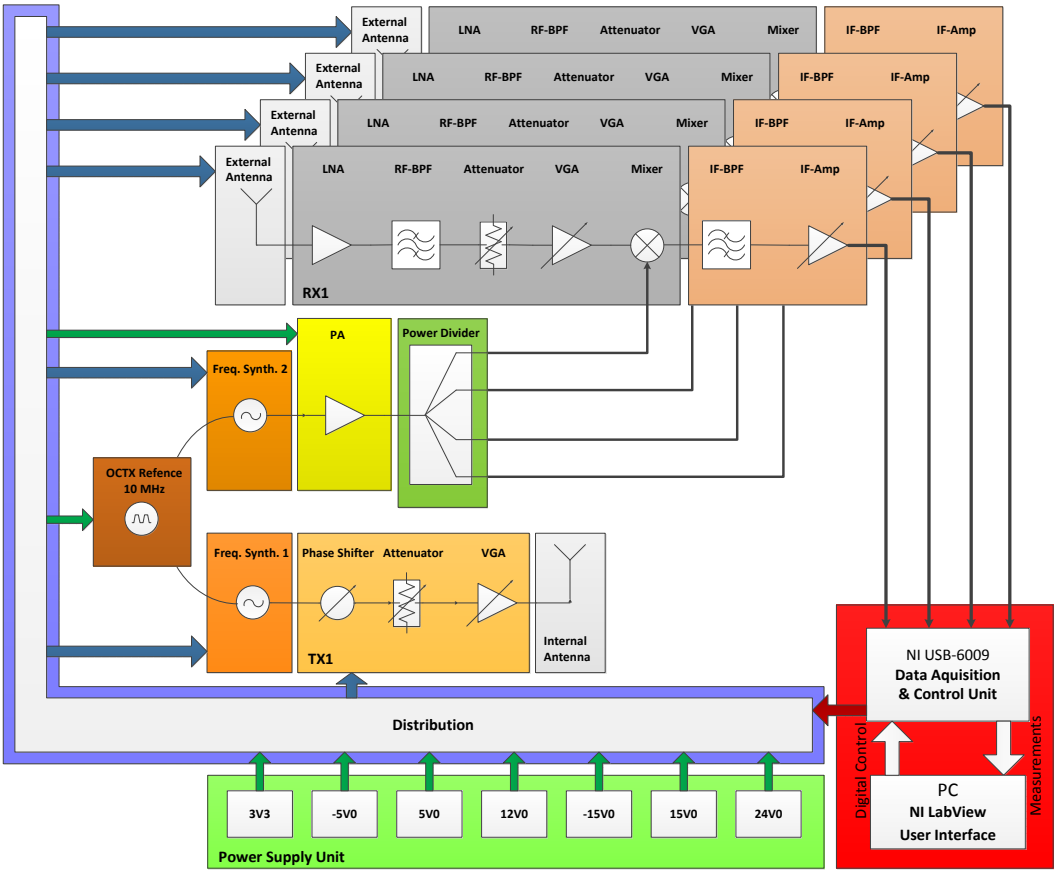

Figure 5.4: A block diagram of the microwave activation system during mapping. The blue distribution lines signify the power supply and digital signal lines being fed to each block. The green distribution lines signify only the power supply being fed to each block.

the decisive factor. The advantages of having a non-zero IF frequency reduces the effect of LO-RF (local oscillator to RF input) leakage as is often a problem in mixers with limited LO-RF isolation in homodyne receivers, especially when downconverting small signals that are over 30-40 dB lower than the LO-drive signal. In such a architecture, the DC offset that is a result of a LO-RF leakage, among other things, can easily be filtered out. A superheterodyne system with adjustable phases and amplitudes is therefore considered to be the most suitable for the microwave activation system. Figure 5.4 shows a block diagram of the microwave activation system during mapping.

First of all, the attention should be directed to the four receivers at the top of the figure. Each of these receivers have, an external antenna connected to their input. Furthermore every receiver includes a low noise amplifier (LNA), a radio frequency band-pass filter (RF-BPF), a variable

attenuator (VA), a variable gain amplifier (VGA), and a mixer. Included in each receiver is the intermediate frequency band-pass filter (IF-BPF). The IF-BPF is an active filter with a variable gain amplifier. The IF output of each of the receivers is fed into a data acquisition device which is connected to a personal computer (PC). Each receiver along with the external antenna is mounted on one of the four arms, illustrated in Figure 5.2

A local oscillator (LO) frequency synthesizer (Freq. Synth. 2) feeds a power amplifier (PA) that amplifies the signal from Freq. Synth. 2 before a 4-way power division. Each branch of the power divider is fed into the LO port of the mixer in every receiver.

Another frequency synthesizer, Freq. Synth. 1, feeds the input of a transmitter. This transmitter's objective is to generate the power to be sent from within the human torso phantom. The transmitter consists of a variable phase shifter (VPS), a variable attenuator and a variable gain amplifier, and it is connected to the internal antenna which is situated inside the phantom. There is no real usage for the variable phase shifter in the mapping setup, it will however be useful in the focusing setup, covered in the next section.

Both frequency synthesizers have the same oven controlled crystal oscillator reference which provides coherence between the two frequency synthesizers.

A PC with LabView user interface is connected to the data acquisition device. This device both collects the amplitudes and phases from the four receivers as well as controlling the variable components. Not indicated in Figure 5.4 are the interpreter modules that consist mainly of a single microcontroller. Each receiver, transmitter and frequency synthesizer have their own interpreter module. These modules, as the name indicates, interpret signals coming from the data acquisition device and then set the correct values to the relevant variable component, according to the user inputs.

A switch-mode power supply converts and filters a single valued voltage, 5 V, to numerous other needed voltages. The number of different voltages is mainly determined by the frequency synthesizers that require various voltages in order to operate correctly.

All the voltages from the power supply and the digital control signals from the data acquisition device are fed together to a single distribution board for the sake of reducing the number of cables to each module. From there, all the voltages and digital control signals are fed to each receiver, the transmitter and each frequency synthesizer. Only 5 V are fed to the power amplifier and the crystal oscillator, separately, as they are not tuneable like some of the other modules. This unification of the power supply and digital signals in a single cable does not cause any digital-noise related problems in the power supply as the variable components will only receive digital control signals before a measurement is initiated.

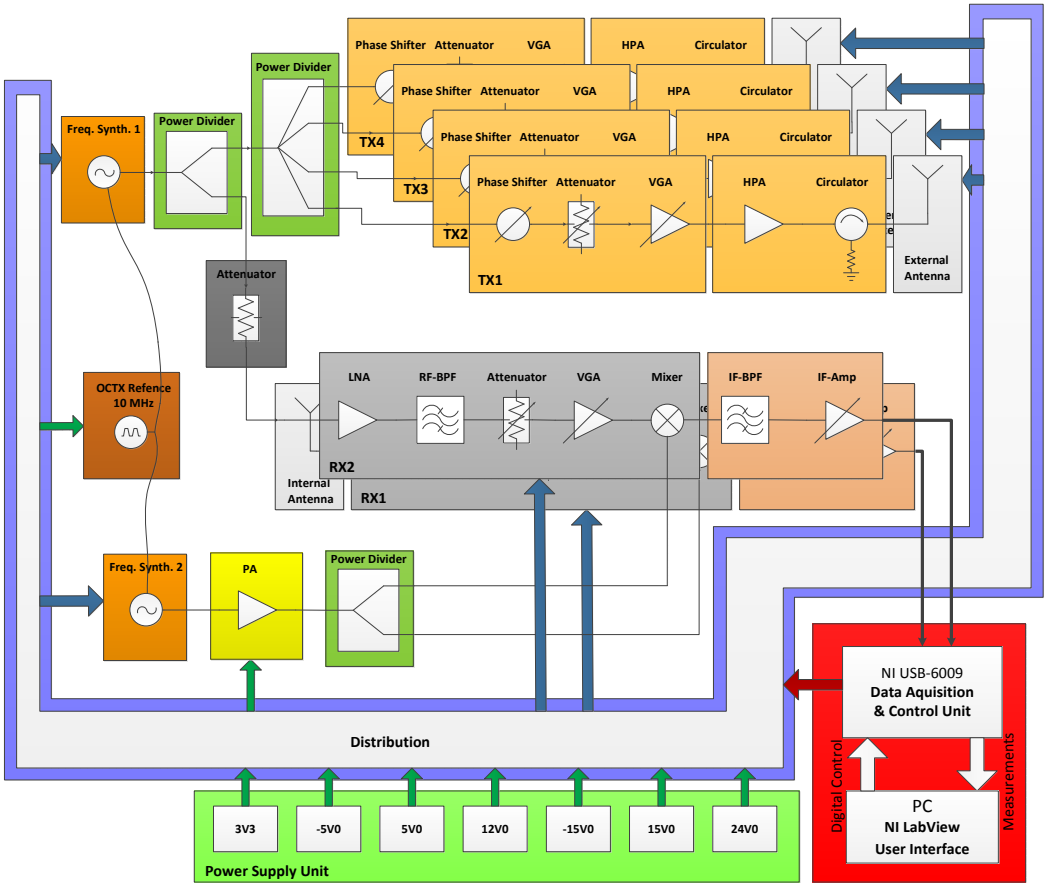

Figure 5.5: A block diagram of the microwave activation system during focusing.

5.6 System-Level Block Diagram - *Focusing*

Similar to the previous section on the mapping setup, the microwave activation system during focusing is shown in Figure 5.5.

During focusing, almost all the modules and components are the same as during mapping, although the arrangement is slightly different. Noticeably, there are now four transmitters and two receivers.

Each of the transmitters have additionally a high power amplifier (HPA) and a terminated circulator (effectively an isolator). This additional power stage is to provide the possibility of increased power to be radiated onto the human torso phantom. Freq. Synth. 1 feeds a power divider with a signal that is split between the 4-way power divider with the signal component that is to be transmitted and a reference signal towards the input of one receiver, RX-2. Each branch of the power divider is connected to an input of a single transmitter chain. Individual phases and amplitudes are controlled

with the variable phase shifter, the variable attenuator and the variable gain amplifier in every transmitter chain. Each external antenna is connected to the output of the circulator.

A receiver, RX-1, is connected to the internal antenna. The overall gain of the receiver and ultimately the amplitude of the received signal can be adjusted with the variable attenuator, variable gain amplifier and the IF amplifier, which also has variable gain. This is especially convenient during measurements of signals of large dynamic range.

The power level of Freq. Synth. 2 is amplified in the PA before it is split in two in a power divider and each part of the signal is fed to the mixers of the two receivers.

The input of the receiver, RX-2, is connected to an attenuator that attenuates the output from Freq. Synth. 1. This setup of having an additional receiver, such as RX-2, connected to the output of Freq. Synth. 1 (RF input) and Freq. Synth. 2 (LO input) provides a constant phase reference to the received signal of the internal antenna (RF input of RX-1). This is used in the calibration process for the focusing.

Similarly as in the mapping setup, the power supply voltages and the digital control signals are combined and then distributed to each transmitter, the receiver and to each frequency synthesizer. Not indicated in Figure 5.5 is the power supply for each of the HPA which is kept separate due to their high current consumption.

Both Freq. Synth. 1 and 2 can be used interchangeably in both setups since they are identical. The specific naming of each synthesizer is arbitrary and is only to distinguish between the two. This is also valid for the receivers mentioned here, RX-1 and RX-2 which could just as well have been RX-3 and RX-4 instead or any combination of the four manufactured.

All electronic modules and components will be covered in more detail in the next chapter.

Chapter 6

Microwave Activation System - Development

The development of the components and the modules for the microwave activation system is described in this chapter. The design of every module is not necessarily fully optimized since the requirements of some modules were difficult to identify due to unknowns and uncertainties in the system, especially regarding the complex wave propagation inside and around the phantom. Rather, a general good-practice method, based on practical experience was utilized, in order to have the modules flexible in regards to dynamic range, gain, noise, bandwidth and return loss, where applicable. The optimization of each individual module is not the focus of this thesis and should not be treated as such. The microwave activation system consists of the developed components and modules where, in this chapter, the details of discussion on each item depends on its novelty and design complexity.

The chapter is started by describing the internal antenna design. Subsequently, the external antenna development is discussed. The main microwave modules, i.e. the transmitters, the receivers and various other microwave components necessary for the system are presented. The chapter is rounded off by introducing the digital aspects of the system, such as microcontroller modules, the data acquisition module and the graphical user interface.

6.1 Encapsulated Coaxially Fed Sleeve Dipole

One of the most challenging aspects of this project was the development of an antenna that can be submerged in a liquid, is matched within the operational band, is omnidirectional in the horizontal (ϕ-) plane and is coaxially fed for symmetry. The purpose of the encapsulated antenna is to be submerged in a tissue mimicking liquid and to transmit and receive power in the horizontal plane of the antenna from within a phantom. An omnidirectional gain pattern is desired as the received power, at various equidistant

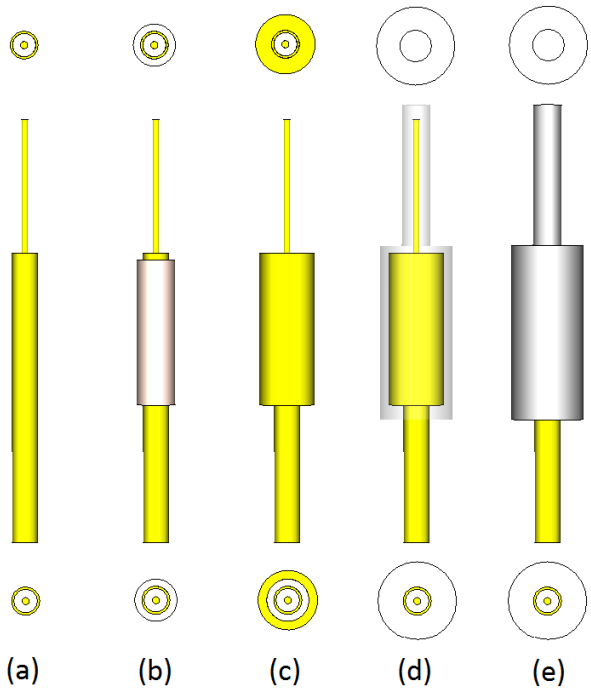

Figure 6.1: Design of the encapsulated antenna in steps. Figure (a) shows the semi-rigid coax with the inner conductor exposed. Figure (b) illustrates a Teflon sleeve on the outer conductor of the coax. In (c), the antenna now has a copper sleeve around the Teflon sleeve. The copper sleeve has a large opening in the bottom end for the Teflon sleeve and a small opening in the top end for the inner conductor. Figures (d) and (e) show two different views of the sleeve antenna completely encapsulated with Teflon.

locations around the phantom, is then independent of the relative directivity variations in the horizontal plane of the antenna.

6.1.1 Design

A sleeve dipole, also called vertical bazooka antenna, was constructed from available semi-rigid coaxial cable, copper sleeve and PTFE (Teflon) for encapsulation and isolation of the antenna from the lossy muscle tissue that surrounds it. The copper sleeve both acts as one half of the dipole and as a sleeve balun. The design of the antenna is shown in steps (a) to (d) in Figure 6.1. Step (e) is a non-transparent view of step (d).

The requirements were an omnidirectional directive antenna for the ISM band 2.4 - 2.5 GHz that is physically large enough for simple fabrication and in order to reduce influence of the fabrication tolerances on the antenna characteristics. The wavelength (λ_m) at 2.45 GHz in muscle tissue with a

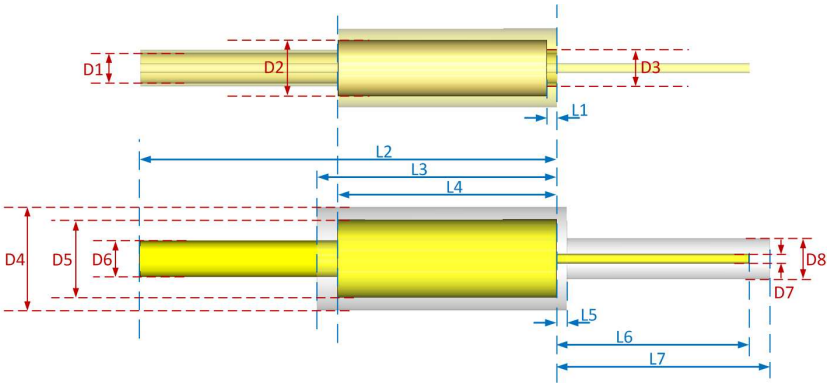

Figure 6.2: Dimensions of the encapsulated sleeve dipole. Notations refer to Table 6.1.

relative permittivity of 53.6 [114] is approximately 16.7 mm, compared to a wavelength of 122 mm in free space. The sleeve antenna was encapsulated with Teflon that has a relative permittivity of 2.1 and since a part of the reactive field would be in the Teflon, this lowers the effective permittivity of the surrounding medium of the antenna and had therefore to be taken into consideration when determining the length of the dipole as a fraction of λ_m, i.e. the wavelength in the muscle tissue medium.

Dimensions of the encapsulated sleeve antenna are indicated in Figure 6.2 and are referred to Table 6.1. The sleeve dipole was designed in the 3D electromagnetic simulation software CST to acquire the desired resonance frequency. The fabricated antenna is shown in Figure 6.3.

Table 6.1: Dimensions of the encapsuled sleeve dipole.

Diameter	Value [mm]	Length	Value [mm]
D1	2.98	L1	1
D2	5.4	L2	40
D3	3.58	L3	23
D4	10	L4	21
D5	7.6	L5	1
D6	3.58	L6	18.5
D7	0.92	L7	20.5
D8	4		

Figure 6.3: Photo of the constructed encapsulated sleeve dipole.

6.1.2 Measurements

In order to measure the return loss of the encapsulated sleeve dipole, the dipole was connected to a calibrated vector network analyzer, through a coaxial cable. The dipole was submerged in the muscle tissue mimicking media described in Section 4. The reflection coefficient measurement results, along with a corresponding simulation in CST are shown in Figure 6.4. The resulting 10 dB bandwidth (BW) is 1.424 GHz which is 51% fractional BW around a centre frequency of 2.8 GHz. The simulation of the reflections and the measurements agree well and show the same tendency over the measured frequency range. While the antenna was submerged, the outer conductor of the coaxial cables was touched by my hand to see if there were any changes to the S_{11}. This was done as a crude check to indicate whether the balun of the antenna was working. Having a sleeve antenna that has a balun that is not operating correctly, could result in a current flowing along the outer conductor of the coaxial cable and a touch by a grounded human could change the reflection parameters. This was, however, not the case as the S_{11} parameters remained unaltered.

A transmission measurement was performed by using the two identical encapsulated sleeve dipoles. The measurement was done with a signal generator at 2.45 GHz and a spectrum analyzer for power measurement, each connected to a sleeve antenna. A large plastic container was used as a container for the muscle tissue mimicking media and each antenna was kept more than 10 cm from the edge of the container during the measurement and 15 cm below the surface of the liquid. The S_{11} values stayed stable within this area and therefore this criteria was considered sufficient. The transmission measurement setup is shown in Figure 6.5.

The transmitted power at the input of the transmitting antenna was

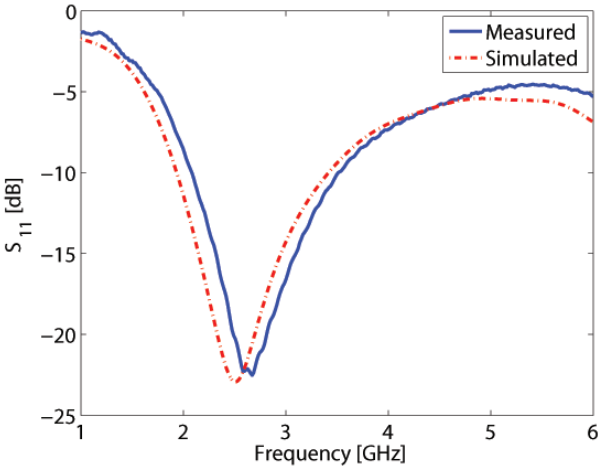

Figure 6.4: Measured and simulated S_{11} parameter of the encapsulated sleeve antenna.

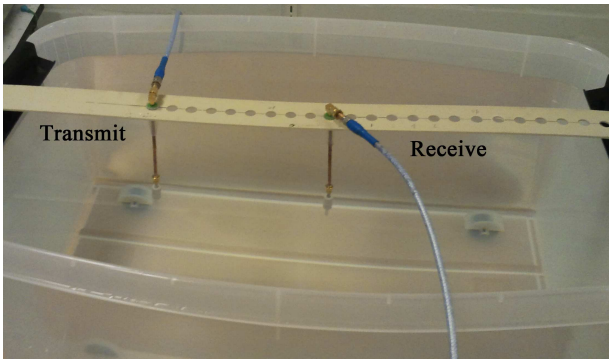

Figure 6.5: Photo of the antenna gain measurement setup.

17.67 dBm. The received power was measured when the two antennas were separated by 2 cm up to 26 cm, in steps of 2 cm. Despite the support structure the dipoles were placed in, shown in Figure 6.5, the dipoles could be offset in respect to each other in the liquid. The distance between the dipoles was measured in the liquid (and not on the support structure), while I held them in place. The measured received power is shown in Figure 6.6 where the results approximates a straight line with a -5 dB/cm slope.

A path loss model for wave propagation in homogeneous human muscle tissue media at 2.457 GHz was proposed in [90] and is presented here in a slightly altered form as

$$PL_{dB} = (10\log_{10}e^2)\alpha_e R + C_{dB} \tag{6.1}$$

where α_e is the effective attenuation constant, R is the distance in meters and C_{dB} is a constant in decibels. In [90] an attenuation constant, α, is pro-

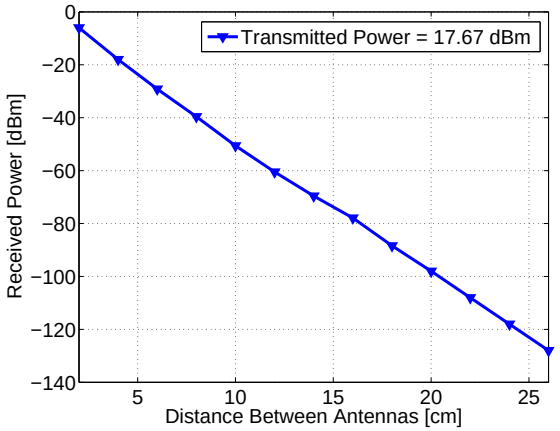

Figure 6.6: Measured received power of the encapsulated sleeve dipole as a function of distance.

posed whereas an effective attenuation constant, α_e, is presented here. The attenuation constant in (6.1), according to the literature, depends on the dielectric properties of the human muscle tissue as well as the encapsulation of the antennas (hence it is antenna dependent). Therefore, here is suggested to use an effective attenuation constant, to distinguish it from α in (3.11). The effective attenuation constant α_e, and C_{dB} values from [90] are shown in Table 6.2. The model is suggested to be valid at a distances between 2.78 cm and 8 cm with these values. From the transmission measurement results presented here, α_e and C_{dB} are also shown in Table 6.2 and are valid for distances between 16 cm and 26 cm. At these distances we are approximately in the far-field of the antenna as is calculated below. The muscle mimicking media presented in [90] had higher conductivity and lower relative permittivity than presented here which explains, in part, the difference between the parameters. Different antennas used in the two setups, are also responsible for the difference.

Table 6.2: Path loss model parameters.

	α_e	C_{dB}
	[Np/m]	[dB]
[90]	66	15.79
This work	57.6	15.68

The path loss model in (6.1) is based on the transmission coefficient, S_{21}, between the two sleeve dipoles and therefore the model includes the gain of the sleeve dipoles.

The far-field zone in the liquid for the sleeve dipoles is calculated by

$$R_{ff} = \frac{|\gamma|\, D^2}{\pi} \approx 19 \text{ cm}, \tag{6.2}$$

and is valid if D (the largest dimension of the antenna) is large compared to $\frac{\pi}{|\gamma|}$, which is the case here [126, pp. 13]. The calculated far-field zone is larger than the radius of the muscle phantom from Section 5.3. From Figure 6.6 it is seen that transmission is approximately linear for all distance values and therefore the path loss model is considered useful even at distances below 16 cm in an approximate manner. Errors in the distance measurement is likely the reason for the slight non-linearity as the placement of the antennas could not be fully fixed at exactly 2 cm intervals.

6.2 Stacked Patch Antenna

The system was designed for 4 external antennas that receive during mapping and transmit during focusing. The antennas should be directive, in order not to radiate power unnecessarily in other directions than at the target and to avoid reflections from external objects. The bandwidth of the designed antennas should cover the entire operating band, i.e. 4.1% in order to accommodate for some shift in frequency of the fabricated antenna as is often the case in the step from design to fabrication with practical antennas. It is preferred that the antennas have better than 10 dB return loss, which is generally considered a good design practice. It is especially important to have decent return loss if high powers are to be transmitted, since a high power that is reflected from the antenna and back into the output of the preceding power amplifier can damage the power amplifier's output. Both the relatively wide bandwidth and the reasonably good return loss assist, in a practical sense, to avoid detuning out of the band and reduce the risk of high reflection from the antenna towards the power amplifier, while a person would be situated near the antennas which might change the antenna properties. Furthermore, it was desired that the antennas should be relatively simple to design in order to reduce development time and, to have the antennas easy to fabricate using a repeatable process that ensures identical properties of all the external antennas. Also the antennas should weigh less than 500 g for the supporting structure to be able to hold them in place.

The antennas were designed to provide a proof of concept for the idea of microwave activation on a system level and not necessarily to be fully optimized in regards to gain, efficiency etc. A simple rectangular or a circular patch antenna fulfilled all those requirements except for the bandwidth, where it was impossible to reach the specified 4.1% without an exceptionally thick substrate (more than 4 mm thick) at the centre frequency of 2.45 GHz [127, pp. 130-137].

The inherent bandwidth problem of a standard patch antenna can be solved using a technique such as stacking a parasitic patch on top of the active patch. This technique reduces the width and length of the active patch but increases the thickness of the overall antenna. The stacking also increases the gain of the antenna and was therefore well suited for the microwave activation system. In Figure 6.7(a), a perspective view of the stacked patch antenna is shown. The parasitic patch is turned inward towards the active element, i.e. the backside of the thin Rogers PCB is in contact with the ambient. The active patch was fabricated on a 1.5 mm Rogers 4003 substrate with 35 μm thick copper, filling the backside, for GND reference. On top of the 1.5 mm Rogers substrate, a 10 mm thick Rohacell intermediate substrate was placed with $\epsilon_r = 1.05$ and $\tan\delta = 0.0002$. The Rohacell substrate was sandwiched between the active patch and the parasitic patch and gives a low-loss, well defined and stable separation of the two PCB's. The parasitic patch was fabricated on a 0.2 mm thick Rogers 4003. All three substrates were glued together and four holes were made in the corners of all the substrates for alignment purposes. A photo of the manufactured stacked patch antenna is shown in Figure 6.8.

The designed active patch of the stacked patch antenna is shown in Figure 6.7(b), where it is seen that microstrip impedance matching elements were added to the feed line to improve matching to 50 Ω. The active element was fed through the backside of the 1.5 mm PCB and the feed point is indicated as a red dot in Figure 6.7(b). The centre pin of the SMA connector was fed through the substrate and soldered at the feed point. The outer conductor of an SMA connector was soldered onto the backside of the 1.5 mm PCB, connecting the GND references of the connector and the active element.

Simulations on the designed antenna shown in Figure 6.7(a) were made in CST. The antenna model includes a short coaxial stub, with the physical dimensions of an SMA connector on the backside of the antenna in order to model the SMA connector in the simulation. The antenna input excitation port was placed at the open end of the coaxial stub. Electrical properties and physical dimensions for all substrates and metals were included in the simulation.

The measured return loss results along with the simulated one from CST, are displayed in Figure 6.9(a). The measurements show good agreement with the simulations. The 10 dB bandwidth of the antenna is 13.5% which is wider than the 4.1% required. Within the 2.4 - 2.5 GHz band, the return loss is better than 17 dB.

The gain and directivity of the stacked patch antenna was measured at the ESA-DTU test facility [128]. Figure 6.9(b) shows the measured directivity pattern of the antenna at 2.45 GHz. The measured directivity of the antenna is 8.83 ±0.15 dBi and the gain is 8.68 ±0.15 dBi compared to the simulated gain of 8.65 dBi. The cross-polarization, which is illustrated in black and purple, are around 40 dB below the co-polarization in the direc-

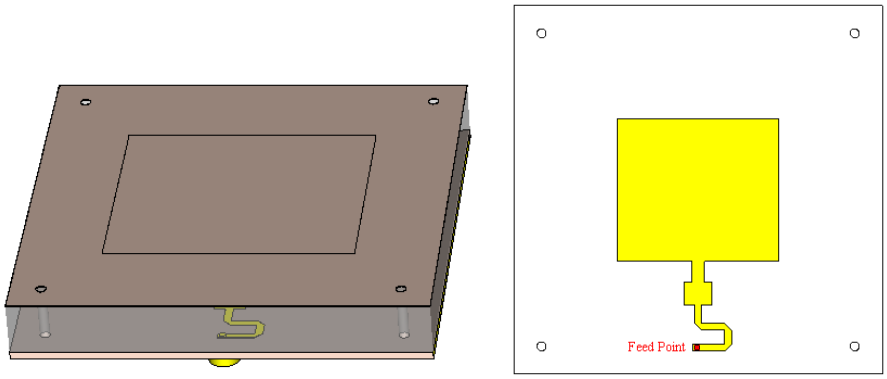

(a) (b)

Figure 6.7: The stacked patch antenna. In (a) the antenna shown with the rohacell layer semi-transparent. In (b) is the active element of the stacked patch antenna, the feed point is marked in red. The upper layers of the antenna are hidden.

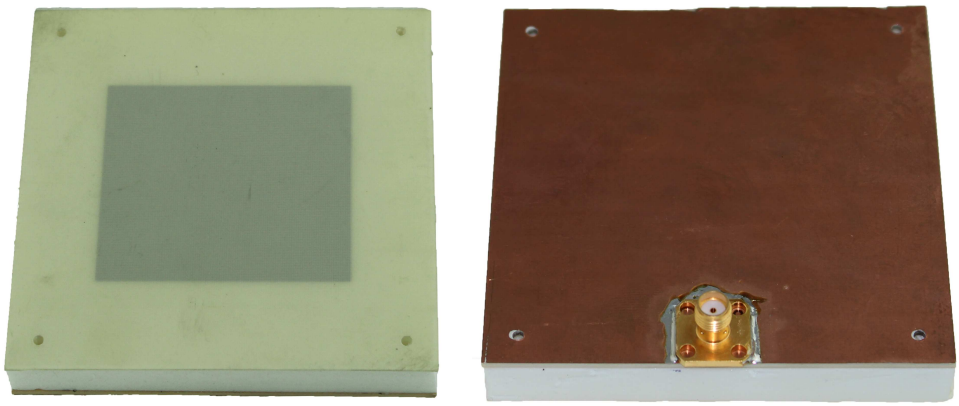

(a) (b)

Figure 6.8: Photo of the stacked patch antenna. (a) shows the frontside and (b) the backside.

tion of maximum gain. The coordinate system is defined such that, x-axis is vertical, from SMA-connector towards the patch, y-axis is horizontal, and z-axis is out of the patch aperture, in the main beam direction.

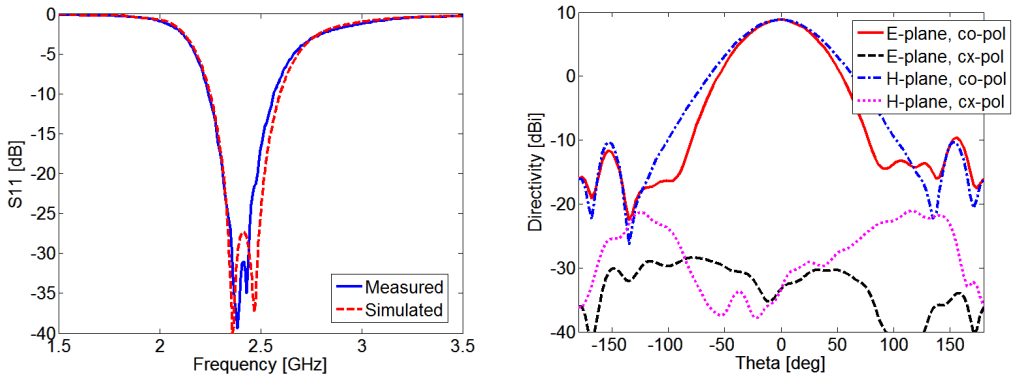

(a) (b)

Figure 6.9: The stacked patch antenna measurements. The S_{11} is shown in (a) and the directivity pattern in (b).

6.3 Transmitter

6.3.1 Design

Due to the high absorption of EM energy in biological tissue, difference in power levels at various locations in the torso phantom can be significant and therefore, a transmitter with variable gain is needed. As the system is designed for both mapping of amplitudes and phases, as well as focusing, the transmitter is to be used in both cases and must therefore be designed accordingly. The transmitter's building blocks are a variable phase shifter (VPS), variable attenuator (VA), variable gain amplifier (VGA), high power amplifier (HPA) and an isolator. A block diagram for the transmitter is shown in Figure 6.10. The high power amplifier and the isolator are kept separate from the rest of the transmitter in order to be able to mount it only when high power levels are needed. From this point on, when the *transmitter* is mentioned, the reference only apply to the first half of the transmitter chain, i.e. the variable phase shifter, variable attenuator and the variable gain amplifier. The high power amplifier and the isolator together are simply just referred to, as the high power amplifier (HPA), unless stated otherwise. The transmitter cascaded with the HPA will be referred to as the transmitter chain.

An initial challenge for the transmitter was to find a suitable, commercially available, variable phase shifter for the frequency band of interest. As the entire microwave activation system was to be controlled via a PC, a digital variable phase shifter was preferred, as this could more easily be integrated in the control system. Commercially available digitally-controlled phase shifters are limited to 6 bits, shifting nearly 6° per unit increase. An analog variable phase shifter along with a digital-to-analog converter (DAC)

were therefore preferred to increase the resolution, for fine-tuning.

During mapping (covered in Chapter 7), a frequency synthesizer with a fixed output power level of approximately 0 dBm, was connected directly to the input of the transmitter. The VGA in the transmitter has a minimum gain of 10 dB therefore, a variable attenuator was needed e.g. for output power levels below 10 dBm. The variable attenuator also increases the tuneable output power range by 31.5 dB which is highly desirable as there are practical uncertainties regarding the actual power levels to be measured by the experimental setup and a wider dynamic range increases the flexibility to accommodate for uncertainties in such a experimental setup. The following VGA has a maximum gain of 41.5 dB, where 31.5 dB are tuneable, again adding to the tuneable output power range of the transmitter. In total, the theoretical output power range is 63 dB, excluding the HPA that may be added to the output of the transmitter.

The HPA could be needed during focusing and can be added to the transmitter for higher output power. The specified 1 dB output compression point (P_{1dB}) is approximately 43 dBm (20 W) and the gain is 29 dB. If the HPA's output is 43 dBm and connected to a stacked patch antenna described above, the power density would be above the recommended SAR (Specific Absorption Rate) limit. In order to remain below the power density reference level of approximately 10 W/m^2 [129], the object would need to be more than 1 m away from the antenna, or the output from the HPA should be reduced below 8 W if distance of 65 cm is maintained. A circulator was connected to the output of the HPA, along with a power termination to avoid potential reflections from the load, burning the LDMOS transistor. This is important especially since the output of the HPA could be connected to an antenna which might change its return loss characteristics simply by unintended introduction of an object in its near-field (e.g. a person walking by). A circulator was used along with the power termination instead of an isolator simply because of price and availability. A list of the core components for the transmitter chain is found in Table 6.3.

All the variable (controllable) components described above (DAC, VA, VGA) are controlled through a so-called Serial Peripheral Interface (SPI)

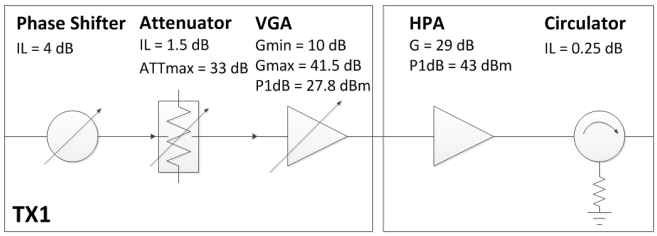

Figure 6.10: Block diagram of the microwave part of the transmitter chain.

Bus, which is supported by all three components. Using the PC, various states of the variable components are controlled. This is described further in Section 6.7.

For interpretation of the control signals from the PC, a microcontroller unit (MCU) based on the 8-bit PIC18F46K22 microcontroller was designed and manufactured. Each transmitter has its own MCU-PCB for PC interpretation, where each MCU-PCB controls 3 variable components. A 25 pin D-Sub connector on the MCU-PCB was used for supplying both the voltages needed as well as the digital control signals, from the so-called distribution PCB. On the MCU-PCB, the power supply voltages are filtered with decoupling capacitors and from there, fed to the microwave PCB.

6.3.2 Fabrication

All the circuits were fabricated on Rogers 4003 substrate with 0.508 mm thickness. The relative permittivity and the thickness of the substrate, result in a 50 Ω microstrip line of approximately 1 mm width which makes soldering of components and connectors easy, avoiding large discontinuities. Photographs of the fabricated transmitter are shown in Figure 6.11. In Figure 6.11(a) the microwave PCB is shown and in Figure 6.11(b) the MCU PCB is shown.

Noticeably each stage of the transmitter is shielded off in the PCB to reduce leakage between each stage and providing a good ground plane. The PCB shields are exposed in grey colour because they do not have solder mask on top of them. This makes it possible to solder metal fence or housing around each stage with openings in the appropriate locations. This can be necessary in noise and leakage reduction as well as decreasing feedback in high-gain stages such as the VGA stage. This was done in all four transmitters in the present system.

The HPA was designed around the MW7IC2425NBR1 LDMOS transistor

Table 6.3: List of transmitter components.

Component	Part no.	Manufacturer
Analog Phase Shifter	HMC928LP5E	Hittite
Digital to Analog Converter	AD5501	Analog Devices
Variable Attenuator	HMC542ALP4E	Hittite
Variable Gain Amplifier	TQM879008	TriQuint
LDMOS Transistor	MW7IC2425NBR1	Freescale
Circulator	MAFR-000229-000001	Skyworks
Microcontroller	PIC18F46K22	Microchip

from Freescale Semiconductor. The datasheet for the LDMOS shows their design of the PCB from which the datasheet specifications were acquired and this was used for designing the input and output matching networks, since no model is offered by Freescale. The PCB substrate used in Freescale's design was not the same PCB substrate as used in this work and therefore all the design parameters are different. The proposed input and output matching networks from the datasheet were modelled in Agilent's Advanced Design System (ADS) and corresponding matching networks were designed, that give similar S-parameter response into a 50 Ω load, for the Rogers 4003 substrate. The measurements of the fabricated amplifier gave 2 dB higher gain and only 1 dB lower P_{1dB} than specified by Freescale.

The transmission lines of the HPA are microstrip even though the ground plane was also kept on the top copper layer, adjacent to the microstrip lines. A photo of the fabricated HPA, top view, is shown in Figure 6.12. The

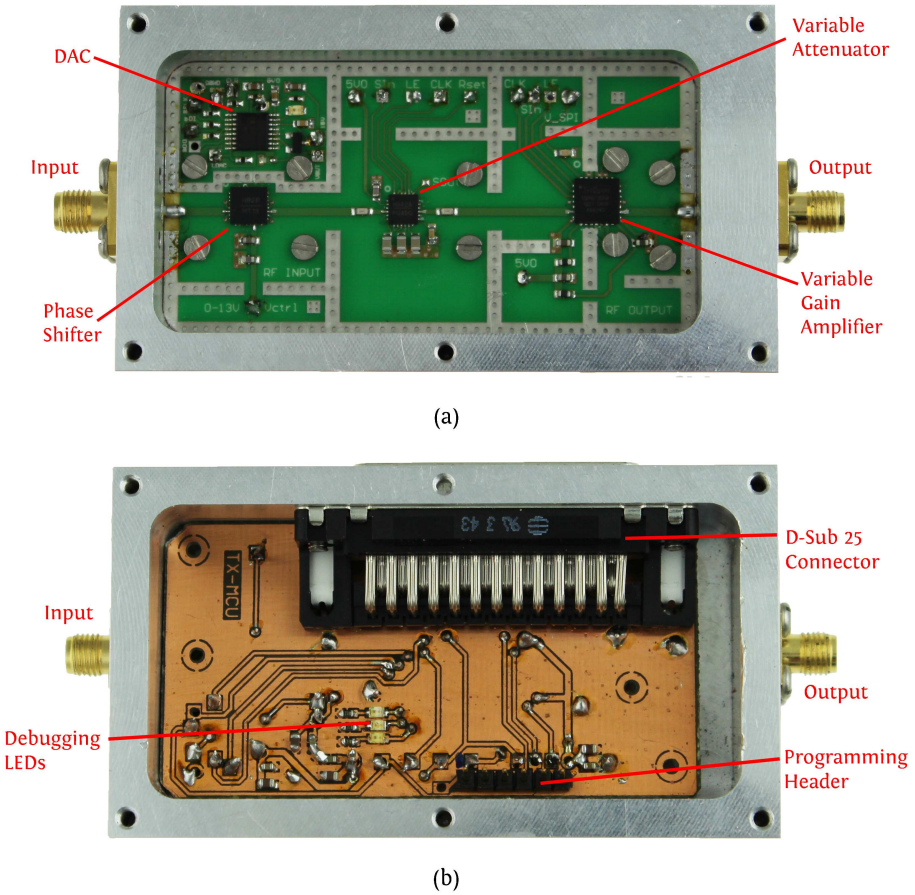

Figure 6.11: Photo of the fabricated transmitter. Top view in (a) and bottom view in (b).

presence of a ground plane near the microstrip line makes it possible to solder capacitors, from the microstrip line to ground in order to tune the input and output matching networks. The ground plane on the top copper layer was kept sufficiently far away from the microstrip line, to avoid noticeable interference with the transmission line impedance. In total, four transmitter chains were fabricated.

6.3.3 Verification

The overall gain and phase behaviour of the transmitter is a function of the three variables, the digital to analog control voltage and the controlled attenuation for both the variable attenuator and the variable gain amplifier. This is shown in Figure 6.13. Notice that e.g. VGA = 16 dB means that the internal controllable attenuator inside the variable gain amplifier is set to attenuate 16 dB, which is subtracted from its nominal gain of 41.5 dB. In Figure 6.13(a) the overall gain of the transmitter is shown as a function of the controlled attenuation for both the variable gain amplifier and the variable attenuator. The two curves are virtually identical and also linear which is not a surprise. Figure 6.13(b) illustrates the phase variation as a function of the controlled attenuation for both the VGA and the VA. The DAC control voltage was kept at 1.5 V during these measurements and the controlled attenuation of the variable attenuator was kept at 0 dB during

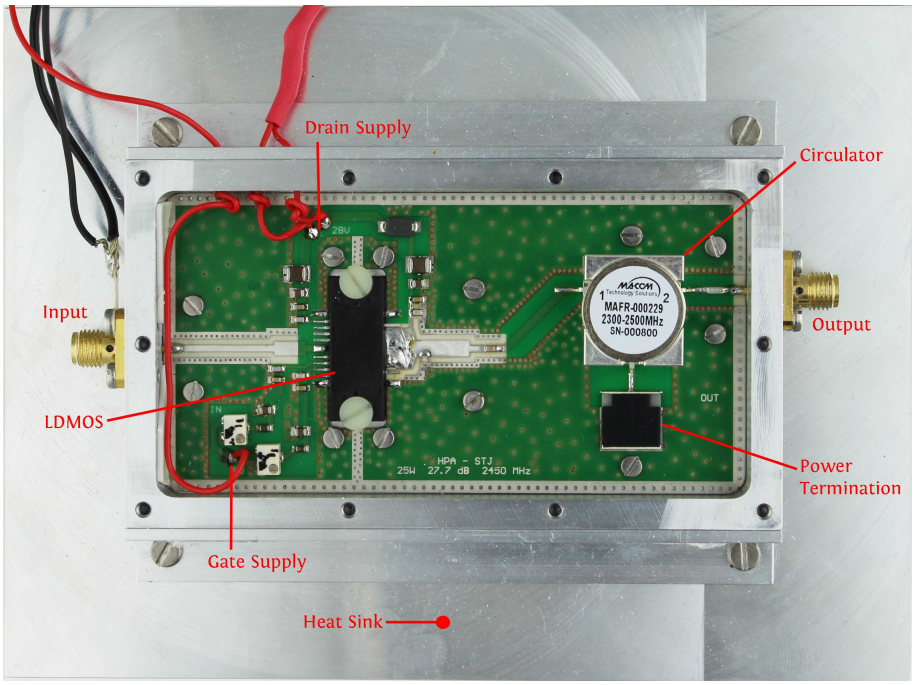

Figure 6.12: Photo of the fabricated high power amplifier, top view.

VGA measurements and vice versa for the variable attenuator measurements. The phase of the VGA in particular experienced a stepwise change as a function of the controlled attenuation. This is perhaps the most evident when the attenuation shifts from 15 dB to 16 dB. The step behaviour is due to the fact that the accumulated phase shift in e.g. the individual 1 dB, 2 dB, 4 dB and the 8 dB attenuators (inside the VGA chip) in series ($1 + 2 + 4 + 8 = 15$ dB) is about 7° lower than the phase shift for only the 16 dB attenuator.

Figures 6.13(c) and 6.13(d) display the gain and phase variation, respectively, as a function of the DAC control voltage. Notice in Figure 6.13(c) that the results seem to be discretely stepped, which is a result of rounding the measurement results to the nearest tenth. The change in gain is 0.6 dB over the entire voltage (phase) range and therefore the output power of each

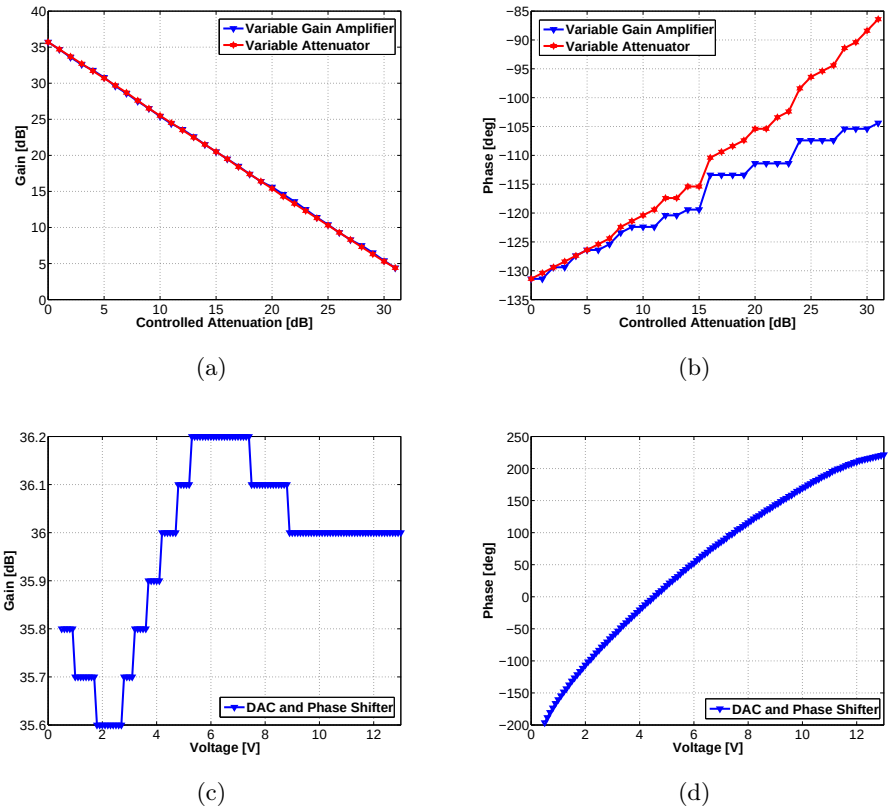

Figure 6.13: Gain and phase measurements of a transmitter. In (a) and (b), the DAC voltage was set to 1.5 V and the VA was set to 0 dB attenuation during VGA sweep and vice versa. In (c) and (d), the VA and VGA were both set to 0 dB attenuation while the DAC voltage was swept.

transmitter does not vary considerably while adjusting the phase for focusing, thus readjustment of the gain could possibly be avoided. The phase variation behaviour is similar to the specifications of the datasheet for the analog phase shifter.

The gain, P_{1dB} and the power added efficiency (PAE) were measured for the high power amplifier and the results are illustrated in Figure 6.14. A gain of over 29 dB was achieved and the P_{1dB} is 43 dBm as shown is Figure 6.14(a). The PAE was measured to be 46.6% at the P_{1dB} point and its dependence is displayed in Figure 6.14(b).

Excessive leakage through the power supply wires was experienced from the HPA during testing of the mapping process. The sensitive receivers picked up the leakage which, at a certain point, overshadowed the signal of interest. By adding capacitor-input filters (PI filters) that are screwed into the wall of the HPA metal case, in series with the power supply lines, the leakage was reduced by approximately 35 dB. The leakage is measured by having a dipole antenna connected to a spectrum analyzer, while the HPA was terminated into a 50 Ω power termination. The antenna was located approximately 2 m from the HPA.

6.4 Receiver

6.4.1 Design

A block diagram of the microwave and IF part of the receiver is illustrated in Figure 6.15. A low noise amplifier (LNA) is the first stage of the receiver input and is followed by a narrow RF band-pass filter (RF-BPF). The LNA has a noise figure of 0.9 dB, a gain of 19 dB and a P_{1dB} of 19.5 dBm. The BPF has a 3 dB bandwidth of approximately 83.5 MHz and is a SAW (surface

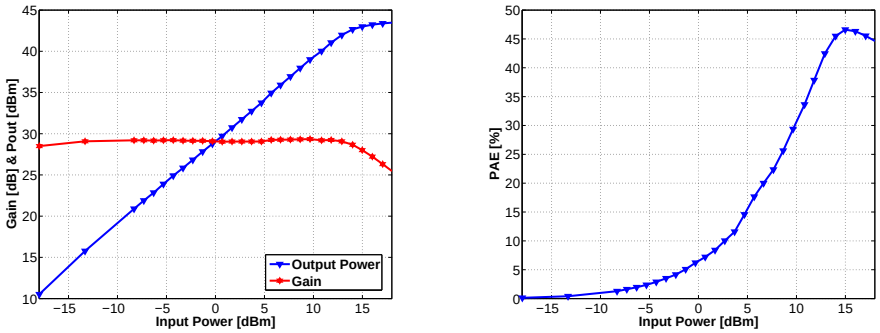

(a) (b)

Figure 6.14: Gain, output power and power added efficiency of the HPA.

acoustic wave) filter, specified to be used for the ISM band around 2.45 GHz. The bandwidth of the receiver, like for other modules of the system is aimed to be approximately 100 MHz to allow for some unexpected shift in frequency during manufacturing of the modules. A BPF of 83.5 MHz is considered sufficiently wideband for the receiver. Similarly to the transmitter, two of the core elements in the receiver are the variable attenuator and the variable gain amplifier which are the same as used in the transmitter. Following the VGA, is a passive mixer that has conversion loss of approximately 6 dB and a compression point, P_{1dB}, at 1 dBm. Even though the VGA has a P_{1dB} at 27.8 dBm which is higher than the following mixer, the benefits of using the same VGA in both the transmitter and the receiver simplifies the attenuation control in a practical sense. The VGA has high gain and a dynamic range of 31.5 dB and therefore fulfils the most important properties, required at the VGA stage.

A very high amplification at a single frequency can make an amplifier become unstable, due to feedback where oscillations may occur. In an effort to divide the total amplification between two frequencies, an active band-pass filter was placed subsequent to the mixer at the IF side. This relaxes the requirements for an amplification at the RF side. The IF filter removes the unwanted DC component with a lower 3 dB cut-off point at approximately 200 Hz as well as having a upper 3 dB cut-off point at 4 kHz thus reducing undesirable higher frequency components before sampling of the analog to digital converter (ADC). The IF was chosen to be 1.2 kHz in order to be able to utilize an existing filter design and to be compatible to the available data aquisition module. The 1.2 kHz was chosen to avoid the in-house WLAN by offseting the transmitted carrier frequency 400 Hz away from 2.45 GHz as is explained in more detail in Section 7.1.

The IF stage is a 3 section active band-pass filter made using operational amplifiers and the design was acquired from another project at DTU-Elektro [130]. The IF-BPF has a programmable digital potentiometer that can also be controlled through the SPI bus, same as the DAC, VGA and VA, thereby the amplitude of the downconverted signal can be adjusted to utilize the range of the ADC.

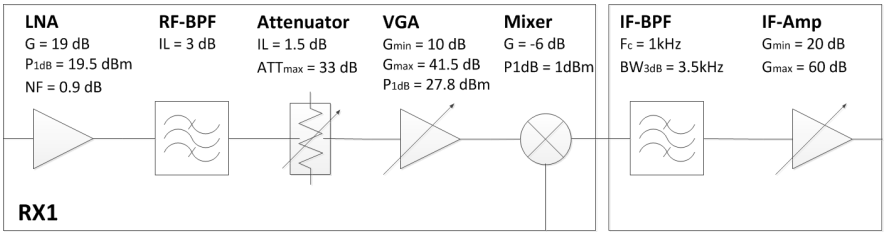

Figure 6.15: Block diagram of the microwave and IF part of the receiver.

The main components in the receivers are listed in Table 6.4. Additionally to the microwave components, the 8-bit MCU is included.

Table 6.4: List of receiver components.

Component	Part no.	Manufacturer
Low Noise Amplifier	HMC715LP3E	Hittite
Bandpass Filter	855916	TriQuint
Analog Phase Shifter	HMC928LP5E	Hittite
Variable Attenuator	HMC542ALP4E	Hittite
Variable Gain Amplifier	TQM879008	TriQuint
Mixer	ADE-3G+	Mini-Circuits
Microcontroller	PIC18F46K22	Microchip

6.4.2 Fabrication

Three PCBs were fabricated as a part of the receiver. First, the microwave PCB containing the LNA, RF-BPF, VA, VGA and the mixer was on a Rogers 4003 substrate, same as the microwave PCB of the transmitter and the HPA PCB. Secondly, the IF stage as well as the MCU PCB were fabricated on a 1.5 mm thick FR4 substrate.

A photograph of the fabricated receiver is shown in Figure 6.16. An aluminium box was milled to fit all the PCBs, separately, for isolation. As in the transmitter, the power supply and digital control lines are fed through a D-sub 25 connector, on the side of the aluminium box, onto the MCU PCB which has the D-sub 25 connector mounted. From there, power supply wires feed the microwave PCB and the IF stage PCB with the necessary power. Small slots were milled in the box to let the power supply and the digital signal wires through, yet keeping good isolation between the PCBs.

Similarly to the transmitter design, each section of the microwave PCB was shielded off with GND plane on the top copper layer and vias through to the bottom GND layer as can be seen as grey stripes on the otherwise green PCB. Again, there exists a possibility for encapsulating each section in a metal housing for increased isolation. In total, four receivers were fabricated, each with a metal housing.

6.4.3 Verification

The receiver has both a variable attenuator and a variable gain amplifier, similar to the transmitter. The gain and phase dependence of them in the receiver can therefore be found in Figure 6.13. The resulting voltage mea-

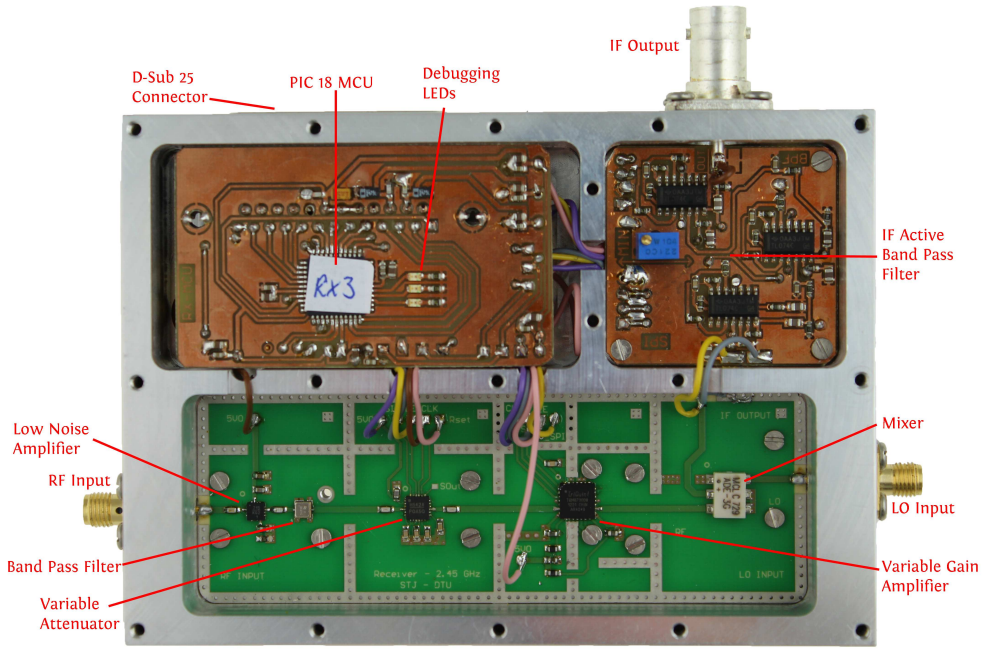

Figure 6.16: A photograph of the fabricated receiver, view from the top.

sured by the ADC for various input powers and settings of the VA, VGA and IF stage are displayed in Figure 6.17.

Figure 6.17(a) shows sweeps for the VA and the VGA, having the VGA = 16 dB and VA = 31.5 dB attenuation, as well as -40 dBm and -20 dBm input power, respectively, and a minimum amplification of the IF stage. The descent of the curves on the left side (i.e. maximum gain) of Figure 6.17(a) is caused by the compression point of the mixer which, at those power levels is reached.

Figure 6.17(b) illustrates a VGA sweep for lower power levels than in the previous figure and shows the level of voltages to expect for these low input power levels. Figures 6.17(c) and 6.17(d) display the cases of full attenuation and 16 dB VGA and VA attenuation at -40 dBm input power, respectively when the IF amplification (IF ctrl) was swept. The IF ctrl is a value between 0 and 127 that is loaded into the digital potentiometer in the IF stage and controls the amplification of the second stage in the active IF-BPF chain.

The lowest RF input signal level above noise floor that could be detected was measured to be -120 dBm by having the attenuations of the VGA and VA at a minimum and the IF stage gain at a maximum. This RF input signal level is the level at which only a small noticeable signal peak in the user interface of the PC can be detected after the Analog-to-Digital conversion. At the PC stage, the signal was digitally processed through a 99th order FIR

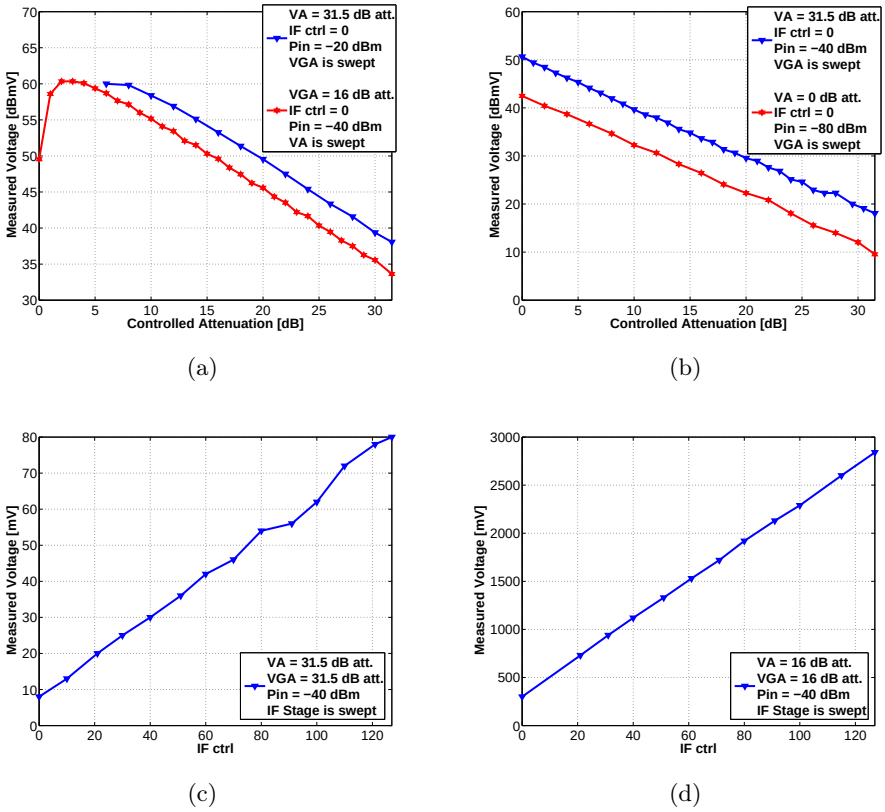

Figure 6.17: Output voltage measurements of a receiver. In (a) a comparison of a VA and VGA sweep while the input power was set to -20 dBm and -40 dBm, respectively is shown. In (b) a comparison of a input power of -80 and -40 dBm for a VGA sweep using different VA settings is shown. In (c) measured voltage with -40 dBm input power while the VA and VGA were fully attenuating is shown. In (d) measured voltage with -40 dBm input power while the VA and VGA were both set at 16 dB attenuation is shown.

BPF with a 3 dB bandwidth of 40 Hz which is the smallest bandwidth in the system. The sensitivity of the system is, in theory, limited by the Analog-to-Digital converter which has 14-bits over a range of 20 V, making the lowest detectable amplitude approx. 8 dBmV, assuming 3 dB signal to noise ratio. This corresponds to a theoretical smallest detectable input signal of approx. -149 dBm, having a system with about 110 dB overall maximum gain. The highest allowed RF input signal level is 0 dBm and that is limited by the 1 dB compression point of the LNA in the input stage of the receiver. This results in a dynamic range of 120 dB in the receiver.

6.5 Various Microwave Parts

Besides the transmitters and receivers, various other microwave parts were required for the system as was illustrated in the block diagrams of Figures 5.4 and 5.5. These include a power amplifier, a power divider and frequency synthesizers. The main microwave components are listed in Table 6.5 and are covered individually in the following sections.

Table 6.5: List of other system components.

Component	Part no.	Manufacturer
Power Amplifier	MMG20271H9T1	Freescale Semiconductor
4-Way Power Divider	S4D1525	Synergy Microwave Corporation

6.5.1 Power Amplifier

During the mapping process, a power amplifier (PA) is needed in order to drive the mixers of all four receivers with the specified local oscillator (frequency synthesizer) power. The LO drive power affects the matching of the mixer, the isolation between ports and conversion loss. The mapping setup was shown in Figure 5.4. The output power of the frequency synthesizer is 0 dBm which was to be divided by the 4-way power divider, which would reduce the available power to -6 dBm at each branch of the power divider, neglecting losses and mismatch. While focusing, a power amplifier is required to amplify the power from the frequency synthesizer to the mixer of the receiver as was shown in Figure 5.5. A photo of the fabricated power amplifier is shown in Figure 6.18.

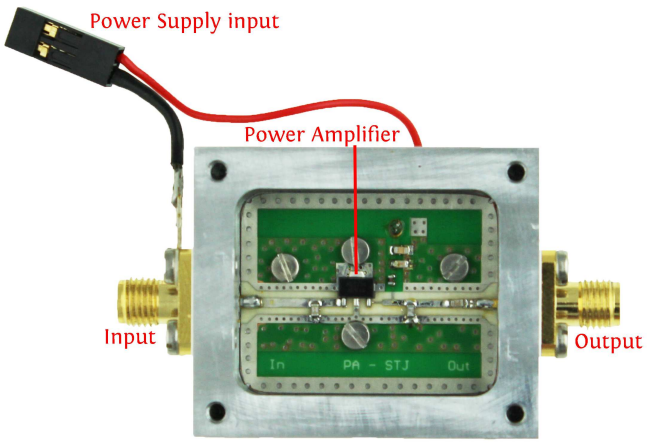

Figure 6.18: A photograph of the power amplifier, top view.

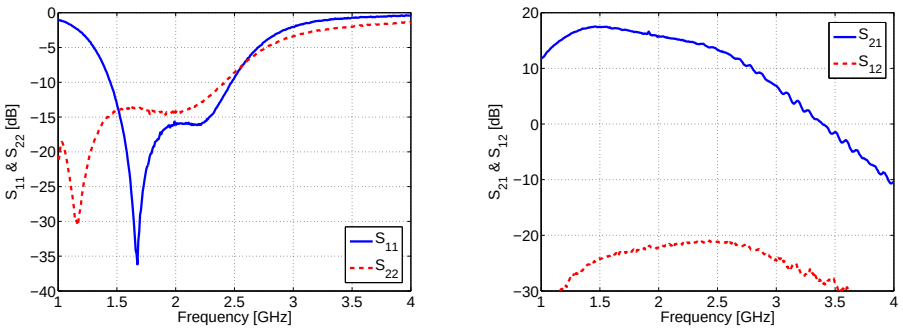

(a) (b)

Figure 6.19: S-parameter measurements of the power amplifier

As the power amplifier, MMG20271H9T1, is not fully matched to 50 Ω, external matching was required. Using the S-parameter model for the amplifier as well as models for the RF matching capacitors from ATC (American Technology Ceramics), the microstrip matching network on Rogers 4003 substrate was designed, simulated in ADS and ultimately fabricated. The resulting S-parameter measurements of the fabricated power amplifier are shown in Figure 6.19. The input and output return losses are at around 10 dB while the gain is at 13.8 dB at 2.45 GHz.

6.5.2 Power Divider

The purpose of the power divider is twofold. First, during mapping it divides the local oscillator power to be fed to the local oscillator ports of each of the four mixers in the receivers. Secondly, while focusing it divides the power of the frequency generator to be transmitted between the four transmitters. A photo of the simple construction is shown in Figure 6.20 and is merely based on a 4-way power divider module. Practically though, the SMA connectors used, had to be separated with a certain spacing and therefore the electrical length of the microstrip transmission lines from the module to the SMA connectors was kept approximately equal for all four lines. Even though the system does not depend on the phase shift of the outputs to be equal since phase differences can be calibrated out, it is considered a good design practice to design them to be equal, if possible. The transmission lines were designed in Altium Designer 09 which did a good job at designing four transmission lines simultaneously of equal electrical length and pre-determined separation. Before fabrication, the geometry of the transmission lines were exported to ADS and simulated, where the phase balance was verified.

S-parameter measurement of the 4-way power divider are illustrated in Figure 6.21 with port numbering as shown in Figure 6.20. The return loss,

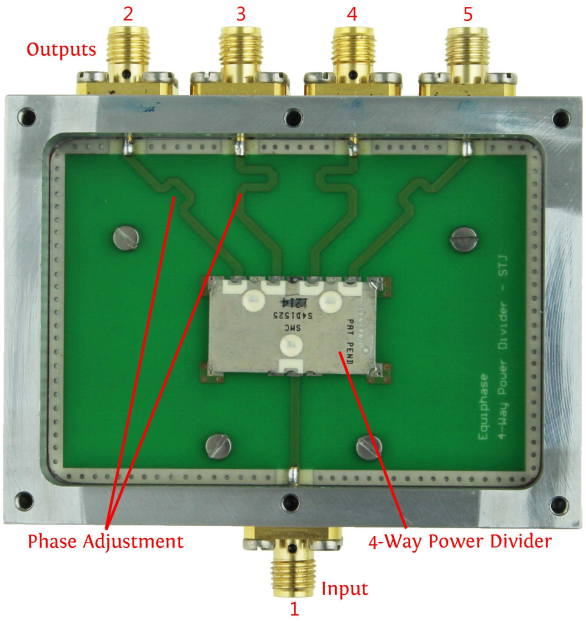

Figure 6.20: A photograph of the 4-way power divider, top view.

shown in Figure 6.21(a) is better than 19 dB. The transmission between the input and each output is displayed in Figure 6.21(b) and lies between -6.3 dB and -6.6 dB of the input. Finally, the phases between the input and the outputs are shown in Figure 6.21(c) and a more zoomed in view in Figure 6.21(d). The phase balance at 2.45 GHz is considered good, only 1.6° difference between the output ports, at maximum.

6.5.3 Frequency Synthesizer

Two identical frequency synthesizers were used both during mapping and focusing. One served as the local oscillator, driving the mixers whereas the signal from the other one got transmitted from within the phantom (mapping) as well as from the outside, towards the phantom (focusing). The synthesizers were designed and fabricated in my M.Sc. project [131] and were retrieved from there since they operate at the desired frequency range, have a suitable output power level, use the same crystal oscillator reference, are small in size, can be controlled via the PC and last but not least, were easily available. The technical specification for the frequency synthesizer can be seen in Table 6.6.

Similarly to all the transmitters and the receivers, a special MCU-PCB was created for each of the synthesizers to serve as a link between the PC and the phase locked loop chip, which controls the operating frequency of the synthesizers. A photo of the frequency synthesizer, including the MCU-PCB is shown in Figure 6.22.

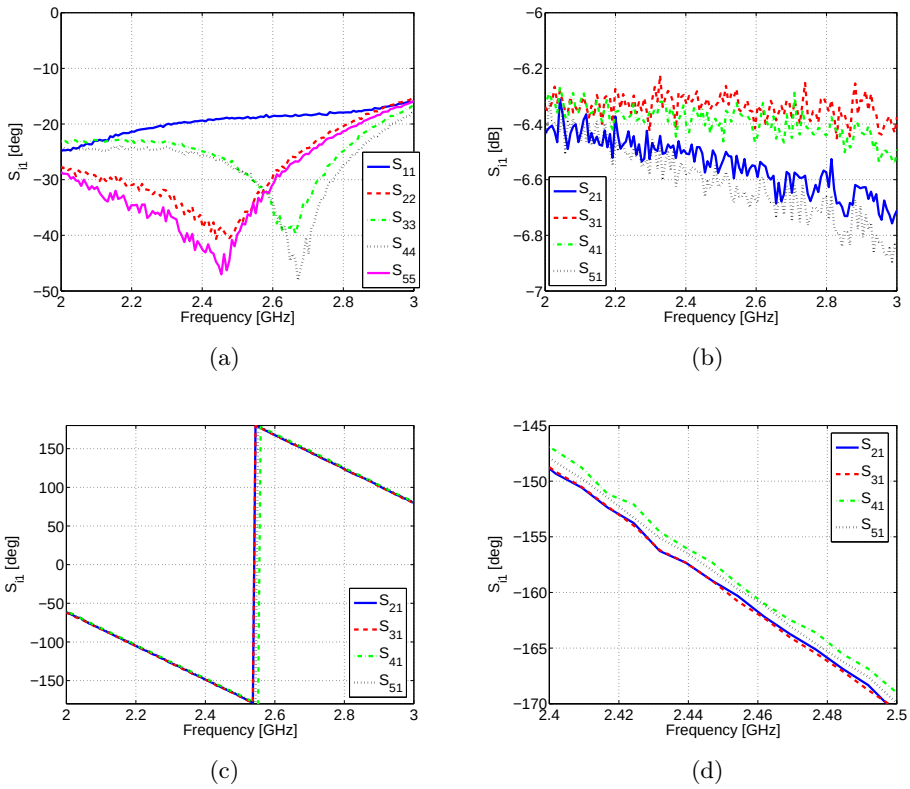

Figure 6.21: S-parameter measurements of the 4-way power divider. In (a) are the input and output return losses. In (b) is the insertion loss. In (c) are comparison of the phases from the input to each output and in (d) the phases are shown again, only between 2.4 and 2.5 GHz.

Table 6.6: Frequency synthesizer specification.

Output Frequency [GHz]	Output Power [dBm]	PN @1kHz [dBc/Hz]	Reference Frequency [MHz]
2.0 - 4.0	0 ±0.5	-85	10

6.6 Microcontroller Modules

All the transmitters and all the receivers, along with both frequency synthesizers have microcontroller modules (MCU-PCB) integrated. The functionality of the MCU-PCB is to interpret digital control signals from the PC to set the appropriate values in each of the controllable components. A simple protocol was developed for the microwave activation system in order for the PC to communicate with each MCU-PCB and thus each transmitter, receiver and frequency synthesizer individually. Every transmitter,

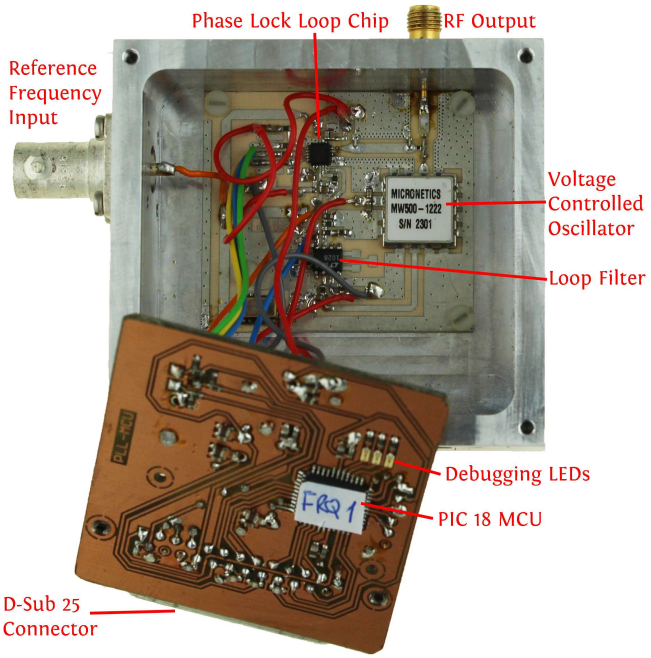

Figure 6.22: A photograph of the frequency synthesizer, top view.

receiver and frequency synthesizer have their own address, and furthermore every controllable component (DAC, VGA, VA, IF-Amp and PLL chip) have their own sub-address. Each individual component can therefore be directly controlled by the PC without interfering with the rest of the controllable components.

The core of the MCU-PCBs is the PIC18F46K22 which is an 8-bit microcontroller from Microchip. This MCU has SPI support which is necessary for easily communicating with each of the controllable components. Although all the components have SPI support as well, a slight difference of each manufacturer (Hittite, Analog Devices, TriQuint, Maxim Integrated) in implementing the SPI protocol required attention to the „latch" input of the components which deals with latching the received bit-stream into the component's memory.

The MCU-PCBs have D-sub 25 connectors for connecting to the distribution network, discussed above. From the connector, the power supply voltages are decoupled with capacitors for noise reduction and fed to the MCU as well as to the microwave PCB and IF PCB.

The MCU-PCB can be seen in Figures 6.11, 6.16 and 6.22. The MCU-PCB is similar for all three modules (TX, RX and Freq. synth.) in regards to functionality.

6.7 Data Acquisition and User Interface

6.7.1 Data Acquisition and Digital Control

A USB data acquisition module from National Instruments (NI), called USB-6009 was used for controlling each of the components discussed in previous sections. The USB-6009 has eight, 14-bit, 48k Samples/s analog inputs and 12 digital I/O. This module provides an easy way of both communicating with the components as well as being integrated in LabView, which was used for user interface. The module is shown in Figure 6.23. On the left side of the module, a shielded cable with multiple wires were connected to the digital outputs of the USB-6009. These digital outputs provide the digital control signals for setting the desired values in each controllable component that ultimately controls the amplitudes and phases of the transmitters/receivers and the operational frequency of the frequency synthesizers. The digital control signals were fed to the distribution network from which they were further distributed to each transmitter/receiver/freq.synth. module. The cable from the USB-6009 to the distribution network and also the cables from the distribution network to each module are shielded as can be seen from Figure 6.23 to minimize interference.

On the right side of the USB-6009 in Figure 6.23, the IF signals from each of the four receivers were fed into the analog inputs of the USB-6009 with shielded coaxial cables, again to minimize interference. The IF signals were connected to every other analog input, i.e. 0, 2, 4 and 6, whereas inputs 1, 3, 5 and 7 were terminated in 50 Ω. When using four adjacent inputs (0, 1, 2 and 3 e.g.) sometimes the measured signals were incorrect. This is believed to be due to the fact that the analog inputs are multiplexed sequentially where the multiplexer is connected to a single analog to digital converter that samples the input signals, one input at a time. Every time

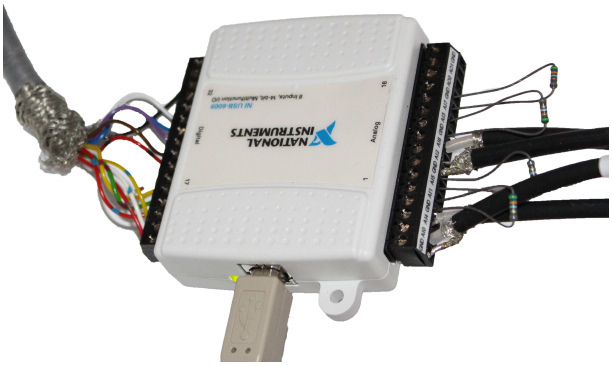

Figure 6.23: A photograph of the USB-6009 data acquisition module from NI.

an input was sampled, a capacitor in the ADC was charged up and when multiplexing fast between the inputs, it could cause some residual voltage on the ADC input from the previous sample. By terminating every other analog input this was avoided as the terminations make sure that the input capacitor was uncharged before next sampling.

6.7.2 User Interface

The amplitude, phase and frequency of each module were controlled from a LabView virtual instrument (VI), I developed for the microwave activation system. Figure 6.24 illustrates a part of the digital control user interface in LabView. The frequency control for frequency synthesizer 1 is displayed along with the DAC voltage control and the attenuation for TX-1 as well as the attenuation and amplification for RX-1.

A reference frequency along with the operational frequency of each frequency synthesizer were typed in, in the frequency control tab where the appropriate register values were calculated and sent to the MCU-PCB of the frequency synthesizers. In the transmitter tab, the DAC voltage was set which ultimately controls the phase as illustrated in Figure 6.13(d). In both the transmitter and receiver tabs each individual attenuator setting, 0 - 31.5 dB attenuation with 0.5 dB steps were set for both the variable attenuator and the variable gain amplifier and are represented with 16, 8, 4, 2, 1 and 0.5 dB buttons. Finally, the IF amplifier was controlled with a slider in the receiver tab.

The received IF signals are illustrated in graphs in tabs for each individual receiver, RX-1 to RX-4. This includes a fast Fourier transform (FFT) of the received signals before and after software filtering for visualization of the frequency content of each IF signal. The amplitudes and relative phases are displayed in the total received signal tab where the IF signals can be compared. From this tab, the automatic measurements are controlled. A measurement was taken every 20 seconds, which provided a pause to change the position of the internal antenna before the next measurement. A screenshot of few of the tabs is shown in Figure 6.25.

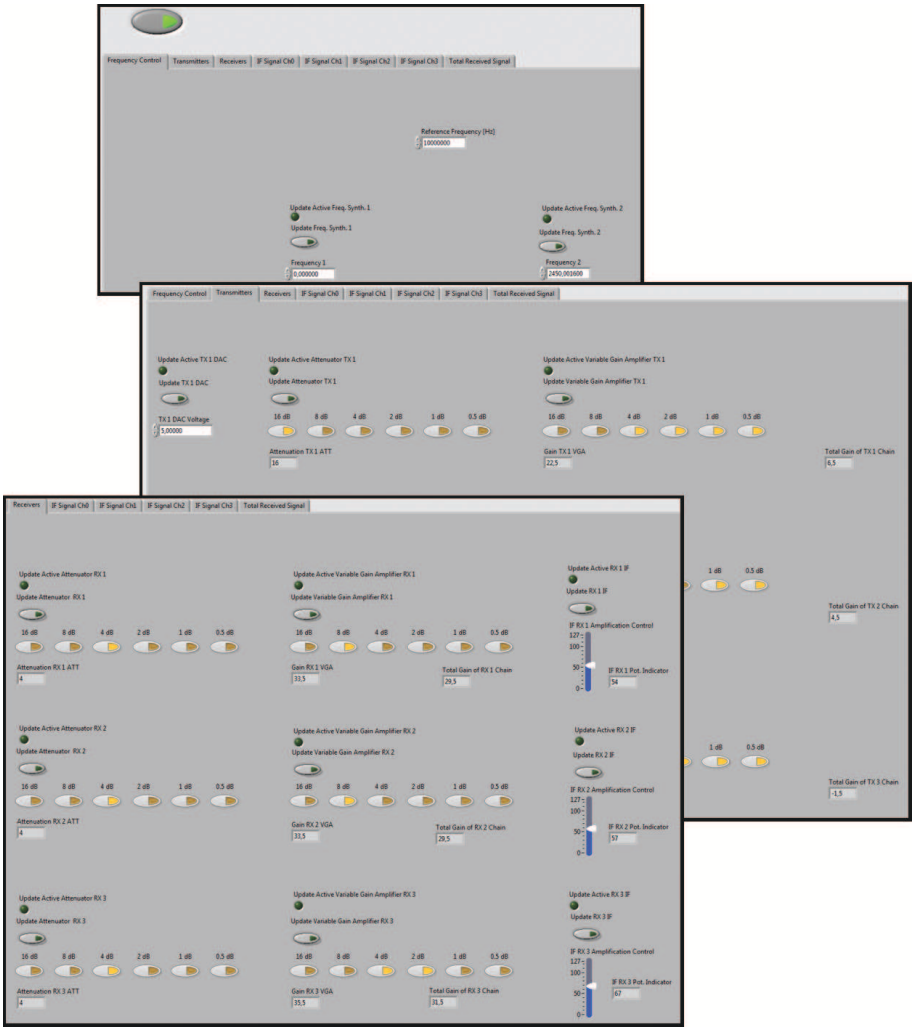

Figure 6.24: A screenshot of the digital control user interface.

6.8 The Microwave Activation System

This section contains photos of the microwave activation system after integration of all the components and modules. Figures 6.26 and 6.27 show the entire microwave activation system from above and from the side, respectively. Figure 6.28 displays a part of the torso phantom and two of the antennas along with two transmitters.

Figure 6.29 shows the phantom, without its inner cylinder and with the submerged antenna inside the cylinder, for visual illustration. Microwave absorbers are seen around the microwave activation system for reduction of reflections from external objects and will be discussed further in Section 7.

Figure 6.30 shows a close up photo of one of the external stacked patch

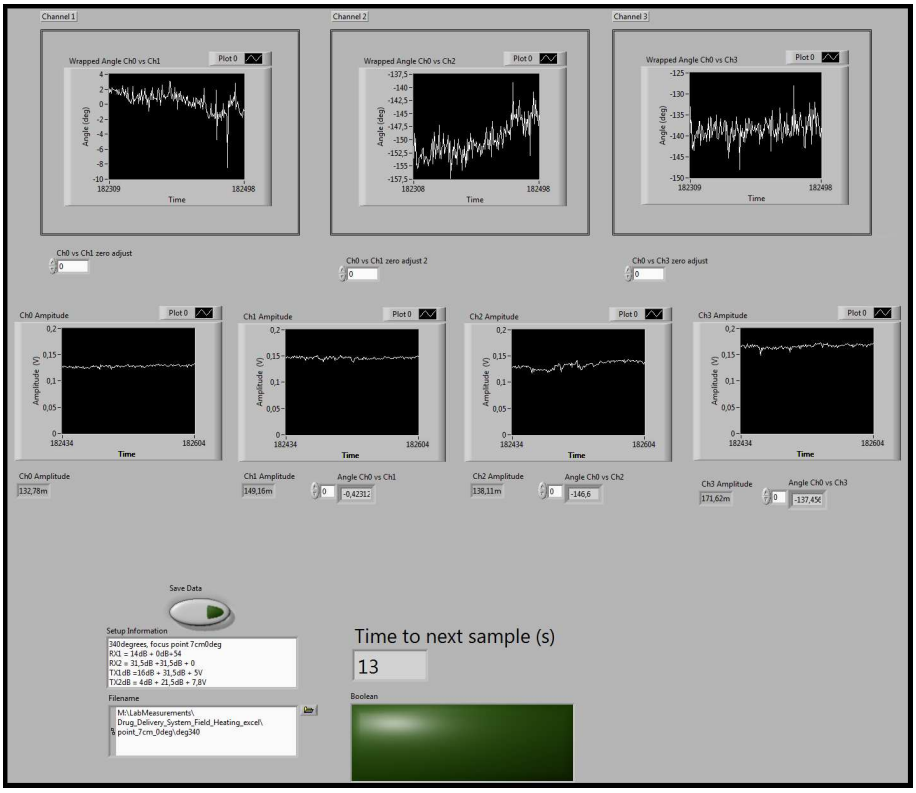

(a)

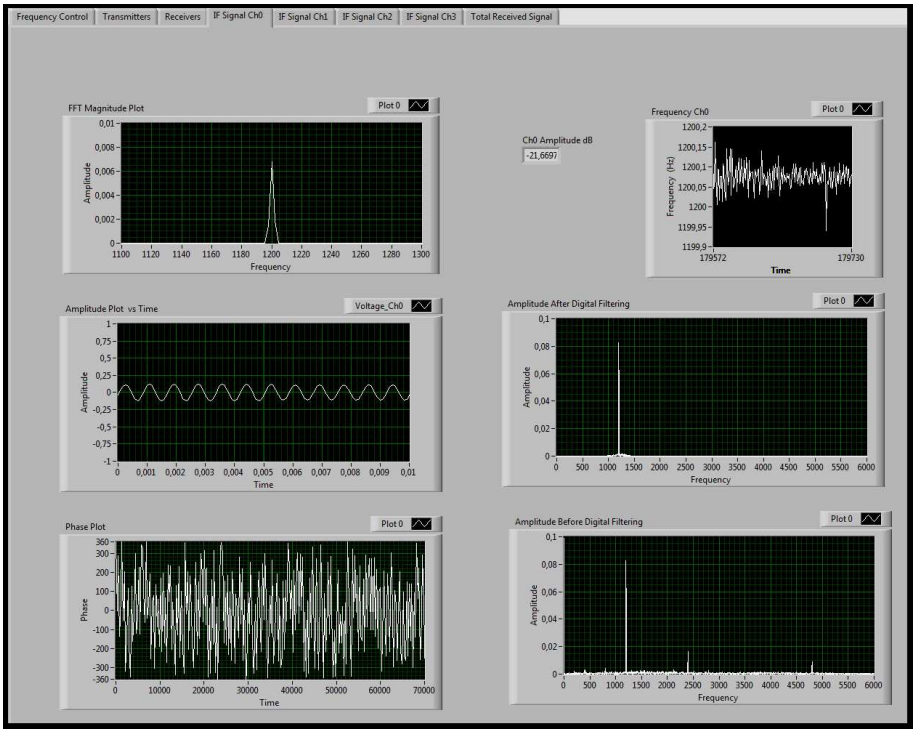

(b)

Figure 6.25: A screenshot of the received signals. (a) shows the amplitudes and phases while (b) shows a IF signal in time and frequency domain.

antennas connected to a transmitter. On the power supply cable to the transmitter, a clip-on ferrite core electromagnetic interference filter can be seen, for noise reduction.

Figure 6.31 displays the internal antenna mount and the slot in the phantom lid, it moves along. A semi-rigid cable is connected to the internal antenna as it prevents liquid to penetrate into the cable in comparison to a flex cable. It also has better isolation and phase stability.

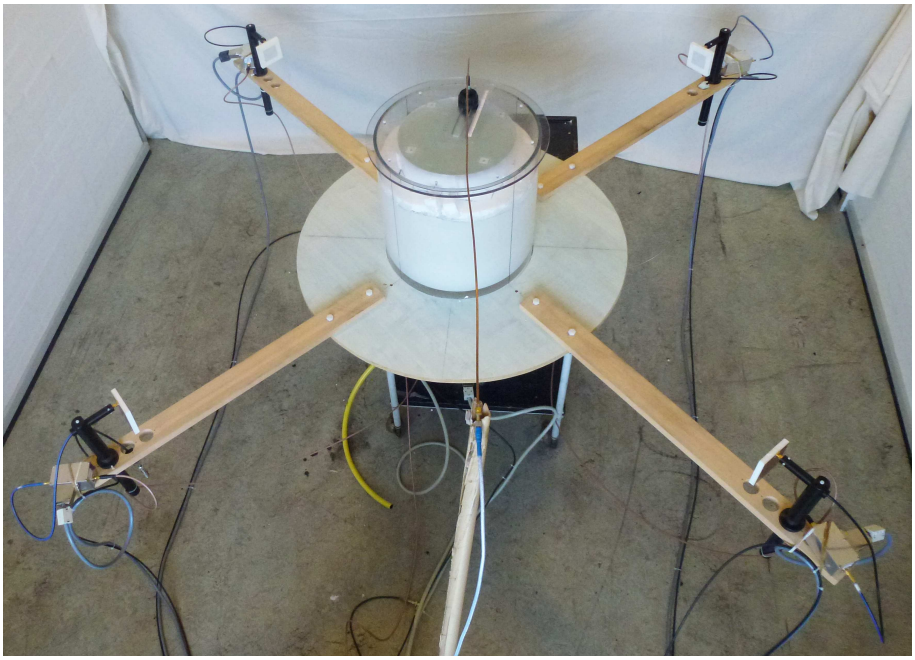

Figure 6.26: A photo of the microwave activation system seen from above.

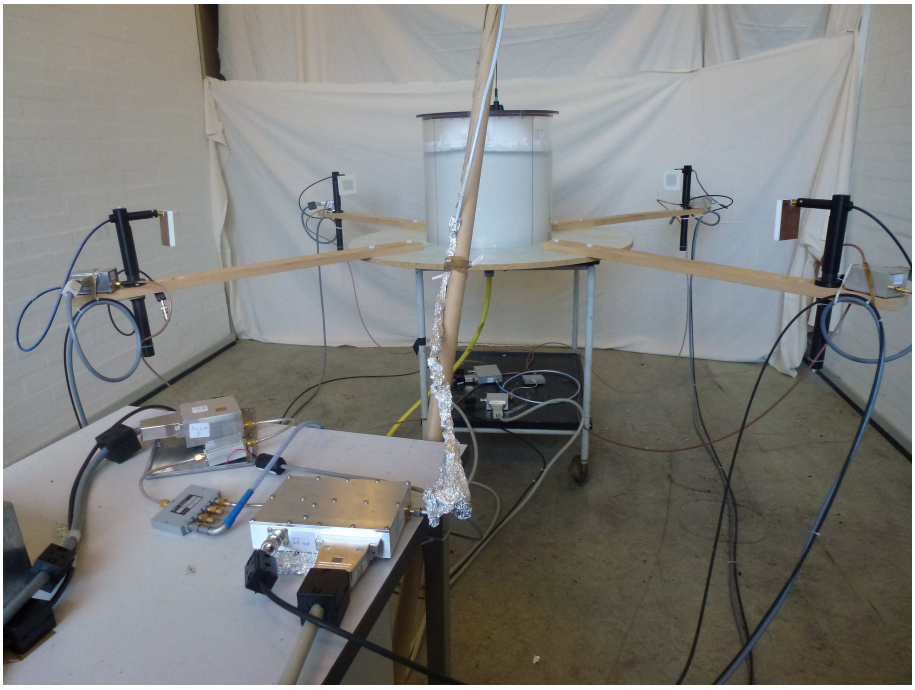

Figure 6.27: A photo of the microwave activation system seen from the side.

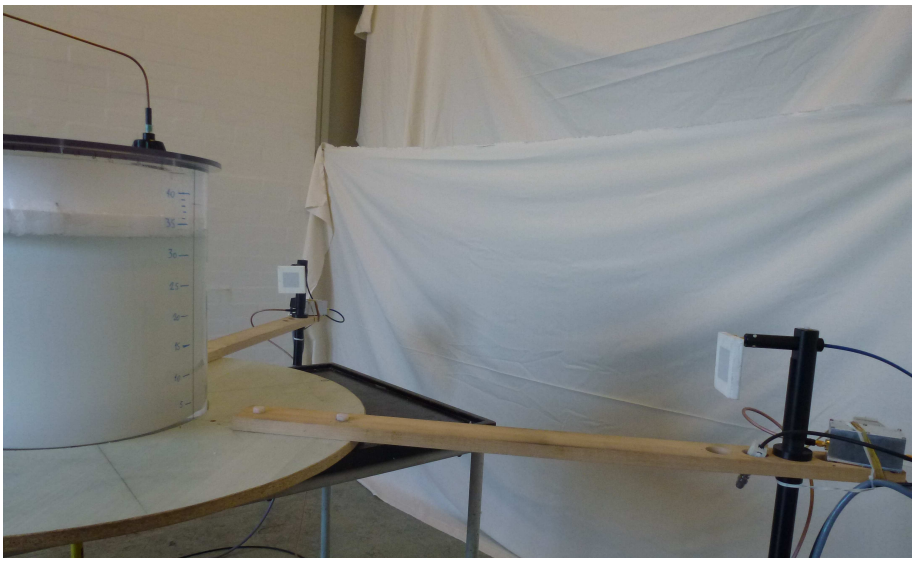

Figure 6.28: A photo of part of the phantom along with two transmitters and external antennas.

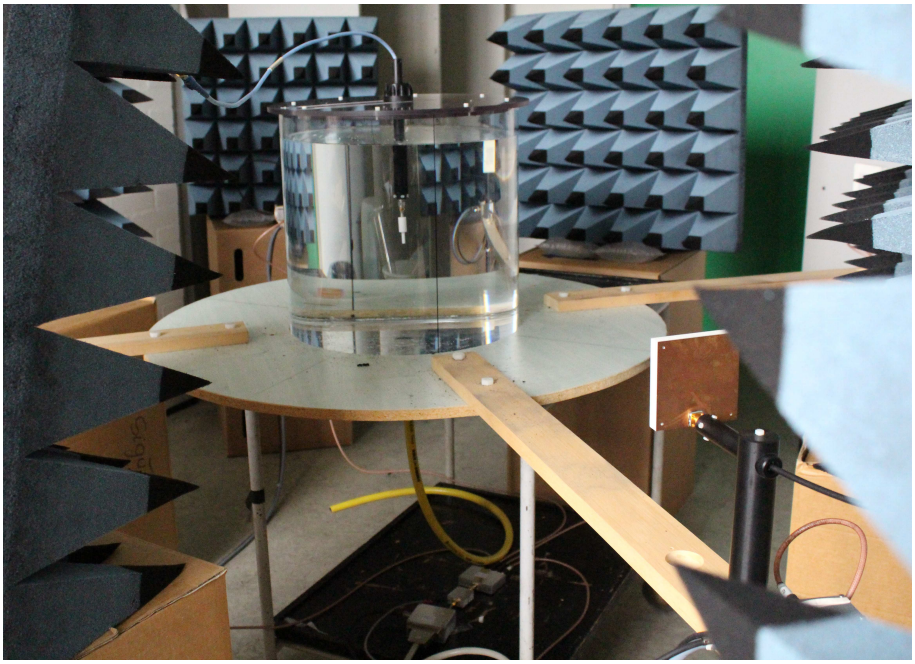

Figure 6.29: A photo of the phantom without its inner cylinder for visualization purposes. Microwave absorbers are placed around the microwave activation system for reflection reduction.

Figure 6.30: A close up photo of the external stacked patch antenna mounted on one of the system's wooden arms. A transmitter is fastened on the arm behind the antenna.

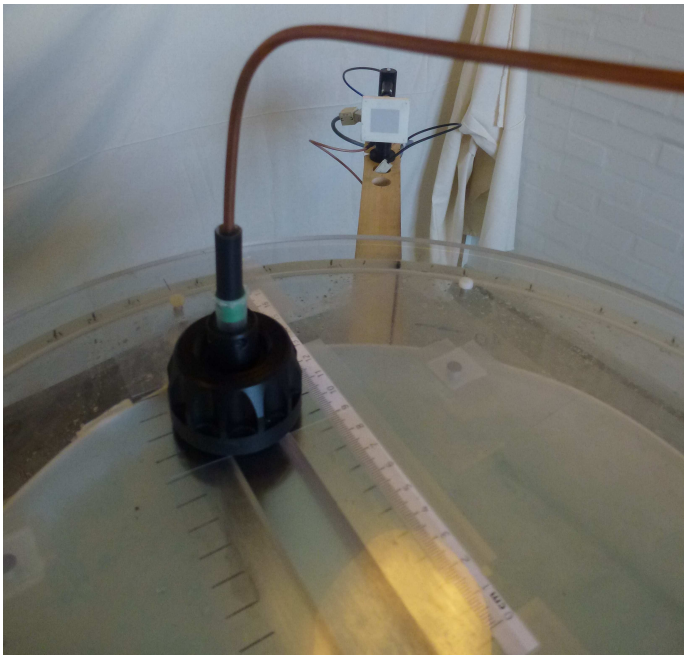

Figure 6.31: A photo of the internal antenna mount on top of the lid of the phantom. The slot where the internal antenna moves along is also seen with a ruler that indicates the distance offset from the centre of the phantom.

Chapter 7

System Measurements - *Mapping*

In this chapter, attention is directed at a source, transmitting from within a phantom that is representing the human torso. Four receivers are distributed around the phantom in an annular manner to measure the resulting fields. Transmission from within a cylindrically layered structure such as the human torso phantom is of great interest when examining the wave behaviour inside and around a human torso. Amplitudes and phases on the outside of the phantom will vary as the transmitting source inside the phantom is moved around. This dependency will be mapped with measurements, based on the experimental setup that was introduced in Section 5.5 using the manufactured modules presented in Chapter 6. The measurement results are compared to simulation results and their deviations are discussed in this chapter.

7.1 Measurement Setup

In the microwave activation system where high dynamic range is required to measure high signal levels at one point and very low signal levels at another, the influence of reflections from external objects had to be minimized. If e.g., the transmitted signal from within the phantom has a high power level when it exits at one point of the phantom and a very low power level at another point, external objects can in fact reflect the high level signal in a way that it overshadows the low level signal. This would cause an incorrect measurement and distort the overall mapping. The risk of reflections from external objects was reduced with the introduction of microwave absorbers. In Figure 7.1, a simple representation of the microwave activation system is illustrated along with the microwave absorbers. Eight microwave absorbers were placed in the plane of measurement, where one was placed behind each receiver and one between each receiver as shown in the figure. The absorbers

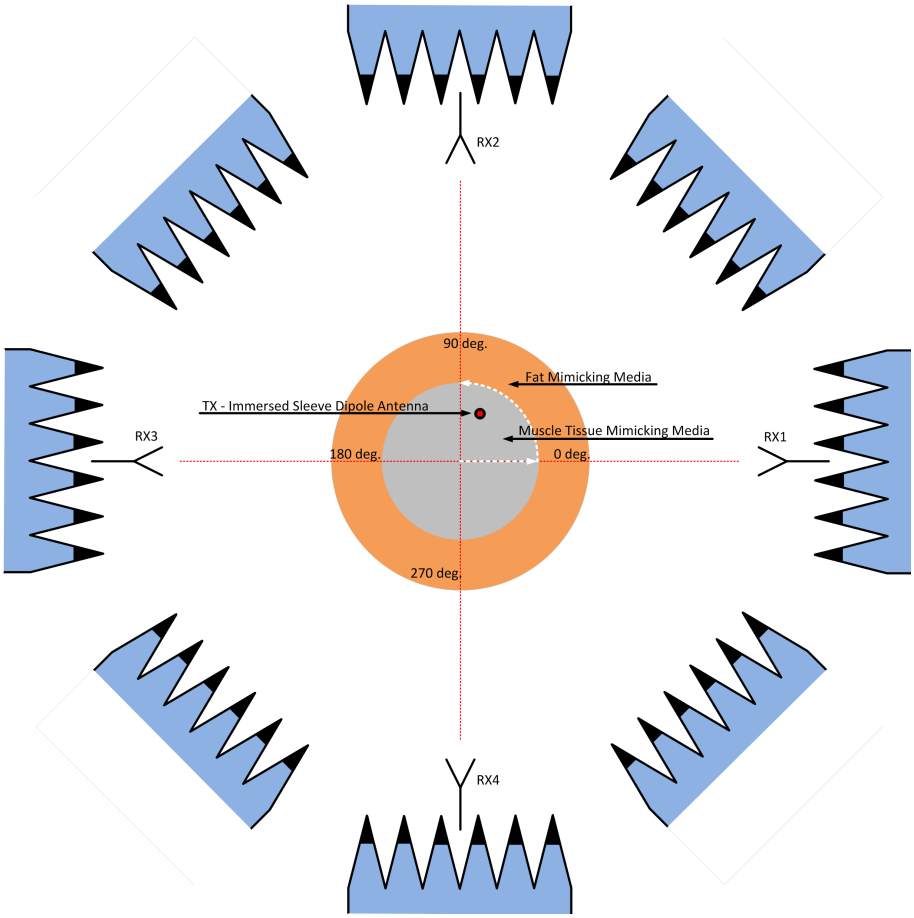

Figure 7.1: A simplified measurement setup of the microwave activation system (not to scale).

attenuate waves at 2.45 GHz approximately 20 dB one way and 40 dB on reflection according to the in-house expert on absorbers, and are typically utilized in anechoic chambers.

Each receiver is labelled RX-1 to RX-4, depending on its position. RX-1 was the receiver placed at the 0° position, RX-2 at the 90° position, RX-3 at the 180° position and RX-4 at the 270° position.

The submerged sleeve dipole antenna was mounted on the lid of the phantom as mentioned before. The lid can be rotated 360° in a continuous movement. The submerged antenna can also be moved continuously back and forth, from the centre of the phantom and 11 cm outwards.

In a single measurement round, the lid was positioned according to the desired angle in respect to the 0° position. The submerged antenna was step-wise moved from the centre (r, ϕ) = (0 cm, 0°) and outwards until it had reached 11 cm. The submerged antenna was moved in steps of 2 mm

with a typical uncertainty of ±0.5 mm, for each measurement. The 2 mm step were chosen as this is approximately $\lambda_m/8$ and was the smallest step size the antenna can be reliably moved in a manual manner. The submerged antenna mount was made of a plastic screw on the lid, and when displacing the antenna, the screw was loosened, moved and then tightened again before a new measurement was taken. Alongside the slot in the lid, where the antenna moved back and forth, there is a fixed ruler with 1 mm resolution and on the antenna mount there is a slot, used as a reference for the internal antenna in respect to the ruler. A close-up of the antenna mount and the slot with the ruler was shown in Figure 6.31. The displacement of the antenna was controlled manually which explains the uncertainty of typically ±0.5 mm.

An automatic measurement could be started as described in Section 6.7 where the computer took a measurement every 20 seconds. After each repositioning of the internal antenna, I stepped behind one of the absorbers to reduce the risk of being a source of reflection and therefore disturbing the measurements.

The frequency of synthesizer 1 was set to 2450.0004 MHz and the frequency of synthesizer 2 was set to 2450.0016 MHz. This provided an IF of 1.2 kHz. It was found that there was a constant carrier signal at 2450.0000 MHz in the ambient, probably due to the in-house wireless network and therefore synthesizer 1 was set at a 400 Hz offset from 2450.0000 MHz. This ambient noise was measured using a spectrum analyzer with a dipole antenna connected to its input. The carrier in question was concluded to be from the ambient as when the experimental setup was powered down, the carrier signal remained unchanged in both amplitude and frequency.

TX-1 was the transmitter used in the mapping process. The attenuator setting was set to attenuate 8 dB and the VGA has also enabled 10 dB attenuation. The receivers, RX-1 to RX-4 had attenuator settings set to 14 dB and VGA set to 8 dB attenuation and finally the variable gain IF stage at a factor 23/127. This modest gain settings for the receivers prevented the ADC to saturate when the antenna was closest to the outskirt of the phantom as well as the overall signal quality was better. The noise floor was below 5 mV for these settings on the receivers and was determined from the display showing the measured voltage of the IF signal in the Labview user interface.

The height of the internal antenna was such that, the centre of the antenna was (vertically) in the middle from the bottom of the cylinder and the top of the fat mimicking media. The fat mimicking media was not filled all the way to the top of the outer cylinder as mentioned before, due to the problem with buoyancy of the inner cylinder containing the muscle tissue mimicking media. The heights of the four external antennas were adjusted so the centres of the stacked patch antennas were in the same horizontal plane as the internal antenna. The maximum gains of the external antennas

were therefore in the same horizontal plane, and full advantage was taken of their high gain.

7.2 Calibration

When the internal antenna was placed at the centre of the phantom, the receivers did not measure the same phase. A 0° position e.g. resulted in a slightly different phase measurements than e.g. at 135° position of the lid.

Due to variations from receiver to receiver, variation in length of SMA coaxial cables connecting the receivers to the antennas and the local oscillator as well as difference in distance between each external antenna to the internal antenna, the measured phases in the receivers needed calibration.

For every measurement round, at a certain position of the lid, the internal antenna was placed at the centre of the phantom. In software, the phases are adjusted to zero. The phase control was displayed in Figure 6.25. This zeroing of the phases was repeated for every rotational position of the lid, immediately before measuring.

Note that when mentioning some values in degrees in the text below, it typically refers to the phantom lid's position and not a phase, unless stated otherwise.

7.3 Results and Discussion

Referring to Figure 7.1, a measurement round was acquired for every 10° rotational increment of the internal antenna orientation from 0° to 360°. Additionally, measurements were obtained between every two receivers, i.e. at 45°, 135°, 225° and 315° for a symmetry comparison. The starting position, defined as 0° was at the location of RX-1 as indicated in Figure 7.1 for convenience. Every measurement round includes 55 measurements points, from 0 (centre of the phantom) and to 11 cm outwards. Since each measurement point was taken discretely and the internal antenna was repositioned for every measurement point, a limited number of points had to be taken. A step radially outwards of 2 mm provided a relatively dense phase and amplitude information as every step is about 1/8 of the wavelength in the muscle tissue mimicking media. In total, the number of discrete measurements points of the mapping process was 2200, which was rather time consuming. The number of points also had to be restricted because of long term variation of, especially, the tissue mimicking media which evaporated and deteriorated over time. Each of the four receivers RX-1 through RX-4, measured an amplitude and a phase. The measured phases of RX-2, RX-3 and RX-4 were taken relative to the phase of RX-1, which was the reference.

A simulation model was created in COMSOL Multiphysics. A 2-D dual-layer phantom with a line current source (out of plane) that represents the

human torso phantom and the internal antenna. The simulation model was created from measured inner and outer diameters of the two phantom cylinders presented in Table 5.1. The cylinders were included in the simulation model as Plexiglas. The simulation model was like a slice of the horizontal plane which was the plane of measurements. The mesh was a so-called free triangular mesh with a maximum element size of 1 mm in the fat and muscle zones and 4 mm maximum size in the area around the phantom with radius of 1 m, defined as vacuum. The simulation results were normalized to the initial (x = 0) measured values.

The muscle was simulated with $\epsilon_r' = 42.6$ and $\sigma = 1.63$ S/m which is slightly lower parameters than presented in Section 4. The reason for this was that, at the point of the measurements presented here, a part of the water in the muscle tissue mimicking media had evaporated and therefore changed the parameters of the MTMM which were measured to have the values used in the simulation. Around 3 weeks had gone by, from making of the MTMM and until the final mapping measurements were made.

Figure 7.2 shows the amplitude measurement and simulation results of all four receivers at 0°, while moving the internal antenna, which was transmitting, from the centre of the phantom and outwards. In Figures 7.2(a) and 7.2(b) the amplitudes are displayed on a logarithmic scale (dBV). Figures 7.2(c) and 7.2(d) shows linear amplitudes for the first 6 cm in order to illustrate the dependence of the small amplitudes to the displacement close to the centre of the phantom in linear scale. The internal antenna was, at 0°, essentially moving towards RX-1 and therefore directly away from RX-3, the RX-1 measured the highest amplitudes and RX-3 the lowest which was also the case most of the way. There is a difference in the measured amplitudes of RX-2 and RX-4, which up until approximately 4 cm are similar. This was most likely due to differences in gain of the two receivers, or difference in losses or distance of the traveling wave from the internal antenna to the receiving antennas due to a position offset of the inner cylinder in respect to the outer (they are not perfectly concentric). This is covered in further detail in Section 10.4 on possible performance-reduction factors. This is not believed to be due to multiple reflections as this difference seemed approximately constant above 4 cm and one might expect destructive interference at some points as the position of the antenna was varied.

The ripples evident at high measured voltages in Figure 7.2(a), when the internal antenna was close to the edge of the inner cylinder of the phantom are believed to be caused by standing waves due to the presence of the conducting antenna close to the discontinuity. A summation of a transmitted and a reflected wave of the boundaries between the receiving antenna and the phantom as well as inside the phantom, composed the standing waves. This behaviour was not predicted by the simulation results. The comparison is more clear in Figure 7.3 where the measurement and simulation results are plotted against each other.

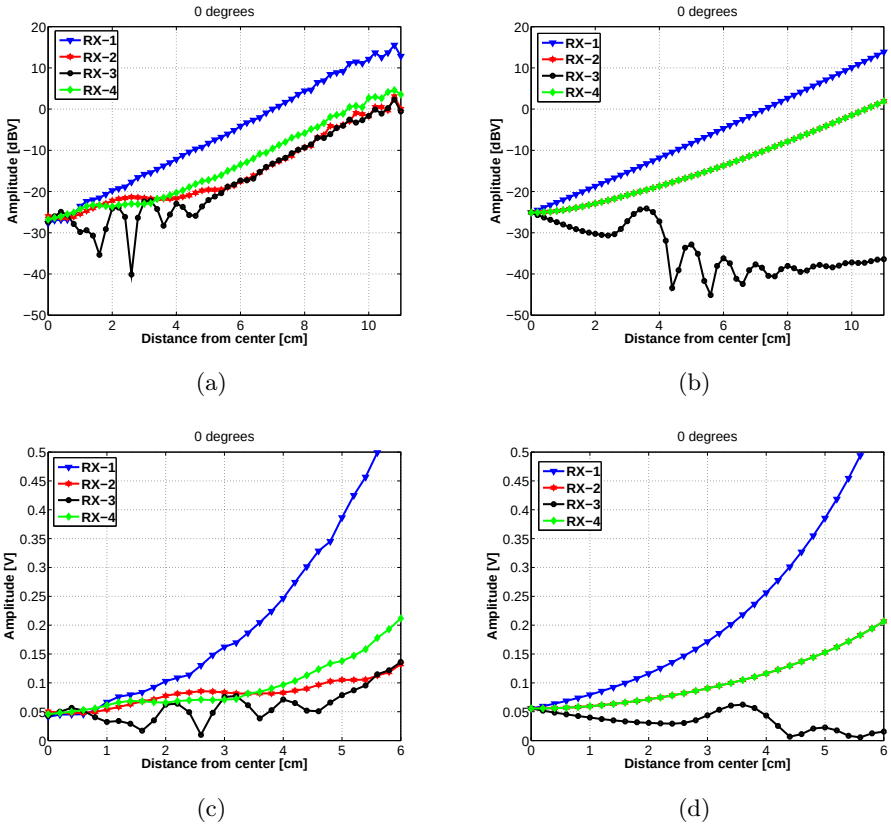

Figure 7.2: Amplitude measurements (left) and simulations (right) at 0°. In (a) is measurement results in logarithmic scale, (b) simulation results in logarithmic scale, (c) measurement results while zoomed-in to the lower part in linear range and (d) simulation results while zoomed-in to the lower part in linear range.

The ripple behaviour of the RX-3 curve (black) in Figure 7.2(a) for distance between 1.5 and 5 cm are not believed to be due to standing waves but are believed to be due constructive and destructive interferences of so-called creeping waves. Similar ripple behaviour is seen in the simulation results shown in Figure 7.2(b) but in the simulations they appeared at distances further than 3 cm from the centre. A comparison between the two is shown in Figure 7.3. The measured amplitude of RX-3 is also higher than the simulated one and it starts to rise in the measurements as the internal antenna was moved towards the edge of the phantom. The reason for this discrepancy is believed to be a underestimation of the effect of creeping waves when the source was approaching the edge of the inner cylinder of the phantom, in the simulation.

The logarithmic amplitude slope of RX-1 and RX-3 in Figure 7.3(a), and

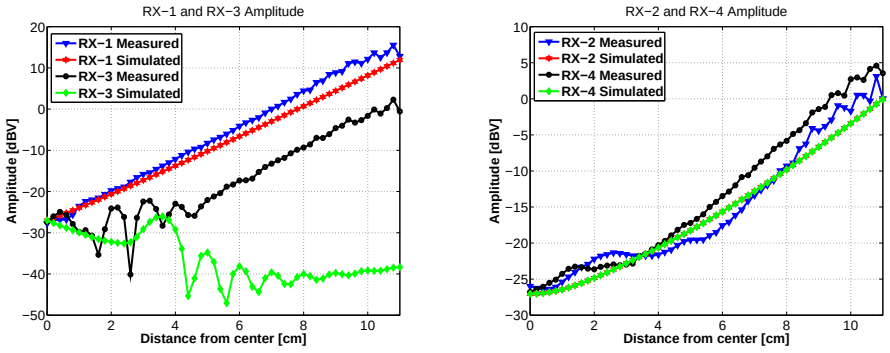

(a) (b)

Figure 7.3: Amplitude measurement and simulation comparison at 0°. In (a) results for RX-1 and RX-3 and in (b) results for RX-2 and RX-4.

RX-2 and RX-4 in Figure 7.2(b) is different between the measured and the simulated results. This might suggest that either the permittivity or the conductivity, or both, are not modelled entirely correct with $\epsilon_r' = 42.6$ and $\sigma = 1.63$ S/m. There appears to be lower losses in the simulated results since the slope is less than the measured one. Underestimation of path losses in the simulation is one possibility. Another possibility is an erroneous measurement of ϵ_r' and σ for the muscle tissue mimicking media where they are in fact closer to the design values of $\epsilon_r' = 53.6$ and $\sigma = 1.81$ S/m. Inaccurate representation of ϵ_r' and σ for the fat mimicking media in the simulation could also contribute to this discrepancy.

The measured and simulated relative phases at 0° are found in Figure 7.4. The measured phases were unwrapped on the fly by the Labview aquisition program, since this gives a clearer picture of the phase dependence with displacement.

Interestingly, the phase of RX-3 - RX-1, shown in Figure 7.4(a) does not decrease linearly with displacement, all the way from the centre (r, ϕ) = (0 cm, 0°) towards the end of the measurement area (11 cm). This happens in a similar manner for both the measured results and the simulated results. The linear phase increase is typically what one would expect when moving a transmitting antenna directly towards one receiver and away from another receiver, where their relative phase is measured. The phase in Figure 7.4(a) actually flattens out, at around 3.2 - 3.4 cm for the measurement and 5 cm for the simulation and stays approximately constant for the remaining distance. This phase flattening is believed to be due to creeping waves at the surfaces of the muscle tissue mimicking and fat mimicking media.

A plot of the E-field amplitude in a logarithmic scale simulated in COMSOL when the line current source is approaching the edge of the muscle

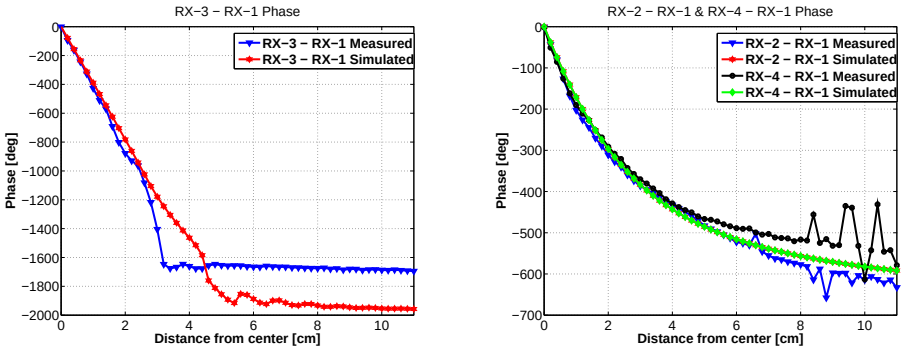

(a) (b)

Figure 7.4: Phase measurements and simulation in COMSOL at 0°. In (a) is the results for RX-3 - RX-1 and in (b) is the results for RX-2 - RX-1 and RX-4 - RX-1.

phantom is shown in Figure 7.5. Red colour indicates high intensity and blue colour low intensity. The graph's purpose is give an indication of the behaviour of the field and not exact amplitude values. Interestingly, there are two low amplitude stripes away from the bottom of the phantom. It is seen that on the opposite site to the source, in the muscle phantom there is a low-amplitude (blue) zone. Yet, outside the phantom radially away, downwards from this blue zone, the amplitude is at places green, i.e. with higher amplitude than the blue zone. This indicates that the direct path from the source was not alone determining the amplitudes at locations away from the source and therefore it is suggested to be due to diffraction, often referred to as creeping waves.

When the internal antenna was at distances above 3.2 mm from the centre (5 cm in the simulation), the received power of RX-3 must have originated from the area of the phantom that faces RX-1. With increasing internal antenna displacement from the centre, the power exiting the phantom towards RX-1 rose and the power exiting the phantom towards RX-3 was reduced. Up until the „knee" (above 3.4 cm for the measurement or 5 cm for the simulation) of the RX-3 - RX-1 curve, the received power of RX-3 arose from the direct path from the internal antenna towards RX-3 as expected. At around the knee, the power from the direct path was approximately equal to the power from the creeping waves and at displacements above the knee, the creeping wave dominated the received power of RX-3. This phenomenon of creeping waves is further explained in Chapter 9. The steeper slope of the measured phase, seen in Figure 7.4(a), compared to the simulated one, indicates a lower relative permittivity of the muscle or the fat in the simulations than in the measurements.

In Figure 7.4(b) the measured and simulated relative phases of RX-2

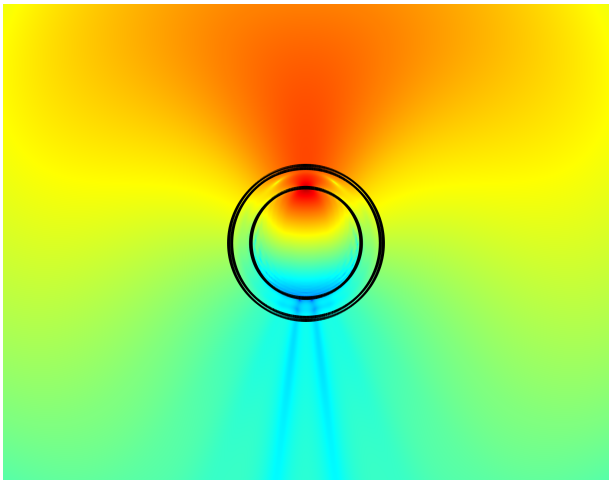

Figure 7.5: Simulated E-field amplitude plot in logarithmic scale from COMSOL of the phantom and its surroundings when the source is near the edge of the muscle tissue model. Red colour indicates high intensity E-field and blue colour low intensity.

- RX-1 and RX-4 - RX-1 are shown. At least until at around 6 cm from the centre the simulated phase and the measured phases agree quite well. Same tendencies are seen for the entire span for the simulated phases and the measured ones.

The ripples seen in Figure 7.4(b), in the black and blue curves between 8 and 11 cm are due to averaging of the wrapped phases. If a phase was close to either 180° or -180°, small variations between samples could make the phase jump between 180° and -180°. At every phase measurement an average of 10 samples was acquired and if some of the 10 samples were at around 180° and other samples were at around -180°, the average becomes very skewed and does not represent the correct phase. This was corrected in the raw measurement data where it was obvious that the phase was $\pm 180^\circ$. At places where the actual phase could not be established to be $\pm 180^\circ$, the raw data was not altered. This averaging was done on the on the fly while aquiring data in the Labview program and can therefore not be reversed. Averaging should be done after unwrapping of the phase to avoid this issue in the future.

Similar to the measurements when the phantom lid was at 0° discussed above, measurements are presented for when the lid was at 45°, i.e. just in between RX-1 and RX-2, referring to Figure 7.1. Figure 7.6 displays amplitude measurements and simulations at 45°. Figures 7.6(a) and 7.6(b) display measurement and simulations results, respectively in logarithmic scale. Figures 7.6(c) and 7.6(d) show measurement and simulations results, respectively, the first 6 cm in a linear range.

The measured amplitudes of the RX-1 and RX-2 follow each other quite

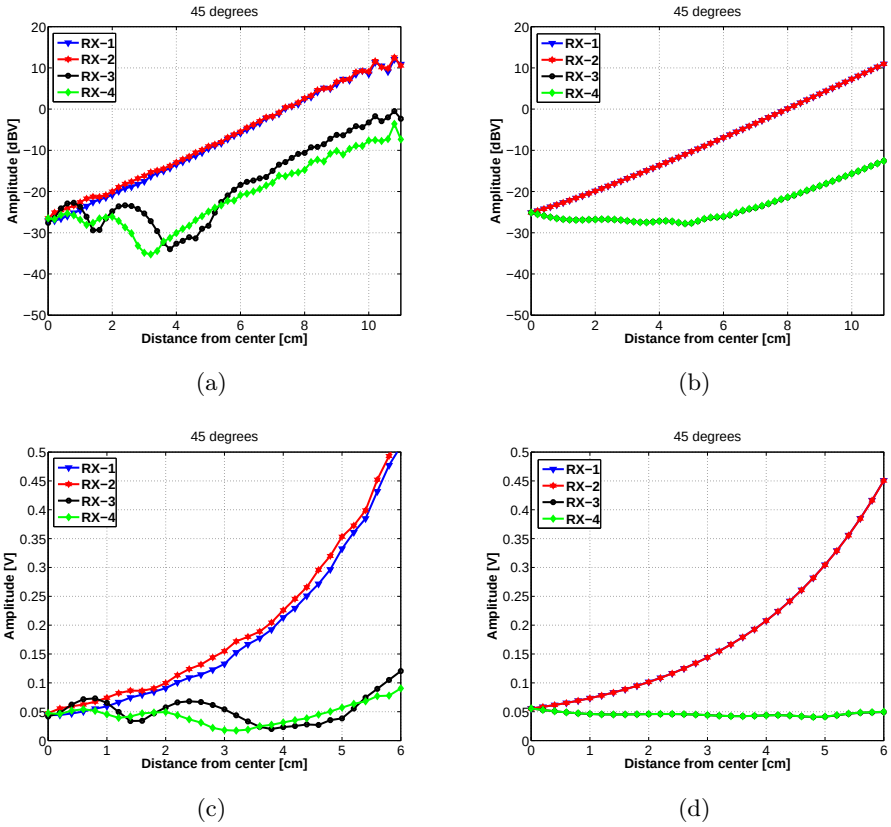

Figure 7.6: Amplitude measurements (left) and simulations (right) at 45°. In (a) are measurement results in logarithmic scale, (b) simulation results in logarithmic scale, (c) measurement results while zoomed-in to the lower part in linear range and (d) simulation results while zoomed-in to the lower part in linear range.

well and the balance of the two receivers is demonstrated to be good. Compared to the simulated results, similar tendencies can be seen. The difference in the slope of the amplitudes between the measured and the simulated are evident here as for the 0° case. There are ripples at internal antenna offsets above 9 cm approximately for the high amplitude signals of RX-1 and RX-2 believed to be due to standing waves, similar to the 0° case. The measured amplitudes of RX-3 and RX-4 show similar behaviour to each other. Compared to the simulation, there is approximately 10 dB difference at distances from centre above 7 cm.

A comparison between the measurements and the 2-D simulation in COMSOL of the phases with the lid at a 45° angle is shown in Figure 7.8. The measured and simulated phases for RX-3 - RX-1 and RX-4 - RX-1 are displayed in Figure 7.8(a) and the corresponding phases for RX-2 - RX-1

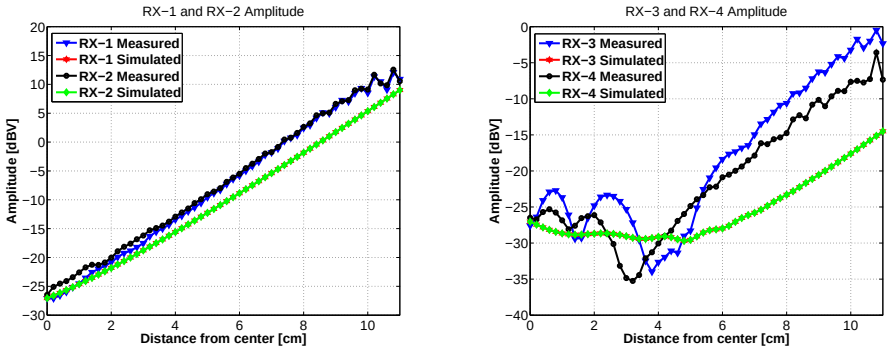

(a) (b)

Figure 7.7: Amplitude measurement and simulation comparison at 45°. In (a) results for RX-1 and RX-2 and in (b) results for RX-3 and RX-4. The simulated (red) curves for RX-1 in (a) and RX-3 in (b) cannot be clearly seen as they are behind the green curve in both cases.

in Figure 7.8(b). The agreement between the measured and the simulated phases is shown.

The measured phases of RX-3 and RX-4, relative to RX-1 follow the simulated ones well in Figure 7.8(a). There are some deviations between the two, however. Again, ripples can be seen in the measured phases between locations of 6 and 11 cm. As explained above, this is due to errors in the averaging of the wrapped phase at around $+180°$ and $-180°$.

The phase difference of RX-2 and RX-1 is supposed to be zero, and this is the case in the simulation. The measurements also show a phase at around zero but the phase goes to a minimum of $-10°$ at most which is encouraging considering that 5° in the muscle tissue mimicking media represents 0.2 mm.

A collection of amplitude measurements on a logarithmic scale for RX-1 is shown in Figure 7.9. Each measurement round at every 10°, is plotted in the figure. Comparable amplitude measurement results for receivers RX-2, RX-3 and RX-4 are displayed in Appendix D. A collection of phase measurement results presented in a similar way as the amplitude results for RX-2 - RX-1, RX-3 - RX-1 and RX-4 - RX-1, also in 10° steps can be found in Appendix D.

For each receiver, the received signal amplitudes were plotted as a function of the internal antenna's position within the inner cylinder. The results for RX-1 can be seen in Figure 7.10 and is merely another way of plotting the data from Figure 7.9. Similar amplitude plots for RX-2, RX-3 and RX-4 can be found in Appendix D. In these figures, RX-1 is located at 0° (right), RX-2 is at 90° (up), RX-3 is at 180° (left) and finally RX-4 which was at 270° (down). This placement was the same as presented in Figure 7.1.

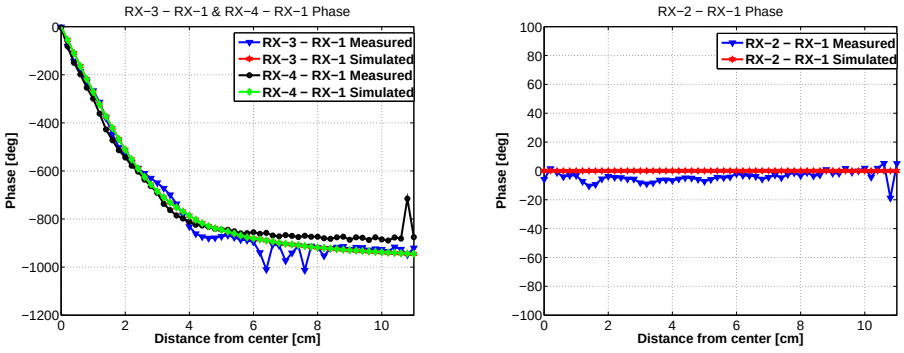

(a) (b)

Figure 7.8: Phase measurement and simulation in COMSOL at 45°. In (a) is the results for RX-3 - RX-1 and RX-4 - RX-1 and in (b) is the results for RX-2 - RX-1. The phase for RX-3 - RX-1 (red) is not easily seen for the simulation as it lies behind the green curve.

The graphs were plotted with a positive x-axis pointing in the direction of RX-1 and a negative y-axis pointing in the direction of RX-2. Both axis are specified from -110 mm to +110 mm, where 110 mm or 11 cm is the distance the internal antenna can move, from the centre of the phantom and outwards. The centre point is therefore (x,y) = (0,0). All the measurement rounds can be seen for angles of 0°, 10°, 20° etc. in addition to the diagonals, i.e. 45°, 135°, 225° and 315°, all going from the centre and outwards.

From Figure 7.10, it can be seen that the amplitude is higher on the right side than on the left. This is naturally the case since on the right side of the figure, the internal antenna was closer to RX-1 than on the left side.

On the left side of Figure 7.10 a rather interesting phenomenon can be noticed. First of all notice that while moving from the centre and to the left in the figure, the amplitude lowers (blue colour) and then rises again (yellow) if moving even closer to the edge on the negative x-axis (left side). This effect was also displayed in Figure 7.2 in the curve for RX-3. There, the internal antenna was moved in the positive x-axis direction (to the right), i.e. the internal antenna was in fact moving directly away from RX-3 and as the antenna was getting closer to the outskirts of the phantom (close to the 11 cm), the amplitude of RX-3 actually started to rise. This is believed to be due to the creeping waves as was shortly described above. At a certain internal antenna displacement point, the majority of the power was exiting the phantom at the location that faced RX-1 and what the RX-3 was receiving on the opposite side was the creeping wave crawling along the surface of the phantom from the location that faced RX-1.

The second interesting occurrence to observe in Figure 7.10, which was actually also caused by creeping waves, are the dark-blue (very low ampli-

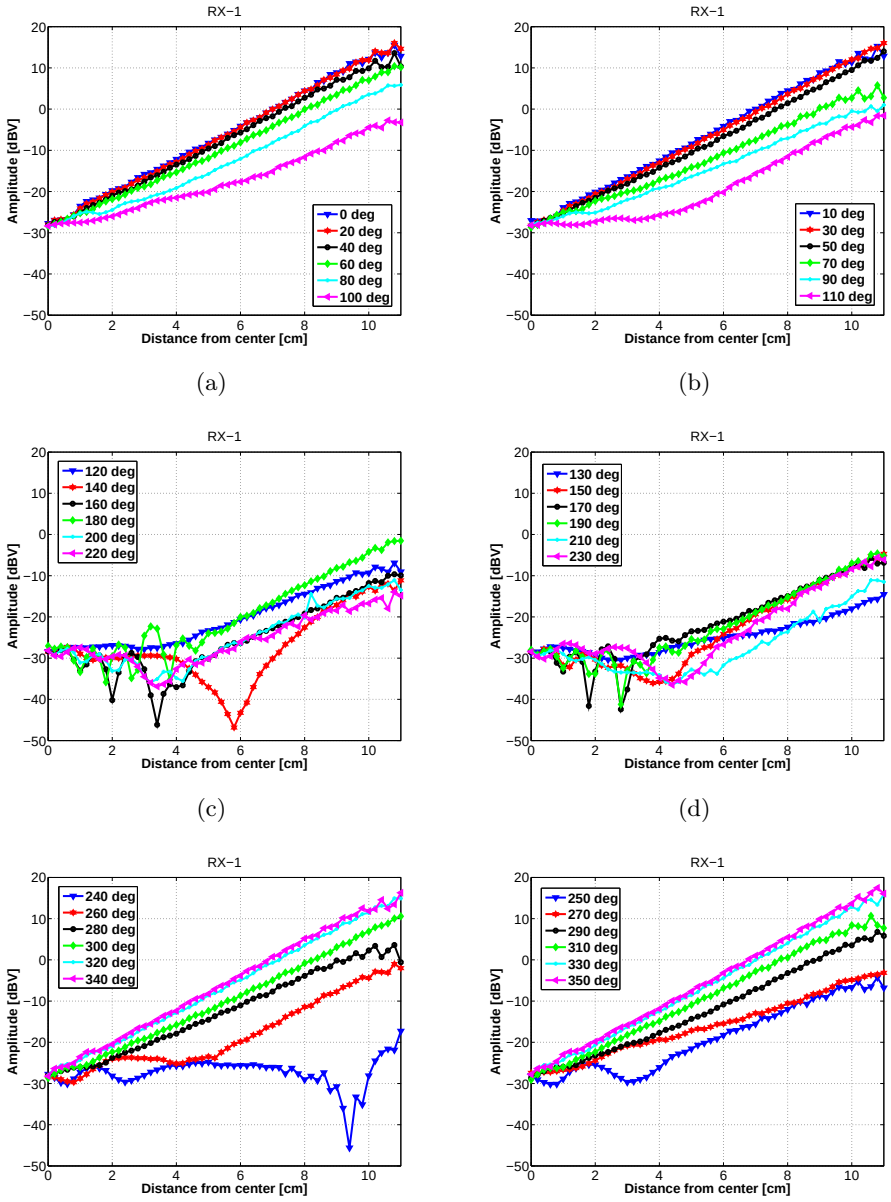

Figure 7.9: Amplitude measurements of RX-1 in logarithmic scale for every 10° step. In (a), (c) and (e) are 0°, 20°, 40°, 60° etc. In (b), (d) and (f) are 10°, 30°, 50°, 70° etc.

tude) areas on the left side of the figure. When transmitting from the very low amplitude locations, RX-1 was receiving only a very weak signal, if any signal at all. This is believed to be due to destructive interference of creeping

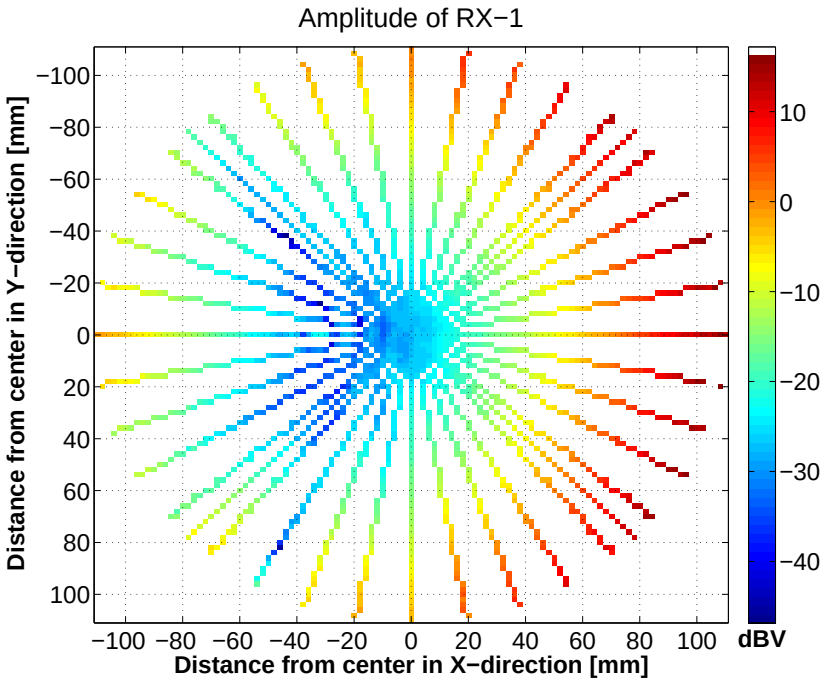

Figure 7.10: Amplitude measurements in dBV scale of RX-1 as function of the internal antenna location inside the inner cylinder.

waves. When transmitting from one of these very low amplitude locations, the majority of the power exited the phantom on its left side. The power exiting had a creeping wave component that crawled around the phantom in a clockwise direction and another one in the counter-clockwise direction. At the location of RX-1, the two creeping wave components were added together in anti-phase and destructive interference occurred thus, RX-1 therefore received a very low amplitude signal.

The dark-blue areas in Figure 7.10 do not appear at the 180° angle (on the negative part of x-axis), but rather in two areas on opposite sides of the x-axis, approximately between 135° and 160° as well as between 200° and 230°. While moving the internal antenna at the 180° angle, on the negative x-axis, the potential creeping waves that was going around the phantom in both clockwise and counter-clockwise direction would (theoretically) always add up in a constructive way at RX-1. Since RX-1 lied on the same axis as the internal antenna while it was moving on the x-axis, the distance travelled by the two opposing creeping waves would always be the same, assuming total symmetry across x-axis. Further investigation on creeping waves is presented in Chapter 9.

In Figure 7.11 a logarithmic scale of the magnitude of the phases for RX-2 - RX-1 is plotted in a similar manner as the previous amplitude figure.

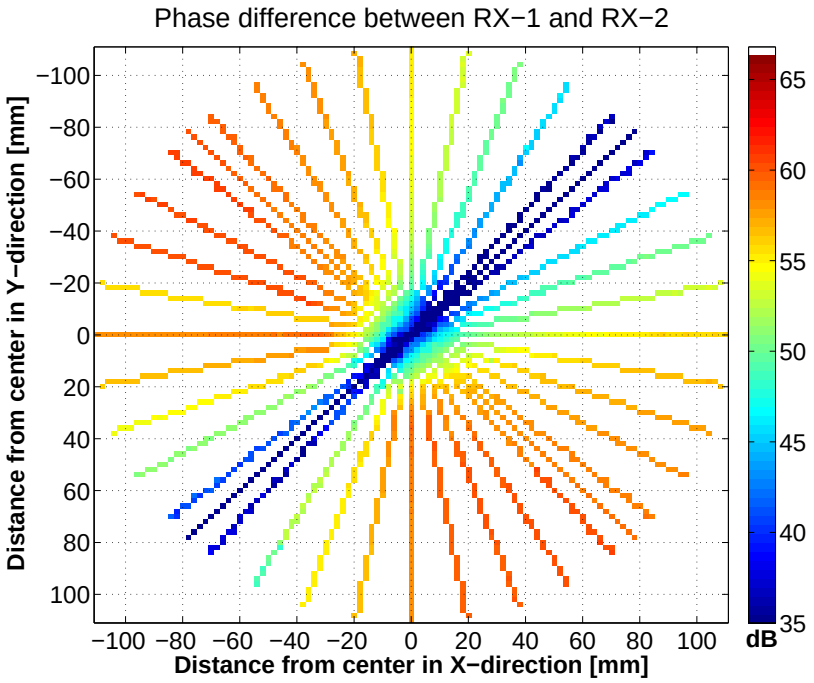

Figure 7.11: Phase measurements of RX-2 - RX-1 in logarithmic scale as function of the internal antenna location inside the inner cylinder.

Figure 7.11 illustrates the phase difference between RX-2 and RX-1, whereas the measured phases for RX-3 - RX-1 and RX-4 - RX-1 can be found in Appendix D. The phase of RX-1 was the reference to all the other phases.

These figures show a level of symmetry, i.e. phase balance between RX-1 on one hand and the other three receivers on the other hand. Figure 7.11 is approximately symmetrical around the 45°/225° line, which is expected since if the internal transmitting antenna was moved along this diagonal line, the phase difference between RX-1 and RX-2 should, theoretically, have been zero. The same kind of symmetry was for RX-3 - RX-1 across the 90°/270° line and across the 135°/315° line for RX-4 - RX-1.

There was a slight unbalance in the phases when comparing each of the allegedly symmetrical halves in the figures. This is not surprising in such a complicated system that has so many variables. It does in fact not make any difference as long as the physical structure of the phantom as well as the electromagnetic properties of the equivalent tissue mimicking media stay constant. The latter poses a problem over time due to evaporation of the liquids. The inner cylinder could have been placed with a significant offset from the centre, and the mapping and focusing processes remains theoretically valid if the system stays unchanged. The human torso was not exactly

symmetrical and there was not a special requirement for the torso phantom to be symmetrical. However, it was preferred and attempted to have the torso phantom and the microwave activation system as symmetrical as possible during the initial measurements in order to verify the balance and similarities between the transmitters on one hand and the receivers on the other.

Chapter 8

System Measurements - *Focusing*

The essence of the external activation of pharmaceutical drugs with microwaves, depends on the ability to induce EM power at certain areas inside the body. A documented side effect of being irradiated by EM waves is that, unwanted heating of areas, other than intended, can occur. A method for reducing the side effects is, to superimpose EM waves from multiple sources, creating a focus point which inherently has higher amplitude than its surroundings, thus allowing for reduction of the radiated power from individual sources. This chapter describes the focusing experiments of the microwave activation system on the human torso phantom where measurement results are presented along with a discussion.

8.1 Measurement Setup

There are many similarities in the focusing case and in the mapping case when it comes to the measurement setup. Eight microwave absorbers were also utilized here to minimize reflections from clutter. Clutter are objects that are not part of the microwave activation system and are dependent on the current surroundings of the systems such as e.g. walls, chairs, tables and shelves. During focusing, the position of the external antennas was unchanged in respect to the mapping and the phantom was the same. The setup was shown in Figure 7.1, but now with RX interchanged with TX. The component block diagram of the focusing setup was illustrated in Figure 5.5. Now, the external antennas were connected to the outputs of the transmitters, without the HPA boosting stage.

The four transmitters TX-1 to TX-4 were at the same locations as the receivers RX-1 to RX-4 were in the mapping case, respectively, i.e. TX-1 was at 0°, TX-2 at 90° etc.

8.2 Focusing

Before discussing the method of focusing using the experimental setup, a 2-D E-field amplitude simulation from COMSOL at 2.45 GHz is presented. Figure 8.1 shows four in-phase sources radiating at a torso phantom. Figure 8.1(a) shows the entire simulation space, including the outer boundaries and the sources themselves in dark red colour and the torso phantom in the centre. Figure 8.1(b) shows a zoom-in view of only the torso phantom in order to visually indicate the E-field distribution inside the phantom. From Figure 8.1(a) destructive interference pattern is visible around the phantom at the centre with lower amplitude fields close to the phantom. From Figure 8.1(b) the constructive and destructive interference pattern can be seen especially well inside the inner cylinder (in muscle). Visible from Figure 8.1(b) are the multiple local maxima close to the centre of the phantom as well as lower field strength near the centre of the phantom compared to the outskirts of the inner cylinder, as expected. These simulation results indicate the effect of focusing with four sources, all in phase.

The experimental setup was, however, utilized to experimentally try to focus electromagnetic waves inside the torso phantom and is presented below. Due to the presence of the second receiver, named RX-2 in Figure 5.5 it was possible to determine the phase of each individual transmitter. This receiver mixed the two signals directly from both frequency synthesizers providing

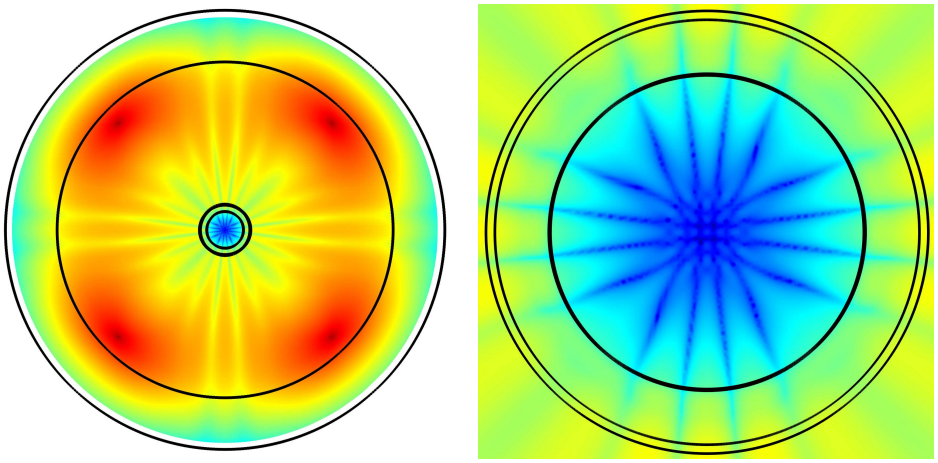

(a) (b)

Figure 8.1: COMSOL simulation of four sources radiating at a torso phantom. All sources were in-phase with each other. In (a) the E-field amplitude of the entire simulation area is shown with the four sources in dark red. In (b) is a zoom-in of the E-field amplitudes in the torso phantom. The colour scale is logarithmic with dark red as high intensity areas and dark blue as low intensity areas.

a constant phase point for reference. This constant reference phase was essential for phase determination of all transmitters. The other receiver, named RX-1 in the same figure, was connected to the internal antenna, whose signal phase changes with position of that antenna.

When all the transmitters were transmitting, resulting in a similar individual amplitude contribution at the focus point, the total measured phase was a sum of all the individual phases from each transmitter. The amplitude contribution from every transmitter, at the focus point, was kept at a similar level and in phase in order for each wave to have approximately equal influence on the field intensity at the focus point. Surrounding the focus point, some of the waves were out of phase and therefore subtracting each other, to a certain extent, with a comparable influence, providing low-amplitude zones.

For focusing at a certain point in the human torso phantom, the internal antenna was moved to that point and all the transmitters, except for one, TX-1, were set to maximum attenuation with the user interface in the PC. In this way, the significant majority of the signal the internal antenna received stemmed from only a single transmitter (TX-1) without having to disconnect the other transmitters in the meantime. The constant phase reference from RX-2 was subtracted from the phase of the received signal from RX-1 in order to get the relative phase of TX-1. With this, only the phase of the signal provided by TX-1 was measured.

The amplitude of the received signal could be adjusted by changing the attenuation in TX-1 and the phase was adjusted to a pre-determined phase, by the DAC voltage that ultimately controls the phase shift in the analog phase shifter. The pre-determined phase chosen was 0°, but can be any other phase as long as we are consistent. The same method are used for the other transmitters, one by one, i.e. three of the transmitters were fully attenuated while only one was transmitting a significant part of the signal that was received in RX-1. The amplitude of the received signal, from each transmitter, was adjusted by the attenuation in the corresponding transmitter to be at approximately the same level as from the previous transmitter and the phase of the transmitter in use, was adjusted to 0°. With this method, the signal amplitude contributions from all transmitters, at the focus point were the same, as well as their phases. This ensured even contribution from all four transmitters at the focus point.

When a suitable combination of attenuation settings and DAC voltage for 0° phase, was found for each transmitter individually, all the transmitters were simultaneously set to those determined values. The superposition of similar amplitudes and phases of each individual transmitter provided a constructive interference and therefore a focus point.

A possible alternative to this technique is to directly use the mapped phases and amplitudes to set each individual transmitter. This would require all the cables, transmitters, receivers and location of external antennas to

be measured for phase shift and remain stable and constant between the mapping process and the focusing process. The human torso phantom would also be required to keep its shape as well as its EM properties. This method is challenging due to the multiple variables (VA, VGA, DAC and IF-BPF) in the transmitters and the receivers where each element influences both the phase and the output power in every setting. The deterioration of the phantom's mimicking media with time, also needs to be further examined.

8.3 Results

A number of arbitrary focusing points were pre-determined in order to examine the focusing possibilities of the microwave activation system. The points are given as a radius from the centre of the phantom and an angle, (r, ϕ), which represents the position of the phantom lid, referred to 0° at the location of TX-1 as before.

Since the microwave activation system is approximately symmetrical, all the focusing points were chosen to be between 0° and 45°of the phantom lid for easier measurements and comparison. All focusing points are marked in the plotted figures with a black dotted circle.

For almost all the focusing points chosen, the attenuation (gain) settings of the transmitters were set such that the receiver RX-1, would receive approximately 50 mV from each individual transmitter, totally resulting in 200 mV or -14 dBV from the contribution of all four transmitters simultaneously. These values are arbitrary and could be exchanged with other values, if preferred.

Similar to the mapping procedure, the focusing measurements were executed as a sweep of 2 mm steps at certain angles of the phantom lid, around the pre-determined focus point. This resulted in graphs with numerous amplitude lines, indicating each sweep.

Figure 8.2 shows a measurement for a focusing point of (r, ϕ) = (0 cm, 0°), i.e. at the centre of the phantom. Interestingly, there is a clear focusing point at the centre of the figure, where the black dotted circle marks the pre-determined focusing point. A profile view of focusing at (r, ϕ) = (0 cm, 0°) is shown in Figure 8.3 when $\Delta y = 0$. A local maxima is seen at 0 cm as is expected.

The nearest point with similar amplitude, i.e. the next local maxima was at a radius of approximately 1.6 - 1.8 cm from the focus point. From Table 3.2 the wavelength, λ, is around 1.7 cm in muscle tissue which is indeed the same as the distance between the focus point and the nearest local maxima. It is therefore observed that ϵ_r' is similar to that of muscle tissue, as is presented in Table 3.1.

Pay special attention to the x- and y-axis range because for all the focusing points, only a part of the inner cylinder is shown, i.e. only the sur-

roundings of each of the focus points was examined.

The next focus point was set to (r, ϕ) = (2 cm, 20°) and the result is shown in Figure 8.4. Again, a clear focus point is seen at the location of the pre-determined focusing point marked with black circle. The nearest point with similar amplitude was at a radius of 2.1 cm from the focus point. The nearest surroundings to the focus point were considerably lower in amplitude than the focus point itself. Notice that, the scale for this figure is not the

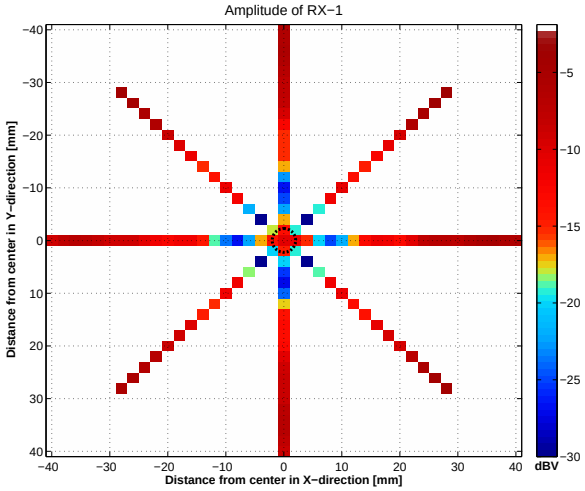

Figure 8.2: Focusing at the centre of the phantom (r, ϕ) = (0 cm, 0°).

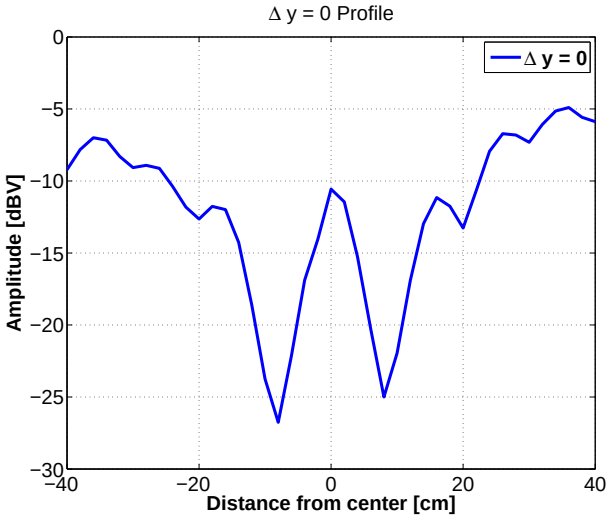

Figure 8.3: Focusing at the centre of the phantom (r, ϕ) = (0 cm, 0°). A profile view when $\Delta y = 0$.

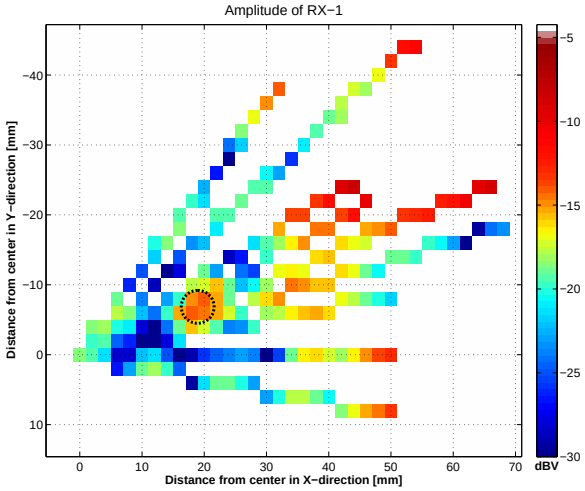

Figure 8.4: Focusing at (r, ϕ) = (2 cm, 20°).

same as for the previous figure.

The importance of evaluating whether microwaves are a viable solution for pharmaceutical drug release or not, depends on the available power level at the focus point. Obviously, the radiated power has to be limited to the maximum power that is allowed to radiate onto humans. This maximum power level depends on the maximum specific absorption rate (SAR) in tissue, which again depends on the tissue type, making the relationship rather complicated and will not be covered here.

The power at the focus point in relation to the radiated power of the four transmitters is estimated below. The radiated power of each transmitter for the (r, ϕ) = (2 cm, 20°) focus point is shown in Table 8.1.

The VA in RX-1 was set to 14 dB attenuation and the VGA was set to have 0 dB attenuation, i.e. max gain and the IF-AMP was set to 54/127.

A 50 mV measured voltage corresponds to a received power of approximately -90 dBm from a single transmitter, with the RX-1 settings above.

Table 8.1: Transmitter settings when the focus point was set to 2 cm and 20 deg.

TX no.	VA [dB]	VGA [dB]	DAC [V]	P_{rad} [dBm]
1	0	28.5	6.1	9.2
2	0	17	8.8	10.7
3	2	16.5	1.37	19.7
4	1	20.5	1.65	16.2

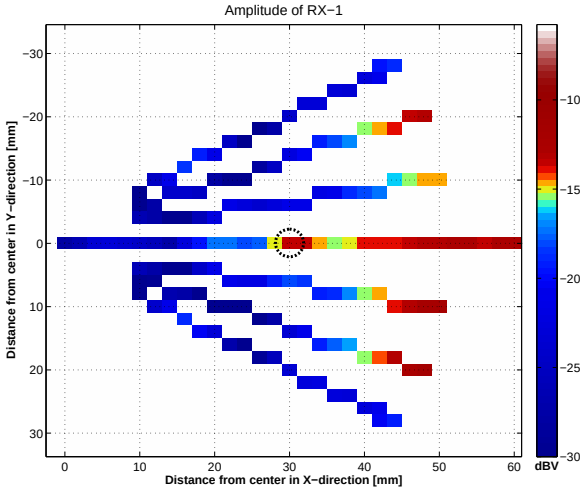

Figure 8.5: Focusing at (r, ϕ) = (3 cm, 0°).

Total radiated power of over 100 mW from the (r, ϕ) = (2 cm, 20°) case, resulted in a total focused power of approximately 4 pW from the four transmitters. An increase of radiated power e.g. up to 43 dBm (20 W) from each transmitter could result in approximately 1-10 nW. The thicknesses of the phantom's fat and muscle layers have to be taken into an account. The depth of the location of the focus point in the muscle tissue that have been measured here, was generally at least several centimetres more than the muscle thickness at the abdominal and back region of a person. An increased power level at the focus point would be accomplished in a more realistic model, which means e.g. less muscle thickness (or simply a cylinder with a smaller diameter). It would, however, most likely be in the sub-mW range due to the inherent path loss and power loss.

Focusing of point (r, ϕ) = (3 cm, 0°) is displayed in Figure 8.5. Focusing was also accomplished at this point. The surroundings, especially closer to the centre of the phantom, had considerably lower amplitude than the focus point. An exception for this was at points near the edge of the phantom, where the amplitude seemed to rise between 340° (−20°) and 20°. In this case, the nearest point with similar amplitude was at a radius of 1.8 cm from the focus point.

A focus point of (r, ϕ) = (3 cm, 45°), i.e. same radius as previously but with the lid rotated 45° is shown in Figure 8.6. Focusing was also seen to be possible in this case. The scale is however different in this case compared to the previous case. Actually, the amplitude of this focus point was practically the same as the one shown in Figure 8.5. The nearest point with similar amplitude was at a radius of 1.9 cm from the focus point.

Next, the focus point of (r, ϕ) = (4 cm, 30°) was pursued. The results are

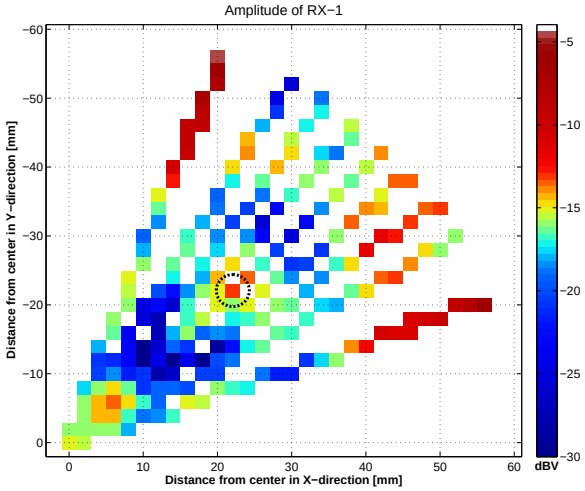

Figure 8.6: Focusing at (r, ϕ) = (3 cm, 45°).

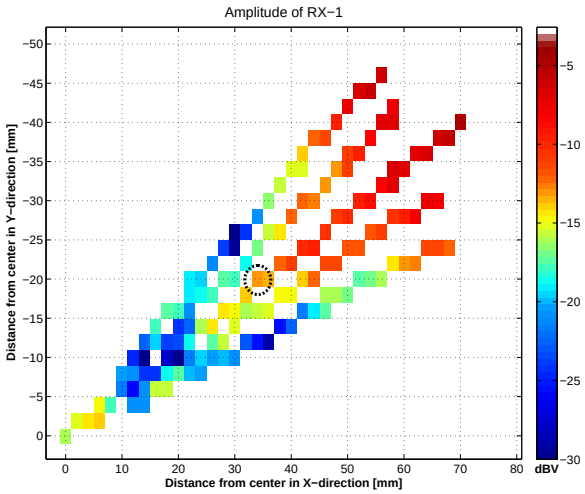

Figure 8.7: Focusing at (r, ϕ) = (4 cm, 30°).

shown in Figure 8.7 and in this case, no clear focusing point can be noticed, unlike in the four previous cases. A black dotted circle reveals where the pre-determined focusing point was set. These results are at least as noteworthy as the cases where focusing was actually successful. The reason why this location of the pre-determined focus point, does in fact not result in a focus point is believed to be due to the creeping waves mentioned in the previous chapter. Creeping waves are discussed further in Chapter 9.

At even farther distances from the centre, a pre-determined focus point was set to be at (r, ϕ) = (7 cm, 30°). The results, shown in Figure 8.8

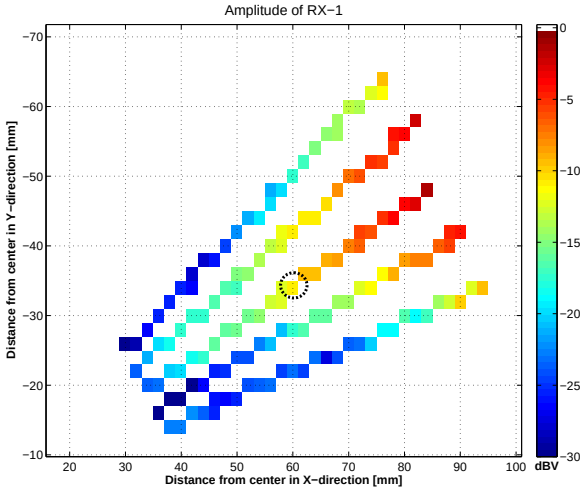

Figure 8.8: Focusing at (r, ϕ) = (7 cm, 30°).

indicate similar results as the previous case, i.e. no visible focus point. In common for both this case and the previous one, is the elevated amplitude of the axis along the 30° line (the line with the pre-determined focus point indicated with a black circle), compared to the axis going through the other angles.

Excluding the possibility that the arbitrary angle of 30° was in some way responsible for the lack of focusing, a location of (r, ϕ) = (7 cm, 0°) was set to be the focus point. The results, shown in Figure 8.9, indicate similar effect as the previous focusing, i.e. no visible focus point.

8.4 Discussion

Focusing at arbitrary points inside a simple cylindrical human torso phantom was successful only to a certain extent. Clear focusing points were achieved at the pre-determined locations for points less than 4 cm from the centre of the phantom, i.e. deep inside the lossy phantom. In those cases, the focus point was the highest amplitude-point across a diameter larger than 3.6 cm. For comparison, the small intestine in humans are typically less than 3 cm in diameter [7, pp. 272] and is the place where the drug release is meant to take place. Higher amplitudes at the focusing point can be achieved by increasing the transmit power.

Unavoidably, high-amplitude zones and spots (hot spots) appeared at other locations than at the focusing point as was expected. This is a persistent problem in non-invasive hyperthermia systems as well. Increase of transmitters and external antennas could reduce the number of hot-spots

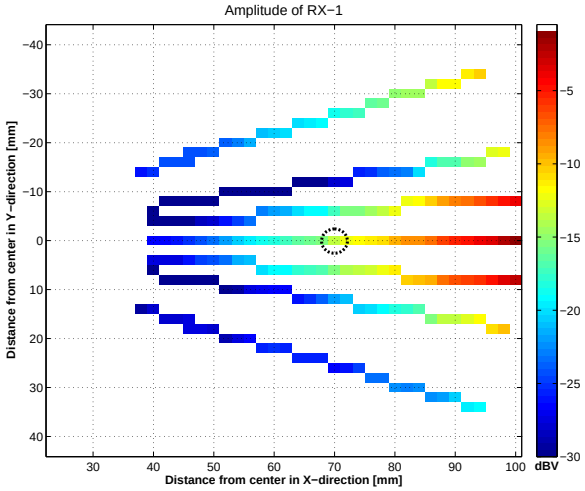

Figure 8.9: Focusing at (r, ϕ) = (7 cm, 0°).

outside the focus point and could increase the power density at the focus point [17, 18, 45, 66, 67]. The microwave activation system was developed with the possible extension to 8 transmitters in mind. The digital control and distribution network were already set up in such a way and would only require a minimum effort to adjust the system to more transmitters.

Reducing the operating frequency to, e.g. 800 MHz - 1000 MHz would result in a lower attenuation, thus better penetration of EM power into tissue. The focus point would become larger in diameter with this larger wavelength as well as the external radiators. The larger wavelength would predictably extend the area of possible focusing beyond the 3 - 4 cm in the present system. As will be presented in a later chapter, this, however, increases the challenge of developing sufficiently small receiving structure for the pharmaceutical drug capsule that are meant to contain the medicine.

Similar behaviour to the torso phantom could be expected in an actual human torso. Although the presented torso phantom did not include bones or internal organs, it was very conservative when it came to the thickness of the fat layer, thickness of the muscle layer and the losses of the fat layer. In the phantom, the muscle layer and fat layer were thicker than what would be considered an average as well as the fat mimicking media was much more lossy than in an actual human. In fact, 2/3 of the muscle tissue's relative permittivity and conductivity is sometimes used to represent the human body [101, pp. 34]. As the phantom represented a rather pessimistic form of a human torso regarding muscle thickness, the focusing point was limited to the inner most 3 - 4 cm from the centre of the phantom. In a less lossy and in a thinner media, such as a typical human torso, these limits would expectedly be closer to the surface of the actual torso. That would mean

that there is probably a larger zone inside an actual human that creation of a focus point would be possible. Also a higher-amplitude focus point would also be accomplished in a human due to less losses and thinner structures.

The simple 2-D model in COMSOL shows good agreement with the experimental dual-layered phantom. This implies that a 2-D model in COMSOL of a actual human torso slice, of the patient in question, could possibly be utilized for predicting and adjusting the phases and amplitudes of the external transmitters to obtain a pre-determined focus point.

Chapter 9

Creeping Waves

In the previous chapters on system measurements for the mapping and the focusing, creeping waves were presented. Creeping waves is a name of a case of diffraction where an electromagnetic wave can propagate along a curved path into a shadow zone (out of line of sight). In this chapter the behaviour of the creeping waves and their effect on external microwave activation of pharmaceutical drug release are examined.

9.1 Creeping Wave Behaviour

A similar behaviour to the creeping waves, described in the previous chapters for the phantom, would be expected when transmitting from within, or at, a human torso, resulting in some noteworthy effects.

The principle of the creeping waves on a biological tissue equivalent phantom is presented in a simplistic manner in Figure 9.1. Figure 9.1(a) indicates how the power reaches receivers RX-1 and RX-3 on opposite sides when the internal antenna is at the centre of the phantom, with blue and red arrows when only two main paths are considered. In this case, power would be radiated radially away from the internal antenna to RX-1 and RX-3. Figure 9.1(b) shows a case when the internal antenna is offset from the centre enough for the creeping waves to overshadow the direct waves as was discussed in Chapter 7. This was at least 3.2 cm offset from the centre of the phantom when the lid was positioned at 0°. In the creeping wave case, the majority of the power would exit the phantom, facing RX-1. Creeping waves follow the curvature of the phantom and would ultimately be received by RX-3. A part of the power would also travel in the direct path towards RX-3 but its amplitude would be lower than from the creeping wave. The waves can also travel along other paths, but only these three paths are considered in this example. The creeping waves do not strictly confine themselves to boundaries or surfaces, but also travel in both media, with a different velocity due to a different permittivity. Figure 9.1 shows only the principle of the creeping

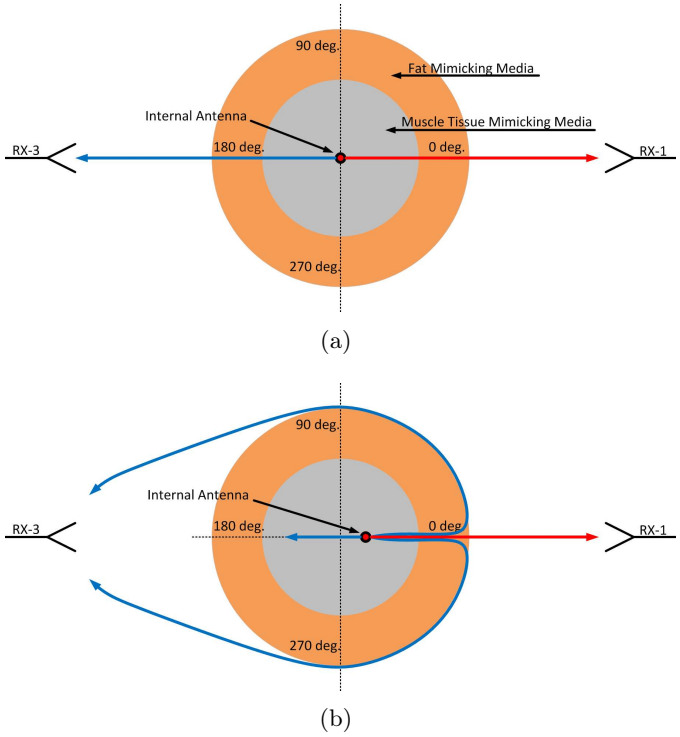

Figure 9.1: Illustration of how creeping waves could propagate at the surface of the phantom and backwards away from the displacement of the internal antenna. In (a) if power would be transmitted evenly, outwards from the centre of the phantom and no creeping waves would exist. In (b) creeping waves would arise due to the antenna offset inside the phantom and due to the wave attenuation in the phantom.

wave in a simple manner whereas in reality the wave propagation is much more complex.

A 3-D simulation in CST of the human torso phantom is shown in Figure 9.2. In the figure, the average E-field amplitude plot at 2.45 GHz of a 2-D cut is shown in the plane of the excitation source. The excitation was made from within the phantom at a 8 cm offset from the centre. A lumped port was used for the excitation. Figure 9.2(a) shows the phantom along with its surroundings and Figure 9.2(b) shows a zoom-in of the phantom to illustrate the fields in and closely around the phantom. The excitation point is shown in dark red in the figures and is within the MTMM. Notice that the highest amplitude of the E-field is at the top of the phantom as is expected when the excitation point is 8 cm offset from the centre in the upward direction.

The 0° reference is to the right of the phantom (positive x-axis direction) and the angle increases in the counter-clockwise direction. At approximately 60° and 120° in the fat mimicking layer, there is a sudden decrease in amplitude in Figure 9.2(b). These two locations are marked with arrows. The

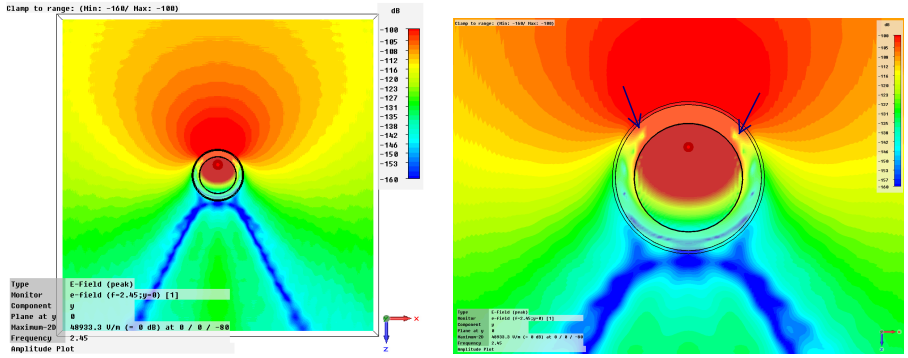

(a) (b)

Figure 9.2: CST simulation, excitation at 8 cm offset from centre from within the human torso phantom. Far view in (a) and zoomed-in view in (b).

attenuation from high E-field (red) to lower E-field (yellow) radially away from the excitation point, is due to losses in the media as well as because of path loss and is not a surprise. If, however, attention is directed to the outside of the phantom it is clear that the high amplitude E-field continues along the sides of the outer cylinder, whose origin is not the radial path from the excitation point and outwards as would perhaps be expected. This is an illustration of the creeping wave described above, where it seems to crawl along the outskirt of the fat mimicking media.

Additionally, Figure 9.2 uncovers a destructive interference at angles of approximately 240° and 300°, clearly seen as the dark blue stripes going from the bottom of the phantom and in the downward direction. The destructive interference is believed to be due to the two creeping waves coming from both sides of the phantom adding together below the phantom. The angles of the destructive interference stripes are dependent on the position of the excitation point and this destructive interference would become weaker as the excitation point would come closer to the centre of the phantom where it ultimately would disappear. Similar behaviour was seen in [132] where simulations were performed on a numerical human body phantom. There, however, the nulls are suggested to be due to a certain muscle group that may have attenuated the waves strongly. This cannot be the case here for the 2-layered phantom and therefore it is believed that the same destructive interference behaviour was the main cause for the nulls seen in [132] as well.

Since the excitation point was positioned upwards from the centre, at 90° angle from the positive x-axis, the destructive interferences were located 150° and 210° from the excitation point, when it was located 8 cm offset from the centre, which was the case of this example.

These dark blue (low amplitude) areas in Figure 9.2 are equivalent to the

low amplitude areas in Figure 7.10.

From the mapping case, where the power is transmitted from within the phantom and outwards, some statements can already be proposed for its reciprocal, the focusing case, deduced from this creeping wave phenomena.

At the locations of the destructive interference, described above, the power is at a minimum. During focusing, if a transmitter would be located at the places having the destructive interference from before, they would not significantly contribute to a focusing of the point of excitation from before (8 cm from the centre). The most effective locations of transmitter placements during focusing would be the locations that show high amplitude E-fields. Un-intuitively, a somewhat effective location to transmit from, is the location directly below the phantom, at 270°. At this location, the creeping waves on both sides of the phantom would be added constructively, at the top of the phantom (90°), and a part of the power at that point would be radiated inward, thus providing power for focusing inside the phantom.

These considerations can be used to assist in selecting the most suitable placements of the transmitting antennas, to focus at a fixed pre-determined location.

Figure 9.3 shows a 3-D simulation in CST where the torso phantom was radiated at, by a single transmitter at 2.45 GHz. Figure 9.3(a) illustrates a 2-D cut in the far view whereas Figure 9.3(b) shows the effects in the phantom when zoomed in. Figure 9.3 shows the instantaneous E-field peak amplitude to indicate the wave behaviour in and around the torso phantom. It can be seen from Figure 9.3(b) how the waves follow the shape of the cylinder. Furthermore notice at the top of the cylinder that, the contribution from the creeping waves actually radiates into the inner cylinder as was discussed above. It is therefore suggested that, a focus point close to the top of the inner cylinder would mainly receive the contribution from the creeping waves from a transmitter on the opposite side of the phantom, while the contribution from the direct path would be attenuated below that level.

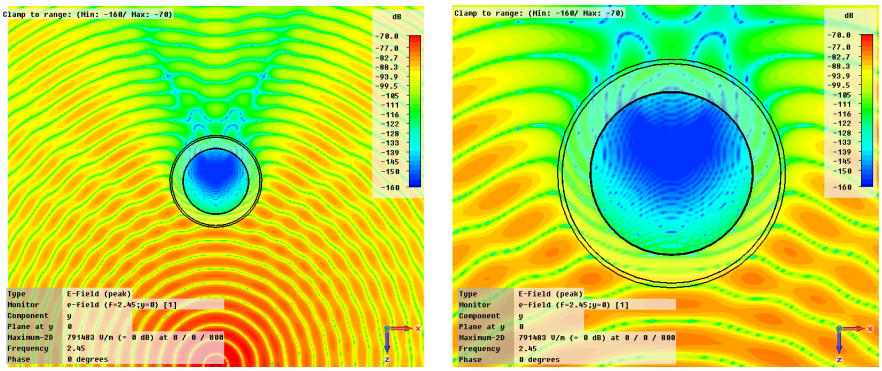

(a) (b)

Figure 9.3: CST simulation, an omnidirectional excitation in the far-field of the human torso phantom, radiating at the phantom. Far view in (a) and zoomed-in view in (b).

9.2 Impact of Creeping Waves in a Human Voxel Model

A human voxel model in CST, named Emma was temporarily acquired, courtesy of CST. Approximately 30 cm torso section (from the gall bladder down to the appendix) of the voxel model was used for the simulation whose purpose was comparison to the simple torso phantom. A single excitation source was placed 80 cm from the centre of the model, similar to the excitation from Figure 9.3 and was transmitting towards the back area of the human voxel model. The vertical component of the E-field was simulated in the plane of the source, which was arbitrarily placed in plane of the voxel model that would cut through the middle of the small intestine, since the small intestine is the optimal location to release pharmaceutical drugs. The cut through the voxel torso is shown in Figure 9.4(a) where the locations of various tissues are specified. Clearly, the voxel model has a thick fat layer and a modest muscle tissue layer.

The E-field simulation results are shown in Figures 9.4(b) through 9.4(e) with the placement of various tissues accentuated. In Figure 9.4(b) the simulation results are shown along with the outline of the voxel model in the cut of interest. A clear perturbation of the field is seen along with reduction in field strength as expected. Figure 9.4(c) emphasizes the fat layer of the voxel model which is relatively thick. The waves penetrating into the fat layer have smaller wavelength which can be seen from the figure.

Figure 9.4(d) illustrates the same simulation results, now with the muscle tissue layer highlighted as a dark transparent cover. On the bottom half of the figure, at the location of the lower back muscles (the thick muscle layer), a reduction in intensity and in wavelength is noticed as expected.

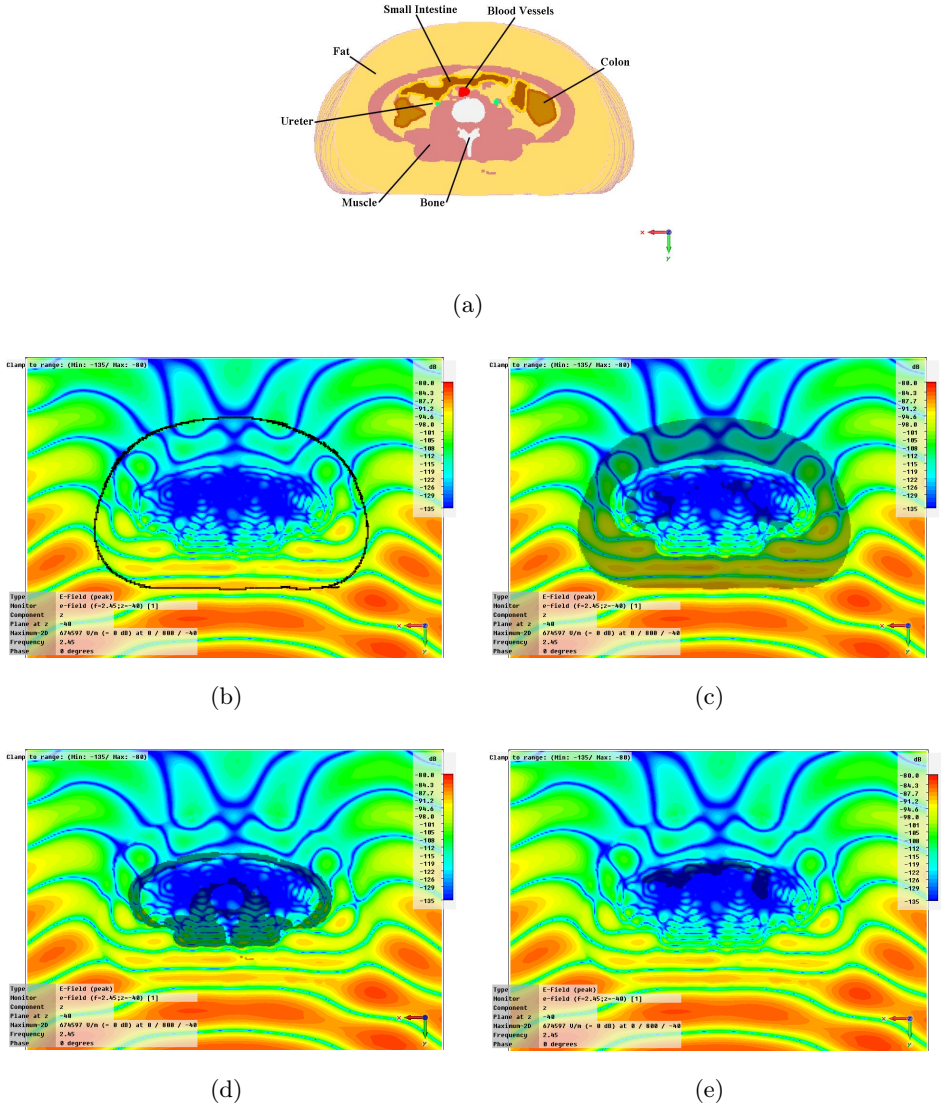

Figure 9.4: CST E-field simulation in a horizontal cut in a human voxel model, named Emma. In (a) is the cut of the model shown along with various tissues specified. In (b) through (e) the E-field simulation results are shown with the outline, fat, muscle and small intestine highlighted in dark transparent cover, respectively.

Although the dual-layered torso phantom is a relatively crude model, some similarities with the voxel model are seen. Comparing Figure 9.3(b) with Figure 9.4, same tendencies are detected. A part of the incident wave crawls around the phantom and the voxel model. Interestingly, as noted above for the torso phantom case, creeping waves that are located on the

front side (upper half) of the voxel model, result in a wave transmission inwards into the voxel model. This is perhaps most clearly illustrated below the abdominal muscle layer, in Figure 9.4(d). A similar effect is displayed at the top of the cylindrical muscle layer, in Figure 9.3(b), where waves were being transmitted into the phantom, from the top (on the other side of the source).

This behaviour of the E-field in the voxel model, which was already predicted by the cylindrical torso phantom, suggests that creeping waves also need to be taken into consideration in actual human torsos. Figure 9.4(e) illustrates the location of the small intestine along with the E-field simulation results. Since the location of drug release is meant to be in the small intestine, the figure reveals that the main contribution of the E-field at the location of the small intestine, from an exciting wave coming from behind of the model, would mostly be due to creeping waves.

9.3 Creeping Wave's Influence on Focusing

Let's consider two separate cases of having four sources transmitting at the phantom for focusing. The first case is where the contribution of the received signal inside the phantom is from the direct path of all the transmitters, as would be the case when the receiving internal antenna (focus point) would be close to the centre of the phantom. The second case is when the internal antenna is closer to an edge of the phantom and assuming that a part of the received signal stems from an indirect path due to creeping waves. For simplicity, let's only consider points on the positive x-axis, i.e. from the centre of the phantom and towards TX-1. The setup was shown in Figure 7.1 where RX are interchanged with TX.

For the first case, imagine a pre-determined focus point close to the centre of the phantom, e.g. (r, ϕ) = (1 cm, 0°). When measuring the received amplitude to the left (towards the centre) of the focus point step by step (i.e. 0.8 cm, 0.6 cm, 0.4 cm etc.), the contribution from TX-3 would increase and the contribution from TX-1 would decrease. When measuring the amplitude to the right of the focus point, the opposite would happen, i.e. the contribution from TX-3 would decrease and the contribution from TX-1 would increase.

For the second case, imagine a pre-determined focus point closer to the edge of the phantom, e.g. (r, ϕ) = (7 cm, 0°). At the left side (near the centre) of the focus point, the contribution from TX-3 would reduce as well as the contribution from TX-1 since both waves are essentially radiating from the edge of the phantom that faces TX-1. Oppositely, the contribution from both TX-3 and TX-1 would increase when moving towards the edge of the phantom. This continuous increase is seen in Figures 8.7 and 8.8 in the 30° line (line of the pre-determined focus point) where no focusing is found.

These behaviours around the focus point of the first and the second case are believed to be the reasons why the results from first case show an evident focus point and the second case does not.

9.4 Creeping Wave Verification Experiment

An experiment was arranged in order to verify the previous creeping wave discussions. The internal antenna was fixed at a 8 cm offset from the centre of phantom, at 0° (directly in front of TX-1's location from before). Microwave absorbers were placed around the phantom to reduce any reflections. A single transmitter, TX-3, was used for the excitation and was located on the opposite side.

Three cases were tested. In the first case, the TX-3 was simply transmitting unobstructed onto the phantom. In the second case a 3 cm thick block of a layered planar microwave absorber was placed in front of the phantom, facing the transmitter TX-3, touching the surface of the outer cylinder of the phantom. This setup is shown in Figure 9.5(a). Figure 9.5(b) shows the third case where the same planar microwave absorber was placed behind the phantom, relative to TX-3. Everything was kept unchanged for the three cases with the exception of the placement of the planar microwave absorber. Since the planar microwave absorber has several layers of various EM properties, it was made sure that in both case 2 and case 3, the same layer was facing the phantom.

The reference case, which is the first case where no planar absorber was used, produced approximately 50 mV in the receiver. In the second case, where the absorber was placed directly in front of the phantom, only a minor change was found in the received signal which read around 48 mV. The most noteworthy results were generated by the third case where the planar absorber was located behind the phantom. Here the signal level dropped to 5 mV. It is believed that there are creeping waves propagating around the phantom, originating from TX-3 and a part of these creeping waves are added in phase behind the phantom, at the location of the layered absorber in case three. The layered microwave absorber, heavily attenuates the fields that otherwise would be transmitted into the phantom, thus the received signal was significantly reduced.

These results support the previous claims of creeping waves crawling around the phantom and are transmitted inwards, from the opposite side of the source.

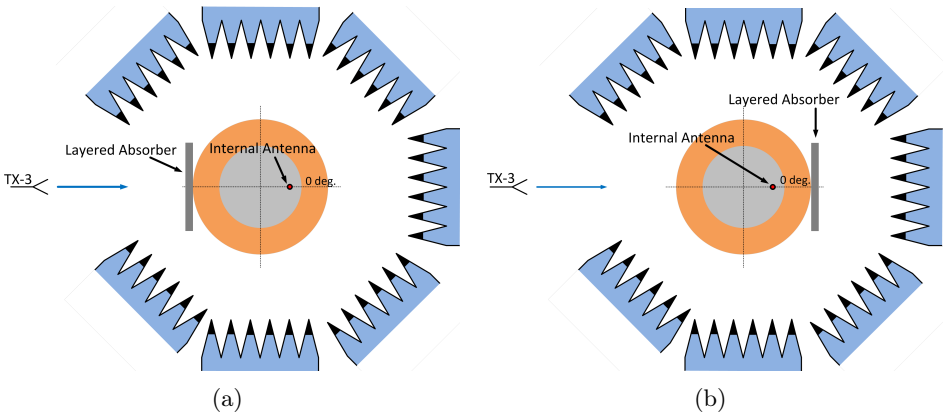

Figure 9.5: A setup of a creeping wave experiment. In (a) a layered microwave absorber is placed in front of the phantom and in (b) the layered microwave absorber is placed behind the phantom, relative to TX-3.

Chapter 10

Performance-Reduction Factors

In this chapter, deviations and practical issues that could have the possibility of influencing the microwave activation system and therefore the measurement results are discussed. Solutions and precautions are described in the relevant cases.

10.1 Antenna Perturbation

In general, the result of direct measurements can get distorted due to the introduction of the measurement device. For example, placing a thermometer in a glass of water e.g. to measure its temperature changes the temperature of the water. E-field measurements are no exception. Typically, the E-field is measured with some sort of metallic probe or an antenna. Due to the inherent properties of metal, the tangential E-field is forced to zero at the surface of the metal and therefore also in the media bordering to it because of Maxwell's boundary condition for highly conductive media such as copper.

The fabricated encapsulated sleeve dipole antenna is 7.6 mm in diameter where the metal is the thickest. This is a bit less than one half of a wavelength in muscle tissue mimicking media, where it was utilized. This surely causes field perturbation around the antenna. A detailed investigation into this is outside the scope of this work but it is worth to mention it, as it could be an interesting topic for additional study.

10.2 Leakage of Microwave Signal through Cables

Leakage through cables was one of the most limiting factors for acquiring high dynamic range and caused problems during measurements. Leakage is unfortunate and has the undesirable effect that, increasing the signal level in a transmitter does not help at all since the leakage level simply rises along with the transmitter's increase.

An ordinary flexible coaxial SMA cable used in the microwave laboratories at DTU has screening effectiveness at around 90 dB [133, pp. 92], meaning that the signals propagating on the cable are attenuated 90 dB when measuring the leakage in the air outside the cable. After propagating 10 cm through muscle tissue, a travelling wave at 2.45 GHz would be attenuated more than 40 dB, in addition to the inherent path loss of the travelling wave.

Not only are the coaxial SMA cables, carrying the 2.45 GHz wave, responsible for leakage to the ambient. The microwave energy can also leak through the power supply and digital control lines, which could also result in crosstalk. During the design process, considerable effort was put into reduction of these leakages such as multiple decoupling capacitors of various values on the power supply lines. In the fabricated transmitter, the microwave PCB was kept on one side of an aluminium box and the digital and power supply circuits were on the other side, separated by a metallic wall. Power supply and digital control lines were fed through small holes in between the two parts. In the fabricated receiver, the microwave PCB was again kept separated from the power supply and digital signal part, with a metallic wall in between. The power supply and digital control lines were fed through holes in the wall between the PCBs.

Even though a considerable effort was put into the design stage, further reduction methods such as inserting capacitor-input filters (PI filters) in series with the power supply lines were introduced to gain even more dynamic range in the system. Low pass filters could also have been introduced in the digital control lines that suppresses the microwaves without distorting the digital signals too much.

Every receiver had a coaxial SMA cable to carry the signal from the receiving antenna, a coaxial BNC cable for the downconverted IF signal and a 25 wire cable that carried both the required voltages and digital control lines. The 25 wire power supply cable is a shielded cable and at each end of the cable there is a shielded DIP-25 connector, intentionally to reduce leakage and interference.

In the microwave activation system, leakage was experienced to such great extent that it interfered with the measurements to begin with. The leakage signal was picked up by all the four receivers during mapping. The signal level was so high that it overshadowed the small signals being transmitted through the lossy torso phantom and the effect could clearly be seen since a movement of the internal antenna close to the centre of the phantom, had no influence on the received signal amplitude.

It could even be seen on the computer screen, that the leakage was in the ambient and not from a direct coupling over a wire, because when moving an object (a piece of cardboard with aluminium foil attached) back and forward near the transmitter, the movement caused Doppler shift in the received frequency. As the cardboard with aluminium foil was moved, the

received IF signal shifted in frequency above and below the operating IF as one would expect with a Doppler shift and suggests that the receivers were receiving a wave that was reflected off the moving aluminium foil. It should be noted that the output of the transmitter was, at this point, terminated directly in a 50 Ω termination without any additional cables between the output and the load which excludes leakage from transmission lines at the transmitter's output side. This strengthens the suggestion that the leakage came in a large part from the digital control lines as they were the only point out of the transmitter's metallic housing that was not low-pass filtered in any way, even though effort was made in keeping them isolated.

The part of the flexible coaxial SMA cable carrying the signal, from the internal antenna and up until the measurement barrier (location of the microwave absorbers), was exchanged with a semi-rigid coaxial SMA cable. The semi-rigid cable has a screening effectiveness of approximately 120 dB [133, pp. 32], 30 dB better than the flex cables. The semi-rigid cable also provided increased mechanical stability in holding the internal antenna in place and eliminated the problem of putting a flex cable into liquid, which deteriorates relatively fast over time, in liquid.

The biggest improvement to the leakage problem was the introduction of the electromagnetic interference (EMI) filters which consists of a snap-on ferrite core. A ferrite core EMI filter was put on every power supply (and digital signal control) cable, as close to the receivers and transmitter as possible as well as ferrite core filters were put on the coaxial BNC cables carrying the IF signal, again as close to the receivers and transmitters as possible. Also ferrite core filters were added to the frequency synthesizer's power supply cables and on the coaxial BNC cable carrying the 10 MHz reference frequency, from a crystal oscillator. All these EMI filters reduced the leakages by approximately 30 dB in total which was seen in the received signal amplitude on the computer screen. With the addition of the snap-on EMI filters, the leakage signal disappeared into the noise floor. This made it possible to actually see directly the change in the received signal amplitude while moving the internal transmitting antenna around in the phantom and was an essential step in being able to measure signals originating from deep inside the phantom and not overshadowed from leakage.

10.3 Symmetry of the Encapsulated Sleeve Dipole Antenna

During measurements and in simulations, the encapsulated sleeve dipole antenna was assumed totally symmetrical in vertical planes, going through its centre. Deviations in the fabrication of the encapsulated antenna make it, however, slightly asymmetric. The antenna is made out of a straight semi-rigid coaxial cable where the inner conductor sticks out as one of the poles

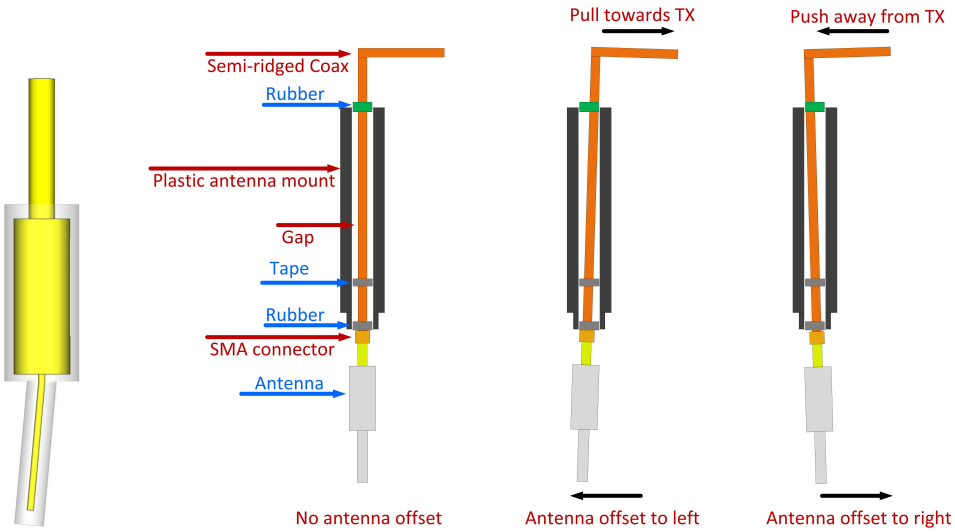

Figure 10.1: Exaggeration of the bended antenna and the vertical rotation.

in a dipole. The inner conductor, which is approximately 1 mm in diameter, has Teflon encapsulating it. The mechanical strength of the inner conductor and the softness of the Teflon makes the antenna sensitive to deviations at the top (or bottom since it was operated upside down) of the antenna. Figure 10.1(a) illustrates an exaggeration of the bending that happens in the dipole. This bending is thought to change the directivity pattern of the antenna slightly, resulting in a non-ideal omnidirectional pattern.

This bending could be calibrated out in the data control and acquisition software by adjusting the phase and amplitude of the received signals from all receivers to zero degrees (when mapping) and so all of the receivers had the same input voltage, when positioned at the centre (r, ϕ) = (0 cm, 0°).

Figure 10.1(b) illustrates another challenge regarding the antenna symmetry. It shows a cut through the internal antenna mount as to illustrate how it looks inside, in three separate cases. In the first case the antenna is positioned straight down and no offset is experienced, which is the ideal case. The next case shows when the semi-rigid coaxial cable is pulled towards the transmitter and the last case shows when the cable is pushed. During the mapping process, by having the slot in the cylinder lid pointing directly away from the transmitter (which was the case when the lid was positioned 135°), the antenna moved farther and farther away from the transmitter in every step. This increased distance from the antenna and to transmitter, which it was connected to, could pull slightly on the semi-rigid coaxial cable and cause the situation in case 2 from Figure 10.1(b) (which is highly exaggerated

for visual purposes).

Case 3 from Figure 10.1(b) could happen when the slot in the lid would be on exactly the opposite as in case 2, i.e. at 315°. Now the internal antenna would get closer to the transmitter and therefore the semi-rigid cable of the internal antenna could be slightly pushed.

The semi-rigid coaxial cable that was connected to the internal antenna is, as the name indicates, rather stiff and did not bend with various positioning of the internal antenna inside the phantom. A super-flex cable connected the semi-rigid cable to the transmitter (receiver) and provided a certain flexibility when moving the internal antenna around. Even though it is much more flexible than the semi-rigid cable, it still needed to maintain certain phase stability, i.e. one typically does not want the phase to shift much when bending the cable. The super-flex cable has a double shielding to reduce leakage. This could, however, limit the flexibility of the cable which makes it not flexible enough to completely eliminate the offset of the internal antenna.

Rubber fittings were placed at the top and at the bottom of the internal antenna mount as is indicated in Figure 10.1(b) to reduce the offset described above. Electrical tape was also wrapped around the coaxial cable, at one point, to fill up the gap between the coaxial cable and the antenna mount which centralizes the antenna even further.

When rotating the lid on top of the outer phantom cylinder, the internal antenna and the semi-rigid coaxial cable did not actually rotate with it, only the internal antenna mount. A compromise had therefore to be made between centralizing the antenna and avoiding to completely fix it in the antenna mount.

10.4 Position Offset of Inner Cylinder

The inner cylinder was not completely fixed to the outer cylinder. This caused a slight position offset of the inner cylinder in respect to the outer one. The submerged antenna was mounted on the lid which rotated on the top of the outer cylinder and did therefore not rotate completely concentric to the inner cylinder. As mentioned before, a doughnut shaped polystyrene was placed in between the two cylinders to hold their respective positions. Even though the polystyrene held the cylinders in place, there was an offset of up to 3 mm due to deviations since the polystyrene was cut by hand. Figure 10.2 shows a much exaggerated example of this offset.

This offset would cause the wave, propagating from the submerged antenna, to travel faster (due to lower permittivity of fat compared to muscle) and therefore with less phase shift towards perhaps one receiver rather than another, even though the antenna is e.g. positioned at (r, ϕ) = (0 cm, 0°). This could skew the phase and amplitudes measurements during mapping

slightly, when comparing the signals from each receiver and needs to be accounted for when interpreting the results. The offset does not make the measured results wrong in any way since a human is not circularly symmetric but this possible offset should be taken into a consideration especially when comparing to concentric simulations of the dual layer phantom.

10.5 Reflections due to Leakage

Eight microwave absorbers were placed around the microwave activation system to reduce the effect of reflections from external objects such as walls or a table. The absorbers attenuate waves, normal to their surface, approximately 20 dB one way or 40 dB on reflection, according to the in-house expert on absorbers at the university. The absorbers covered approximately the height of the outer cylinder and were placed with their bottom in the same height as the outer cylinder. This way, the biggest contributions of possible scattering were taken care of.

However the limited height and number of absorbers introduced open spaces from where waves could be reflected. Also the finite attenuation of the absorbers can indeed reduce a possible reflected wave, but they do not eliminate it. While mapping, a large signal at some location outside the phantom could be scattered and could reach a receiver which should receive a low power signal. The scattered signal can overshadow the wanted low power signal and therefore the measurement would be inaccurate.

When I changed the location of the internal antenna after every measurement point, a clear influence of my presence could be seen in the received signal amplitude. After re-adjusting the antenna's location, I stayed behind one of the absorbers while a measurement was taken. While moving around behind the absorbers, no influence on the received signal was seen which is suggested to be due the attenuation effect of the microwave absorbers.

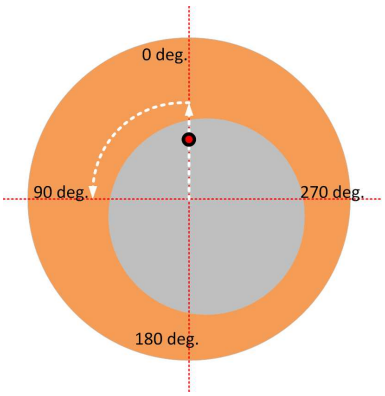

Figure 10.2: A highly exaggerated example of inner cylinder offset.

Chapter 11

Micro-Containers for Pharmaceutical Drugs

11.1 Introduction

Conventional pharmaceutical drug delivery, such as oral delivery of therapeutics, faces several obstacles. There are problems such as low drug penetration through the gastrointestinal wall, degradation of the active pharmaceutical components in the stomach and the lack of external control of the actual time and place of the drug release [2–4]. By externally activating pharmaceutical drug capsules, e.g. by focusing microwaves into the area of interest and heating up the capsule, as shown in Figure 11.1, the time and place for the drug release can be pre-determined.

Various techniques have been suggested for external drug activation that are sensitive to magnetic fields [10], ultrasound [8], light waves [9] and radiowaves below 100 MHz [11] as was presented in Chapter 1. Complex drug delivery modules including a receiving inductor, control circuitry chip and a drug delivery chip that uses low frequency EM waves for excitation, have also been published in the literature, [12]. These techniques have disadvantages such as the inability to focus magnetic fields and low frequency electromagnetic waves, light wave is limited to only surface excitation and a high level of complexity in the control circuitry.

At microwave frequencies, the possibility of focusing inside human bodies could become realizable where the high-amplitude areas could be used for the drug activation. The inherent high losses of biological tissues at microwave frequencies as shown in previous chapters make it challenging to penetrate deep into tissues with sufficient power levels. It is therefore suggested to have a very sensitive receiving structure on the drug capsule to absorb a significant part of the power that is available, in order to use that energy to open the capsule. A highly resonant structure, the split-ring resonator (SRR) is introduced in an attempt to accomplish this. A resonator is able to induce

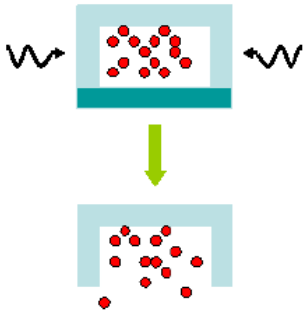

Figure 11.1: Drug capsule activated by microwaves.

locally high intensity fields at the resonance frequency, compared to other frequencies. The physical size of this resonator is important since the idea is for a patient to swallow those capsules. The power required to open such a capsule is currently unknown and depends on multiple variables that are difficult to model and is therefore a subject for a future experimental work. This chapter provides simulations, experiments and discussion on the idea of using resonance structures on drug containers at microwave frequencies for a controlled drug release. This topic is extensive and only a part of it could be examined in a thesis such a this one with numerous other topics. This work does, hopefully, give the reader an idea about the concept and give suggestions where further development is needed for this concept to become a reality.

11.2 Split-Ring Resonator for Drug Activation

Split-ring resonators, originally proposed by Pendry [134], are very compact resonance structures and typically resonate when the electrical size of the structure is less than $\lambda/10$ in comparison to typical microwave resonance structures that resonate at the electrical size of $\lambda/2$ [135]. Because of the SRR's small electrical size and since the highest electric field concentration is close to the edges of the rings, as will be shown later, the SRRs are chosen here for the purpose of drug activation. SRRs consist of two concentric rings with a gap in the ring structures on opposite sides as is indicated in Figure 11.2. SRRs were proposed in [136] by Smith *et al.* to be used as an element in fabricating double-negative metamaterials, where the electric permittivity and permeability are simultaneously negative in a given frequency range and by that, give rise to new applications such as the perfect lens [137].

Split-ring resonators are easily fabricated on printed circuit boards and have therefore also become increasingly popular in microstrip and coplanar waveguide topologies for their compact design and good performance in microwave filters [138].

The concept of using SRRs for drug activation is as follows. SRRs should fabricated on a lid of a micrometre or a millimetre sized pharmaceutical drug capsule as shown in Figure 11.3(a). The capsule should contain a medicine. At the resonance frequency of the SRRs on the drug capsule structure, a relatively strong E-field would be generated in the gaps of the rings and in the separation between them. The alternating E-field would induce currents in the lossy dielectric lid where part of the electric currents would be converted into heat, due to power loss (Figure 11.3(b)). This would cause an increase of the temperature in the lid and by that, open the capsule and release the pharmaceutical drug. This could be accomplished by having the lid constructed of a polymer, such as Intelimer®, which could abruptly change its adhesion, viscosity or permeability (a measure of the ability of a porous material to allow fluids to pass through it) when heated by just a few degrees. A layer of adhesive material, with a melting point several degrees above 37 °C, that could be placed between the lid and the capsule could also operate as a release mechanism for the pharmaceutical drug.

Other techniques have e.g. presented heating of a coil due to the inherent internal ohmic losses of a receiving coil, because of the magnetic fields that generate electrical currents in the receiving coil [11, 139]. Heating of a lossy dielectric media with the use of localized alternating E-fields, have not been proposed before for the purpose of opening pharmaceutical drug capsules, to the knowledge of the author.

11.3 The Structure of the Capsule

The placement of the SRRs on the capsule is of high importance regarding the resonance frequency and the ohmic power loss. If the SRRs are on top of the lid, as is the case of Figure 11.4, the functionality of the SRRs is dependent on external factors. That means that, when a capsule like that would swallowed and when it would be inside the small intestine, where

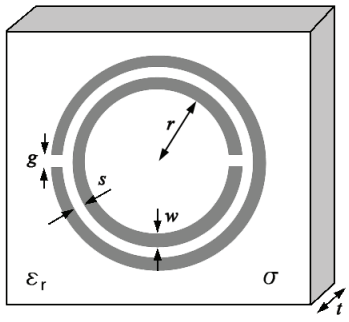

Figure 11.2: A split-ring resonator with dimensional variables.

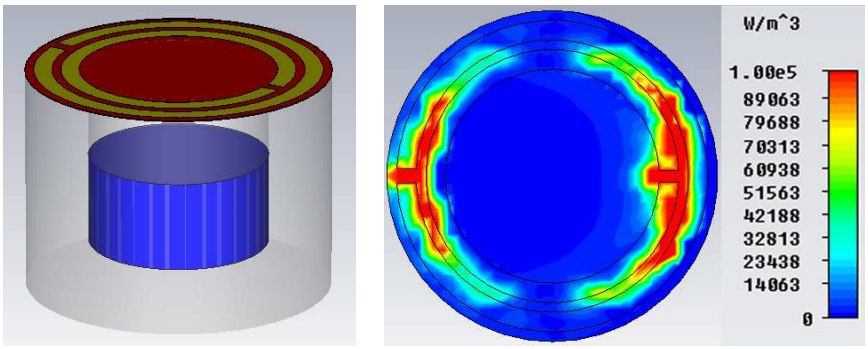

(a) (b)

Figure 11.3: In (a) a semi-transparent cylindrical capsule with the pharmaceutical drug inside and the split-ring resonators on top of a thin lid, on the capsule. In (b) the simulated power loss density in the lid is shown from the top.

the drug release is planned, the unknown media which the SRRs would be close to or covered with, would change the resonance frequency and the power dissipation in the lid. This is important, especially since the small intestine walls have one of the highest relative permittivities (≈ 54.4) in the body and almost the highest conductivity, of 3.17 S/m, second to only the cerebrospinal fluid at 2.45 GHz [98,99]. According to the human voxel model data in CST the content of the small intestines are estimated to have the same EM properties as the small intestine walls. Assuming that the drug capsules would surrounded by this high lossy and high permittivity medium, the effect this media would have on the SRRs needs to be taken into an account at further development stages of the capsule.

Alternative placements of the SRRs have been considered, such as placing them on the inside of the lid. If the lid is thick enough, external media are

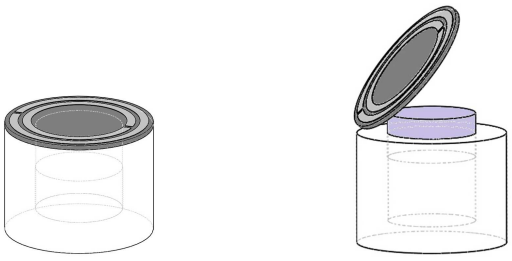

Figure 11.4: Split-ring resonators on a lid on top of a capsule and a drug being released. To the left is the whole, enclosed drug capsule. To the right is the capsule after it has been activated (opened) by microwaves and drug is being released.

not expected to have significant influence on the fields around SRRs. In that case, the medical drug inside the capsule could have an effect. Having the SRRs in a sandwich inside a lid, could potentially avoid both the effect from the outside media and the drug as well.

The SRRs in Figure 11.4 are lying on the capsule's lid and underneath are the cylindrical walls of the capsule. Since a big part of the EM fields of the SRRs, could penetrate through the lid and into the capsule (including the drug), the drug type and height could affect the behaviour of the SRRs. By increasing the thickness of the capsule's walls, the EM field that would be present in the drug would be reduced and the field present in the well-defined walls would be increased, thus minimizing the influence of the drug type and height on the SRR's behaviour. The idea is to make the SRR's behaviour as independent of external variations as possible, such as the small intestine content described above and the type of drug inside the capsule, mentioned here.

Two pharmaceutical drugs were simulated as being the content of the capsule in CST. The first one was paracetamol in a powder form which has $\epsilon'_r = 5$ and $tan\delta = 0.01472$ @1 MHz [140]. The second one was SNEDDS (Self-NanoEmulsifying Drug Delivery System) which are isotropic mixtures of oil, surfactant, cosurfactant, co-solvents and the drug. They spontaneously form a nanoemulsion in the gastro-intestinal tract upon oral administration. The SNEDDS is, at the time of this writing, being developed as a part of the NAMEC project to be put into the micro-containers, also under development in the NAMEC project. The EM properties of SNEDDS, shown in Figure C.1 in Appendix C were measured and result in $\epsilon'_r = 3.5$ and $\sigma = 0.1$ S/m @2.45 GHz. No conclusive difference was found between the two simulated drugs, in their effect on power loss density.

PCL (Polycaprolactone) was used in the simulations for the capsule (container) itself. PCL is a biodegradable plastic and is approved by the FDA (Federal Drug Administration) for drug delivery devices and was therefore a suitable material for the capsule since it was used in the development in the NAMEC project as the drug capsule. PCL has $\epsilon'_r = 3.22$ and $tan\delta = 0.002484$ @1 MHz.

The material of the split-ring resonators themselves is worth to discuss since it would obviously be swallowed along with the rest of the capsule. The power loss density of the lid was simulated with the SRRs either as copper or iron without notable differences in the results. Metals such as iron, calcium, magnesium and zinc are generally already present in humans. In fact, daily dietary supplement intake of minerals such as calcium and magnesium is often suggested by health experts. Selecting one of the suitable minerals for the SRR's material would simply make it a part of the recommended daily intake. The recommended daily intake for calcium is e.g. 1000 - 1300 mg [141]. The metals are, however, typically not supplemented in the form which is presented in the table of elements (Fe, Mg, Ca etc.) but are

given as compounds which are relatively easily absorbed by the body and inexpensive in production. Intake of calcium is e.g. often in the form of calcium carbonate ($CaCO_3$) which has $\epsilon_r' = 2.2$ and $\sigma = 0.0084$ S/m @2.45 GHz [142]. It is obvious that the conductive properties of calcium carbonate are not comparable to that of a metal as is suggested to be used for the SRR material. Even though the general idea for the SRR material is presented here, alternate minerals are a subject to further research into the suitable metal to be used for the SRRs and is outside the scope of this work.

11.4 Heating of the Drug Capsule

The resonance frequency, mentioned above, is defined to be the frequency where the power loss density in the lid of the capsule is at a maximum. CST was used for simulating the power loss density in the lid of the capsule. From a distance of 25 mm, a 100 V/m plane wave, with the E-field component oriented across the gaps (labelled g in Figure 11.2) in the SRRs and H-field component oriented normal to the lid, was used to excite the pharmaceutical drug capsule. For the lid, a media with $\epsilon_r' = 3$ and $\sigma = 0.07$ S/m was used. It is necessary to have conductive media for the lid in order to dissipate power in it and the reason for those specific EM properties used in the lid, is covered below. For the SRRs, iron was used as it is a metal already found in the human body and the capsule itself was made of PCL in the simulations. All media are considered non-magnetic (except for the iron). A sweep over a range of frequencies revealed that a capsule that has SRRs with the dimensions presented in Table 11.1, has a resonance frequency at around 2.5 GHz and the results are shown in Figure 11.5.

Table 11.1: Dimensions of the split-ring resonators in the CST simulation

r [mm]	s [mm]	w [mm]	g_{inner} [mm]	g_{outer} [mm]	t [mm]
7	1	2	1	1.4	0.2

In this simulation, the drug was paracetamol as described above and the drug filled half of the space available in the capsule. The choice of drug amount was arbitrary since the actual drug level would depend on the drug-loading of the capsules. Figure 11.5(a) through 11.5(f) illustrate the power loss density of the lid at frequencies between 2.0 GHz and 2.7 GHz. The figures display the high dependence of the frequency for the capsule and the resonance frequency of about 2.5 GHz where the maximum power loss density is clearly seen. The quality (Q) factor of the structure is found to be

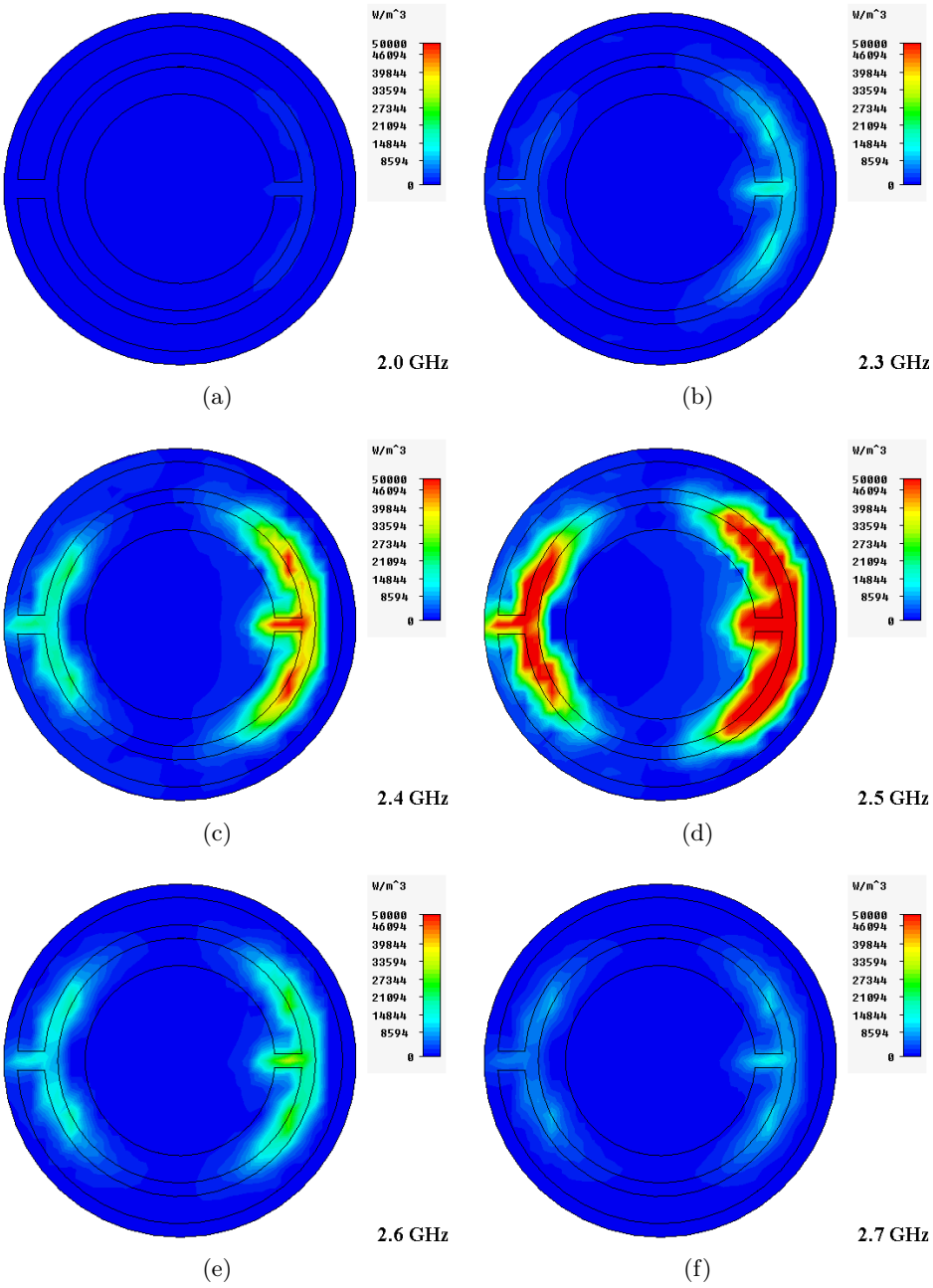

Figure 11.5: Power loss density of a half-filled capsule with split-ring resonators on top of a lid, as a function of frequency. Figure (a) represents 2.0 GHz, (b) 2.3 GHz, (c) 2.4 GHz, (d) 2.5 GHz (resonance), (e) 2.6 GHz and (f) 2.7 GHz. At the resonance, high power loss density is located in the gaps of the split-ring resonators.

approximately 19 from

$$Q = \frac{f_r}{\Delta f}, \tag{11.1}$$

where Q is the quality factor, f_r is the resonance frequency and Δf is the half power density bandwidth of the maximum power density. High Q factor ensures frequency selectivity of the particular capsule. This could e.g. be useful if, say two batches of capsules would each have their own resonance frequencies which would be separated enough for the capsules to be insensitive to the other capsule's resonance frequency. These two batches could store each their own pharmaceutical drug or even the same drug to be activated at different times. The external activation system then would transmit at the resonance frequency for one of the batches at a time. This can obviously be extended to 3 or more different resonance frequencies. The quality factor is limited by the conductivity of the lid. As previously stated, conductivity is necessary in order for power to be dissipated in the lid for heating it up.

A comparison between two cases of drug amount was simulated in CST. In the first case, with results shown in Figure 11.5, paracetamol fills up half of the space inside the capsule. In the second case, paracetamol completely fills up the capsule up to the lid and the comparison is shown in Figure 11.6. The effect seen is a clear shift in resonance frequency. The shift was about 50 MHz. Furthermore, a higher power loss density is found in the second case, where the paracetamol reaches the lid of the capsule. The Q-factor has dropped to 15 and is most likely due to the introduction of paracetamol in the vicinity of the SRRs, which increases the loss, compared to air from before.

The temperature distribution can be generated in CST from the simulated EM data. First, all the materials of the capsule needed to be assigned density, heat capacity and thermal conductivity. The background temperature was set to 37 °C and the ambient had the properties of air which was chosen to avoid the varying influence that different media could have. In this simulation the principle of heating the lid of the capsule itself is of importance and provided a point of reference. With further development, the capsule should be simulated with the kind of media that would typically be present in the small intestine, if not air.

The resulting temperature distribution can be seen in Figure 11.7 for two different frequencies and when the capsule is full with drug. Figure 11.7(a) illustrates the temperature distribution at 2.3 GHz, around 130 MHz from the resonance and Figure 11.7(b) at 2.43 GHz which is at the resonance frequency. A clear effect is seen of the thermal heating that happens at resonance in the lid, by the split-ring resonators. Outside the resonance, only slight heating occurred and the maximum temperature was 37.8 °C in the gap of the inner split-ring. At the resonance frequency, the incoming

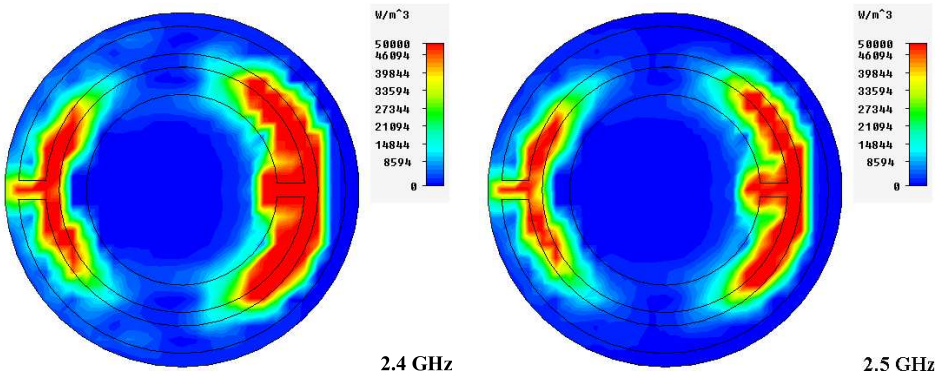

(a) (b)

Figure 11.6: Power loss density of a capsule with split-ring resonators on top of a lid, as a function of frequency when the capsule is filled with paracetamol to the top. Figure (a) represents 2.4 GHz and (b) 2.5 GHz.

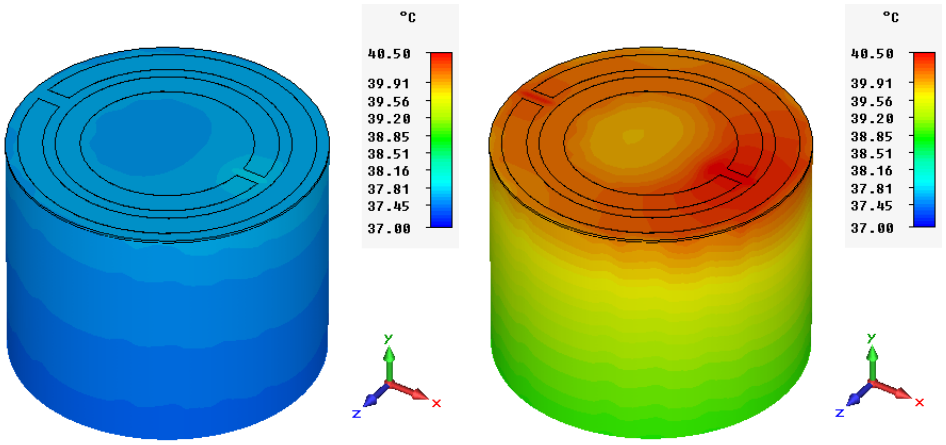

(a) (b)

Figure 11.7: Temperature distribution of the capsule as a result of a power loss in the lid. Figure (a) represents the temperature distribution at 2.3 GHz and (b) at 2.43 GHz. Notice the difference in temperature.

plane wave generated locally high-amplitude E-fields which induced currents in the lossy dielectric lid that resulted in a thermal loss, thus a temperature increase.

The increased temperature in the capsule and consequently, in the drug itself could change not only the EM properties of the drug slightly, but also its chemical properties. In fact, generally, powder solubility increases with increasing temperature [140], which could potentially help with the

absorption efficiency of the drug in the body.

Multiple split-ring resonators, split-rings on the side of the capsule, a rectangular capsule with split-rings on each side and four concentric rings each with their gap at a 90° offset are among the structural possibilities to provide alternate heating spot pattern and different method of drug release, if required.

The diameter of the pharmaceutical capsule presented in these simulations was 26 mm which is relatively large for a capsule to be swallowed and would need to be reduced by at least one half. The SRRs have not been optimized in respect to their physical size in any regards. A media for the lid with higher relative permittivity could be the first step in the size reduction process. By having the SRRs inside the lid or on the other side of the lid, they would be surrounded, effectively, by a media of higher relative permittivity and therefore their size would be reduced, for the same resonance frequency. I believe that the size and the arrangement of the SRRs and therefore the capsule can be reduced significantly, if optimized.

11.5 Optimizing Power Dissipation in the Lid

In general, substrates which are too conductive tend to short-circuit the SRRs which are fabricated on the substrate and kill off any resonance in the rings. On the other hand, substrates that have very low conductivity, dissipate very little power.

Rogers 4003®, for example, is a low-loss substrate with $\sigma = 0.001$ S/m and $\epsilon_r' = 3.55$ @2.5 GHz and SRRs that are fabricated on such a substrate, behave as Hi-Q resonators, as is often the aspired property for filters, and do therefore not dissipate notable power. Most substrates that are used in printed circuit technology are relatively low-loss which means that lossy substrates that can be used in conventional photolithography processes can be difficult to find for the purpose of dissipating power.

Simulations of the optimal conductivity for a given relative permittivity were performed in CST in order to provide the optimal parameters for maximum temperature in the lid. Same as before, at a distance of 25 mm, a 100 V/m plane wave, with the E-field component oriented across the gaps in the SRRs and H-field component oriented normal to the lid, was used to excite the pharmaceutical drug capsule. All parameters were kept constant except for the relative permittivity and the conductivity. The maximum temperature point of the substrate at each combination of ϵ_r' and σ at the resonance frequency was taken. The result is shown in Figure 11.8. For a wide range of conductivities (Figure 11.8(a)) the maximum temperature was found to be 41.5 °C for a substrate with $\epsilon_r' = 3$ and $\sigma = 0.07$ S/m. The power loss density for the case of maximum dissipation is indicated in Figure 11.3(b) where it is illustrated that most of the lost power would be dissipated in the

gaps of each ring as well as in the separation between the rings, close to the gaps. An examination of the narrow range of conductivities for several ϵ_r' is illustrated in Figure 11.8(b) where all the curves have a maximum temperature peak at conductivity-values in the range of $\sigma = 0.07 - 0.12$ S/m. A low-loss substrate such as Rogers 4003® will, according to Figure 11.8, not have notable increase in temperature if used as the material for the lid. The availability of that substrate however, made it the choice for the work in the next section where the orientation of the SRRs is examined.

The temperature and its distribution in the capsule are dependent on several parameters such as the thickness of the lid as well as the thermal conductivity of the lid and the material the lid is mounted on. For this simulation, the thickness of the lid was 0.1 mm, the thermal conductivity of the lid and the cylindrical capsule below it, was 0.2 W/K/m.

11.6 Experimental Split-Ring Resonator on the Lid

As the drug capsules would be swallowed and proceed through the digestive system, their orientation inside the intestine would be impossible to determine. Depending on the structure of the capsule and the SRRs, the polarization of the excitation fields in respect to the orientation of the SRRs may be a critical factor in whether the drug capsules would be activated and drug being released. In this section, an experimental study of the effect the orientation of the SRRs has on their ability to resonate and store energy, relative to the excitation fields, was carried out. The ability to resonate and store energy at certain orientations is, by extension, an indication of the most suitable orientations for a local dissipation of power.

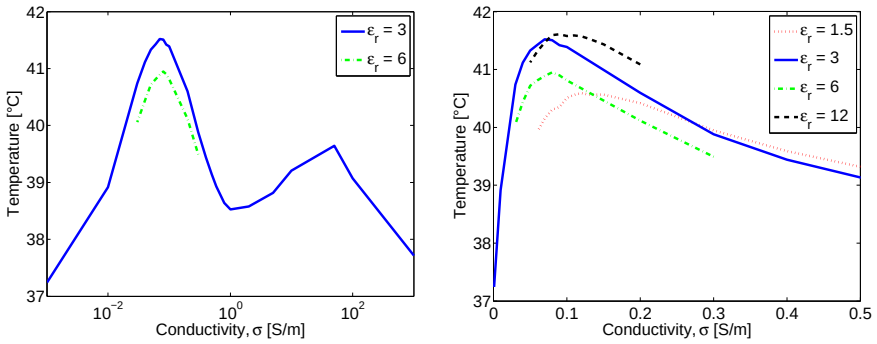

(a) (b)

Figure 11.8: Maximum temperature as a function of conductivity for various relative permittivities of the lid of a pharmaceutical drug capsule. (a) shows a wide range of conductivities while (b) shows narrow range.

11.6.1 Fabrication

Split-ring resonators on top of a 1.5 mm thick Rogers 4003® substrate were fabricated for the experimental study. Each of the SRRs were fabricated on a circular disc with the diameter of 15 mm that functions as an enlarged lid for a drug capsule. The dimensions of the SRRs are shown in Table 11.2 and their notations are referred to Figure 11.2. As mentioned before, the relative permittivity and conductivity at 2.5 GHz are $\epsilon_r = 3.55$ and $\sigma = 0.001$ S/m, respectively.

Table 11.2: Dimensions of the split-ring resonators in the experimental study.

r [mm]	s [mm]	w [mm]	g [mm]	t [mm]
5.1	0.3	0.3	0.2	1.5

11.6.2 Excitation

Having an external antenna array and focusing microwaves inside the human body from a far-field distance, we assume, in general, a propagating transverse electromagnetic (TEM) mode inside the body. This field would excite the pharmaceutical drug capsule and especially the split-ring resonators on top of the lid until the drug would be released. To approximate such a TEM excitation, a coplanar waveguide (CPW) structure was fabricated and is shown in Figure 11.9. Waves on a CPW have typically a quasi-TEM mode since part of the wave is located in the substrate while the other part is located in air. The CPW is approximately a 50 Ω tapered transmission line with a 15 mm gap between the centre conductor and the ground references in the middle of the CPW structure. The large gap makes it possible to fit the lids. This was accomplished by drilling a hole in the substrate in the middle of the gap of the CPW and leaving room for placing the cylindrical lid structures. In the plane of the CPW structure, the E-field component was oriented across the gap where the SRRs are placed, the H-field component was oriented normal to the CPW structure and the direction of propagation, $\hat{k}$, was normal to the E-H plane as is indicated in Figure 11.9.

11.6.3 Measurements

Measurements on six different orientations of the SRRs were performed. The orientations are indicated in Figure 11.10 and are relative to the orientation of the quasi-TEM wave that was propagating in the CPW plane in Fig. 11.9. Each subfigure notation in Fig. 11.10 will be referred to as a case, e.g. the orientation in Figure 11.10(e) is referred to as *case (e)* and so on. For every

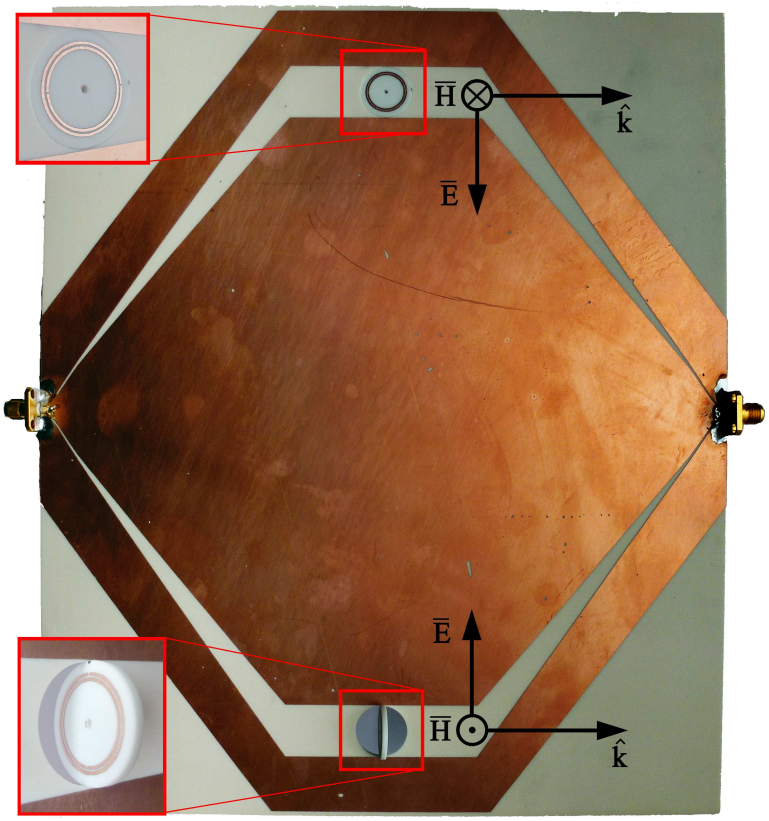

Figure 11.9: Coplanar waveguide (conductors are the dark parts). In the top left corner, an example of a case (e). In the bottom left corner, an example of case (c). The size is 24 cm x 20 cm.

measurement, both SRRs, which are identical, were oriented in a way that was mirrored through the H-k plane of the CPW structure.

The S-parameter measurement results for the CPW structure with SRRs are illustrated in Figure 11.11 and 11.12. The results in Figure 11.11 show S_{21} over the frequency range from 3 GHz to 5 GHz which includes the resonance of the SRR. The reference is a case where there are no SRRs in the holes, i.e. the holes are empty. Outside the resonance, and actually all across the band for the reference, the S_{21} is approximately -10 to -15 dB even though the return loss, shown in Figure 11.12, was better than 6 dB. The reason for this is because the waves traveling in the large gaps of the CPW structure are only loosely bounded to the substrate and therefore radiate into the surroundings and cause the relatively high insertion loss outside the resonance in Figure 11.11.

From the results it can be immediately seen that *cases (a)* and *(d)*, i.e. when the SRRs lie in the H-k plane, do not show a significant response to the propagating wave. In these cases the H-field is parallel to rings and the

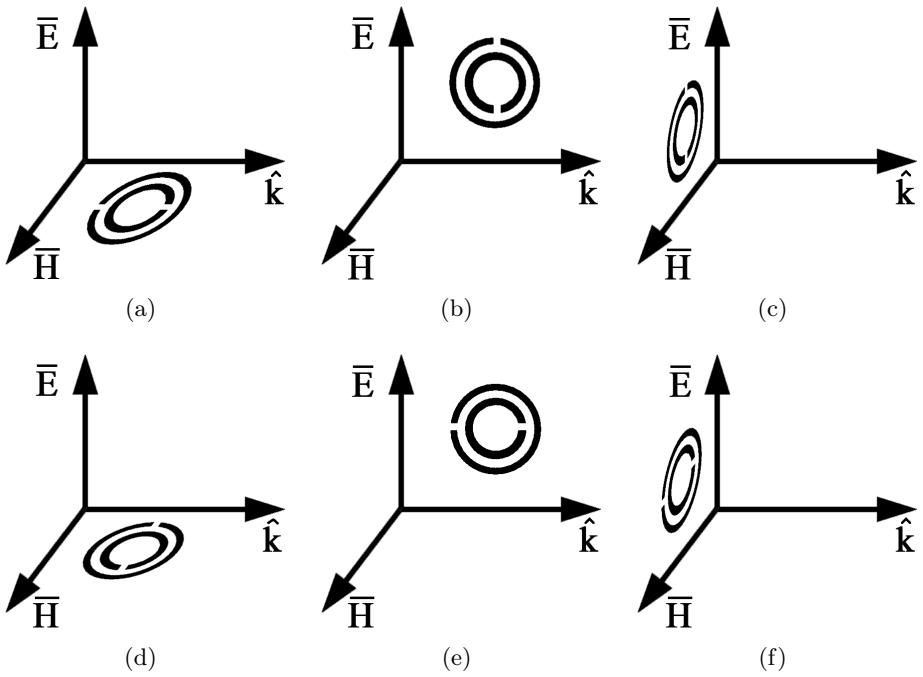

Figure 11.10: Orientation of the split-ring resonators relative to the exciting wave.

E-field is normal to the rings and therefore no excitation is expected. *Case (c)* does not show any resonant response and the S_{21} is approximately the same as that of the reference, but the SRRs do however increase the S_{11} by a few dBs which is an effect of the E-field parallel to the rings that generated a slight potential difference between the rings. *Case (b)* shows a small response in S_{21} where it gets slightly lower than the reference around the resonance frequency and S_{11} is shifted as well. This case indicates the effect that only the H-field component has on the excitation of the SRRs. *Cases (f)* and *(e)* show the largest response. In *case (f)* the H-field is parallel to the SRRs and the E-field is across the gap of the SRRs and the H-field component does therefore not contribute to excitation of the rings. *Case (e)* has the H-field normal to the SRRs and the E-field component across the gaps of the SRRs and that results in a slightly better coupling than *case (f)*.

A planar devices like the SRRs rarely have a resonating response to exciting waves from all directions and polarizations. If a pharmaceutical drug capsule with SRRs on top of a lid would be swallowed it would be a challenge to orient the excitation source correctly to activate the capsule in a controlled manner. Instead of a linear polarization as is the case for the CPW structure, a circular polarization of the exciting wave is suggested and by that, *cases (a)* and *(d)* would also be suitable orientations for resonance

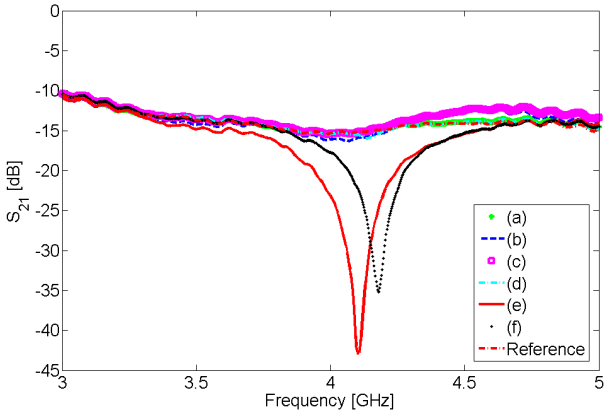

Figure 11.11: Coplanar waveguide transmission (S_{21}) measurement.

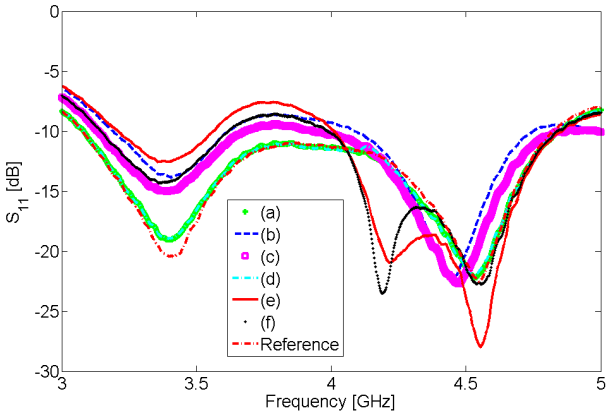

Figure 11.12: Coplanar waveguide reflection (S_{11}) measurement.

and thus, for heat dissipation. It has been shown with the measurements that the optimal orientation for exciting a lid with SRRs on a coplanar waveguide are *cases (f)* and *(e)*.

Chapter 12

Conclusion

In this PhD thesis, a method of externally activating and releasing pharmaceutical drugs inside the human body with the use of microwaves, was investigated. Current limitations in external control of the specific location and the time of a drug release inside the human body formed the motivation for this study. A two-sided solution to this problem was considered. First, a microwave activation system, consisting of four transmitting sources that radiate electromagnetic waves, at a human torso. Secondly, a specially designed micro-container for pharmaceutical drugs with sensitive receiving structure to effectively utilize the received power for releasing the drug.

In the beginning of the thesis, electromagnetic properties of biological tissues were described and especially the wave interaction at a interface between air and fat at an oblique incident angle, which gave rise to possibilities of optimum power transfer under a certain condition. If the angle of incidence is set to be the Brewster angle, maximum power transfer could potentially be accomplished into a lossy media such as a skin or fat layer. At oblique incidence angles, the power loss of the transmitted wave in the lossy media is only dependent on the distance the wave travels in the direction normal to the interface of the lossy media. The combination of utilizing the Brewster angle along with the fact that a wave is only attenuated in the normal direction of an interface, gives the possibility of maximizing the power transfer of a transmitted wave to a pre-determined point inside a lossy tissue.

For representing a human torso, a simple dual-layered cylindrical phantom was proposed. The phantom consists of two concentric plastic cylinders. The inner cylinder holds the muscle tissue mimicking media which, as the name indicates, emulates the electromagnetic properties of muscle tissue at the operating frequency of 2.45 GHz whereas the outer cylinder holds the fat mimicking media. In order to be able to move a measuring or a transmitting antenna around freely, inside the phantom, a low-viscous optically

transparent muscle tissue mimicking media was developed and the resulting recipe is 28% Diethylene Glycol Butyl Ether and 72% de-ionized water. An improved liquid whose properties are within 1% from the reference values for muscle tissue at 2.45 GHz, a recipe of 5% Triton X-100, 23% Diethylene Glycol Butyl Ether and 72% de-ionized water was furthermore produced.

The microwave activation system was developed on the basis of being an unobtrusive system, i.e. without disturbing the prospective patients. To this end, four external antennas were designed to radiate in the far-field, at the torso phantom along with four microwave transmitters and four receivers. The operation of the system was two-fold. First, a mapping of the torso phantom was performed. This required an antenna, submerged in the muscle tissue mimicking medium to transmit from within the phantom and the external antennas were connected to receivers. The transmitting antenna was systematically moved around inside the phantom while phase and amplitude measurements were acquired. The measurement results revealed that creeping waves were travelling along the curvature of the phantom, reaching the receiver furthest away from the transmitting source. If the source was at a certain offset from the centre of the phantom, these creeping waves overshadowed the contribution of the wave travelling along the direct path from the source to the receiver furthest away, due to the high attenuation in the muscle tissue mimicking media.

The measurements also gave an indication of standing waves between the transmitting source and the layers of the phantom as well as the external antennas. This was especially evident at locations inside the phantom where the transmitting source was close to the edge of the phantom.

The measurement results presented in the mapping process disclosed the wave behaviour in the cylindrical phantom. In agreement with Lorentz's reciprocity theorem, these results predicted the behaviour of the second operation, i.e. the focusing.

In the focusing operation, four external transmitters radiated microwaves at the torso phantom from a distance of 65 cm. Two receivers were used. One receiver was connected to the antenna submerged in the muscle tissue mimicking media for the purpose of measuring the amplitude and phase of the received signal. The other receiver was directly connected to both frequency synthesizers and provided a constant phase reference for calibration purposes. The measuring submerged antenna was systematically moved around in the phantom and the amplitudes were measured to uncover the focus point, if any.

Already predicted by the mapping process, it was not possible to focus at 4 cm offset from the centre of the phantom and at larger offsets. This is believed to be due to the contribution of the creeping waves which are also thought to be present if radiating at a human. At 3 cm offset and below, focusing was accomplished. The focusing resulted in a point of a local maximum with a distance of approximately 2 cm to a neighbouring

point of similar amplitude.

Predicted by simulations, a part of the waves that a source radiates at a phantom from one side, crawls along the surface of the phantom, from both sides, where they are added in phase on the opposite side of the phantom. These added creeping waves then radiate partly inwards into the phantom where their power is combined with power radiated from other sources. An experiment was performed that verified the presence of creeping waves. A layered microwave absorber was placed in front of and behind the phantom, relative to a single transmitting source. The received amplitude at the location of the internal antenna, which was offset 8 cm from the centre, revealed a much lower amplitude when the absorber was behind the phantom. These unintuitive results suggest that the absorber attenuates the creeping waves that crawl around the phantom and previously radiated inwards.

Due to the high losses in muscle tissue mimicking media and the large size of the torso phantom, the received signal strength in the phantom were in the order of pW when radiated with approximately hundred mW. The phantom's dimensions are considerably pessimistic regarding the muscle thickness which explains to a large degree, the high attenuation of the signals travelling through the phantom. The high attenuation factor of muscle tissue at 2.45 GHz is also the reason for the low received power, along with the inherent path loss of operating the system in the far-field. A lower operating frequency, of around 1 GHz is suggested for a compromise between increased size of the radiators and the improved penetration into the body. This, however, increases the challenge of developing resonators for the pharmaceutical drug capsule which are sufficiently small. An increased number of radiators is also suggested for higher intensity focus point. By placing the radiators closer to the target, e.g. at the far-field limit, the effects of path loss can be reduced.

A micro-container with split-ring resonators (SRRs) on top of its lid is proposed to be externally activated in order to release a pharmaceutical drug inside the body. The split-ring resonator's resonance frequency was tuned by CST simulation of the container (capsule). At the resonance frequency of the SRRs the external electromagnetic waves excited the SRRs which concentrated high-amplitude electric fields (E-fields) in the gap of the rings and their separation. These high-amplitude fields induced currents in the lossy dielectric substrate that the lid is required to be made of. Too low electric conductivity of the lid and little power would be dissipated in the lid and too high conductivity would short-circuit the SRRs. The optimal conductivity of the dielectric media which the lid is made of was found with simulations to be between 0.07 and 0.12 S/m. The induced currents in the lid resulted in a ohmic power loss, thus the temperature of the lid increased. This increased temperature could be used to melt a type of plastic that has a melting point between 37 and 42 °C or even an adhesive medium that holds

the lid onto the capsule until activated.

An experimental setup to find the most optimal orientation of the capsule's lid was made. Low-loss Rogers 4003 substrate was used as the lid dielectric and SRRs were fabricated on top of it. Together, they represented an enlarged lid. A 50 Ω co-planar transmission line with holes in its gaps was used to place the enlarged lids. In the gap of a co-planar line, quasi-TEM (transverse electromagnetic) fields can exist, approximating pure TEM fields which would be used for exciting the drug capsules. The two most effective orientations of the SRRs are predicted to be when the E-field component is oriented across the gap of the SRRs, in the plane of the SRRs. The optimal orientation is when additionally the magnetic field component is normal to the plane of the SRRs.

The power required for heating up the capsule's lid seems to be orders of magnitude higher than is available from the current experimental microwave setup at locations deep inside the human torso phantom. It does therefore not immediately seem possible to use the current system for releasing medical drugs externally from the body phantom. That being said, the human torso phantom is simple and presents a very pessimistic model for a human torso which results in lower power levels than otherwise would probably be available. An effort should also be made into minimizing the size of the SRRs along with maximizing the dissipated power in the capsule's lid since this work only presents the principle of the concept's operation and optimization has yet to be performed.

References

[1] Qiuping Gu, Charles F. Dillon, and Vicki L. Burt. Prescription drug use continues to increase: U.s. prescription drug data for 2007-2008. *NCHS Data Brief*, 42:1–8, 2010.

[2] Kristy M. Ainslie, Rachel D. Lowe, Tristan T. Beaudette, Lamar Petty, Eric M. Bachelder, and Tejal A. Desai. Microfabricated devices for enchanced bioadhesive drug delivery: Attachement to and small-molecule release trhough a cell monolayer under flow. *Small*, 24:2857–2863, 2009.

[3] Colin W. Pouton. Formulation of poorly water-soluble drugs for oral administration: Physicochemical and physiological issues and the lipid formulation classification system. *European Journal of Pharmaceutical Sciences*, 29:278–287, 2006.

[4] Sanjay B. Bari, Bharati R. Kadam, Yogini S. Jaiswal, and Atul A. Shirkhedkar. Impurity profile: Significance in active pharmaceutical ingredient. *Eurasian Journal of Analytical Chemistry*, 2:32–53, 2007.

[5] Anja Boisen. Naanomechanical sensors and actuators, fundamentals and new direction (namec) - a vkr center of excellence. NAMEC Project proposal to the VKR Foundation.

[6] David R. Friend. Drug delivery to the small intestine. *Current Gastroenterology Reports*, 6:371–376, 2004.

[7] Nazmul Akunjee and Muhammed Akunjee. *The Easy Guide to OSCEs for Final Year Medical Students*. Radcliffe Publishing Ltd., 2007.

[8] Holger Grull and Sander Langereis. Hyperthermia-triggered drug delivery from temperature-sensitive liposomes using mri-guided high intensity focused ultrasound. *Journal of Controlled Release*, 161:317–327, 2012.

[9] Cornelius Diamond and Scott Arouh. Light-activated drug delivery method and device. Patent, 2003. US 2003/0191458 A1.

[10] Jean Brault. Magnetic apparatus used for drug delivery. Patent, 2011. WO2011113140 (A1).

[11] Somayyeh Rahimi, Elie H. Sarraf, Gregory K. Wong, and Kenichi Takahata. Implantable drug delivery device using frequency-controlled wireless hydrogel microvalves. *Biomedical Microdevices*, 13:267–277, 2011.

[12] S. Smith, T.B. Tang, J.G. Terry, J.T.M. Stevenson, B.W. Flynn, H.M. Reekie, A.F. Murray, A.M. gundlach, D. Renshaw, B. Dhillon, A. Ohtori, Y. Inoue, and A.J. Walton. Development of a miniaturised drug delivery system with wireless power transfer and communication. *IET Nanobiotechnology*, 1:80–86, 2007.

[13] Gentei Sato, Chokichiro Shibata, Shuichi Sekimukai, Hiroshi Wakabayashi, Kaoru Mitsuka, and Kenjiro Giga. Phase-controlled circular array heating equipment for deep-seated tumors: Preliminary experiments. *IEEE Transactions on Microwave Theory and Techniques*, 34: 520–525, 1986.

[14] A.J. Fenn and G.A. King. Adaptive radiofrequency hyperthermia-phased array system for improved cancer therapy: phantom target measurements. *International Journal of Hyperthermia*, 10:189–208, 1994.

[15] Paul F. Turner. Hyperthermia and inhomogeneous tissue effects using an annular phased array. *IEEE Transactions on Microwave Theory and Techniques*, 32:874–882, 1984.

[16] Liyong Wu, Robert J. McGough, Omar Ali Arabe, and Thaddeus V. Samulski. An rf phased array applicator designed for hyperthermia breast cancer treatments. *Physics in Medicine and Biology*, 51:1–20, 2006.

[17] M. Seebass, R. Beck, J. Gellermann, J. Nadobny, and P. Wust. Electromagnetic phased arrays for regional hyperthermia: optimal frequency and antenna arrangement. *International Journal of Hyperthermia*, 17: 321–336, 2001.

[18] Margarethus M. Paulides, Jurriaan F. Bakker, Adrianus P. M. Zwamborn, and Gerard C. Van Rhoon. A head and neck hyperthermia applicator: Theoretical antenna array design. *International Journal of Hyperthermia*, 23:59–67, 2007.

[19] J.F. Bakker, M.M. Paulides, A.H. Westra, H.Schippers, and G.C. Van Rhoon. Design and test of a 434 mhz multi-channel amplifier system for targeted hyperthermia applicators. *International Journal of Hyperthermia*, 26:158–170, 2010.

[20] Masahiro Hiraoka, Michihide Mitsumori, Naotoshi Hiroi, Shinji Ohno, Yoshiaki Tanaka, Youji Kotsuka, and Keizo Sugimachi. Development

of rf and microwave heating equipment and clinical applications to cancer treatment in japan. *IEEE Transactions on Microwave Theory and Techniques*, 48:1789–1799, 2000.

[21] Yong-Gang Gu and OM P. Gandhi. Phased-dipole applicators for torso heating in electromagnetic hyperthermia. *IEEE Transactions on Microwave Theory and Techniques*, 32:645–647, 1984.

[22] M.M. Paulides, J.F. Bakker, E. Neufeld, J. Van Der Zee, P.P. Jansen, P.C. Levendag, and G.C. Van Rhoon. The hypercollar: A novel applicator for hyperthermia in the head and neck. *International Journal of Hyperthermia*, 23:567–576, 2007.

[23] S. Jacobsen. Reduction of hot spots in hyperthermia by means of broadband energy transmission. *Electronics Letters*, 34:1901–1902, 1998.

[24] C.K. Chou, J.A. McDougall, K.W. Chan, and K.H. Luk. Effects of fat thickness on heating patterns of the microwave applicator ma-151 at 631 and 915 mhz. *International Journal of Radiation Oncology Biology Physics*, 19:1067–1070, 1990.

[25] Arthur W. Guy, Chung-Kwang Chou, and Kenneth H. Luk. 915-mhz phased-array system for treating tumors in cylindrical structures. *IEEE Transactions on Microwave Theory and Techniques*, 34:502–507, 1986.

[26] A.J. Fenn, G.L. Wolf, and R.M. Fogle. An adaptive microwave phased array for targeted heating of deep tumours in intact breast: animal study results. *International Journal of Hyperthermia*, 15:45–61, 1999.

[27] Eric R. Lee, Tawna R. Wilsey, Peter Tarczy-Horoch, Daniel S. Kapp, Peter Fessenden, Allen Lohrbach, and Stavros D. Prionas. Body conformable 915 mhz microstrip array applicators for large surface area hyperthermia. *IEEE Transactions on Biomedical Engineering*, 39:470–483, 1992.

[28] E.J. Gross, T.C. Cetas, P.R. Stauffer, R.L. Liu, and M.L.D. Lumori. Experimental assessment of phased-array heating of neck tumours. *International Journal of Hyperthermia*, 6:453–474, 1990.

[29] C.K. Chou, J.A. McDougall, K.W. Chan, and K.H. Luk. Heating patterns of microwave applicators in inhomogeneous arm and thigh phantoms. *Journal of Medical Physics*, 18:1164–1170, 1991.

[30] Henry S. Ho, Arthur W. Guy, Rubens A. Sigelmann, and Justus F. Lehmann. Microwave heating of simulated human limbs by aperture

sources. *IEEE Transactions on Microwave Theory and Techniques*, 19: 224–231, 1971.

[31] C. J. Diederich and P.R. Stauffer. Pre-clinical evaluation of a microwave planar array applicator for superficial hyperthermia. *International Journal of Hyperthermia*, 9:227–246, 1993.

[32] Volker Hombach, Klaus Meier, Michael Burkhardt, Eberhard Kühn, and Niels Kuster. The dependence of em energy absorption upon human head modeling at 900 mhz. *IEEE Transactions on Microwave Theory and Techniques*, 44:1865–1873, 1996.

[33] A.P. Anderson, M. Melek, and B.H. Brown. Feasibility of focused microwave array system for tumour irradiation. *Electronics Letters*, 15:564–565, 1979.

[34] Walter Gee, Shung-Wu Lee, Nelson K. Bong, Charles A. Cain, Raj Mittra, and Richard L. Magin. Focused array hyperthermia applicator: Theory and experiment. *IEEE Transactions on Biomedical Engineering*, 31:38–46, 1984.

[35] P.A. Cudd, A.P. Anderson, M.S. Hawley, and J. Conway. Phased-array design considerations for deep hyperthermia through layered tissue. *IEEE Transactions on Microwave Theory and Techniques*, 34:526–531, 1986.

[36] M. Melek, A.P. Anderson, J. Conway, and B.H. Brown. Three dimensional phantom measurements validating the use of phased arrays for deep-seated tumour irradiation. In *Proceedings of the 13th European Microwave Conference*, 1983.

[37] Paul R. Strauffer. Evolving technology for thermal therapy of cancer. *International Journal of Hyperthermia*, 21:731–744, 2005.

[38] J. Conway and A.P. Anderson. Electromagnetic techniques in hyperthermia. *Clinical Physics and Physiological Measurement*, 7:287–318, 1986.

[39] Giorgio Arcangeli, Pietro P. Lombardini, Giorgio A. Lovisolo, Guglielmo Marsiglia, and Maurizio Piattelli. Focusing of 915 mhz electromagnetic power on deep human tissues: A mathematical model study. *IEEE Transactions on Biomedical Engineering*, 31:47–52, 1984.

[40] James R. Wait. Focused heating in cylindrical targets: Part 1. *IEEE Transactions on Microwave Theory and Techniques*, 33:647–649, 1985.

[41] Hana Dobsicek Trefna, Jan Vrba, and Mikael Persson. Evaluation of a patch antenna applicator for time reversal hyperthermia. *International Journal of Hyperthermia*, 26:185–197, 2010.

[42] Paul F. Turner. Mini-annular phased array for limb hyperthermia. *IEEE Transactions on Microwave Theory and Techniques*, 34:508–513, 1986.

[43] Richard L. Magin and Andrew F. Peterson. Noninvasive microwave phased arrays for local hyperthermia: a review. *International Journal of Hyperthermia*, 5:429–450, 1989.

[44] K.S. Nikita, N. Maratos, and N.K. Uzunoglu. Optimum excitation of phases and amplitudes in a phased array hyperthermia system. *International Journal of Hyperthermia*, 8:515–528, 1992.

[45] Keith D. Paulsen, Shireen Geimer, Jingwu Tang, and William E. Boyse. Optimization of pelvic heating rate distributions with electromagnetic phased arrays. *International Journal of Hyperthermia*, 15: 157–186, 1999.

[46] Nagayoshi Morita, Takeshi Hamasaki, and Nobuaki Kumagai. An optimal excitation method in multi-applicator systems for forming a hot zone inside the human body. *IEEE Transactions on Microwave Theory and Techniques*, 34:532–538, 1986.

[47] Paul F. Turner. Regional hyperthermia with an annular phased array. *IEEE Transactions on Biomedical Engineering*, 31:106–114, 1984.

[48] P. Wust, M. Seebass, J. Nadobny, P. Deuflhard, G. Mönicrh, and R. Felix. Simulation studies promote technological development of radiofrequency phased array hyperthermia. *International Journal of Hyperthermia*, 25:517–528, 2009.

[49] Mikaya L.D. Lumöri. Experimentally based modeling of field sources for three-dimensional computation of sar in electromagnetic hyperthermia and treatment planning. *IEEE Transactions on Microwave Theory and Techniques*, 48:1522–1530, 2000.

[50] Alan J. Fenn and Gerald A. King. Experimental investigation of an adaptive feedback algorithm for hot spot reduction in radio-frequency phased-array hyperthermia. *IEEE Transactions on Biomedical Engineering*, 43:273–280, 1996.

[51] H. Griffiths and A. Ahmed. Applied potential tomography for noninvasive temperature mapping in hyperthermia. *Clinical Physics and Physiological Measurement*, 8:147–153, 1987.

[52] Alan J. Fenn, Vythialingam Sathiaseelan, Gerald A. King, and Paul R. Stauffer. Improved localization of energy deposition in adaptive phased-array hyperthermia treatment of cancer. *The Lincoln Laboratory Journal*, 9:187–196, 1996.

[53] C.K. Chou. Evaluation of microwave hyperthermia applicators. *Bioelectromagnetics*, 13:581–597, 1992.

[54] Czeslaw J. Lewa and Jacques D. de Certaines. Body temperature mapping by magnetic resonance imaging. *Spectroscopy Letters*, 27: 1369–1419, 1994.

[55] P. Deuflhard, H.-C. Hege, and M. Seebass. Progress towards a combined mri / hyperthermia system. Technical report, Kanrad-Zuse-Zentrum für Informationstechnik Berlin, 2000.

[56] M.S. Hawley, J. Conway, A.P. Anderson, and P.A. Cudd. The influence of tissue layering on microwave thermographic measurements. *International Journal of Hyperthermia*, 4:427–435, 1988.

[57] Y. Suzuki, M. Baba, M. Taki, K. Fukunaga, and S. Watanabe. Imaging the 3d temperature distributions caused by exposure of dielectric phantoms to high-frequency electromagnetic fields. *IEEE Transactions on Dielectrics and Electrical Insulation*, 13:744–750, 2006.

[58] R.G. Olsen and R.R. Bowman. Simple nonpertubing temperature probe for microwave/radio frequency dosimetry. *Bioelectromagnetics*, 10:209–213, 1989.

[59] R.H. Johnson, A.W. Preece, and J.L. Green. Theoretical and experimental comparison of three types of electromagnetic hyperthermia applicator. *Physics in Medicine and Biology*, 35:761–779, 1990.

[60] Hua-Cheng Chang and Kenneth K. Mei. Penetration of a focused electromagnetic pulse into a biological material and its application to hyperthermia. In *Antennas and Propagation Society International Symposium*, 1989.

[61] Arthur W. Guy. Electromagnetic fields and relative heating patterns due to a rectangular aperture source in direct contact with bilayered biological tissue. *IEEE Transactions on Microwave Theory and Techniques*, 19:214–223, 1971.

[62] M.W. Dewhirst, B.L. Viglianti, M. Lora-Michiels, M. Hanson, and P.J. Hoopes. Basic principles of thermal dosimetry and thermal thresholds for tissue damage from hyperthermia. *International Journal of Hyperthermia*, 19:267–294, 2003.

[63] George M. Hahn. Hyperthermia for the engineer: A short biological primer. *IEEE Transactions on Biomedical Engineering*, 31:3–8, 1984.

[64] E.S.A.M. Lepelaars. Electromagnetic pulse distortion in living tissue. *Medical and Biological Engineering and Computing*, 64:213–220, 1996.

[65] Krishnan Moten, Carl H. Durney, and Thomas G. Stockham Jr. Electromagnetic pulsed-wave radiation in spherical models of dispersive biological substances. *Bioelectromagnetics*, 12:319–333, 1991.

[66] Haralambos N. Kritikos and Herman P. Schwan. Hot spots generated in conducting spheres by electromagnetic waves and biological implications. *IEEE Transactions on Biomedical Engineering*, 19:53–58, 1972.

[67] James R. Wait and Mikaya Lumori. Focused heating in cylindrical targets: Part 2. *IEEE Transactions on Microwave Theory and Techniques*, 34:357–359, 1986.

[68] Marc E. Kowalski, Babak Behnia, Andrew G. Webb, and Jian-Ming Jin. Optimization of electromagnetic phased-arrays for hyperthermia via magnetic resonance temperature estimation. *IEEE Transactions on Biomedical Engineering*, 49:1229–1241, 2002.

[69] Mark Converse, Essex J. Bond, Susan C. Hagness, and Barry D. Van Veen. Ultrawide-band microwave space-time beamforming for hyperthermia treatment of breast cancer: A computational feasibility study. *IEEE Transactions on Microwave Theory and Techniques*, 52:1876–1889, 2004.

[70] Aart Van Halteren, Richard Bults, Katarzyna Wac, Nicolai Dokovsky, George Koprinkow, Ing Widya, Dimitri Konstantas, and Val Jones. Wireless body area networks for healthcare: the mobihealth project. *Wearable eHealth Systems for Personalised Health Management*, 108: 181–193, 2004.

[71] T.G. Zimmerman. Wireless networked digital devices: A new paradigm for computing and communication. *IBM Systems Journal*, 38:566–574, 1999.

[72] Nike; www.nike.com.

[73] Garmin; www.garmin.com.

[74] Nox Medical; www.noxmedical.com.

[75] E.Montón, J.F.Hernandez, J.M.Blasco, T.Hervé, J.Micallef, I.Grech, A.Brincat, and V.Traver. Body area network for wireless patient monitoring. *Telemedicine and E-Health Communication Systems*, 2:215–222, 2008.

[76] Yang Hao and Robert Foster. Wireless body sensor networks for health-monitoring applications. *Physiological Measurement*, 29:R27–R56, 2008.

[77] University of London Yang Hao, Qeen Mary College. Antennas and propagation for body centric wireless communications in healthcare.

[78] Anders J. Johansson. Performance of a radio link between a base station and a medical implant utilising the mics standard. In *Proceedings of the 26th Annual International Conference of the IEEE EMBS*, 2004.

[79] A. Alomainy, A.S.Owadally, Y.Hao, C.G.Parini, Y.I.Nechayev, C.C.Constantinou, and P.S.Hall. Body-centric wlans for future wearable computers. In *International Workshop on wearable and implantable body sensor network*, 2004.

[80] Thomas Zasowski, Gabriel Meyer, Frank Althaus, and Armin Wittneben. Ubw signal propagation of the human head. *IEEE Transactions on Microwave Theory and Techniques*, 54:1836–1845, 2006.

[81] Rihit Chandra and Anders J. Johansson. A link loss model for the on-body propagation channel for binaural hearing aids. *IEEE Transactions on Antennas and Propagation*, 61:6180–6189, 2013.

[82] A.Alomainy, Y.Hao, X.Hu, C.G.Parini, and P.S.Hall. Uwb on-body radio propagation and system modelling for wireless body-centric networks. *IEE Proceedings-Communications*, 153:107–114, 2006.

[83] Laurens Roelens, Wout Joseph, Elisabeth Reusens, Gunter Vermeeren, and Luc Martens. Characterization of scattering parameters near a flat phantom for wireless body area networks. *IEEE Transactions on Electromagnetic Compatibility*, 50:185–193, 2008.

[84] Maciej Klemm and Gerhard Troester. Textile uwb antennas for wireless body area networks. *IEEE Transactions on Antennas and Propagation*, 54:3192–3197, 2006.

[85] A.Pellegrini, A.Brizzi, L.Zhang, K.Ali, Y.Hao, X.Wu, C.C.Constantinou, Y.Nechayev, P.S.Hall, N.Chahat, M.Zhadobov, and R.Sauleau. Antennas and propagation for body-centric wireless communications at millimeter-wave frequencies: A review. *IEEE Antennas and Propagation Magazine*, 55:262–287, 2013.

[86] Dominique L. Paul, Henry Giddens, Michael G. Paterson, Geoffrey S. Hilton, and Joe P. McGeehan. Impact of body and clothing on a wearable textile dual band antenna at digital television and wireless communications bands. *IEEE Transactions on Antennas and Propagation*, 61:2188–2194, 2013.

[87] L. Akhoondzadeh-Asl, Y.Nechayev, and P.S.Hall. Surface and creeping waves excitation by body-worn antennas. In *Loughborough Antennas & Propagation Conference*, 2010.

[88] Thierry Alves, Benoit Poussot, and Jean-Marc Laheurte. Analytical propagation modeling of ban channels based on the creeping-wave theory. *IEEE Transactions on Antennas and Propagation*, 59:1269–1274, 2011.

[89] S.K.S. Gupta, S. Lalwani, Y. Prakash, E. Elsharawy, and L. Schwiebert. Towards a propagation model for wireless biomedical applications. In *IEEE International Conference on Communications*, 2003.

[90] D.Kurup, W.Joseph, G.Vermeeren, and L.Martens. Path loss model for in-body communication in homogeneous human muscle tissue. *Electronics Letters*, 45, 2009.

[91] Divya Kurup, Maria Scarpello, Günter Vermeeren, Wout Joseph, Kristof Dhaenens, Fabrice Axisa, Luc Martens, Dries Vande Ginste, Hendrik Rogier, and Jan Vanfleteren. In-body path loss models for implants in heterogeneous human tissues using implantable slot dipole conformal flexible antennas. *EURASIP Journal on Wireless Communications and Networking*, 51:1–9, 2011.

[92] J. Gemio, J. Parrón, and J. Soler. Human body effects on implantable antennas for ism bands applications: Models comparison and propagation losses study. *Progress In Electromagnetics Research*, 110:437–452, 2010.

[93] E.Reusens, W.Joseph, G. WVermeeren, D.Kurup, and L.Martens. Real human body measurements, model, and simulations of a 2.45 ghz wireless body area network communication channel. In *5th International Workshop on Wearable and Implantable Body Sensor Networks*, 2008.

[94] Anders J. Johansson. *Wireless Communication with Medical Implants: Antennas and Propagation.* PhD thesis, Lund University, 2004.

[95] Akram Alomainy and Yang Hao. Modeling and characterization of biotelemetric radio channel from ingested implants considering organ contents. *IEEE Transactions on Antennas and Propagation*, 57:999–1005, 2009.

[96] A.Alomainy, Y.Hao, Y.Yuan, and Y.Liu. Modelling and characterisation of radio propagation from wireless implants at different frequencies. In *Proceedings of the 9th European Conference on Wireless Technology*, 2006.

[97] David M. Pozar. *Microwave Engineering 3rd ed.* Wiley, 2005.

[98] S. Gabriel, R.W. Lau, and C. Gabriel. The dielectric properties of biological tissues: 3. parametric models for the dielectric spectrum of tissues. *Physics in Medicine and Biology*, 41:2271–2293, 1996.

[99] FCC. Federal Communications Commision. Radio frequency safety. http://transition.fcc.gov/oet/rfsafety/dielectric.html, Visited February 2013.

[100] Constantine A. Balanis. *Advanced Engineering Electromagnetics*. Wiley, 2012.

[101] Cynthia M. Furse, Douglas A. Christensen, and Carl H. Durney. *Basic Introduction to Bioelectromagnetics*. CRC Press, 2009.

[102] Roger D. Radcliff and Constantine A. Balanis. Modified propagation constants for nonuniform plane wave transmission through conducting media. *IEEE Transactions on Geoscience and Remote Sensing*, 20: 408–411, 1982.

[103] Chung-Kwang Chou, Gang-Wu Chen, Arthur W. Guy, and Kenneth H. Luk. Formulas for preparing phantom muscle tissue at various radiofrequencies. *Bioelectromagnetics*, 5:435–441, 1984.

[104] Tuba Yilmaz, Tutku Karacolak, and Erdem Topsakal. Characterization and testing of a skin mimicking material for implantable antennas operating at ism band (2.4 ghz - 2.48 ghz). *IEEE Antennas and Wireless Propagation Letters*, 7:418–420, 2008.

[105] P. Wust, H. Fähling, J. Berger, A. Jordan, G. Mönich, and R. Felix. Solid materials with high dielectric constants for hyperthermia applications. *International Journal of Hyperthermia*, 14:183–193, 1998.

[106] Mariya Lazebnik, Ernest L. Madsen, Gary R. Frank, and Susan C. Hagness. Tissue-mimicking phantom materials for narrowband and ultrawideband microwave applications. *Physics in Medicine and Biology*, 50:4245–4258, 2005.

[107] Teruo Onishi, Ryo Ishido, Takuya Takimoto, Kazuyuki Saito, Shinji Uebayashi, Masaharu Takahashi, and Koichi Ito. Biological tissue-equivalent agar-based solid phantoms and sar estimation using the thermographic method in the range of 3-6 ghz. *IEICE Trans. Commun.*, 88:3733–3741, 2005.

[108] Koichi Ito, Katsumi Furuya, Yoshinobu Okano, and Lira Hamada. Development and characteristics of a biological tissue-equivalent phantom for microwaves. *Electronics and Communications in Japan*, 84:67–77, 2001.

[109] Mark G. Douglas and C.K. Chou. Enabling the use of broadband tissue equivalent liquids for specific absorption rate measurements. In *IEEE International Symposium on Electromagnetic Compatibility*, 2007.

[110] A.P. Gregory, Y. Johnson, K. Fukunaga, R.N. Clarke, and A.W. Preece. Traceable dielectric measurements of new liquids for specific absorption rate (sar) measurement in the frequency range 300 mhz to 6 ghz. In *Conference on Precision Electromagnetic Measurements Digest*, 2004.

[111] J. Barthel, K. Bachhuber, R.Buchner, and H. Hetzenauer. Dielectric spectra of some common solvents in the microwave region. water and lower alcohols. *Chemical Physics Letters*, 165:369–373, 1990.

[112] Agilent Technologies. *Agilent 85070E Dielectric Probe Kit 200 MHz to 50 GHz.*

[113] IEEE Standards Coordinating Committee 34. *IEEE Recommended Practice for Determining the Peak Spatial-Average Specific Absorption Rate (SAR) in the Human Head for Wireless Communications Devices: Measurement Techniques. IEEE Std 1528-2003.* IEEE, 2003.

[114] Camelia Gabriel. Compilation of the dielectric properties of body tissues at rf and microwave frequencies, al/oe-tr-1996-0037. Technical report, Brooks Airforce Base, 1996.

[115] C. Gabriel, S. Gabriel, and E. Corthout. The dielectric properties of biological tissues: 1. literature survey. *Physics in Medicine and Biology*, 41:2231–2249, 1996.

[116] S. Gabriel, R.W. Lau, and C. Gabriel. The dielectric properties of biological tissues: 2. measurements in the frequency range 10 hz to 20 ghz. *Physics in Medicine and Biology*, 41:2251–2269, 1996.

[117] Hao Ling, Shung-Wu Lee, and Walter Gee. Frequency optimization of focused microwave hyperthermia applicators. *Proceedings of the IEEE*, 72:224–225, 1984.

[118] Ada S. Y. Poon, Stephen O'Driscoll, and Teresa H. Meng. Optimal frequency for wireless power transmission into dispersive tissue. *IEEE Transactions on Antennas and Propagation*, 58:1739–1750, 2010.

[119] Bill Riddle, James Baker-Jarvis, and Jerzy Krupka. Complex permittivity measurements of common plastics over variable temperatures. *IEEE Transactions on Microwave Theory and Techniques*, 51:727–733, 2003.

[120] Zheryobkina O.N. and Kazanskiy O.V. About pulse propagation in biological tissues. modeling taking into account dispersion and decay. In *Ultrawideband and Ultrashort Impulse Signals, Sevastopol, Ukraine*, 2008.

[121] Eleanor R. Adair, Kevin S. Mylacraine, and Brenda L. Cobb. Partial-body exposure of human volunteers to 2450 mhz pulsed or cw fields provokes similar thermoregulatory responses. *Bioelectromagnetics*, 22: 246–259, 2001.

[122] Kenneth R. Foster and Michael H. Repacholi. Biological effects of radiofrequency fields: Does modulation matter? *Radiation Research*, 162:219–225, 2004.

[123] Shin-Tsu Lu, Satnam P. Mathur, Yahya Akyel, and Jonathan C. Lee. Ultrawide-band electromagnetic pulses induced hypotension in rats. *Physiologi and Behavior*, 65:753–761, 1999.

[124] Chung-Kwang Chou, Arthur W. Guy, and Robert Galambos. Auditory perception of radio-frequency electromagnetic fields. *Journal of the Acoustical Society of America*, 71:1321–1334, 1982.

[125] Krishnan Moten, Carl H. Durney, and Thomas G. Stockham Jr. Electromagnetic pulse propagation in dispersive planar dielectrics. *Bioelectromagnetics*, 10:35–49, 1989.

[126] Antenna Standards Committee. *IEEE Standard Definitions of Terms of Antennas. IEEE Std 145-1993.* IEEE, 1993.

[127] K.F. Lee and J.S. Dahele. *Handbook of Microstrip Antennas.* Peter Peregrinus Ltd., 1989.

[128] L. Foged, O. Breinbjerg, S. Pivnenko, G. Di Massa, and C. Sabatier. Antenna measurement facility comparison within the european antenna centre of excellence. In *European Microwave Conference 2005*, 2005.

[129] Radio waves and health - mobile communications. ericsson ab.

[130] Brian Sveistrup Jensen. *Microwave Instrument for Human Vital Signs Detection and Monitoring.* PhD thesis, Technical University of Denmark, 2012.

[131] Sævar Þór Jónasson. Microwave components for a breast cancer camera. Master's thesis, Technical University of Denmark, 2009.

[132] Lawrence C. Chirwa, Paul A. Hammond, Scott Roy, and David R.S. Cumming. Electromagnetic radiation from ingested sources in the human intestine between 150 mhz and 1.2 ghz. *IEEE Transactions on Biomedical Engineering*, 50:484–492, 2003.

[133] Huber and Suhner. *Microwave cables and assemblies*, 2010.

[134] J. B. Pendry, A. J. Holden, and D. J. Robbins et al. Magnetism from conductors and enhanced nonlinear phenomena. *IEEE Transactions on Microwave Theory and Techniques*, 47:2075–2084, 1999.

[135] Jesús Martel, Ricardo Marqués, Francisco Falcone, Juan D. Baena, Francisco Medina, Ferran Martín, and Mario Sorolla. A new lc series element for compact bandpass filter design. *IEEE Microwave and Wireless Components Letters*, 14:210–212, 2004.

[136] D. R. Smith, Willie J. Padilla, D. C. Vier, S. C. Nemat-Nasser, and S. Schultz. Composite medium with simultaneously negative permeability and permittivity. *Physical Review Letters*, 84:4184–4187, 2000.

[137] J. B. Pendry. Negative refraction makes a perfect lens. *Physical Review Letters*, 85:3966–3969, 2000.

[138] Joan García-García, Jordi Bonache, Ignacio Gil, Ferran Martín, María del Castillo Velázquez-Ahumada, and Jesús Martel. Miniaturized microstrip and cpw filters using coupled metamaterial resonators. *IEEE Transactions on Microwave Theory and Techniques*, 54:2628–2635, 2006.

[139] Megumi Morita, Takeshi Inoue, Tsutomu Yamada, Yasushi Takemura, Tetsu Niwa, and Tomio Inoue. Resonant circuits for hyperthermia excited by rf magnetic field of mri. *IEEE Transactions of Magnetics*, 41:3673–3675, 2005.

[140] C.M. McLoughlin, W.A.M. McMinn, and T.R.A. Magee. Physical and dielectric properties of pharmaceutical powders. *Powder Technology*, 134:40–51, 2003.

[141] Institute of Medicine of the National Academies. Dietary reference intakes for calcium and vitamin d. Technical report, Institute of Medicine of the National Academies, 2011.

[142] N.G. Evans and M.G. Hamlyn. Alkali metal and alkali earth carbonates at microwave frequencies, i: Dielectric properties. *Journal of Microwave Power and Electromagnetic Energy*, 33:24–26, 1998.

Appendix A

Calibration Verification

In Figures A.1(a) and A.1(b), the relative permittivity and conductivity are illustrated, respectively. As can be seen, the measured parameters are very close to the model and the calibration is considered good.

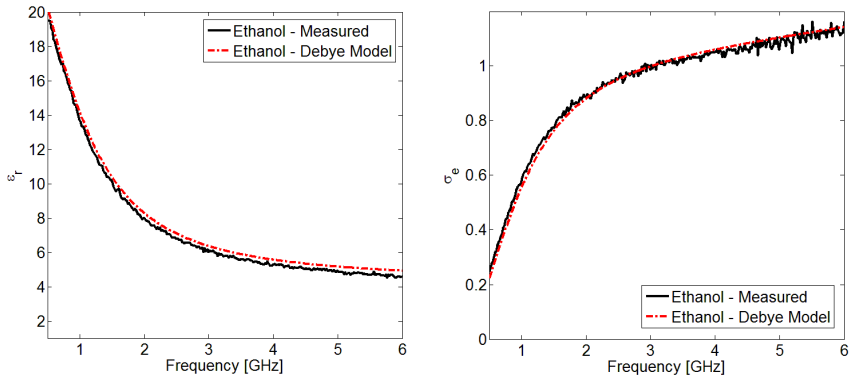

(a) (b)

Figure A.1: Ethanol material parameters. In (a) is measured relative permittivity vs Debye model. In (b) is measured conductivity vs Debye model.

Appendix B

Fat Mimicking Media

In general for biological tissues, the conductivity of media follows the relative permittivity, i.e. media with high permittivity tend to have higher conductivity. An example of this can be found in Table 3.1 where some average permittivity and conductivity values of some typical tissues at 2.45 GHz were presented. Liquids that can emulate electromagnetic properties of fat can be difficult to find due to fat's combination of low conductivity and intermediate relative permittivity. For sanitary reasons, animal fat was not considered for the experimental setup.

Colza frying oil, that one could perhaps consider as a liquid fat, has e.g. $\epsilon_r' = 3.2$ and $\sigma = 0.017$ S/m at 2.45 GHz as can be seen in Figure C.1 in Appendix C. The conductivity of the oil is almost an order lower than that of fat whereas water-based media typically have much higher ϵ_r' and higher σ than fat.

For simplicity, 99.5% pure glycerin is utilized as a fat mimicking media. Glycerin is widely used as a coupling medium for microwave breast cancer imaging cameras and is therefore easily available for this project because such a camera is in operation at the Department of Electrical Engineering, DTU. Glycerin is a thick liquid with vicosity that reminds of syrup. The dielectric properties of glycerin are illustrated in Figure B.1. At around 2.45 GHz, $\epsilon_r' = 5.8$ and $\sigma = 0.48$ S/m. The relative permittivity of glycerin is slightly higher than that of fat and the conductivity is more than 4 times higher. This fat mimicking media can therefore, to some extent, be considered as the effective fat, including both the skin layer as well as the fat layer. The relatively high conductivity, however, causes much more attenuation in the phantom than would be expected in actual fat therefore, less power will penetrate into the phantom. This must be considered when interpreting the measurement results below.

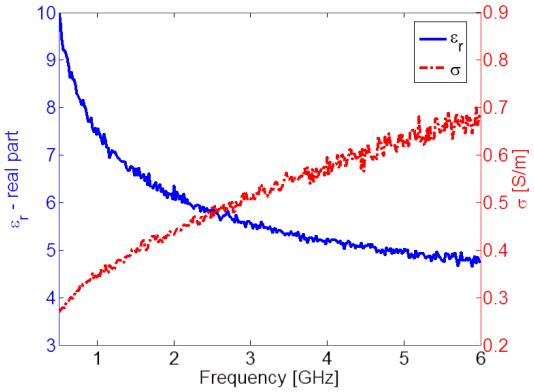

Figure B.1: Measured dielectric properties of glycerin.

Appendix C

Dielectric Measurements

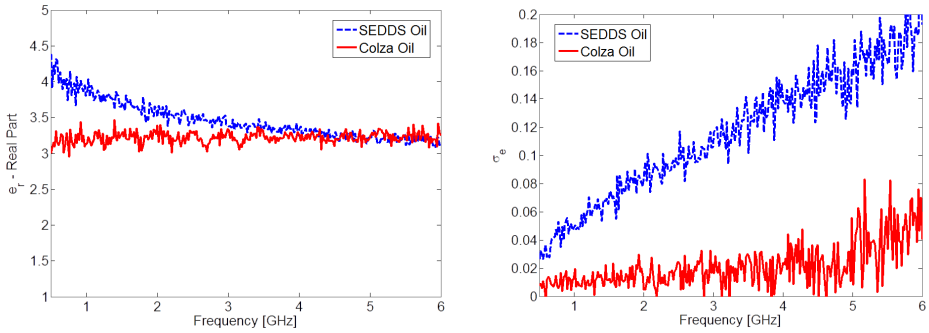

(a) (b)

Figure C.1: Measured dielectric properties of colza oil and SEDDS oil. In (a) is measured relative permittivity. In (b) is measured conductivity.

Appendix D

System Measurements

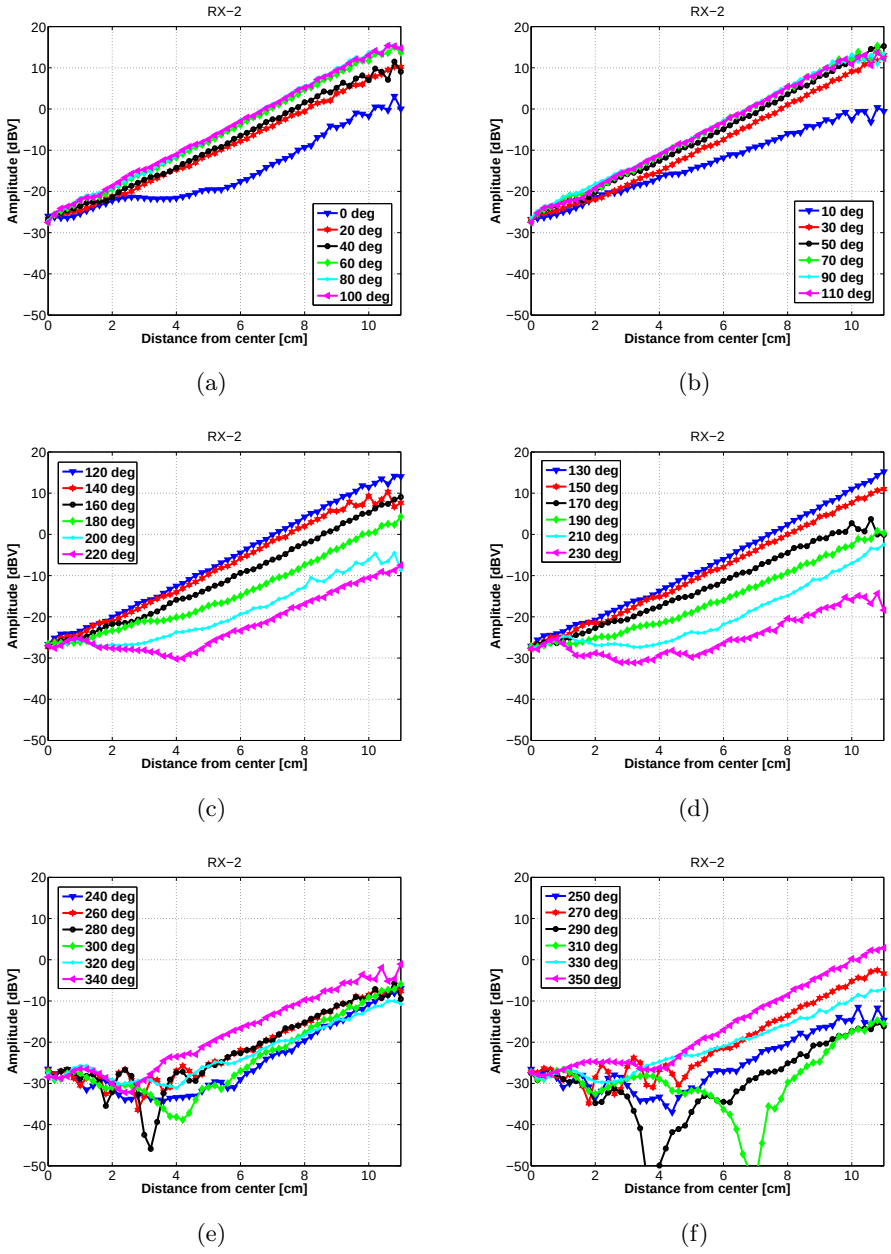

Figure D.1: Amplitude measurements of RX-2 in logarithmic scale for every 10 degree step. In (a), (c) and (e) are 0, 20, 40, 60 degrees etc. In (b), (d) and (f) are 10, 30, 50, 70 degrees etc.

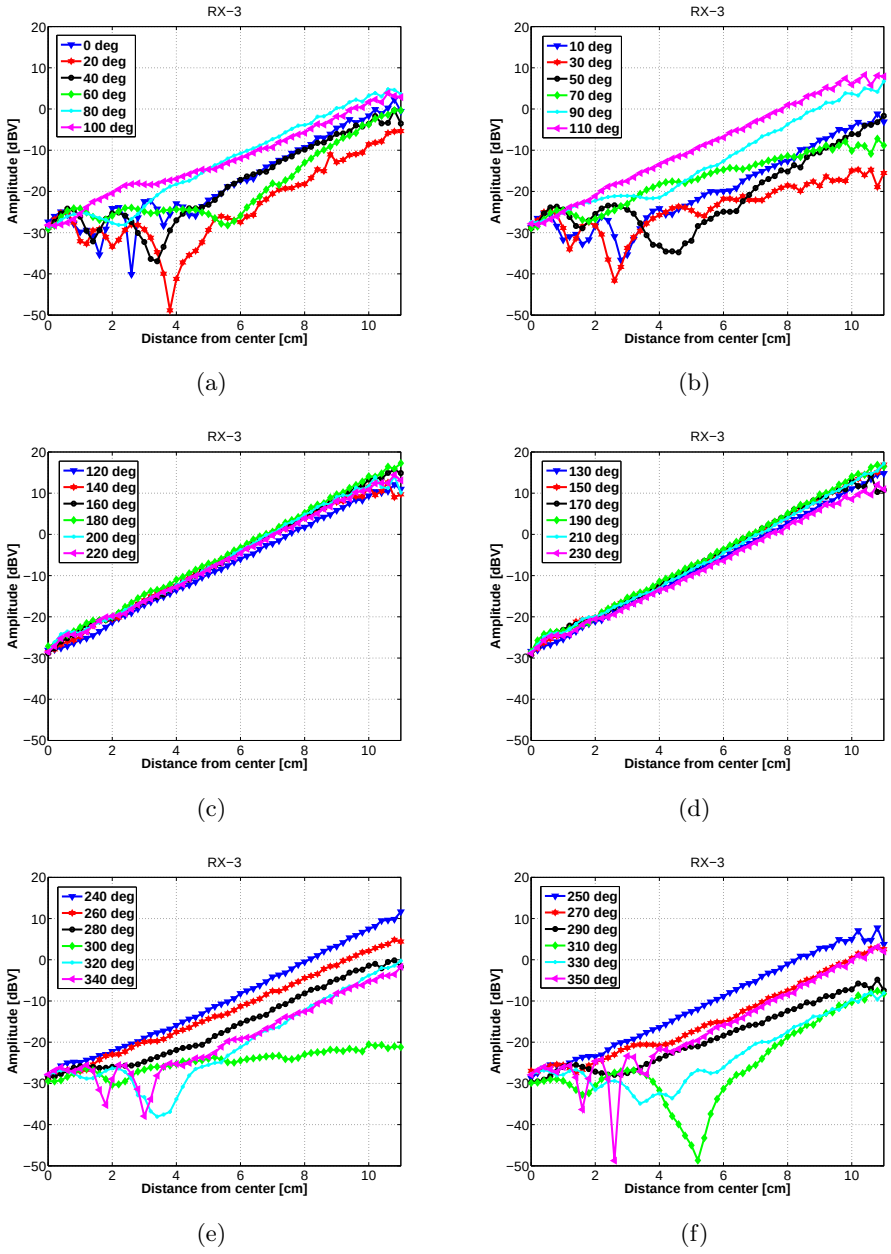

Figure D.2: Amplitude measurements of RX-3 in logarithmic scale for every 10 degree step. In (a), (c) and (e) are 0, 20, 40, 60 degrees etc. In (b), (d) and (f) are 10, 30, 50, 70 degrees etc.

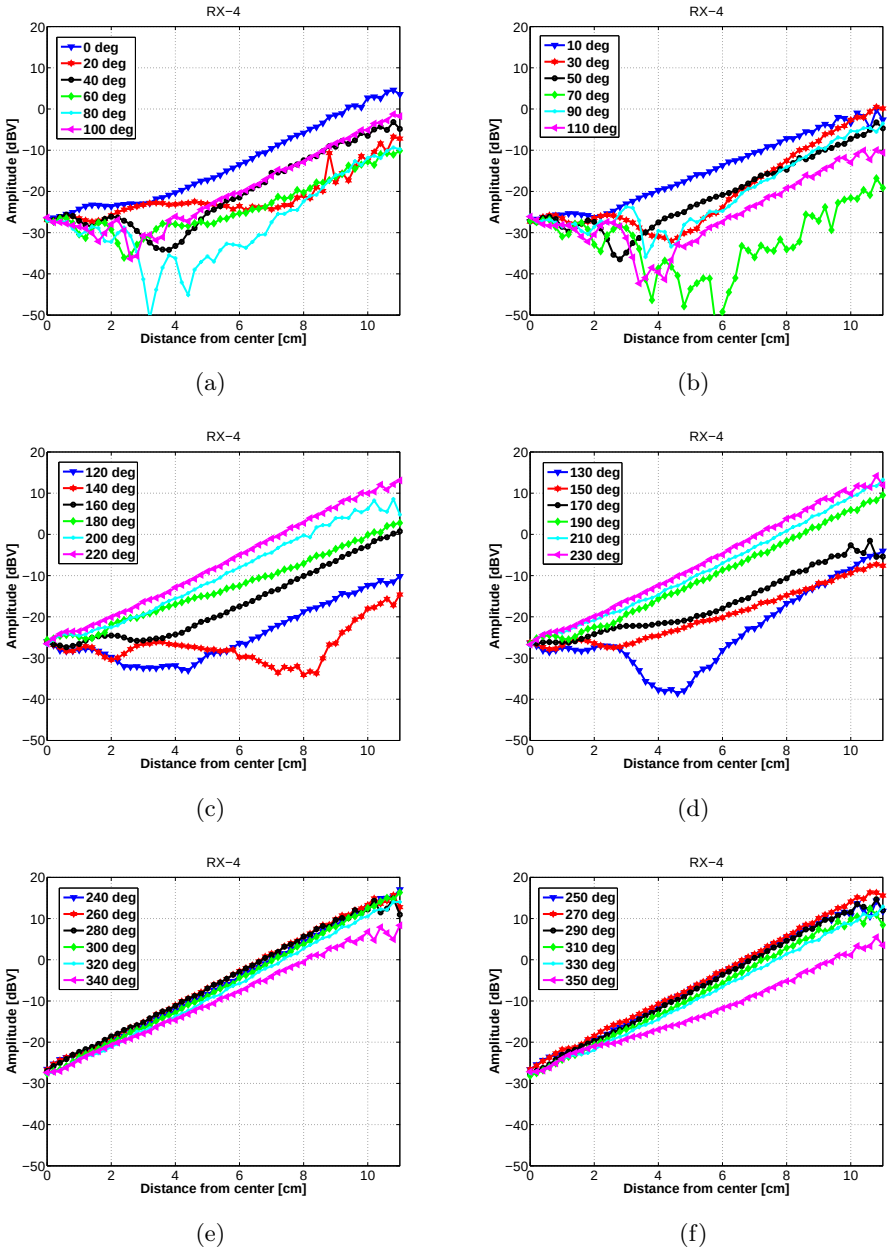

Figure D.3: Amplitude measurements of RX-4 in logarithmic scale for every 10 degree step. In (a), (c) and (e) are 0, 20, 40, 60 degrees etc. In (b), (d) and (f) are 10, 30, 50, 70 degrees etc.

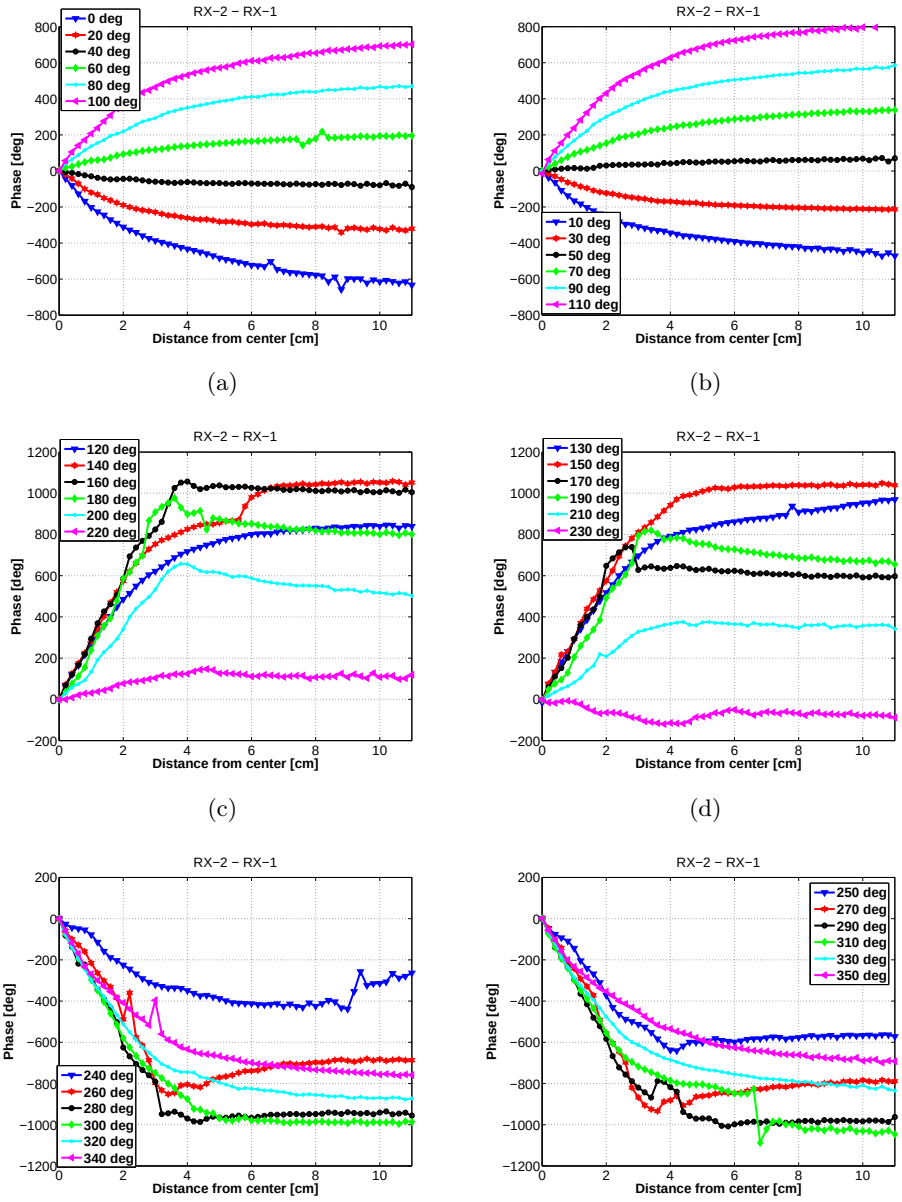

Figure D.4: Phase measurements of RX-2 - RX-1 for every 10 degree step. In (a), (c) and (e) are 0, 20, 40, 60 degrees etc. In (b), (d) and (f) are 10, 30, 50, 70 degrees etc.

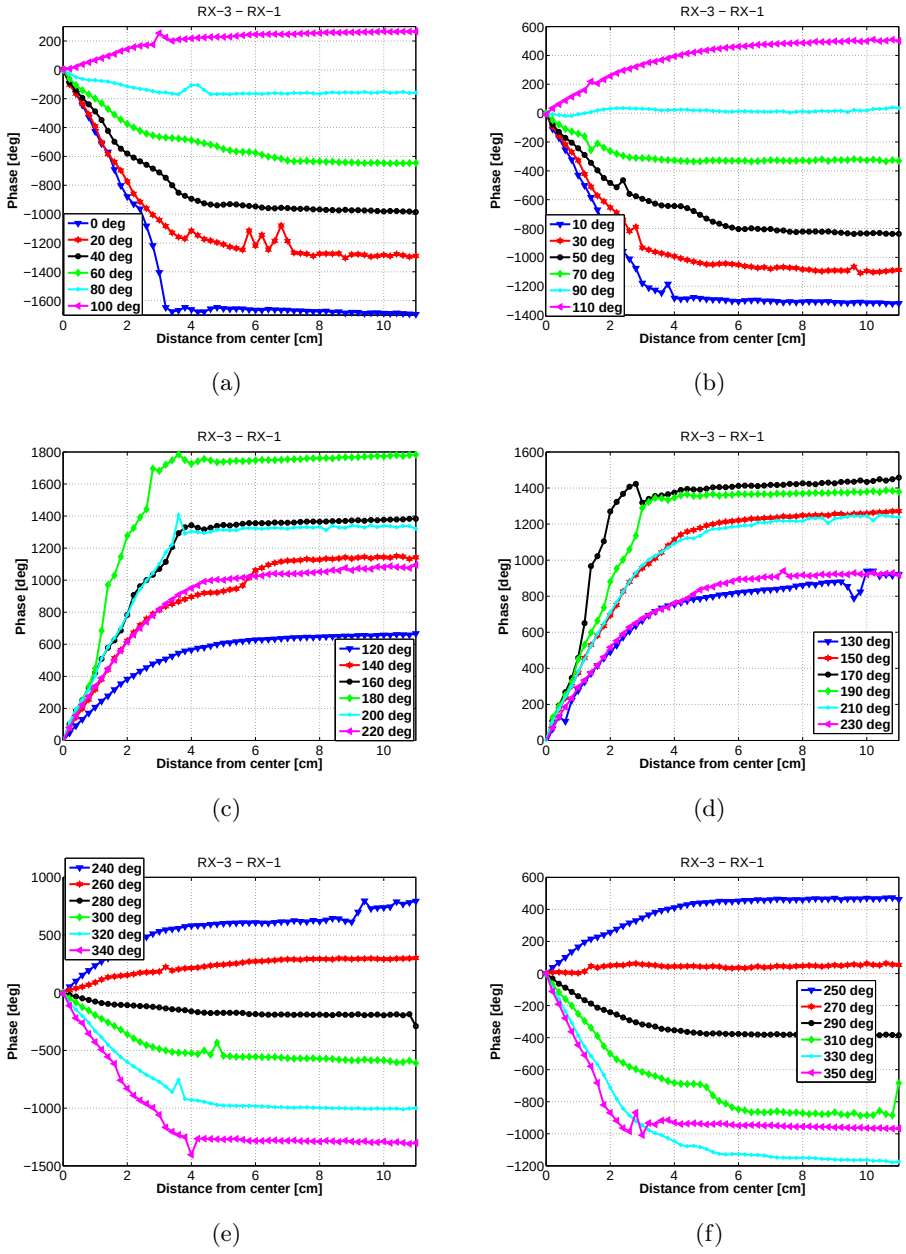

Figure D.5: Phase measurements of RX-3 - RX-1 for every 10 degree step. In (a), (c) and (e) are 0, 20, 40, 60 degrees etc. In (b), (d) and (f) are 10, 30, 50, 70 degrees etc.

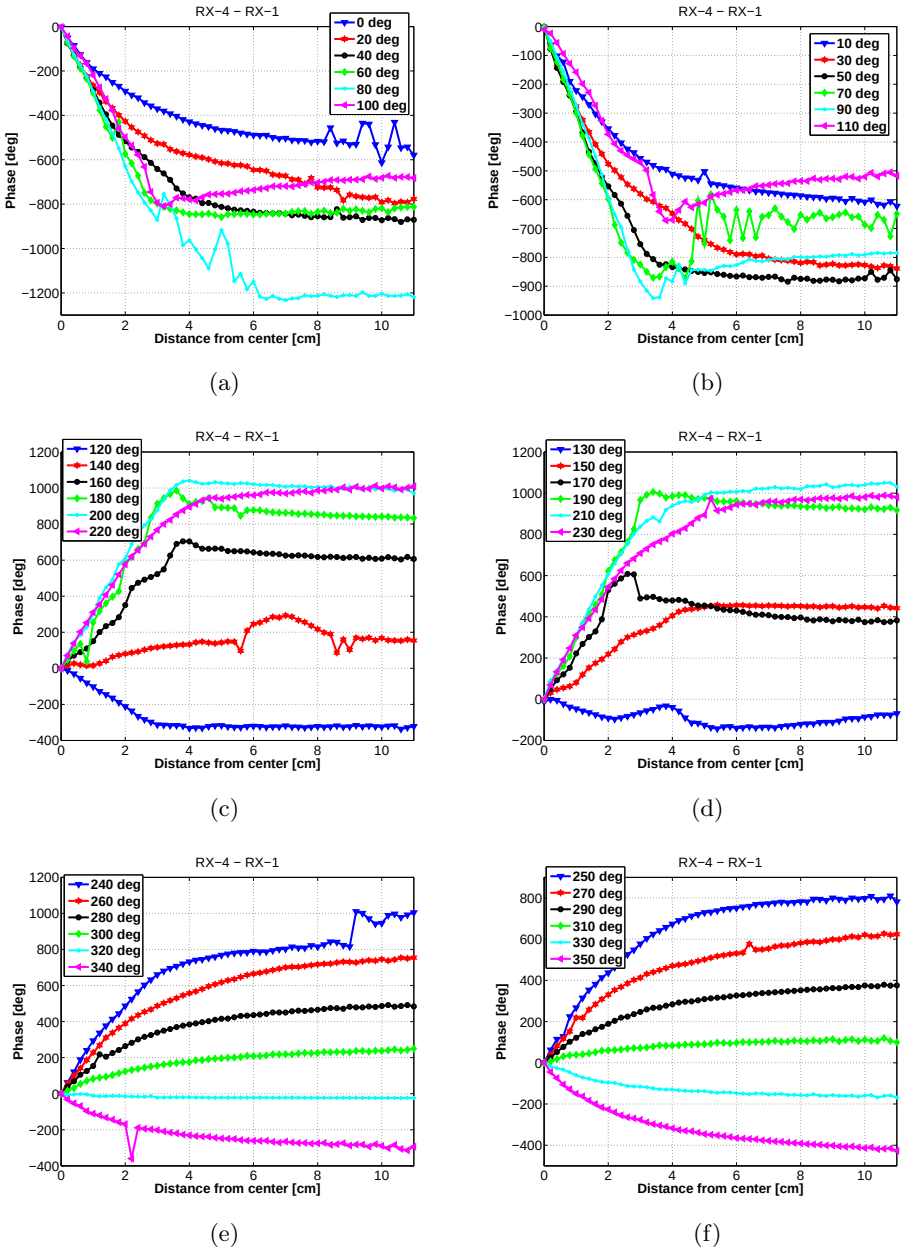

Figure D.6: Phase measurements of RX-4 - RX-1 for every 10 degree step. In (a), (c) and (e) are 0, 20, 40, 60 degrees etc. In (b), (d) and (f) are 10, 30, 50, 70 degrees etc.

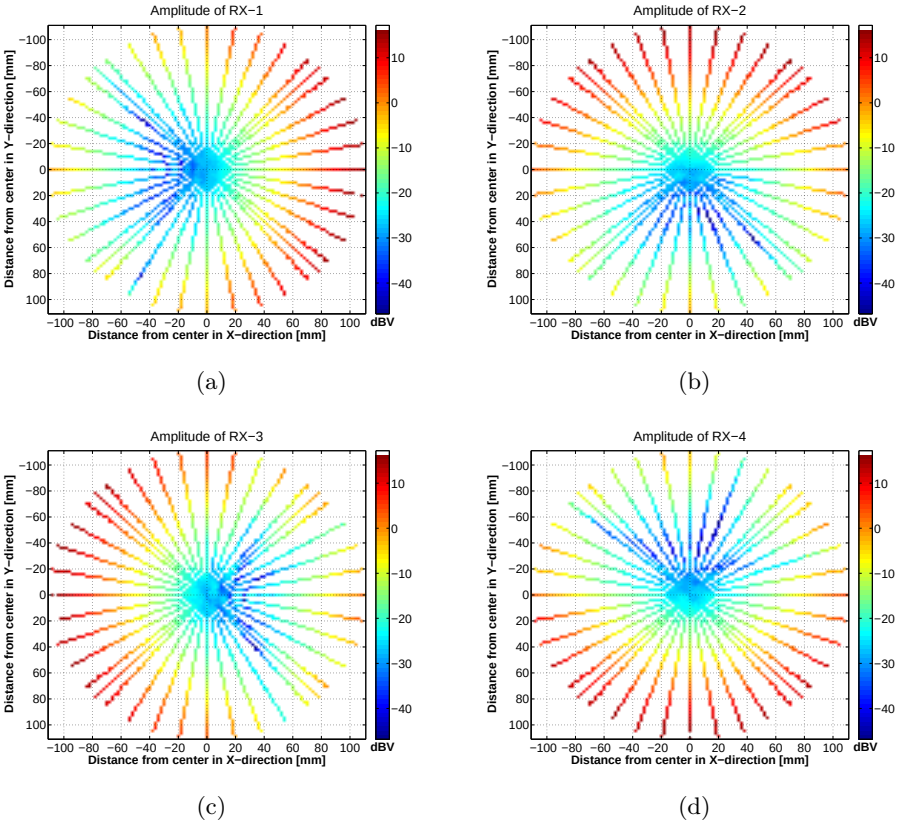

Figure D.7: Amplitude measurements in dBV scale of all the receivers as function of the internal antenna location inside the inner cylinder. (a) shows the amplitude for RX-1, (b) for RX-2, (c) for RX-3 and (d) for RX-4.

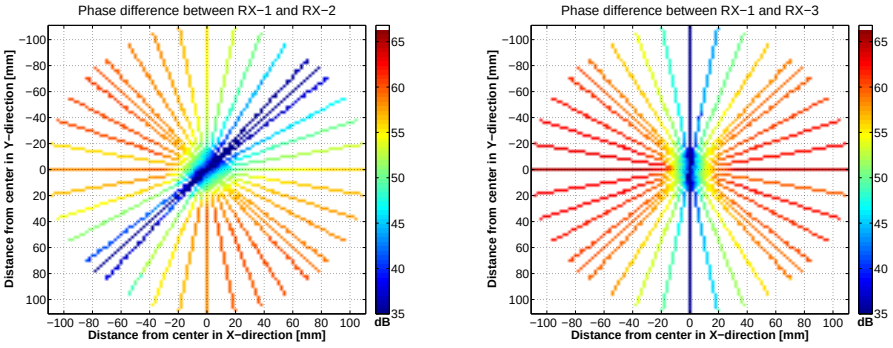

(a)

(b)

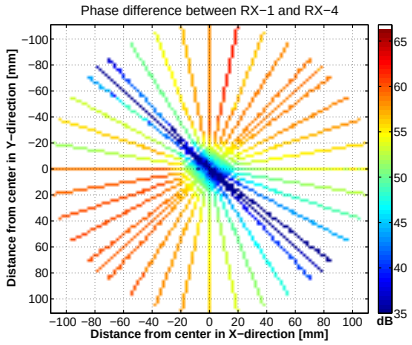

(c)

Figure D.8: Phase measurements in dBV scale as function of the internal antenna location inside the inner cylinder. (a) shows for the RX-2 - RX-1, (b) shows for the RX-3 - RX-1 and (c) shows for the RX-4 - RX-1

Patent Application 1 [PA1]

Ingestible Capsule for Remote Controlled Release of a Substance

Sævar Þór Jónasson

Patent Office	:	European Patent Office
Priority Date	:	3. October 2012

(12) INTERNATIONAL APPLICATION PUBLISHED UNDER THE PATENT COOPERATION TREATY (PCT)

(19) World Intellectual Property Organization
International Bureau

(43) International Publication Date
10 April 2014 (10.04.2014)

WIPO | PCT

(10) International Publication Number
WO 2014/053352 A1

(51) **International Patent Classification**:
A61M 31/00 (2006.01) ***H01P 1/203*** (2006.01)
A61K 9/48 (2006.01)

(21) **International Application Number**:
PCT/EP2013/069788

(22) **International Filing Date**:
24 September 2013 (24.09.2013)

(25) **Filing Language**: English

(26) **Publication Language**: English

(30) **Priority Data**:
12187095.0 3 October 2012 (03.10.2012) EP

(71) **Applicant**: **DANMARKS TEKNISKE UNIVERSITET** [—/DK]; Anker Engelundsvej 1, Bygning 101A, 2. sal, DK-2800 Kgs. Lyngby (DK).

(72) **Inventor**: **JÓNASSON, Sævar Þór**; Kagsåkollegiet 234, DK-2730 Herlev (DK).

(74) **Agent**: **OLSEN, Henrik Bagger**; Guardian IP Consulting I/S, Diplomvej, Building 381, DK-2800 Kgs. Lyngby (DK).

(81) **Designated States** *(unless otherwise indicated, for every kind of national protection available)*: AE, AG, AL, AM, AO, AT, AU, AZ, BA, BB, BG, BH, BN, BR, BW, BY, BZ, CA, CH, CL, CN, CO, CR, CU, CZ, DE, DK, DM, DO, DZ, EC, EE, EG, ES, FI, GB, GD, GE, GH, GM, GT, HN, HR, HU, ID, IL, IN, IS, JP, KE, KG, KN, KP, KR, KZ, LA, LC, LK, LR, LS, LT, LU, LY, MA, MD, ME, MG, MK, MN, MW, MX, MY, MZ, NA, NG, NI, NO, NZ, OM, PA, PE, PG, PH, PL, PT, QA, RO, RS, RU, RW, SA, SC, SD, SE, SG, SK, SL, SM, ST, SV, SY, TH, TJ, TM, TN, TR, TT, TZ, UA, UG, US, UZ, VC, VN, ZA, ZM, ZW.

(84) **Designated States** *(unless otherwise indicated, for every kind of regional protection available)*: ARIPO (BW, GH, GM, KE, LR, LS, MW, MZ, NA, RW, SD, SL, SZ, TZ, UG, ZM, ZW), Eurasian (AM, AZ, BY, KG, KZ, RU, TJ, TM), European (AL, AT, BE, BG, CH, CY, CZ, DE, DK, EE, ES, FI, FR, GB, GR, HR, HU, IE, IS, IT, LT, LU, LV, MC, MK, MT, NL, NO, PL, PT, RO, RS, SE, SI, SK, SM, TR), OAPI (BF, BJ, CF, CG, CI, CM, GA, GN, GQ, GW, KM, ML, MR, NE, SN, TD, TG).

Published:

— *with international search report (Art. 21(3))*

WO 2014/053352 A1

(54) **Title**: INGESTIBLE CAPSULE FOR REMOTE CONTROLLED RELEASE OF A SUBSTANCE

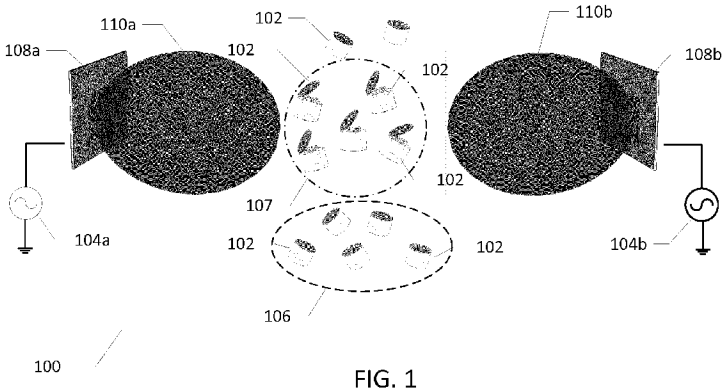

FIG. 1

(57) **Abstract**: The application relates to an ingestible capsule (102) for delivery of a substance e.g. a pharmaceutical drug, to a human or animal. The ingestible capsule comprises a capsule wall structure (202) forming a substantially sealed reservoir or lumen holding the substance (204). An electrical resonance structure, responsive to microwave electromagnetic radiation, is attached to a first wall portion of the capsule wall structure which comprises a lossy dielectric material. At least a predetermined segment of the first wall portion is heated by received microwave electromagnetic radiation to trigger a release mechanism of the ingestible capsule.

INGESTIBLE CAPSULE FOR REMOTE CONTROLLED RELEASE OF A SUBSTANCE

The present invention relates to an ingestible capsule for delivery of a substance e.g. a pharmaceutical drug, to a human or animal. The ingestible capsule comprises a capsule wall structure forming a substantially sealed reservoir or lumen holding the substance. An electrical resonance structure, responsive to microwave electromagnetic radiation, is attached to a first wall portion of the capsule wall structure which comprises a lossy dielectric material. At least a predetermined segment of the first wall portion is heated by received microwave electromagnetic radiation to trigger a release mechanism of the ingestible capsule.

BACKGROUND OF THE INVENTION

Ingestible capsules such as pharmaceutical drug capsules with controlled release of a substance held in a capsule reservoir are known in the art. Various kinds of waves have been used or proposed to externally trigger a release mechanism in the drug capsule such as ultrasound, light waves or alternating low-frequency magnetic fields. Suitable antenna structures have been mounted in, or on, the drug capsule for receipt of the relevant type of waves inside the patient's organism.

However, the application of ultrasound waves heats organs and tissue of the patient under treatment. Too much heat damages cells and causes burns. Light-sensitive chemical compounds have been developed that react to the presence of (laser) light. The clear disadvantage of the latter concept is that light is only able of penetrating a few millimetres below the patient's skin since light propagation in human tissue suffers from very high losses. Alternating low-frequency magnetic fields are widely used for controlled drug delivery or release. In this connection, the applied magnetic fields are of sufficiently low frequency to be considered de-coupled from the electric field. However, magnetic fields are extremely hard to focus due the low excitation frequency and correspondingly low resonance frequency of the antenna structure attached to the drug capsule. Hence, it is not possible to focus an alternating magnetic field to a specific portion of the patient's body.

Furthermore, receipt of the alternating magnetic field also requires a relatively complex electronic receiving circuit mounted inside the drug capsule. The receiving circuit of prior art capsules converts the received magnetic field to a resonating voltage or current signal in the receiving circuit that dissipates power in a resistive heating element.

U.S. 2012/116358 A1 discloses an ingestible drug capsule for delivering a pharmaceutical substance. The drug capsule includes a drug compartment with a window. The window is sealed by a foil with an embedded heating wire. The foil breaks along the heating wire when the latter is heated and expels the drug. The foil is made of a material such as LDPE that breaks when heated above a threshold temperature. The heating wire is heated by the supply of an intense electrical pulse supplied by a battery or capacitor of an electronics module inside the drug capsule.

WO 2008/059728 A1 discloses a drug capsule for dispensing a medicament to the digestive tract. A permanent magnet based drive system removes a plug that releases the medicament by a dispensing command. The drug capsule comprises an inductor resonator responsive to low-frequency magnetic fields to energize a complex electronic circuit of the drive system that pushes the plug out.

CN 200984246Y discloses an ingestible drug capsule for delivering a pharmaceutical substance to a chosen location in the alimentary tract of humans. The drug capsule includes a receiving circuit for receipt of applied electromagnetic radiation for remote control of drug release. The receiving structure may include a coiled coupling antenna embedded in an outer cylindrical wall structure of the drug capsule. The frequency of the applied electromagnetic radiation is specified as larger than 100 kHz. The drug release mechanism includes a movable piston arranged in a cylindrical drug reservoir inside the drug capsule and locked by a low melting point polymeric wire. A micro-thermal resistor, coupled to the receiving circuit, is heated by the received electromagnetic radiation and is operative to melt the locking wire which in turn releases the movable piston and expels the drug.

U.S. 6,632,216 B2 discloses an ingestible drug capsule for delivering a pharmaceutical substance to a chosen location in the gastrointestinal tract (GI tract) of humans.

The drug capsule includes a receiving structure for receipt of electromagnetic radiation for remote control of drug release. The receiving structure may include a coiled antenna wire including 60-100 turns and embedded in an outer cylindrical wall structure of the capsule as illustrated. The frequency of the applied electromagnetic radiation is specified as limited to the range 1–14 MHz. The drug release mechanism includes a movable piston arranged in a cylindrical drug reservoir inside the drug capsule and locked by a thread of sharp melting point material. A resistor heater is heated by the received electromagnetic radiation and is operative to melt the thread which releases the movable piston and expels the drug.

Hence, it would be highly desirable to provide a source of wave radiation with sufficient focusing capability to allow selective irradiation of a specific target area or volume of the patient's body. In this manner, release of the drug or other substance from the drug capsule can be confined to a specific region of the patient's body and be released to the target volume at a desired point in time. The radiation should preferably be capable of penetrating deeply into the patient's body with sufficient strength to be picked-up by a practical antenna structure on the drug capsule and trigger drug release.

It would desirable provide an antenna structure which is responsive to microwave electromagnetic radiation to reduce the size of the antenna structure and thereby reduce dimensions of the controlled release ingestible capsule. It would likewise be desirable to eliminate complex electronic circuitry inside the drug capsule and eliminate the need for energy storage devices such as batteries and capacitors associated with energizing heating wires.

The present invention addresses these problems and numerous others as described in further detail below.

SUMMARY OF THE INVENTION

A first aspect of the invention relates to an ingestible capsule for delivery of a substance to a human or animal. The ingestible capsule comprises:

-a capsule wall structure forming a substantially sealed reservoir or lumen holding the substance,

an electrical resonance structure attached to a first wall portion of the capsule wall structure and responsive to microwave electromagnetic radiation by generation of an alternating electric field,

the first wall portion comprising a lossy dielectric material absorbing energy from the alternating electric field to heat at least a predetermined segment of the first wall portion,

a release mechanism responsive to a predetermined temperature increase of the predetermined segment of the first wall portion.

In the present specification the term 'microwave electromagnetic radiation' refers to electromagnetic waves with a frequency above 100 MHz. In the frequency range above 100 MHz, the magnetic field and the electric field become coupled which is a property that allows focusing of the emitted microwave electromagnetic radiation to particular portions of the patient's body by appropriate interference mechanisms. The interference may be accomplished by emitting microwave electromagnetic radiation from two or more cooperating transmitting antennas with appropriate phase relationship.

The focusing capability of the microwave electromagnetic radiation utilized in accordance with the present invention and the responsiveness of the electrical resonance structure thereto allow selective irradiation of a specific target area or volume of the patient's body from remotely located microwave transmitting antenna structure(s). In this manner, the controlled release of a pharmaceutical agent, drug or other substance can be confined to the target volume of the patient's body such as a particular portion of a gastrointestinal tract. The release of the pharmaceutical agent, drug or other substance can furthermore be accomplished externally or remotely at any desired point in time by applying the microwave electromagnetic radiation. The substance may comprise a pharmaceutical drug in solid, liquid or powder form. The substance may also be held in a plurality of smaller containers.

The skilled person will understand that the first wall portion of the capsule wall may be a lid, side wall, bottom portion or any other suitable wall portion of the capsule wall structure possessing sufficient dimensions to support the electrical resonance structure.

The skilled person will appreciate that the term 'ingestible' as utilized herein means that the drug capsule is shaped and sized such that the capsule can be swallowed by a human or animal. The skilled person will appreciate that the ingestible drug capsule therefore in some embodiments may be sufficiently small to allow injection into the bloodstream of the human or animal, e.g. a patient undergoing a medical procedure. In the latter embodiment, the pharmaceutical agent or drug may be controllably released near or inside selected organs or target objects (e.g. a cancerous tumour) of the patient under treatment.

In accordance with the present invention, the first wall portion comprises a lossy dielectric material. This lossy dielectric material is arranged to absorb energy from the alternating electric field generated in the electrical resonance structure in response to receipt of the microwave electromagnetic radiation, in particular microwave electromagnetic radiation located at or close to a resonance frequency of the electrical resonance structure. The alternating electric field induces electric currents in the predetermined segment of the first wall portion due to its electric conductance as described below. The electric currents cause power loss in, and heating of, the predetermined segment. Depending on the shape and size of electrical resonance structure the predetermined segment may comprise smaller or larger area of the first wall portion. In some embodiments, the predetermined segment is essentially confined to one or more gaps in the electrical resonance structure attached to the first wall portion.

The direct heating induced by the electrical resonance structure of the lossy dielectric material of the capsule wall of the ingestible capsule in response to externally applied microwave electromagnetic radiation eliminates the need of electronic RF receiving circuits, electronic components and energy storage devices like batteries or capacitors as widely used in prior art devices as previously described. This feature leads to significant size and costs reductions, simplification of electric circuitry, improved reliability, removal of patient safety concerns and other benefits in the present ingestible capsule.

In the present patent specification the term 'lossy dielectric material' refers to a material with a specific electrical conductance, σ, between 0.01 and 1000 Sm^{-1}, more

preferably between 0.02 and 10 Sm^{-1}, and even more preferably between 0.05 and 0.2 Sm^{-1}, at a frequency of operation such as at the resonance frequency of the electrical resonance structure . Preferably, the lossy dielectric material possesses in addition a relative permittivity, ϵ_r, between 1.0 and 80 such as between 2.0 and 15, at the frequency of operation. Experimental results obtained by the present inventor suggest that these ranges of electrical conductance, σ, of the lossy dielectric material enable the alternating electric field to dissipate sufficient power in the lossy lid material to produce useful temperature increases for triggering the release mechanism as described below in additional detail.

The lossy dielectric property of the substrate or base material may be achieved in numerous ways. In one embodiment, the base material comprises a bio-degradable polymer mixed with a conductive powder, such as a metallic powder, of sufficient density to reach the above-mentioned preferred ranges of specific electrical conductance of the lossy dielectric material. Other types of bio-degradable dielectrics or semiconductors doped with materials which increase or decrease the electric conductivity such that the resulting conductivity falls within the above specified ranges could also be used.

According to a preferred embodiment, the polymer comprises a bio-compatible polymer, preferably a temperature sensitive bio-compatible polymer, which abruptly changes its chemical or mechanical properties within a predetermined temperature span such as a span less than 10, 5 or 3 °C. The chemical or mechanical properties that changes within the predetermined temperature span may be properties like adhesion, viscosity or permeability. In one preferred embodiment, the polymer may comprise a semi-crystalline graft copolymer (Intelimer®).

The temperature increase induced in the predetermined segment of the first wall portion may trigger the release mechanism in various ways. In a number of useful embodiments, the release mechanism comprises a transition of the predetermined segment of the first wall portion from a first chemical state to a second chemical state or a transition from a first mechanical state to a second mechanical state. The transition from the first to the second state takes place within a predetermined temperature span such as a temperature span of less than 10 °C, or less than 5 °C, or

even more preferably less than 3 °C. In these embodiments, the temperature increase leads to a change of the chemical or mechanical state or property of the segment itself. In the manner, the release mechanism is directly triggered by the heating of the predetermined segment of the first wall portion. The transition between the first and second states of the predetermined segment of the first wall portion may include a change to numerous physical properties like adhesion, viscosity, state (e.g. from solid to liquid) or permeability etc.

In a number of alternative and likewise useful embodiments, the temperature increase in the predetermined segment of the first wall portion is conveyed by thermal coupling to a separate release mechanism. In one such embodiment, the separate release mechanism comprises a structure thermally, coupled to the predetermined segment of the first wall portion, transiting from a first chemical state to a second chemical state or transiting from a first mechanical to a second mechanical state. In one such embodiment, a layer of a temperature sensitive adhesive agent is interposed between the first wall portion and the residual capsule wall structure to firmly bond these at room temperature and at temperatures up to about 37 °C. The bond between the temperature sensitive adhesive agent and the first wall portion couples these thermally. The temperature sensitive adhesive agent has a melting point several degrees above 37 °C for example around 40 °C. In effect, the bond between the above-described wall structures of the ingestible capsule is released by the melting of the temperature sensitive adhesive agent once the temperature thereof exceeds 40 °C and the substance captured or enclosed in the ingestible capsule released. The skilled person will understand that the first wall structure may comprise a lid, sidewall or bottom portion of the present ingestible capsule.

The electrical resonance structure functions as a receiving antenna for the microwave electromagnetic radiation emitted by the above-described transmitting antenna structure. The electrical resonance structure may be shaped and sized in numerous ways to efficiently receive the microwave electromagnetic radiation above 100 MHz. The electrical resonance structure is preferably shaped and sized to provide a resonance frequency higher than 100 MHz, preferably in the range 300 MHz - 3 GHz, such that the frequency of applied microwave electromagnetic radiation can be

tuned to the selected resonance frequency and the previously described focusing capability of electromagnetic waves in this frequency range exploited.

According to one embodiment, the electrical resonance structure comprises a metallic loop structure with one or more gap(s). The metallic loop structure tend to focus the alternating electrical field across the gap(s) such that the above-discussed predetermined segment of the first wall portion can be efficiently heated by arranging the segment in the gap(s), or at least proximate to the gap(s). Furthermore, the electrical resonance structure may be formed as a substantially flat metallic structure deposited on the first wall portion of the ingestible capsule such that any space occupation can be largely neglected. The maximum dimension will vary depending on the selected resonance frequency of the metallic loop structure, but may be less than 15 mm such as between 0.2 mm and 10 mm.

In a particularly useful embodiment of the electrical resonance structure, the metallic loop structure comprises a split-ring resonator. Split-ring resonators are very compact resonance structures and typically resonate when an electrical size of the structure is less than λ/10 (λ being the wavelength of the microwave electromagnetic radiation in the first wall material (in comparison to typical microwave resonance structures or antennas that resonate at wavelengths of the electrical size of λ/2. The small electrical size of split-ring resonators makes these highly advantageous as receiving antennas in the present ingestible drug capsule compared to λ/2 antenna structures because dimensions of the electrical resonance structure, and thereby dimensions of the ingestible drug capsule, are markedly smaller for a given resonance frequency. Or stated in an alternative way, for a given size of the ingestible drug capsule, the frequency of the applied microwave electromagnetic radiation can be significantly lowered which enables deeper penetration into the patient's body

The split-ring resonator may comprise one or more gaps and generally exhibit numerous different more or less complex shapes such as those depicted in the accompanying figures. The split-ring resonator preferably comprises at least two curved and substantially continuous metallic strips or traces each interrupted by a short gap, i.e. each strip possessing a semi-closed shape. In one embodiment, the split-ring resonator comprises a pair of co-axially arranged loops of metal. The pair

of loops may in principle have an arbitrary shape for example substantially rectangular, oval, circular etc. In one embodiment, the pair of co-axially arranged loops comprises an inner substantially circular ring with a first gap arranged therein and an outer substantially circular ring with a second gap arranged therein. The first and second gaps are rotationally displaced relative to each other by an angle of about 180 degrees. The height of each of the first and second gaps may lie between 0.01 mm and 0.75 mm, such as between 0.1 mm and 0.5 mm, depending on the maximum dimension of the resonator structure. In another embodiment, the electrical resonance structure is formed as a substantially flat spiral conductor structure comprising a largely continuous gap formed between facing edges of individual revolutions or arms of the spiral.

In a preferred embodiment of the present ingestible capsule, the predetermined segment is formed as a bridge structure interconnecting otherwise unattached areas of the first capsule wall portion. The bridge structure is placed in the gap of the electrical resonance structure such that the bridge becomes heated and melts or dissolves by the temperature increase. In one such embodiment, the segment of the lossy dielectric material forms a bridge between an inner unattached part of the first capsule wall portion arranged inside the electrical resonance structure and an outer attached part of the first wall portion arranged outside the electrical resonance structure. Hence, in the latter embodiment the melting of the bridge detaches the inner unattached part of the first capsule wall portion to open up the sealed reservoir or lumen of the ingestible capsule and release the substance held therein.

To reach practical dimension of the present ingestible capsule there are limits to the maximum dimensions and form of the capsule wall structure. The constraints of the capsule dimensions depend on the particular application in question and naturally also impose certain restrictions on the maximum dimension and shape of the electrical resonance structure. In a number of useful embodiments, the electrical resonance structure is formed as a substantially flat structure having a maximum dimension less than 15 mm.

A second aspect of the invention relates to a method of delivering a substance held in a ingestible capsule according to any of the preceding claims to the alimentary

canal of human or animal. The method comprising steps of:

a) causing the human or animal to ingest the ingestible capsule,

b) placing the human or animal in predetermined location of a support,

c) generating microwave electromagnetic radiation by a microwave antenna structure,

d) adjusting an excitation frequency of the microwave electromagnetic radiation to a resonance frequency of the electrical resonance structure attached to the wall structure of the ingestible capsule,

e) directing the microwave electromagnetic radiation to a target portion of the alimentary canal to heat at least the predetermined segment of the first wall portion and increase the temperature of the lossy dielectric material to trigger the release mechanism. The excitation frequency of the microwave electromagnetic radiation is preferably larger than 100 MHz for the reasons discussed above.

BRIEF DESCRIPTION OF THE DRAWINGS

Preferred embodiments of the invention will be described in more detail in connection with the appended drawings, in which:

FIG. 1 illustrates schematically a system for controlled release of a substance held in an ingestible capsule,

FIG. 2 is a 3D perspective view of an ingestible drug capsule in accordance with a first embodiment of the invention,

FIG. 3A) is a schematic top view of the lid of the pharmaceutical drug capsule depicted on FIG. 2 illustrating geometry of the electrical resonance structure according to the first embodiment of the invention,

FIG. 3B) shows simulated power loss density across a surface of the lid of the pharmaceutical drug capsule for the case of maximum temperature increase as illustrated in FIG. 4A),

FIG. 4A) is a graph depicting maximum temperature as a function of specific electrical conductance for a wide range of conductivities of the lid material of the pharmaceutical drug capsule depicted on FIG. 2, for relative permittivities of 3 and 6,

FIG. 4B) is a graph depicting the same variables as FIG. 4A) but zoomed to a narrow range of values of the specific electrical conductance of the lid material, for relative permittivities 1.5, 3, 6 and 12,

FIG. 5) is a side perspective view of the lid of the pharmaceutical drug capsule depicted on FIG. 2 with dimensions of the electrical resonance structure added; and FIGS. 6A) and 6B) are respective schematic top views of alternative electrical resonator designs.

DETAILED DESCRIPTION OF PREFERRED EMBODIMENTS

FIG. 1 illustrates schematically a set-up or system allowing externally controlled release of a pharmaceutical drug or other substance from ingestible drug capsules 102 held in the alimentary canal of a patient. In practice, the patient subjected to the treatment procedure may be fixed at a predetermined location such as arranged on an examination table or bed. The fixed placement of the patient ensures that applied microwave electromagnetic radiation is directed to the target or intended portion of the alimentary canal. The overall procedure comprises steps of causing the patient ingest a plurality of the ingestible capsules or containers 102. Thereafter, the patient is placed at a predetermined location of a support as explained above. The support may be placed between a pair of cooperating microwave antenna structures 108a, 108b that each emits directive microwave electromagnetic radiation as schematically illustrated by directivity patterns 110a, 110b. The distance between the patient and each of the microwave antenna structures 108a, 108b may lie between 1 and 3 meters under typical circumstances but may be smaller or larger in other situations.

A first and a second RF source 104a, 104b, respectively, supply the respective RF signals to the microwave antenna structures 108a, 108b which emits the resulting microwave electromagnetic radiation towards the target area of the patient's alimentary canal (not shown). The patient's alimentary canal comprises the schematically illustrated upper and lower volumes 107, 106 wherein the upper volume is the target area for drug delivery in the present example. In the present embodiment, the excitation frequency of the microwave electromagnetic radiation has been set to about 1.8 GHz which matches the resonance frequency of the electrical resonance structure attached to, or integrated with, of the ingestible drug capsule (refer to FIG. 2). Furthermore, by adjusting a phase between the RF signals, the constructive interference pattern of the microwave antenna structure can be adjusted. The external excitation antenna(s) should be designed to accommodate for transmissions of electromagnetic waves at the resonance frequency of the chosen electrical resonance structure(s) on the ingestible capsule wall structure.

As mentioned above, each of the ingestible capsules 102 comprises one or more miniscule electrical resonance structure(s) (attached to a lid and/or other capsule wall structure(s). The miniscule electrical resonance structure(s) functions as receiving antenna(s) for the applied microwave electromagnetic radiation as described in further detail below. By directing the microwave electromagnetic radiation 110a, 110b to the target volume or portion 107 of the alimentary canal, a substantial alternating electric field is generated in each of the electrical resonance structures of the capsules 102 held in the target volume. The electrical field increases the temperature of selected segments or portions of a lossy dielectric material which functions as a base material of the lid (212 of FIG. 2) as explained in additional detail below. The heating of these selected segments or portions of lid triggers a release mechanism of the capsule 102 which opens the lid and frees the encapsulated drug to the patient's organism in the target volume 107. On the other hand, lids of the ingestible capsules 102 held outside the target volume, e.g. within the illustrated volume 106, are not heated in any noticeable manner, or least not enough to trigger the release mechanism, due to the lower intensity of the microwave electromagnetic radiation 110a, 110b in this volume. Hence, the applied microwave electromagnetic radiation is focused at the desired target volume of the patient allowing a selective and remotely controlled activation of the ingested drug capsules 102.

FIG. 2 is a schematic 3D perspective view of a single one of the above-described ingestible drug capsules 102 in accordance with a first embodiment of the invention. The ingestible drug capsule 102 comprises a capsule wall structure 202 forming a substantially sealed reservoir or lumen holding the substance 204 that is intended for delivery a human or animal. The capsule wall structure 202 accordingly forms the exterior barrier of the ingestible drug capsule 102 and should preferably be shaped and sized to allow trouble free ingestion by patients. The substance comprises a drug in solid, liquid, gaseous or powder form in the present embodiment of the invention. The skilled person will understand that numerous other types of substances may be held in the drug capsule. The capsule wall structure 202 comprises a lid 210 that forms a first wall portion of the capsule wall structure. The lid 210 comprises an attached split-ring resonator comprising pair of co-axially arranged substantially annular rings or loops 206, 208 of metal, preferably essentially non-magnetic metal.

The split-ring resonator comprises an inner substantially annular ring 208 with a first gap 209 arranged therein and an outer substantially circular ring 206 with a second gap 207 arranged therein. The first and second gaps 207, 209 are rotationally displaced relative to each other with an angle of about 180 degrees.

The split-ring resonator functions as an antenna structure that is receptive to externally applied microwave electromagnetic radiation in a certain predefined frequency range or band. In the present embodiment, the dimensions of the split-ring resonator are chosen such that the above-mentioned resonance frequency of 1.8 GHz is achieved as described below in additional detail. Split-ring resonators are very compact electromagnetic wave resonance structures and typically resonate when an electrical size of the structure is less than λ/10 in comparison to typical microwave resonance structures or antennas that resonate at the electrical size of λ/2. The small electrical size of split-ring resonators makes these highly advantageous for application in remote drug capsule activation compared to λ/2 antenna structures because dimensions of the electrical resonance structure, and thereby dimensions of the ingestible drug capsule, are markedly smaller for a given resonance frequency the electrical resonance structure. Or stated in an alternative way, for a given size of the ingestible drug capsule, the frequency of the applied microwave electromagnetic radiation can be significantly lower which enables deeper penetration into the patient's body.

The split-ring resonator is firmly attached or bonded to an outer surface of the lid 210 for example by an adhesive agent or by soldering etc. In one embodiment, the split-ring resonator may be fabricated by applying UV lithography and etching techniques to a suitable substrate material covered by a thin metallic layer. The substrate or base material of the lid comprises a lossy dielectric material with a specific electrical conductance, σ, between 0.01 and 1000 Sm-1, more preferably within a range between 0.07 and 0.12 Sm^{-1} for the reasons discussed below in additional detail. The lossy dielectric property of the substrate or base material may be achieved in numerous ways. In one embodiment, the base material comprises a biocompatible temperature sensitive polymer mixed with a conductive powder of sufficient density to reach the above-mentioned preferred ranges of specific electrical conductance. The temperature sensitive polymer may be a semi-crystalline graft copolymer (Intelimer®) which abruptly changes its chemical or mechanical proper-

ties like adhesion, viscosity or permeability, in response to a predetermined temperature increase. In one embodiment, the temperature sensitive polymer changes its adhesion within a temperature span less than 3 degree °C starting with strong adhesion below a temperature of 37 °C. The adhesive characteristics of the lid material changes from very strong below a temperature of 37 °C to very weak at or above 40 °C such that a bond between the lid 210 and the residual capsule wall structure 202 along the lid edge 206 is dissolved or eliminated and the lid 210 released. In another embodiment, the release mechanism comprises a lid, or other capsule wall structure, with a temperature dependent porosity. In this embodiment, the lid exhibits a porosity capable of withholding the pharmaceutical substance at a temperature at and below 37°C, but unable to do so at a higher temperature such as 40°C. The porosity of the porous lid material increases markedly above 40°C and the pharmaceutical substance is released from the capsule.

In response to exposure to the applied microwave electromagnetic radiation 110a, 110b at, or close to the, resonance frequency of the split-ring resonator, a strong alternating electric field is generated in the gaps 207, 209 of the annular rings or loops 206, 208 and in a separation between them. Due to the lossy property of the lid base material, the strong alternating electric field induces electric currents in selected portions or segments of the lid 210 where part of these currents are converted into power loss as illustrated by the power loss density map of the lid 210 on FIG. 3B. This power loss causes an overall increase of the temperature of the lid 210, and a particularly pronounced temperature increase in the lid segments in and close to the gaps 207, 209.

FIG. 3A) is a schematic top view of the lid 210 of the pharmaceutical drug capsule 102 depicted on Figs 1 and 2 for the purpose of cross-referencing the geometry of the electrical resonance structure with the simulated power loss density in FIG. 3B). FIG. 3B) shows the simulated power loss density across the lid surface for the case of maximum power dissipation as discussed in additional detail below in connection with FIG. 4A). The power loss density is mapped on a grey-black scale wherein completely black correspond to a power density on or above 100000 Wm^{-3}. The lightest discernible grey scale value corresponds to a power density about 17000 Wm^{-3}. It is evident that maximum power density is reached in the lid segments in or

close to the gaps 207, 209 such that the largest temperature increase of the lid structure 210 therefore occurs at these locations as well.

FIG. 4A) is a graph depicting the simulated maximum temperature of the lid 210 of the pharmaceutical drug capsule depicted above on Figs. 2 and 3 as a function of specific electrical conductance , σ, of the lid base material for two different relative permittivities, ϵ_r, of the lid material, as determined at the resonance frequency of the resonating structure. The depicted temperature behaviour of the drug capsule was analysed in the 3D electromagnetics (EM) simulation tool CST. Simulations of the optimal specific electrical conductance or conductivity for a given relative permittivity were performed in CST to find optimal parameters for the substrate material for inducing maximum temperature increase in the lid. CST was used for calculating the current- and power loss densities in the lid base material or substrate. These power loss densities are used as sources from which CST calculates thermal losses and the accompanying local lid temperature increase with a surrounding ambient air temperature of 37 °C.

For these simulations, the applied electromagnetic radiation was transmitted from a distance of 25 mm resulting in a 100 V/m plane wave, with an E-field component oriented across to the gaps 207, 209 of the spilt-ring resonator and an H-field component oriented normal to the lid 210. All relevant measurement parameters were kept constant throughout the simulation except for the relative permittivity and specific electrical conductance. The maximum temperature point of the lid substrate at each combination of relative permittivity, ϵ_r, and relative specific electrical conductance, σ, at the resonance frequency of the spilt-ring resonator is taken. The resonance frequency of the spilt-ring resonator was located at 1.8 GHz for the present design as previously mentioned.

The upper unbroken temperature curve depicts simulated maximum temperatures for the condition $\epsilon_r = 3$ and the dotted curve the same quantity for $\epsilon_r = 6$. The maximum temperature was found to be approximately 41.5 °C for a lid base material with $\epsilon_r = 3$ and σ = 0.07 S/m at the resonance frequency of 1.8 GHz. As indicated by the depicted temperature curves, substrate materials which are too conductive, i.e. having a large specific electrical conductance such as above 1000 S/m (Sm^{-1}), tend to

short-circuit the split-ring resonator (receiving antenna) and eliminate any resonance therein. On the other hand, lid materials that have very small specific electrical conductance dissipate very little power as indicated by the depicted temperature curves which rapidly approach 37 ◦C (no heating) for specific electrical conductance below approximately 0.01 Sm^{-1}. Consequently, it is evident that the optimal range for the specific electrical conductance of the lid material in the present embodiment lies approximately between 0.01 and 1000 Sm^{-1} which can been seen as an intermediate electrical conductance range in-between the conductance of good conductors (like copper with about $6*10^{7}$ Sm^{-1}) and bad conductors (like rubber with 10^{-14} Sm^{-1}). Lid materials exhibiting specific electrical conductance within the latter range can accordingly be considered lossy dielectric materials in the present context. This electrical conductance or conductivity range lies furthermore outside the specific electrical conductance provided by substrates utilized in ordinary printed circuit technology. These are generally based on relatively low-loss substrates like glass-epoxy, ceramics, etc.

FIG. 4B) is a graph depicting a simulated maximum temperature of the lid 210 similar to FIG. 4A) above, but zoomed to a narrow range of specific electrical conductance, σ, of the lid material around the maximum temperature peak depicted on FIG. 4A) above. Furthermore, the graph also includes simulated temperature curves for four different relative permittivities, ϵ_r, of the lid material ranging from 1.5 to 12 as indicated by the curve line type on the graph. It is evident that all temperature curves exhibit a temperature peak within a relatively narrow range of specific electrical conductance from σ = 0.07 to about 0.12 Sm^{-1} despite the varying maximum temperatures. It is also evident that for the present lid design, the optimum value for ϵ_r is either about 3 or about 12 even though the entire range from 1.5 to 12 provides a pronounced and useful temperature increase of the lid.

FIG. 5) is a side perspective view of an experimental lid structure, suitable for a large-sized pharmaceutical drug capsule, with dimensions added. The dimensions of the split-ring resonator are:

r [mm]	*s* [mm]	*w* [mm]	*g* [mm]	*t* [mm]
5.1	0.3	0.3	0.2	1.5

Accordingly, the maximum dimension (a diameter between outer edges of the outer ring 206) of the split-ring resonator can be computed from the depicted geometry as: 2 * (r + 2*w + s) = 12 mm. However, the above-listed dimensions were primarily chosen for fabrication convenience in connection with experimental measurements of orientation effects on the experimental split-ring resonator. Accordingly, practical dimensions may be considerably smaller in numerous applications of the present ingestible capsule.

FIG. 6A) is schematic top view of a first alternative electrical resonance structure 600 attached to the first wall portion of the ingestible drug capsule discussed above. The resonator 600 is formed as a substantially flat and circular metallic structure 608 with a pair of radially projecting legs placed opposite to each other. The radially projecting arms face each other across a gap 609 formed between facing straight edges of the legs. The lossy dielectric material of the first wall portion is arranged in, or adjacent (e.g. below), the first wall portion such that the entire continuous gap 609 is heated leading to a more evenly distributed heating of the first wall portion compared to the localized heating at the gaps of the earlier discussed split-ring resonator as depicted on FIG. 3B.

FIG. 6B) is schematic top view of a second alternative electrical resonance structure 650 for application as electrical resonance structure on the first wall portion of the ingestible drug capsule discussed above. The resonator 650 is formed as a substantially flat and continuous metallic spiral structure 658 with mating continuous gap 609 formed between facing edges of individual revolutions or arms of the spiral. The alternating electrical field is induced between facing segments of the revolutions across and along the continuous gap 659. The lossy dielectric material of the first wall portion is arranged in, or adjacent (e.g. below), the first wall portion such that the entire continuous gap 659 becomes heated leading to a more evenly distributed heating of the first wall portion compared to the localized heating at the gaps of the earlier discussed split-ring resonator as depicted on FIG. 3B.

CLAIMS

1. An ingestible capsule for delivery of a substance to a human or animal, comprising:

a capsule wall structure forming a substantially sealed reservoir or lumen holding the substance,

an electrical resonance structure attached to a first wall portion of the capsule wall structure and responsive to microwave electromagnetic radiation by generation of an alternating electric field,

the first wall portion comprising a lossy dielectric material absorbing energy from the alternating electric field to heat at least a predetermined segment of the first wall portion,

a release mechanism responsive to a predetermined temperature increase of the predetermined segment of the first wall portion.

2. An ingestible capsule according to claim 1, wherein the lossy dielectric material has a specific electrical conductance, σ, between 0.01 and 1000 Sm^{-1}, more preferably between 0.05 and 0.2 Sm^{-1}.

3. An ingestible capsule according to claim 2, wherein the lossy dielectric material has a relative permittivity, ϵ_r, between 1.0 and 80.

4. An ingestible capsule according to any of the preceding claims, wherein the electrical resonance structure is shaped and sized to provide a resonance frequency higher than 100 MHz.

5. An ingestible capsule according to claim 4, wherein the electrical resonance structure is shaped and sized to provide a resonance frequency between 300 MHz and 3 GHz.

6. An ingestible capsule according to any of the preceding claims, wherein the release mechanism comprises a transition of the predetermined segment of the first wall portion from a first chemical state to a second chemical state or a transition from a first mechanical state to a second mechanical state.

7. An ingestible capsule according to any of the preceding claims, wherein the release mechanism comprises a structure, thermally coupled to predetermined segment of the first wall portion, transiting from a first chemical state to a second chemical state or transiting from a first mechanical state to a second mechanical state.

8. An ingestible capsule according to any of the preceding claims, wherein the electrical resonance structure comprises a metallic loop structure with a gap.

9. An ingestible capsule according to claim 8, wherein the metallic loop structure comprises a split-ring resonator.

10. An ingestible capsule according to claim 9, wherein the split-ring resonator comprises a pair of co-axially arranged loops of metal

11. An ingestible capsule according to claim 10, wherein the pair of co-axially arranged loops comprises an inner substantially circular ring with a first gap arranged therein and an outer substantially circular ring with a second gap arranged therein; the first and second gaps being rotationally displaced relative to each other with an angle of about 180 degrees.

12. An ingestible capsule according to any of claims 8-11, wherein the predetermined segment of the first wall portion comprises lossy dielectric material arranged in one or more gap(s) of the electrical resonance structure.

13. An ingestible capsule according to any claims 6-12, wherein the first wall portion comprises a temperature sensitive polymer, such as a semicrystalline graft copolymer, changing chemical or mechanical properties, such as adhesion, viscosity or permeability, in response to the predetermined temperature increase.

14. An ingestible capsule according to any claims 7-13, wherein the first wall portion is attached to a residual portion of the capsule wall structure with a temperature sensitive adhesive agent.

15. A method of delivering a substance held in an ingestible capsule according to any of the preceding claims to the alimentary canal of human or animal, the method comprising steps of:

a) causing the human or animal to ingest the ingestible capsule,

b) placing the human or animal in predetermined location of a support,

c) generating microwave electromagnetic radiation by a microwave antenna structure,

d) adjusting an excitation frequency of the microwave electromagnetic radiation to a resonance frequency of the electrical resonance structure attached to the wall structure of the ingestible capsule,

e) directing the microwave electromagnetic radiation to a target portion of the alimentary canal to heat at least the predetermined segment of the first wall portion and increase the temperature of the lossy dielectric material to trigger the release mechanism;

wherein the excitation frequency of the microwave electromagnetic radiation is higher than 100 MHz.

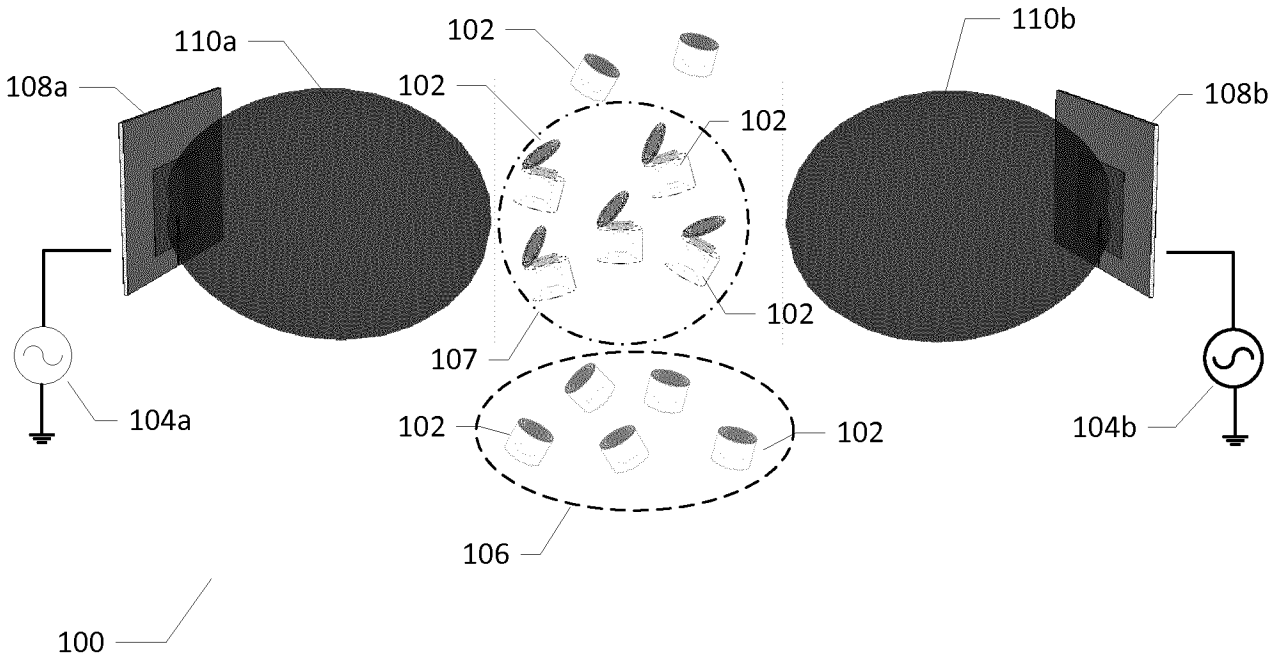
110a
102
110b
108a
102
102
108b
102
107
104a
102
102
104b
106
100

FIG. 1

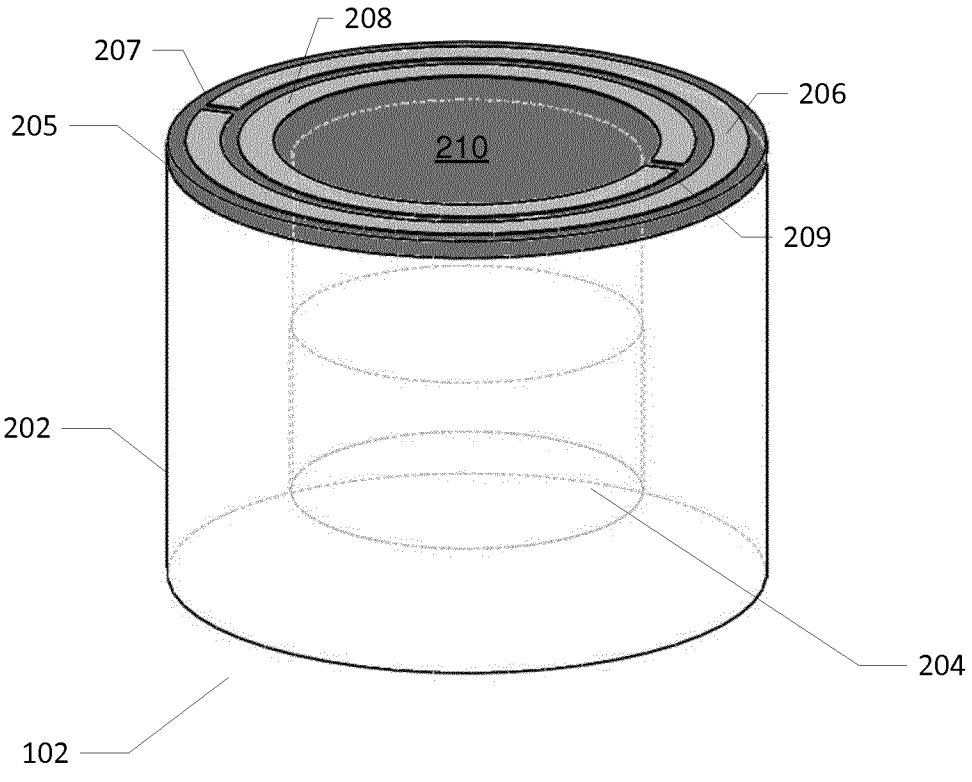

FIG. 2

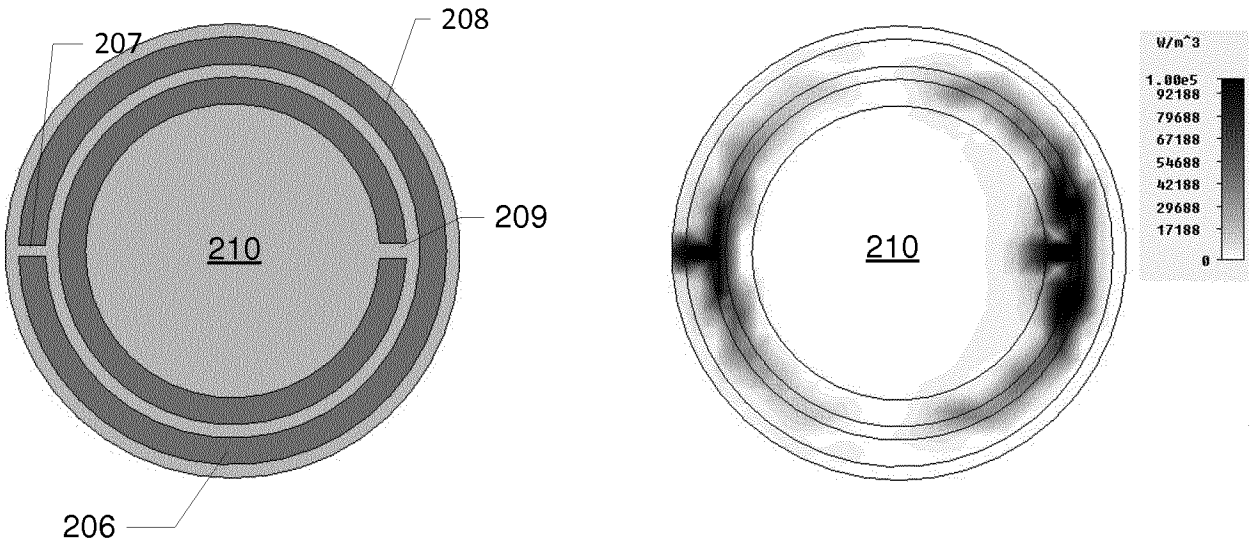
207
208
209
210
206
A)
210
W/m^3
1.00e5
92188
79688
67188
54688
42188
29688
17188
0
B)

FIG. 3

A)

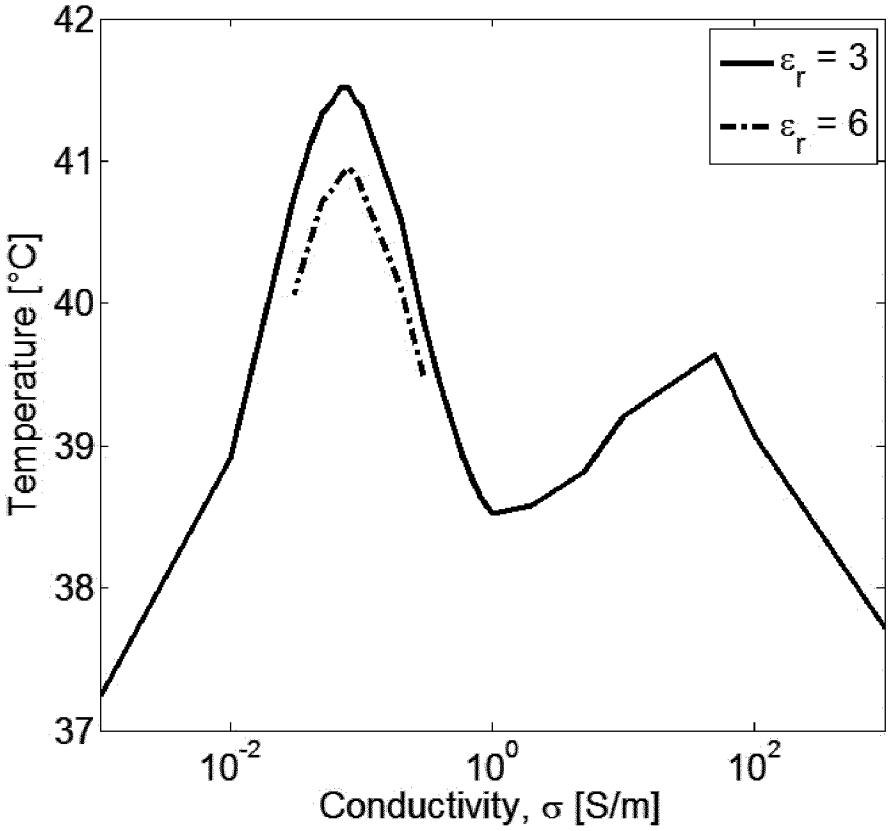
42
41
40
39
38
37
Temperature [°C]
10^{-2}
10^{0}
10^{2}
Conductivity, σ [S/m]
ε_r = 3
ε_r = 6

B)

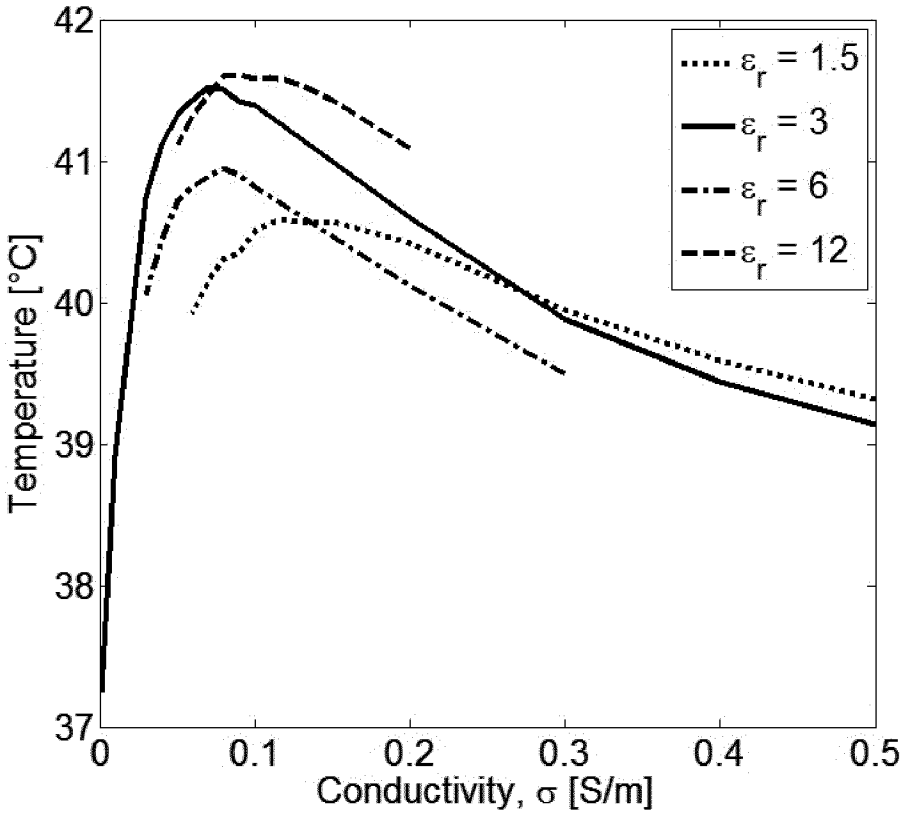
42
41
40
39
38
37
Temperature [°C]
0
0.1
0.2
0.3
0.4
0.5
Conductivity, σ [S/m]
ε_r = 1.5
ε_r = 3
ε_r = 6
ε_r = 12

FIG. 4

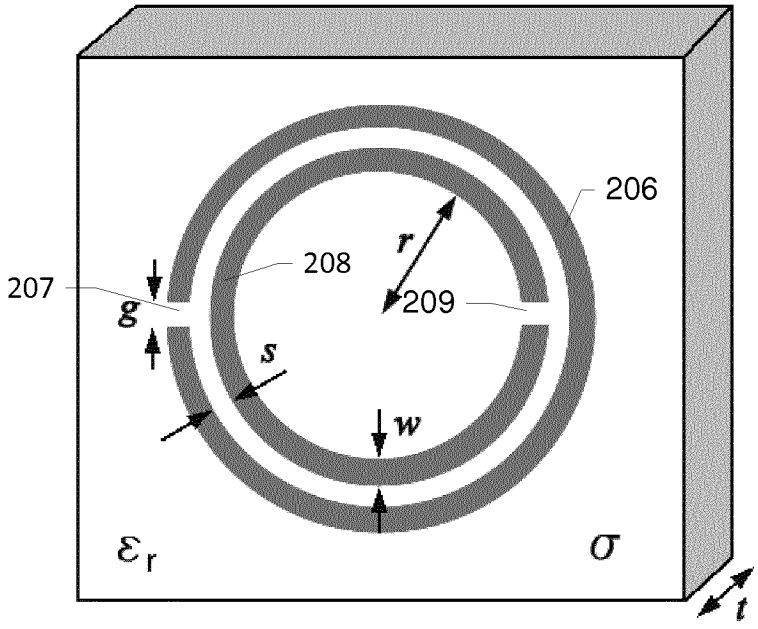

FIG. 5

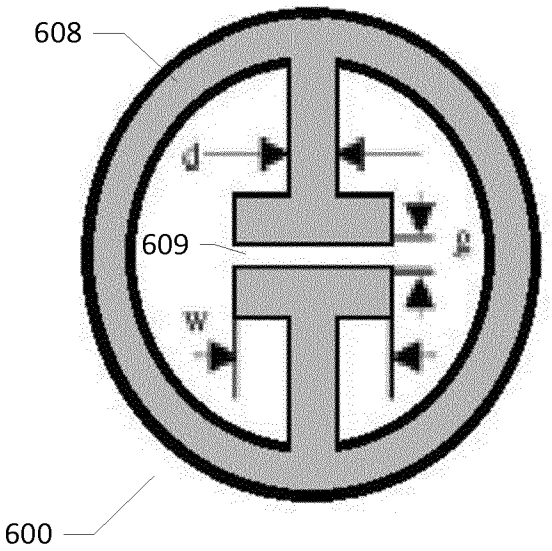

A)

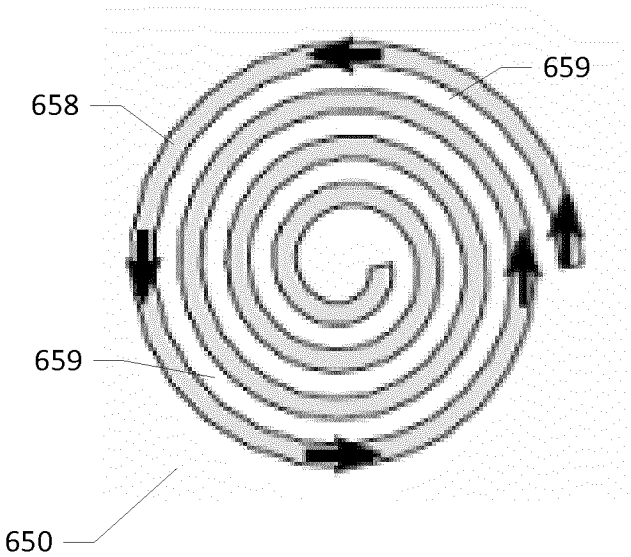

B)

FIG. 6

INTERNATIONAL SEARCH REPORT

International application No.
PCT/EP2013/069788

Box No. II Observations where certain claims were found unsearchable (Continuation of item 2 of first sheet)

This international search report has not been established in respect of certain claims under Article 17(2)(a) for the following reasons:

1. [X] Claims Nos.: 15
because they relate to subject matter not required to be searched by this Authority, namely:

Rule 39.1(iv) PCT - Method for treatment of the human or animal body by therapy

2. [ ] Claims Nos.:
because they relate to parts of the international application that do not comply with the prescribed requirements to such an extent that no meaningful international search can be carried out, specifically:

3. [ ] Claims Nos.:
because they are dependent claims and are not drafted in accordance with the second and third sentences of Rule 6.4(a).

Box No. III Observations where unity of invention is lacking (Continuation of item 3 of first sheet)

This International Searching Authority found multiple inventions in this international application, as follows:

1. [ ] As all required additional search fees were timely paid by the applicant, this international search report covers all searchable claims.

2. [ ] As all searchable claims could be searched without effort justifying an additional fees, this Authority did not invite payment of additional fees.

3. [ ] As only some of the required additional search fees were timely paid by the applicant, this international search report covers only those claims for which fees were paid, specifically claims Nos.:

4. [ ] No required additional search fees were timely paid by the applicant. Consequently, this international search report is restricted to the invention first mentioned in the claims; it is covered by claims Nos.:

Remark on Protest

[ ] The additional search fees were accompanied by the applicant's protest and, where applicable, the payment of a protest fee.

[ ] The additional search fees were accompanied by the applicant's protest but the applicable protest fee was not paid within the time limit specified in the invitation.

[ ] No protest accompanied the payment of additional search fees.

INTERNATIONAL SEARCH REPORT

International application No
PCT/EP2013/069788

A. CLASSIFICATION OF SUBJECT MATTER
INV. A61M31/00 A61K9/48 H01P1/203
ADD.

According to International Patent Classification (IPC) or to both national classification and IPC

B. FIELDS SEARCHED

Minimum documentation searched (classification system followed by classification symbols)
A61M H01P

Documentation searched other than minimum documentation to the extent that such documents are included in the fields searched

Electronic data base consulted during the international search (name of data base and, where practicable, search terms used)
EPO-Internal, WPI Data

C. DOCUMENTS CONSIDERED TO BE RELEVANT

Category*	Citation of document, with indication, where appropriate, of the relevant passages	Relevant to claim No.
X	US 2012/116358 A1 (DIJKSMAN JOHAN FREDERIK [NL] ET AL) 10 May 2012 (2012-05-10) paragraph [0020] paragraph [0021] figures 1, 2	1-14
X	WO 2008/059728 A1 (MATSUSHITA ELECTRIC WORKS LTD [JP]; KOBAYASHI MITSURU [JP]) 22 May 2008 (2008-05-22) figures 1, 2, 3, 7, 8, 9	1-14
A	EP 0 022 540 A1 (BATTELLE INSTITUT E V [DE]) 21 January 1981 (1981-01-21) the whole document	1-14
A	& US 3 608 549 A (MERRILL EDWARD W) 28 September 1971 (1971-09-28) the whole document	1-14

☐ Further documents are listed in the continuation of Box C.

☒ See patent family annex.

* Special categories of cited documents :

"A" document defining the general state of the art which is not considered to be of particular relevance

"E" earlier application or patent but published on or after the international filing date

"L" document which may throw doubts on priority claim(s) or which is cited to establish the publication date of another citation or other special reason (as specified)

"O" document referring to an oral disclosure, use, exhibition or other means

"P" document published prior to the international filing date but later than the priority date claimed

"T" later document published after the international filing date or priority date and not in conflict with the application but cited to understand the principle or theory underlying the invention

"X" document of particular relevance; the claimed invention cannot be considered novel or cannot be considered to involve an inventive step when the document is taken alone

"Y" document of particular relevance; the claimed invention cannot be considered to involve an inventive step when the document is combined with one or more other such documents, such combination being obvious to a person skilled in the art

"&" document member of the same patent family

Date of the actual completion of the international search	Date of mailing of the international search report
30 October 2013	07/11/2013

Name and mailing address of the ISA/	Authorized officer
European Patent Office, P.B. 5818 Patentlaan 2 NL - 2280 HV Rijswijk Tel. (+31-70) 340-2040, Fax: (+31-70) 340-3016	Przykutta, Andreas

1

INTERNATIONAL SEARCH REPORT

Information on patent family members

International application No
PCT/EP2013/069788

Patent document cited in search report	Publication date	Patent family member(s)	Publication date
US 2012116358 A1	10-05-2012	CN 102481437 A	30-05-2012
		EP 2416834 A1	15-02-2012
		JP 2012522616 A	27-09-2012
		KR 20120006040 A	17-01-2012
		US 2012116358 A1	10-05-2012
		WO 2010116312 A1	14-10-2010
WO 2008059728 A1	22-05-2008	NONE	
EP 0022540 A1	21-01-1981	CA 1160122 A1	10-01-1984
		DE 2928477 A1	15-01-1981
		EP 0022540 A1	21-01-1981
		JP S5618915 A	23-02-1981
		US 4425117 A	10-01-1984

Conference Paper 1 [CP1]

Study of Split-Ring Resonators for use on a Pharmaceutical Drug Capsule for Microwave Activated Drug Release

Sævar Þór Jónasson, Brian Sveistrup Jensen
and Tom Keinicke Johansen

Conference:	European Microwave Conference, Amsterdam RAI, The Netherlands, 2012
Published :	Oct. 2012

Study of Split-Ring Resonators for use on a Pharmaceutical Drug Capsule for Microwave Activated Drug Release

Sævar Þór Jónasson, Brian Sveistrup Jensen and Tom Keinicke Johansen
Department of Electrical Engineering
Technical University of Denmark
Kongens Lyngby, DK-2800, Denmark
Email: stj@elektro.dtu.dk, Phone: +45 45253871

***Abstract*—In this paper, a novel method for externally activating a pharmaceutical drug capsule by use of split-ring resonators (SRR) is introduced. To this end, the effect of the orientation of the SRRs on the ability to activate the capsules is examined. A coplanar waveguide is used to excite an identical pair of SRRs fabricated on a substrate, representing an enlarged lid for a pharmaceutical drug capsule. Orientations where the electric field component of a quasi-TEM wave lies across the gap of the SRRs provides the largest response. The optimal case is when the electric field component lies across the gap simultaneously with the magnetic field component normal to the SRRs. Furthermore, an analysis of the optimal conductivity and relative permittivity for enhanced temperature rise in the lid is performed. Conductivity of 0.09 S/m and relative permittivity of 12 shows the highest temperature rise.**

***Index Terms*—Split-ring resonator, drug delivery, drug activation, drug release.**

I. Introduction

Conventional pharmaceutical drug delivery, such as oral delivery of therapeutics, face several obstacles. There are problems such as low drug penetration through the gastrointestinal wall, degradation of the active pharmaceutical components in the stomach and the lack of external control of the actual time and place of the drug release [1],[2]. By externally activating pharmaceutical drug capsules, e.g. by focusing microwaves into the area of interest, heating it up and thereby activating the drug capsule, as shown in Fig. 1, the time and place for the drug release can be pre-determined.

Due to high water content and the presence of ions, biological tissues suffer from high attenuation of electromagnetic (EM) waves. These losses generally increase with frequency and microwaves are therefore attenuated very severely and the power is lost as heat. The high losses make it challenging to penetrate deep into the muscles with sufficient power levels and therefore it is required to have a very sensitive receiving structure on the drug capsule to absorb a significant part of the available power in order to use that energy to open the capsule. To accomplish this, we introduce a novel solution based on a highly resonant structure, namely the split-ring resonator (SRR). We propose to use SRRs for externally activating a pharmaceutical drug capsule with microwaves. To this end, we examine how the orientation of a split-ring resonator, relative to the alignment of the exciting EM-wave, influences its resonance response. This response can predict at which orientations power is absorbed by a capsule that uses SRRs to activate it, since the orientation of a swallowed capsule inside the stomach or small intestine would be unknown. Also, an investigation of the effect of the relative permittivity (ϵ_r) and the conductivity (σ) in a lid of a pharmaceutical drug capsule is performed, where optimum ϵ_r and σ values for a maximum temperature increase, are proposed.

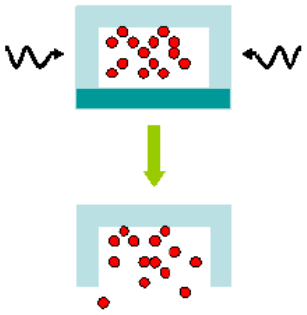

Fig. 1. Drug capsule activated by microwaves.

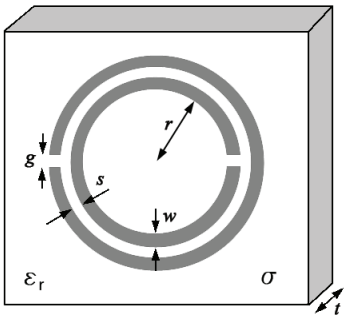

Fig. 2. A split-ring resonator with dimensional variables.

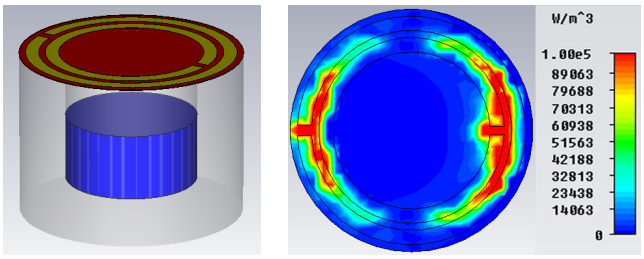

(a) (b)

Fig. 3. In (a) a semi-transparent cylindrical capsule with the pharmaceutical drug inside and the split-ring resonators on top of a thin lid, on the capsule. In (b) the simulated power loss density in the lid is shown from the top.

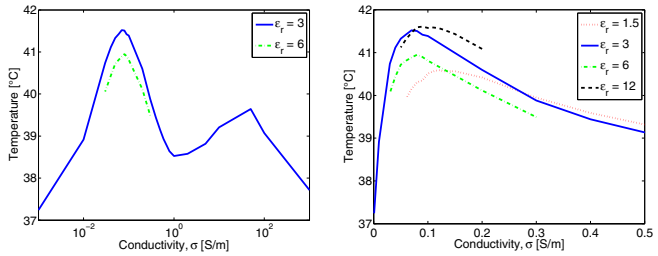

(a) (b)

Fig. 4. Maximum temperature as a function of conductivity for various relative permittivities of the lid of a pharmaceutical drug capsule. Fig. (a) shows a wide range of conductivities while (b) shows narrow range.

II. Split-Ring Resonator for Drug Activation

Split-ring resonators, originally proposed by Pendry [3], are very compact resonance structures and typically resonate when the electrical size of the structure is less than $\lambda/10$ in comparison to typical microwave resonance structures that resonate at the electrical size of $\lambda/2$ [4]. Because of the SRR's small electical size and since the highest electric field concentration is close to the edges of the rings, as will be shown later, the SRRs are chosen here for the purpose of drug activation. SRRs consist of two concentric rings with a gap in the ring structures on opposite sides as is indicated in Fig. 2. SRRs were proposed in [5] by Smith *et al.* to be used as an element in fabricating double-negative metamaterials, where the electric permittivity and permeability are simultaneously negative in a given frequency range and by that, give rise to new applications such as the perfect lens [6].

Split-ring resonators are easily fabricated on printed circuit boards and have therefore also become increasingly popular in microstrip and coplanar waveguide topology for their compact design and good performance in microwave filters [7]. The concept of using SRRs for drug activation is as follows. SRRs are fabricated on a lid of a millimeter sized pharmaceutical drug capsule as shown in Fig. 3(a). The capsule contains a medicine. At the resonance frequency of the SRRs on the drug capsule structure, a relatively strong E-field is generated in the gaps of the rings and in the separation between them. The alternating E-field induces currents in the lossy dielectric lid where part of the electric currents are converted into power loss (Fig. 3(b)). This causes an increase of the temperature in the lid and by that, opens the capsule and releases the pharmaceutical drug. This can be accomplished by having the lid constructed of a polymer, such as Intelimer®, which can abruptly change its adhesion, viscosity or permeability (a measure of the ability of a porous material to allow fluids to pass through it) when heated by just a few degrees. A layer of adhesive material, with a melting point several degrees above $37\,^{\circ}\mathrm{C}$, placed between the lid and the capsule could also operate as a release mechanism for the pharmaceutical drug. The drug capsule in Fig. 3 is simulated in the 3D EM simulation tool CST and is discussed further in the next section.

III. Optimizing Power Dissipation in the Lid

In general, substrates which are too conductive, tend to short-circuit the SRRs which are fabricated on the substrate and kill off any resonance in the rings. On the other hand, substrates that have very low conductivity dissipate very little power.

Rogers 4003®, for example, is a low-loss substrate with ϵ_r = 3.55, σ = 0.001 S/m @2.5 GHz and SRRs that are fabricated on such a substrate, behave as Hi-Q resonators, as is often the aspired property for filters, and do therefore not dissipate notable power. Most substrates that are used in printed circuit technology are relatively low-loss which means that lossy substrates that can be used in conventional photolithography processes can be difficult to find for the purpose of dissipating power.

Simulations of the optimal conductivity for a given relative permittivity were performed in CST in order to provide the optimal parameters for maximum temperature in the lid. CST is used for calculating the current- and power loss densities in the lid substrate. These densities are used as sources from which CST calculates the thermal losses and temperature rise. With a surrounding ambient temperature of $37\,^{\circ}\mathrm{C}$ and having the ambient parameters same as that of air, for simplicity, the capsule in Fig. 3 was used in the simulation. From a distance of 25 mm, a 100 V/m plane wave, with the E-field component oriented across to the gaps in the SRRs and H-field component oriented normal to the lid, is used to excite the pharmaceutical drug capsule. All parameters were kept constant except for the relative permittivity and the conductivity. The maximum temperature point of the substrate at each combination of ϵ and σ at the resonance frequency is taken. The result is shown in Fig. 4. For a wide range of conductivities (Fig. 4(a)) the maximum temperature is found to be $41.5\,^{\circ}\mathrm{C}$ for a substrate with ϵ_r = 3 and σ = 0.07 S/m at 1.8 GHz. The power loss density for the case of maximum dissipation is indicated in Fig 3(b) where it is illustrated that most of the lost power is dissipated in the gaps of each ring as well as in the separation between the rings, close to the gaps. An examination of narrow range of conductivities for several ϵ_r is illustrated in Fig. 4(b) where all the curves have a maximum temperature peak in the range of $\sigma = 0.07 - 0.12$ S/m. A low-loss substrate such as Rogers 4003® will, according to Fig. 4, not have notable

increase in temperature if used as the material for the lid. The availability of that substrate however, makes it the choice for the work in the next section where the orientation of the SRRs is examined and is considered satisfactory for that purpose.

The temperature and its distribution in the capsule is dependent on several parameters such as the thickness of the lid as well as the thermal conductivity of the lid and the material the lid is mounted on. For this simulation, the thickness of the lid is 0.1 mm, the thermal conductivity of the lid and the cylindrical capsule below it is 0.2 W/K/m.

IV. Split-Ring Resonator on the Lid

A. Fabrication

Split-ring resonators on top of a 1.5 mm thick Rogers 4003® substrate were fabricated for the experimental study. Each of the SRRs are fabricated on a circular disc with the diameter of 15 mm that functions as an enlarged lid for a drug capsule. The dimensions of the SRRs are shown in Table I and their notations are referred to Fig. 2. As mentioned before, the relative permittivity and conductivity at 2.5 GHz are $\epsilon_r = 3.55$ and $\sigma = 0.001$ S/m, respectively.

TABLE I
Dimensions of Split-Ring Resonators

r [mm]	s [mm]	w [mm]	g [mm]	t [mm]
5.1	0.3	0.3	0.2	1.5

B. Excitation

Having an external antenna array and focusing microwaves inside the human body from a far-field distance, we assume, in general, propagating transverse electromagnetic (TEM) mode inside the body. This field excites the pharmaceutical drug capsule and especially the split-ring resonators on top of the lid until the drug is released. To approximate such a TEM excitation, a coplanar waveguide (CPW) structure has been fabricated and is shown in Fig. 5. Waves on a CPW have typically a quasi-TEM mode since part of the wave is located in the substrate while the other part is located in air. The CPW is approximately a 50 Ω tapered transmission line with a 15 mm gap between the center conductor and the ground references in the middle of the CPW structure. The large gap makes it possible to fit the lids discussed in the previous subsection. This is accomplished by drilling a hole in the substrate in the middle of the gap of the CPW and leaving room for placing the cylindrical lid structures. In the plane of the CPW structure, the E-field component is oriented across the gap where the SRRs are placed, the H-field component is oriented normal to the CPW structure and the direction of propagation, $\hat{k}$, is normal to the E-H plane as is indicated in Fig. 5.

C. Measurements

Measurements on six different orientations of the SRRs were performed. The orientations are indicated in Fig. 6 and are relative to the orientation of the quasi-TEM wave

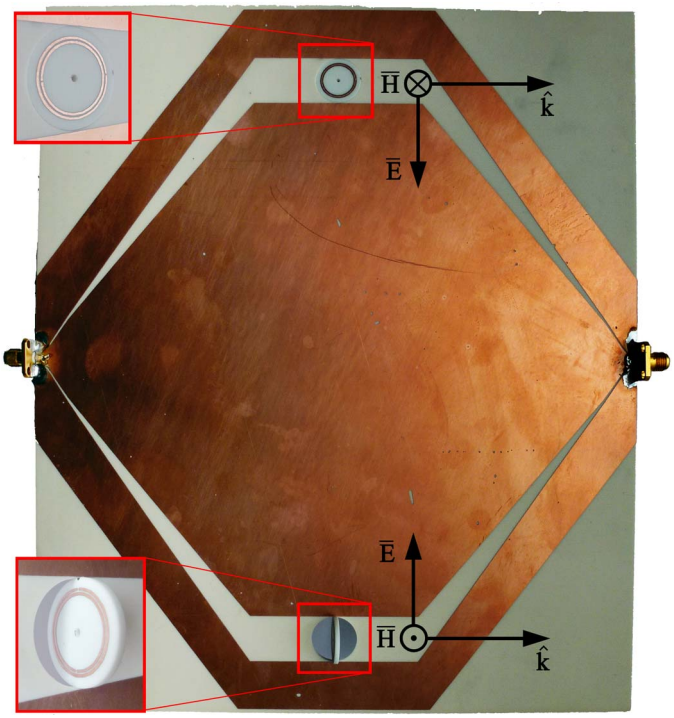

Fig. 5. Coplanar waveguide (conductors are the dark parts). In the top left corner, an example of a case (b) or (e). In the bottom left corner, an example of case (c) or (f). The size is 24 cm x 20 cm.

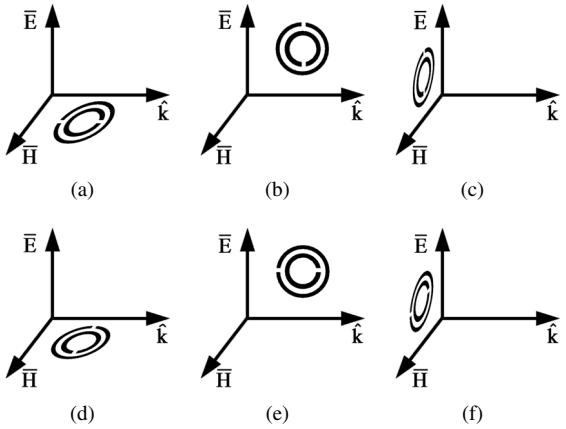

Fig. 6. Orientation of the split-ring resonators relative to the exciting wave.

propagating in the CPW plane in Fig. 5. Each subfigure notation in Fig. 6 will be referred to as a case, e.g. the orientation in Fig. 6(e) is referred to as *case (e)* and so on. For every measurement of each orientation, both SRRs, which are identical, are oriented in the same way, i.e. as mirrored through the H-k plane of the CPW structure.

The S-parameter measurement results for the CPW structure with SRRs are illustrated in Fig. 7 and 8. The results in Fig. 7 show S_{21} over the frequency range from 3 GHz to 5 GHz which includes the resonance of the SRR. The reference is a case where there are no SRRs in the holes, i.e. the holes are empty. Outside the resonance, and actually all across the band for the reference, the S_{21} is approximately -10 to -15 dB

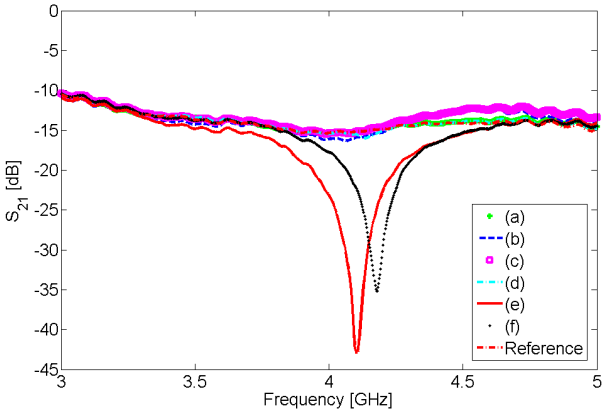

Fig. 7. Coplanar waveguide transmission (S_{21}) measurement.

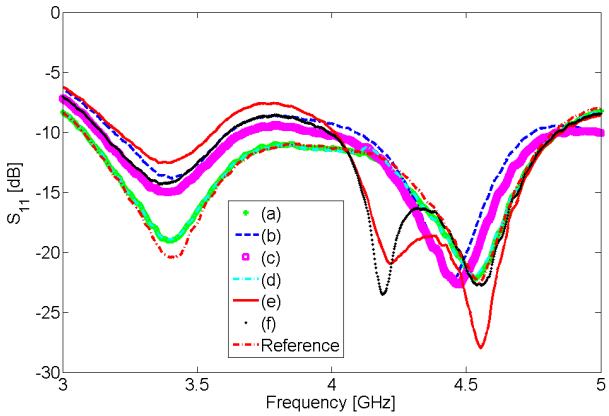

Fig. 8. Coplanar waveguide reflection (S_{11}) measurement.

even though the return loss, shown in Fig. 8, is better than 6 dB. The reason for this is because the waves traveling in the large gap of the CPW structure are only loosely bounded to the substrate and therefore radiate into the surroundings and cause the relatively high insertion loss outside the resonance in Fig. 7.

From the results it can be immediately seen that *cases (a)* and *(d)*, i.e. when the SRRs lie in the H-k plane, do not show a significant response to the propagating wave. In these cases the H-field is parallel to rings and the E-field is normal to the rings and therefore no excitation is expected. *Case (c)* does not show any resonant response and the S_{21} is approximately the same as that of the reference, but the SRRs do however increase the S_{11} by a few dBs which is an effect of the E-field parallel to the rings that generates a slight potential difference between the rings. *Case (b)* shows a small response in S_{21} where it gets slightly lower than the reference around the resonance frequency and S_{11} is shifted as well. This case indicates the effect that only the H-field component has on the excitation of the SRRs. *Cases (f)* and *(e)* show the largest response. In *case (f)* the H-field is parallel to the SRRs and the E-field is accross the gap of the SRRs and the H-field component does therefore not contribute to excitation of the rings. *Case (e)* has the H-field normal to the SRRs and the E-field component across the gaps of the SRRs and that results in a slightly better coupling than *case (f)*.

A planar device like the SRRs rarely has resonating response to exiting waves from all directions and polarizations. If a pharmaceutical drug capsule with SRRs on top of a lid is swallowed it is a challenge to orient the excitation source correctly to activate the capsule in a controlled manner. Instead of a linear polarization as is the case for the CPW structure, a circular polarization of the exciting wave is suggested and by that, *cases (a)* and *(d)* would also be suitable orientations for resonance and thus, for heat dissipation. It has been shown with the measurements that the optimal orientation for exciting a lid with SRRs on a coplanar waveguide are *cases (f)* and *(e)*.

V. Conclusion

Conventional pharmaceutical drug delivery, such as oral delivery of therapeutics, have problems such as external control of the actual time and place of the drug release. In this paper, we introduced a method of externally activating parmaceutical drug capsules by use of split-ring resonators. For that purpose, the optimal electric conductivities and relative permittivities were simulated for highest power dissipation and temperature increase in the lid of the drug capsule. Conductivity of 0.09 S/m and relative permittivity of 12 were found to give the highest temperature increase. Furthermore, we measured the effect that the orientation of split-ring resonators, relative to the excitation source, has on the resonance response of the split-ring resonators. It was shown that the preferred orientation of the SRRs is when the H-field component is normal to the plane of the split-ring resonators and the E-field component lies across the gaps of the split-ring resonators. These results can form the basis for further studies of external microwave activation methods of drug release using split-ring resonators.

References

[1] C. W. Pouton, "Formulation of poorly water-soluble drugs for oral administration: Physicochemical and physiological issues and the lipid formulation classification system," *European Journal of Pharmaceutical Sciences*, vol. 29, pp. 278–287, 2006.

[2] S. B. Bari, B. R. Kadam, Y. S. Jaiswal, and A. A. Shirkhedkar, "Impurity profile: Significance in active pharmaceutical ingredient," *Eurasian Journal of Analytical Chemistry*, vol. 2, pp. 32–53, 2007.

[3] J. B. Pendry, A. J. Holden, and D. J. R. et al., "Magnetism from conductors and enhanced nonlinear phenomena," *IEEE Transactions on Microwave Theory and Techniques*, vol. 47, pp. 2075–2084, 1999.

[4] J. Martel, R. Marqués, F. Falcone, J. D. Baena, F. Medina, F. Martín, and M. Sorolla, "A new lc series element for compact bandpass filter design," *IEEE Microwave and Wireless Components Letters*, vol. 14, pp. 210–212, 2004.

[5] D. R. Smith, W. J. Padilla, D. C. Vier, S. C. Nemat-Nasser, and S. Schultz, "Composite medium with simultaneously negative permeability and permittivity," *Physical Review Letters*, vol. 84, pp. 4184–4187, 2000.

[6] J. B. Pendry, "Negative refraction makes a perfect lens," *Physical Review Letters*, vol. 85, pp. 3966–3969, 2000.

[7] J. García-García, J. Bonache, I. Gil, F. Martín, M. del Castillo Velázquez-Ahumada, and J. Martel, "Miniaturized microstrip and cpw filters using coupled metamaterial resonators," *IEEE Transactions on Microwave Theory and Techniques*, vol. 54, pp. 2628–2635, 2006.

Conference Paper 2 [CP2]

Design and Characterization of a Low-Viscous Muscle Tissue Mimicking Media at the ISM-band (2.4-2.48 GHz) for Easy Antenna Displacement in In Vitro Measurements

Sævar Þór Jónasson, Tom Keinicke Johansen
and Vitaliy Zhurbenko

Conference:	Asia-Pacific Microwave Conference, Kaohsiung, Taiwan, 2012
Published :	Dec. 2012.

Design and Characterization of a Low-Viscous Muscle Tissue Mimicking Media at the ISM-band (2.4-2.48 GHz) for Easy Antenna Displacement in *In Vitro* Measurements

Sævar Þór Jónasson, Vitaliy Zhurbenko, and Tom Keinicke Johansen

Department of Electrical Engineering, Technical University of Denmark,
Oersteds Plads, Kgs. Lyngby, DK-2800, Denmark

***Abstract* — Phantoms mimicking electromagnetic properties of biological tissues are widely used in evaluation of electromagnetic field distribution in human body. In this paper, low-viscous, optically transparent liquids that mimic muscle tissue, are designed and characterized. Various mixing ratios of de-ionized water and diethylene glycol butyl ether are examined in range of widely used biomedical frequencies. A recipe for 2.45 GHz is given, which provides less than 5.6% deviation from the reference. With help of curve fitting of the discrete measurement points, recipes for other parts of the body can be produced. For example, a recipe for the grey matter of the human brain is suggested, resulting in less than 4.7% deviation. An improved recipe for muscle tissue, where Triton X-100 is added, improves the target recipe to less than 1% deviation from the reference.**

***Index Terms* — Muscle tissue mimicking media, Diethylene Glycol Butyl Ether (DGBE), Polyethylene Glycol Mono Phenyl Ether (Triton X-100).**

I. Introduction

In microwave-activated drug release, microwaves are focused at an area inside the body, to activate drug capsules and release medicine which is located there, at a given time. Focusing of microwaves inside the human body is challenging and is dependent of number of parameters such as frequency, geometry of the object and electrical properties of the tissue [1]. Modeling the human body is of high importance to successfully focus the microwaves with a predemined phase and amplitude at the specific target. Muscles are, in general, a large part of the human body and an accurate modeling of its electromagnetic (EM) properties is crucial for that purpose.

Human phantoms in form of cylinders and human head shapes have been used for representing the human body parts for focusing radio waves for tissue-heating in hyperthermia or measuring the fields generated by mobile phone antennas [1], [2]. These phantom structures contain materials that have similar EM properties as fat, muscle and skin in humans to name a few [3], [4], [5]. Those types of mimicking medias are often optically non-transparent, solids or high-viscous gels that make it impossible to move an antenna freely around inside the media for measurements at different locations. An antenna transmitting from within a human phantom can provide relative phase- and amplitude information, measured outside the phantom. Using the measured fields, the original transmitted field can be reconstructed for focusing.

In this paper a low-viscous, optically transparent muscle tissue mimicking media (MTMM) is characterized with only two ingredients for the ISM-band, 2.40 - 2.4835 GHz. With help of curve fitting of the measurement points, recipes for some other parts of the human body can be produced. A recipe for the grey matter of the human brain is suggested, as an example of this. A more optimized media is additionally developed, to more accurately model muscle tissue with only three ingredients. The liquids are measured and verified by comparing the measurement results to a widely used 4-Cole-Cole model.

II. Design and Characterization of a Muscle Tissue Mimicking Media

Several MTMMs have been suggested for various frequencies and consisting of diverse materials such as polyethelene powder, aluminum powder, brass powder, TX-151, sugar, NaCl, de-ionized water and polyester resin [3], [4]. In order to be able to move an antenna freely within the MTMM, it requires a low viscous liquid. The media proposed by Chou et al. in [3] has been widely used [6, pp. 98-99]. It is a mixture of de-ionized water, NaCl, polyethylene powder and TX-151. The polyethylene powder lowers the relative permittivity of water and makes the mixture non-transparent. The TX-151, which is a gelling medium, transforms the water-based formula into a high-viscous gel which, prevent the polyethylene powder to rise to the surface of the water and the gel has the tendency to entrap air bubbles. In [5] and [7] diethylene glycol butyl ether (DGBE), polyethylene glycol mono phenyl ether (Triton X-100), and de-ionized water have been used to mimic the EM behavior of the skin and the human head respectively. NaCl was additionally used in the mixture for the human head media to increase its conductivity.

In Fig. 1 and Fig. 2 the relative permittivity (ε_r) and the conductivity (σ) respectively of a liquid mixture consisting of DGBE in de-ionized water as a function of the weight-ratio of DGBE in the mixture, are shown at 0.5 GHz, 0.75 GHz, 0.915 GHz, and 2.45 GHz. As can be seen, the relative variation of the relative permittivity over frequency of the mixture is very small compared to the relative variation of the conductivity for the same liquid. The conductivity is therefore

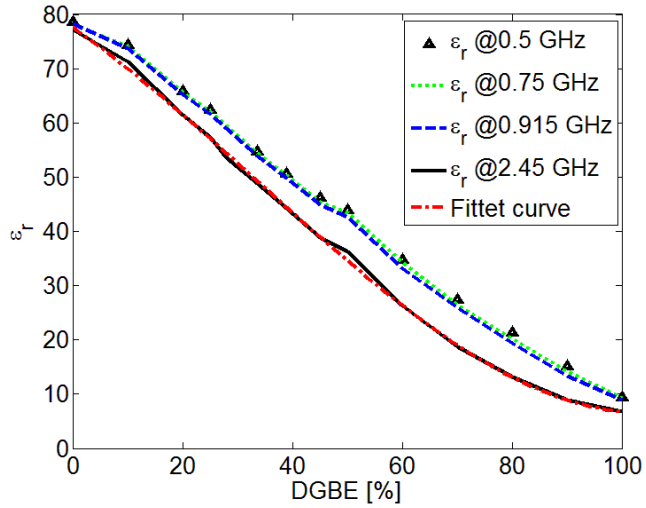

Fig. 1. Measured relative permittivity of DGBE as a weight-ratio of the total DGBE and de-ionized water mixture.

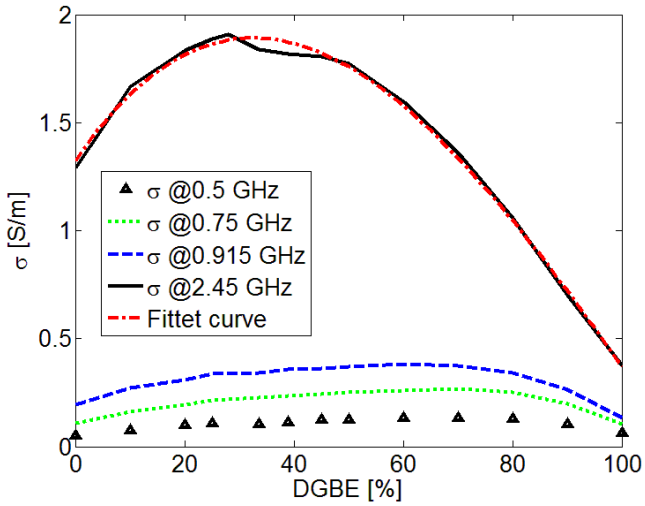

Fig. 2. Measured conductivity of DGBE as a weight-ratio of the total DGBE and de-ionized water mixture.

low for lower frequencies which is an advantage since it is generally easier to increase conductivity rather than decreasing it, e.g. by adding NaCl.

The reference values of the relative permittivity and conductivity of a muscle tissue, that are 53.6 and 1.81 S/m respectively [8]. The closest permittivity of 53.5 is acquired when the DGBE weight-ratio is 28%, from Fig. 1. The conductivity is found from Fig. 2 to be 1.91 S/m, both at 2.45 GHz. The deviations of the measured values, relative to the reference values are indicated in (1) and (2). Muscles, such as the ones in the abdominal region consist of muscle groups that have both transverse and parallel muscle fibers. Parallel muscle fibers are the fibers that lie along the human height and transverse are the ones which lie across it. The design values (from [8]) are an average of both transverse and parallel muscle fibers.

$$Error_{\varepsilon_r} = \frac{|\varepsilon_{r_{meas}} - \varepsilon_{r_{ref}}|}{\varepsilon_{r_{ref}}} < 0.19\%, \quad (1)$$

$$Error_{\sigma} = \frac{|\sigma_{meas} - \sigma_{ref}|}{\sigma_{ref}} < 5.53\%. \quad (2)$$

Two fitted, 3rd order polynomial curves are shown in Fig. 1 and Fig. 2 for the 2.45 GHz frequency measurements. The polynomial has the form of (3) and parameters, p_n, for the permittivity and conductivity are listed in Table I.

$$p(x) = p_1 x^3 + p_2 x^2 + p_3 x + p_4, \quad (3)$$

where $p(x)$ is the polynomial as a function of the variable x which, in the present case, is the weight-ratio of DGBE in the mixture.

TABLE I

PARAMETERS OF THE POLYNOMIAL FITTED CURVE AT 2.45 GHZ.

Parameter	ε_r	σ
p_1	$6.18363728 \cdot 10^{-5}$	$2.04026154 \cdot 10^{-6}$
p_2	$-6.25630329 \cdot 10^{-3}$	$-6.70726099 \cdot 10^{-4}$
p_3	$-7.00787624 \cdot 10^{-1}$	$3.71651344 \cdot 10^{-2}$
p_4	$7.75912484 \cdot 10^{1}$	$1.32226342 \cdot 10^{0}$

The polynomials are employed for developing liquids having different permittivities and conductivities than the ones presented here, for other parts of the body. The grey matter of the brain e.g., has relative permittivity of 48.91 and conductivity of 1.8077 S/m. A value of 48.96 (having a 101 point polynomial over the range of 0-100%), is found for ε_r, using the permittivity polynomial function and is close to permittivity of 48.91 which corresponds to a DGBE ratio of 34%. Following the 34% ratio in the polynomial for the conductivity, the corresponding conductivity is 1.891 S/m which is within 4.7% of the aimed value.

III. IMPROVING THE MUSCLE TISSUE MIMICKING MEDIA

Deviations in the order of 4-6% are in some cases unacceptable. The simplicity of having only two materials, DGBE and water, limits the degrees of freedom and there is therefore, a restriction for how well the MTMM can be matched to the reference. However it is possible to fine-tune the MTMM by introducing a third material. In order to reduce the conductivity error, Triton X-100 can be used to replace a part of the DGBE since Triton X-100 has both lower conductivity and permittivity than DGBE, but the relative difference in conductivity is larger than for the permittivity. Fig. 3 illustrates the relative permittivity and Fig. 4 the conductivity as a function of frequency for the improved recipe which is given in Table II for 2.45 GHz.

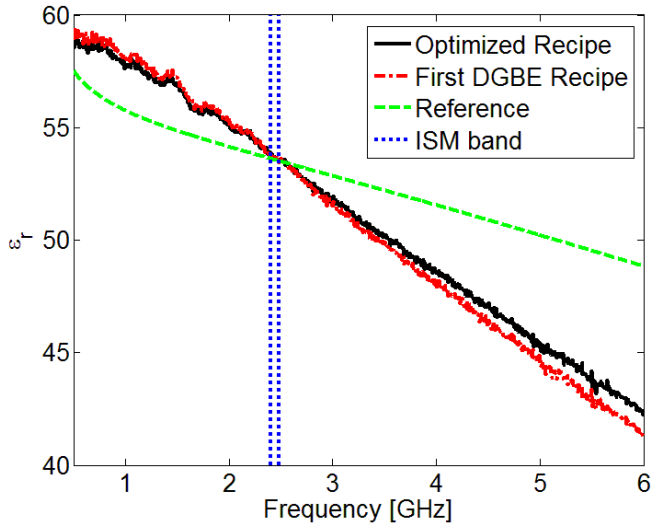

Fig. 3. Measured relative permittivity of DGBE, Triton X-100 and de-ionized water as a function of frequency.

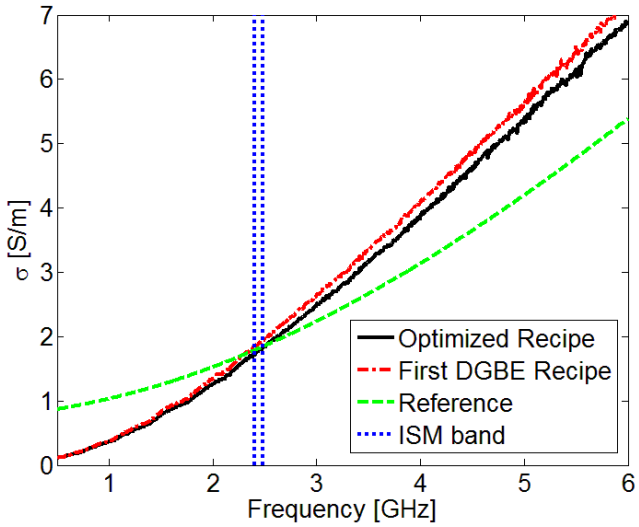

Fig. 4. Measured conductivity of DGBE, Triton X-100 and de-ionized water as a function of frequency.

TABLE II

IMPROVED MUSCLE TISSUE MIMICKING MEDIA RECIPE AT 2.45 GHZ

De-ionized water	DGBE	Triton X-100
72%	23%	5%

For comparison, the first recipe discussed above, including only DGBE and de-ionized water are illustrated in Fig. 3 and Fig. 4 as well as a 4-Cole-Cole model from the reference in [8]. The new ε_r and σ are measured to be 53.67 and 1.797 S/m respectively which means that the error is reduced below 1% for both the permittivity and the conductivity or 0.131% and 0.719% respectively. The EM properties of all MTMM were measured using Agilent's 85070E dielectric probe kit and a HP 8753C vector network analyzer at room temperature of 23°C ± 1°.

VII. CONCLUSION

Tissue mimicking media are often solids or very viscous gels. This makes it impossible to move a measuring antenna freely, inside the phantom media. In this paper we presented a recipe for a low-viscous muscle tissue mimicking media for the ISM band (2.4-2.4835 GHz) and its characterization at various frequencies and with various mixing ratios. The proposed media is optically transparent making positioning of the antenna in the media easier. The media is made from a mixture of de-ionized water and DGBE. With 28% of DGBE, relative permittivity and conductivity is measured to be within 5.53% of the reference values. An improved recipe requires the addition of a third material, Triton X-100. Mixing 72% of de-ionized water, 23% DGBE and 5% Triton X-100 reduces the errors below 1% at 2.45 GHz.

ACKNOWLEDGEMENT

The authors wish to thank Villum Kann Rasmussen Foundation for partial support of this work.

REFERENCES

[1] A. W. Guy, C.-K. Chou and K. H. Luk, "915-MHz phased-array system for treating tumors in cylindrical structures," *IEEE Transactions on Microwave Theory and Techniques,* pp. 502-507, 1986.

[2] V. Homback, K. Meier, M. Burkhardt, E. Kuhn and N. Kuster, "The dependence of EM energy absorption upon human head modeling at 900 MHz," *IEEE Transactions on Microwave Theory and Techniques,* pp. 1865-1873, 1996.

[3] C.-K. Chou, G.-W. Chen, A. W. Guy and K. H. Luk, "Formulas for preparing phantom muscle tissue at various radiofrequencies," *Bioelectromagnetics,* pp. 435-441, 1984.

[4] P. Wust, H. Fahling, J. Berger, A. Jordan, G. Mönich and R. Felix, "Solid materials with high dielectric constants for hyperthermia applications," *International Journal of Hyperthermia,* pp. 183-193, 1998.

[5] T. Yilmaz, T. Karacolak and E. Topsakal, "Characterization and testing of a skin mimicking material for implantable antennas operating at ism band (2.4 GHz - 2.48 GHz)," *IEEE Antennas and Propagation Letters,* pp. 418-420, 2008.

[6] "IEEE Recommended Practice for Measurements and Computations of Radio Frequency Electromagnetic Fields With Respect to Human Exposure to Such Fields, 100 kHz-300 GHz," IEEE-SA Standards Board Std., 2008.

[7] "IEEE Recommended Practice for Determining the Peak Spatial-Average Specific Absorption Rate (SAR) in the Human Head from Wireless Communications Devices: Measurement Techniques. IEEE Std 1528-2003," The Institue of Electrical and Electronics Engineers, Inc. Std., 2003.

[8] C. Gabriel, "Compilation of the dielectric properties of body tissues at rf and microwave frequencies," Brooks Airforce Base Technical Report AL/OE-TR-1996-0037, 1996.

Conference Paper 3 [CP3]

Microwave Assisted Drug Delivery

Sævar Þór Jónasson, Vitaliy Zhurbenko
and Tom Keinicke Johansen

Conference:	URSI General Assembly and Scientific Symposium
Accepted :	Aug. 2014

Microwave assisted drug delivery

Sævar Þór Jónasson, Vitaliy Zhurbenko* and Tom K. Johansen

Technical University of Denmark, 2800 Kgs. Lyngby, Denmark
stj / vz / tkj@elektro.dtu.dk

Abstract

In this work, the microwave radiation is adopted for remote activation of pharmaceutical drug capsules inside the human body in order to release drugs at a pre-determined time and location. An array of controllable transmitting sources is used to produce a constructive interference at a certain focus point inside the body, where the drugs are then released from the specially designed capsules. An experimental setup for microwave activation has been developed and tested on a body phantom that emulates the human torso. A design of sensitive receiving structures for integration on a drug capsule is presented.

1. Introduction

In the year 2008, 48% of the people in the United States took at least one prescription drug in a single month. The prescription drug use had increased by 4% compared to 1998 [1]. With current increasing intake of drugs, a more efficient and controllable way of delivering the drugs is of great interest.

Oral delivery of pharmaceuticals is the preferred method compared to intravenous injection because of lower costs, reduced risks associated with the injection, and higher patient compliance due to self-administration. However the traditional oral delivery faces several challenges such as low drug permeability (not to be confused with electromagnetic permeability) through the gastrointestinal epithelium [2,3] and degradation of the active pharmaceutical components in the stomach [4].

Inherently the problem with current drug delivery systems, e.g. in the form of pills is the limited external control of when the drug is dissolved and absorbed by the body. Typically, the drug release is controlled by the intestinal pH gradient and is therefore released over a large segment of the intestine. The drugs are coated with special protective coatings which dissolve at a certain pH value. The time and the location for the drug release is therefore difficult to control. For certain diseases such as schizophrenia and diabetes, dosing must be stable and reliable [5].

Pharmaceutical drugs taken orally are normally designed to release the drug in the small intestine because there, the drugs typically exhibit maximal absorption [6]. The small intestines are less than 3 cm in diameter [7, pp. 272].

A number of techniques have been developed to externally control the drug delivery. These include, but are not limited to, the use of ultrasound [8], light waves [9], magnetic fields [10] and radio waves below 100 MHz [11]. Complex systems have also been integrated into a drug delivery module consisting of a receiving inductor, control circuitry chip and a drug delivery chip [12]. Each of these methods has its pros and cons.

The alternative method that described in this work is to focus microwave energy inside the human body to get localized high-amplitude fields. These are then used to activate the specially designed micro-containers.

2. Microwave Activation of Drug Release

The purpose of the described here microwave activation system is to provide a method of releasing drugs inside the body, unobtrusively, i.e. without disturbing a patient. The concept is illustrated in Figure 1, where one of the anticipated scenarios is shown. A person is lying on a bed, sleeping after having ingested numerous capsules that contain pharmaceutical drugs. At a certain time, and at a pre-determined location inside the human body, the microwave activation system focuses electromagnetic energy that opens the capsules and releases the medical drug.

Obviously, the essence of the external activation of pharmaceutical drugs with microwaves depends on the ability to induce electromagnetic power at certain areas inside the body. A documented side effect of being irradiated by electromagnetic waves is that unwanted heating of areas, other than intended, can occur. A method for reducing the side effects is, to superimpose electromagnetic waves from multiple sources, creating a focus point.

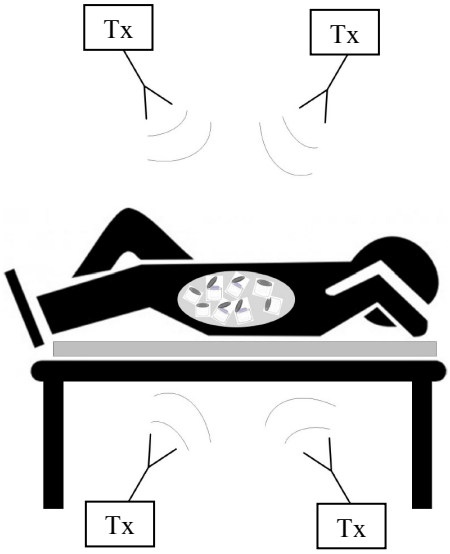

Figure 1. Remote activation of drug release using electromagnetic radiation.

There are a number of critical design-choices to be made in a system that is to radiate electromagnetic waves inside the human body. These include operating frequency, number and location of transmitting antennas, pulsed vs. continuous wave operation, power level and flexibility of the system.

Generally with increasing frequency, attenuation in biological tissues increases and makes it more challenging to penetrate deeper into the body. Higher frequency signals, due to smaller wavelength, are able to focus onto smaller areas. Components, such as antennas, can be made smaller and that impacts the overall size of the system. Considering these tradeoffs, the operating frequency of the experimental setup described in this work has been chosen in ISM band and is approximately 2.45 GHz.

In Figure 2, a schematic drawing of the implemented setup is presented. A human torso phantom is in the center of the setup. To simplify the setup only four transmitters were implemented. They are evenly distributed around the phantom as it is shown in the Figure. Focusing of the electromagnetic energy is achieved by choosing the amplitude and phase of the transmitted signal. Microwave absorbers are placed in the plane of measurement, where one is placed behind each receiver and one between each receiver as shown in the Figure.

The submerged in the phantom sleeve dipole antenna (red dot in Figure 2) is mounted on the lid of the phantom and used as a probe for measuring the field distribution inside the phantom. The lid can be rotated 360 deg in a continuous movement. The submerged antenna can also be moved continuously back and forth, from the centre of the phantom.

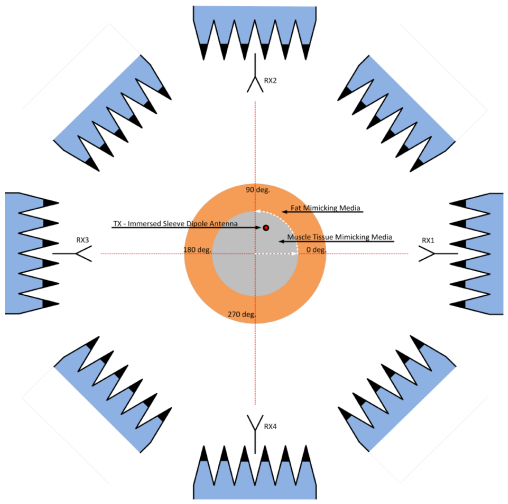

Figure 2. Schematic representation of the experimental setup.

In the conducted experiments a number of arbitrary focusing points were pre-determined in order to examine the focusing abilities of the microwave activation system. The experimental data showed clear focusing points at the pre-determined locations for points less than 4 cm from the centre of the phantom, i.e. deep inside the lossy phantom. In those cases, the focus point is the highest amplitude-point across a diameter larger than 3.6 cm. For comparison, the small intestine in humans are typically less than 3 cm in diameter [7, pp. 272] and is the place where the drug release is meant to take place. High-amplitude areas and spots (hot spots) appeared also at other locations than at the focusing point as was expected. This is a persistent problem in non-invasive hyperthermia systems as well. Increase of transmitting antennas should reduce the number of high-amplitude areas outside the focus area. A more detailed description and analysis of the achieved experimental results will be given at the conference presentation.

3. Drug Capsule

The inherent high losses of biological tissues at microwave frequencies make it challenging to penetrate deep into tissues with sufficient power levels. It is therefore required to have a very sensitive receiving structure on the drug capsule to absorb a significant part of the available power in order to use that energy to open the capsule. The anticipated scenario is illustrated in Figure 3 (a). A highly resonant structure, the split-ring resonator, is introduced on a lid of the capsule which contains a medicine. A resonator is able to induce locally high intensity fields at the resonance frequency, compared to other frequencies (refer to Figure 3. (b) and (c)) [13].

At the resonance frequency of the SRRs on the drug capsule structure, a relatively strong electric field is generated in the gaps of the rings and in the separation between them. The alternating field induces currents in the lossy dielectric lid where part of the electric currents are converted into heat, due to power loss (Figure 2(c)). This causes an increase of the temperature in the lid and by that, opens the capsule and releases the pharmaceutical drug. Practically, this can be accomplished by having the lid constructed of a polymer, which can abruptly change its adhesion, viscosity or permeability (a measure of the ability of a porous material to allow fluids to pass through it) when heated by just a few degrees. A layer of adhesive material, with a melting point several degrees above the ambient temperature, placed between the lid and the capsule could also operate as a release mechanism for the pharmaceutical drug.

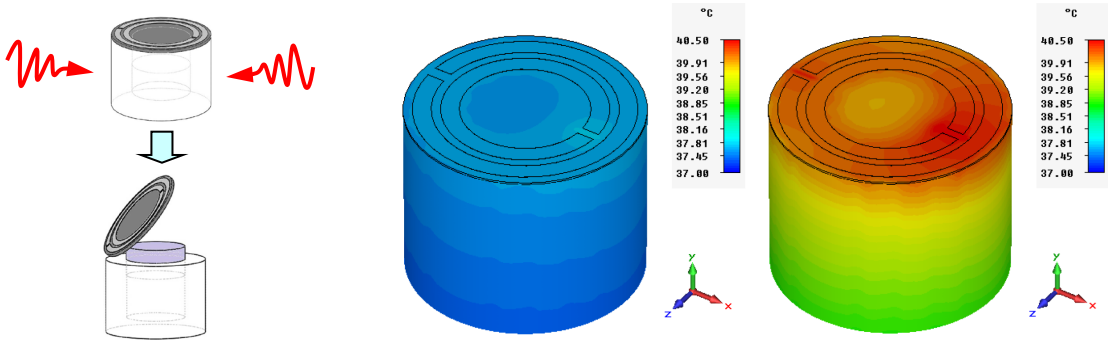

(a) (b) (c)

Figure 3. Illustration of the activation (opening) process. (a) - Split-ring resonators on a lid on top of a capsule and a drug being released. (b) and (c) - Temperature distribution of the capsule as a result of a power loss in the lid. (b) represents the temperature distribution at 2.3 GHz and (c) at 2.43 GHz. Notice the difference in temperature.

The analysis in [13] shows the existence of an optimal complex permittivity of the lid material which results in the highest temperature rise.

4. Summary

In this work, a method of remotely activating and releasing pharmaceutical drugs inside the human body with the use of microwaves was investigated. Current limitations in external control of the specific location and the time of a drug release inside the human body formed the motivation for this study. The microwave activation system was developed on the basis of being an unobtrusive system, i.e. without disturbing the prospective patients. Four external antennas were designed to irradiate the torso phantom along with four microwave transmitters.

The measurement results revealed the wave behavior in the cylindrical phantom and the challenges of the focusing process. Even though focusing in the central part of the body can be achieved using the present setup, surface waves excited on the body-air interface disturbed the focusing of electromagnetic energy further away from the center of the body.

It was also found that by optimizing the complex permittivity of the capsule lid, one can maximize temperature increase in the lid. The temperature increase can then be used to melt the lid and release the drugs.

5. Acknowledgments

The authors would like to thank the Villum Kann Rasmussen Fonden for the partial financial support of the study.

6. References

1. Qiuping Gu, Charles F. Dillon, and Vicki L. Burt. Prescription drug use continues to increase: U.s. prescription drug data for 2007-2008. NCHS Data Brief, 42:1–8, 2010.
2. Kristy M. Ainslie, Rachel D. Lowe, Tristan T. Beaudette, Lamar Petty, Eric M. Bachelder, and Tejal A. Desai. Microfabricated devices for enchanced bioadhesive drug delivery: Attachement to and small-molecule release trhough a cell monolayer under flow. Small, 24:2857–2863, 2009.
3. Colin W. Pouton. Formulation of poorly water-soluble drugs for oral administration: Physicochemical and physiological issues and the lipid formulation classification system. European Journal of Pharmaceutical Sciences, 29:278–287, 2006.
4. Sanjay B. Bari, Bharati R. Kadam, Yogini S. Jaiswal, and Atul A. Shirkhedkar. Impurity profile: Significance in active pharmaceutical ingredient. Eurasian Journal of Analytical Chemistry, 2:32–53, 2007.
5. Anja Boisen. Naanomechanical sensors and actuators, fundamentals and new direction (namec) - a vkr center of excellence. NAMEC Project proposal to the VKR Foundation.
6. David R. Friend. Drug delivery to the small intestine. Current Gastroenterology Reports, 6:371–376, 2004.
7. Nazmul Akunjee and Muhammed Akunjee. The Easy Guide to OSCEs for Final Year Medical Students. Radcliffe Publishing Ltd., 2007.
8. Holger Grull and Sander Langereis. Hyperthermia-triggered drug delivery from temperature-sensitive liposomes using mri-guided high intensity focused ultrasound. Journal of Controlled Release, 161:317–327, 2012.
9. Cornelius Diamond and Scott Arouh. Light-activated drug delivery method and device. Patent, 2003. US 2003/0191458 A1.
10. Jean Brault. Magnetic apparatus used for drug delivery. Patent, 2011.WO2011113140 (A1).
11. Somayyeh Rahimi, Elie H. Sarraf, Gregory K. Wong, and Kenichi Takahata. Implantable drug delivery device using frequency-controlled wireless hydrogel microvalves. Biomedical Microdevices, 13:267–277, 2011.

12. S. Smith, T.B. Tang, J.G. Terry, J.T.M. Stevenson, B.W. Flynn, H.M. Reekie, A.F. Murray, A.M. gundlach, D. Renshaw, B. Dhillon, A. Ohtori, Y. Inoue, and A.J. Walton. Development of a miniaturised drug delivery system with wireless power transfer and communication. IET Nanobiotechnology, 1:80–86, 2007.
13. Jónasson, Sævar Þór, Jensen, Brian Sveistrup, Johansen, Tom Keinicke, "Study of split-ring resonators for use on a pharmaceutical drug capsule for microwave activated drug release," Proceedings of European Microwave Conference 2012, pp. 76-79.

Conference Paper 4 [CP4]

Vital Signs Detection Radar using Low Intermediate-Frequency Architecture and Single-Sideband Transmission

Brian Sveistrup Jensen, Sævar Þór Jónasson,
Thomas Jensen and Tom Keinicke Johansen

Conference: EuRAD 2012 Amsterdam

Published : Oct. 2012

Vital Signs Detection Radar using Low Intermediate-Frequency Architecture and Single-Sideband Transmission

Brian Sveistrup Jensen, Sævar Þór Jónasson
and Tom Keinicke Johansen
Department of Electrical Engineering
Technical University of Denmark
2800 Kgs. Lyngby, Denmark
Email: bsj@elektro.dtu.dk

Thomas Jensen
Ferdinand-Braun-Institut
Leibniz-Institut für Höchstfrequenztechnik
12489 Berlin, Germany
Email: thomas.jensen@fbh-berlin.de

***Abstract*—This paper presents a continuous wave vital signs detection radar that utilizes a heterodyne transceiver architecture with a 10 MHz intermediate frequency to remove both unwanted DC offsets in the electronic components and the so-called null-detection-points. For successful removal of the latter, it is shown that single-sideband transmission (or demodulation) must be used. Measurements verify this behaviour.**

I. Introduction

Measuring human vital signs (heartbeat and respiration rate) unobtrusively has been of great interest since the first wireless sensors were demonstrated in the early 1970's, [1]. The most commonly used non-contact sensor types are in the form of continuous-wave (CW) and ultra-wide-band (UWB) radars, [2]-[4], among which this paper concentrates on the CW type.

The vital signs detection (VSD) radar technology is mainly of interest in medical applications where it has the potential to eliminate the need for wired sensors that often induce discomfort for the patients. Furthermore, it has the potential to be of use for monitoring of infants and the elderly in their homes as well as for certain search and rescue operations and military applications. For these types of sensors to be a viable alternative, they of course need to exhibit a performance comparable with traditional worn sensors.

Typically, due to phase noise limitations of oscillators, especially at radio frequencies, and the fact that the desired vital signs signals are only 0.1 - 3.0 Hz offset from the carrier, mainly direct conversion architectures (also called homodyne or zero-IF) in the form of quadrature (I/Q) and double-sideband (DSB) systems have been used for CW-VSD applications; see the simplified block diagrams of Fig. 1(a) and (b) and [2]-[3].

Going to a low intermediate-frequency (low-IF) heterodyne architecture ([5]-[6]), see Fig. 1(c), has several advantages. In particular DC offsets in the electronic components and channel mismatches seen in homodyne I/Q systems are eliminated. This leads to reduced complexity in the signal processing steps, as curve fitting- and estimation algorithms are not necessary in order to carry out proper arctangent demodulation

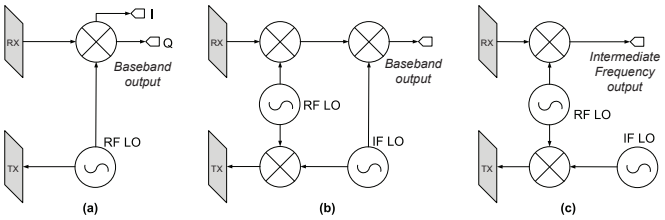

Fig. 1. Simplified block diagrams of (a) traditional quadrature architecture, (b) double-sideband architectures and (c) a low-IF architecture.

of the phase signal, [8]. Furthermore, frequency tuning as implemented in the DSB system of [3] is not required.

While [5] presented the first instrument build heterodyne VSD radar system using a digital I/Q receiver and further [6] sought to evaluate the noise benefits of using a coherent heterodyne architecture compared to homodyne I/Q systems, this paper focuses on the signal theory governing the choise between single- and double-sideband (SSB and DSB) transmission/demodulation. As will be shown, both theory and test measurements dictates that SSB signals should be used in order to eliminate null-detection points.

The heterodyne architecture used in this paper for measurements, implements a 10 MHz IF while data aquisition is carried out on an oscilloscope using sub-sampling techniques. Measurements performed on a living subject is presented and verifies the system's ability to track heart- and respiration rates.

II. DSB vs. SSB transmission/demodulation in Low-IF VSD Radar Instruments

The block diagram of the proposed CW-VSD radar is shown in Fig. 2. The main building blocks consist of an HP 8671B RF signal generator, two Hittite HMC521LC4 I/Q mixers and an AFS42-08001200-15-10P-42 LNA from MITEQ. The IF oscillator is a Vectron C4400A1 oven controlled crystal oscillator (OCXO) followed by a bandpass filter to remove the DC offset and harmonics of the 10 MHz square wave signal. The up-conversion mixer is configured as an SSB mixer (using

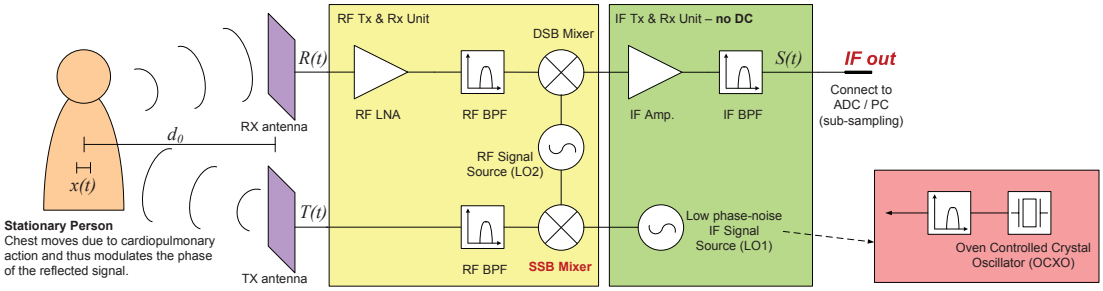

Fig. 2. Block diagram of the proposed low-IF VSD radar architecture.

an IF I/Q splitter). As will be shown next, this configuration is essential for proper removal of the null-point problem.

A. DSB Transmission

To form the transmitted DSB signal, $T_{DSB}(t)$, two frequencies are mixed together. These are the $LO_{RF}(t)$ and $LO_{IF}(t)$ signals respectively,

$$LO_{RF}(t) = \cos\left(\omega_{RF}t + \theta_{RF} + \phi_{nRF}(t)\right) \tag{1a}$$
$$LO_{IF}(t) = \cos\left(\omega_{IF}t + \theta_{IF} + \phi_{nIF}(t)\right) \tag{1b}$$

where ω_{XX} are the angular frequencies and θ_{XX} are phase constants associated with each LO. Furthermore, $\phi_{nXX}(t)$ represent phase noise in each oscillator. Mixing the two signals and keeping only the relevant mixing terms (i.e. sum and difference frequencies), we obtain

$$\begin{aligned} T_{DSB}(t) &= LO_{RF}(t) \cdot LO_{IF}(t) \\ &= \frac{1}{2}\cos\left(\omega_L t + \theta_L + \phi_{nL}(t)\right) \\ &+ \frac{1}{2}\cos\left(\omega_U t + \theta_U + \phi_{nU}(t)\right) \end{aligned} \tag{2}$$

where

$$\omega_L = \omega_{RF} - \omega_{IF} \quad , \quad \theta_L = \theta_{RF} - \theta_{IF} \tag{3a}$$
$$\omega_U = \omega_{RF} + \omega_{IF} \quad , \quad \theta_U = \theta_{RF} + \theta_{IF} \tag{3b}$$

represent the lower and upper sideband frequencies as well as the associated phase terms, respectively. Furthermore,

$$\phi_{nL}(t) = \phi_{nRF}(t) - \phi_{nIF}(t) \tag{4a}$$
$$\phi_{nU}(t) = \phi_{nRF}(t) + \phi_{nIF}(t) \tag{4b}$$

represent the total phase noise associated with each of the two sidebands.

Using the notation from Fig. 2, the time varying distance to the target and back can be represented as

$$d(t) = 2\left(d_0 + x(t)\right) \tag{5}$$

where d_0 is the nominal distance to the target and $x(t)$ is the time varying chest wall movement due to respiration and heartbeat. This change in distance will modulate the phase of the transmitted signal according to

$$\theta_m(t) = \frac{2\pi}{\lambda_i} \cdot d(t) \tag{6}$$

where λ_i is the wavelength of the carrier frequency. In the following, constant phase shifts encountered in the electronic components are assumed to be included in the travel path from (5). Neglecting any path loss, the received signal can now be represented as follows

$$\begin{aligned} R_{DSB}(t) = &\frac{1}{2}\cos\left(\omega_L t + \theta_L + \frac{2\pi}{\lambda_L}d(t) + \phi_{nL}\left(\Delta t\right)\right) \\ &+ \frac{1}{2}\cos\left(\omega_U t + \theta_U + \frac{2\pi}{\lambda_U}d(t) + \phi_{nU}\left(\Delta t\right)\right) \end{aligned} \tag{7}$$

where the phase noise terms have been shifted in time using

$$\Delta t = t - \frac{d(t)}{c} \approx t - \frac{2d_0}{c} \tag{8}$$

where c is the speed of light in air and where the approximation can be used for $d_0 \gg |x(t)|$. The received signal is downconverted using the RF LO signal from (1a). Thus, after band-pass filtering to reject all frequencies outside the IF band, the received IF signal, $S_{DSB}(t)$, can be represented as

$$\begin{aligned} S_{DSB}(t) &= R_{DSB}(t) \cdot \cos\left(\omega_{RF}t + \phi_{nRF}\left(t\right)\right) \\ &\approx \frac{1}{4}\cos\left[\frac{2\pi}{\lambda_L}d(t) + \theta_{RF} + \Delta\phi_{nRF}(t)\right. \\ &\qquad \left. - \omega_{IF}t - \theta_{IF} - \phi_{nIF}\left(\Delta t\right)\right] \\ &+ \frac{1}{4}\cos\left[\frac{2\pi}{\lambda_U}d(t) + \theta_{RF} + \Delta\phi_{nRF}(t)\right. \\ &\qquad \left. + \omega_{IF}t + \theta_{IF} + \phi_{nIF}\left(\Delta t\right)\right] \end{aligned} \tag{9}$$

where

$$\Delta\phi_{nRF}(t) = \phi_{nRF}\left(t - \frac{d_0}{c}\right) - \phi_{nRF}(t) \tag{10}$$

is the residual phase noise from the RF oscillator and where the LO signal for down-conversion is assumed to have a zero phase offset, in accordance with the previous assumption, that any phase offsets are included in the travel path from (5).

At GHz carrier frequencies with low IF offsets it can be assumed that $\lambda_L \approx \lambda_U = \lambda$. Substituting this into (9) and inserting (5), the IF signal, S_{DSB}, can now be rewritten as

$$\begin{aligned} S_{DSB}(t) = &\frac{1}{2}\cos\left(\frac{4\pi}{\lambda}x(t) + \theta_\Sigma + \Delta\phi_{nRF}(t)\right) \\ &\cdot \cos\left(\omega_{IF}t + \theta_{IF} + \phi_{nIF}(\Delta t)\right) \end{aligned} \tag{11}$$

where

$$\theta_\Sigma = \frac{4\pi}{\lambda} d_0 + \theta_{RF} \tag{12}$$

is the constant phase term associated with the RF oscillator and the travel path, $2d_0$. In (11) it can be seen, that the baseband signal is merely a sine wave at the IF frequency with the envelope modulated by the chest wall movement. Although DC offsets can easily be removed, the null-points and optimum-points seen for direct conversion VSD radars will also occur for a low-IF system that transmits (or downconverts with) a DSB signal. Whether the reception is located at a null-point is determined by θ_Σ (i.e. the distance to the target, d_0).

B. SSB Transmission

To avoid the null-point problem in the low-IF architecture, SSB transmission must be used. This can be seen by considering once more the transmitted signal from (2) although now with the lower sideband removed. The transmitted SSB signal can thus be represented as

$$T_{SSB}(t) = \frac{1}{2}\cos\left(\omega_U t + \theta_U + \phi_{nU}(t)\right) \tag{13}$$

while the received signal, $R_{SSB}(t)$, takes the form

$$R_{SSB}(t) = \frac{1}{2}\cos\left(\omega_U t + \theta_U + \frac{2\pi}{\lambda_U} d(t) + \phi_{nU}\left(\Delta t\right)\right). \tag{14}$$

Finally, after down-conversion and filtering to retain only the IF frequency component, the IF signal can now be written as

$$S_{SSB}(t) = \frac{1}{4}\cos\Bigg[\omega_{IF} t + \frac{4\pi}{\lambda_U} x(t) + \theta_\Sigma + \theta_{IF} + \Delta\phi_{nRF}(t) + \phi_{nIF}\left(\Delta t\right)\Bigg] \tag{15}$$

which can not be further reduced. For the case of SSB transmission it is thus seen that the IF signal consists of a carrier at the IF frequency with a phase modulated according to the chest wall movement of the subject in front of the VSD instrument. The constant phase term associated with the nominal distance to the target and back no longer affects the signal, because the constant angular frequency, ω_{IF}, ensures that the demodulation will be carried out continuously at different points on the circular signal phasor trajectory, [8].

In the above mathematical treatment, the residual phase noise terms where included for completeness. For a detailed treatment on this noise component and the associated range correlation effect, the interested reader should consult [7].

III. Experimental Measurements

To verify the functionality of the proposed system, several measurements were performed with a laboratory radar setup. Due to limitations of the equipment, coherent measurements, in which the ADC sampling circuitry is locked to the IF oscillator, could not be carried out. This typically results in poorer phase noise performance and greater spectrum spreading. A TekTronix TDS725B oscilloscope was used for sampling and although it has the capability to lock the internal time base to an external 10 MHz source, this feature cannot be used since direct tracking of the IF frequency together with the sub-sampling process will place the signal spectrum at DC. This effectively means that null-points arise once more, which is not desirable for the further processing of the signals. Nonetheless, measurements have been carried out and they show promising results, and for the first time in litterature (at the time of writing at least), heartbeat and respiration signals have been obtained using a low-IF VSD radar architecture.

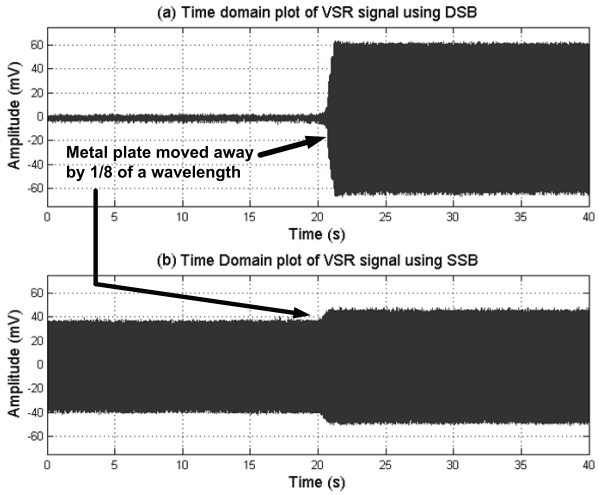

Fig. 3. Metal plate test illustrating SSB versus DSB performance.

To verify the theory from Section II and to illustrate that SSB signals are indeed prefered over DSB signals, a simple test was set up. A metal plate acting as a strong and constant target was placed in front of the VSD instrument and the distance to the plate was tuned for lowest amplitude output (i.e. null-point), and then halfway through the measurement period, the plate was moved away from the radar 1/8 of a wavelength (≈4.7 mm at 8 GHz carrier). The measurements for both DSB and SSB transmission are shown in Fig. 3. The envelope of the DSB case clearly illustrates that a null-point is present in the beginning of the measurement, while at the end, an optimum point is present. For the SSB case, the change in envelope is approximately 12-15% when the plate is moved. This change agrees well with the finite image rejection of approximately 20 dB in the up-conversion mixer. The measurements verifies that null-points are no longer present in the SSB case.

Fig. 4(a) shows a typical time domain plot of a measurement performed on a subject seated approximately 1 meter from the radar. The frequency difference between the IF oscillator and the internal reference of the oscilloscope is approximately 21.8 Hz and the signals are sampled at 500 Samples/s. The result is a digital signal spectrum going from -250 Hz to +250 Hz with signals located at a center frequency of $\pm$21.8 Hz, as seen in Fig. 4(b). Although null-points are not present, the signal envelope is still modulated. This modulation must be ascribed to changes in effective radar cross section, from when the chest wall is tightened and relaxed during respiration, as well as if

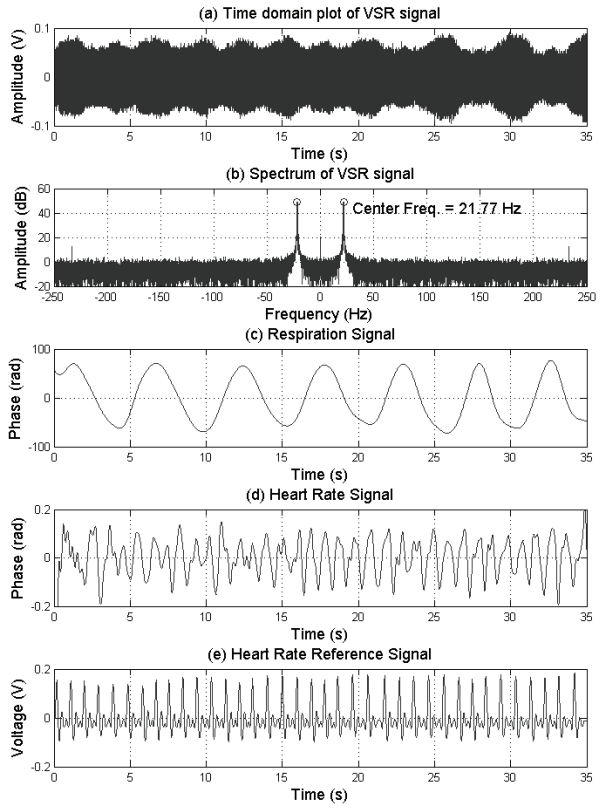

Fig. 4. (a) Time domain and (b) spectrum of raw signal from vital signs measurement (SSB transmission). (c) Respiration and (d) heartbeat signals obtained after digital down-conversion (using method from Fig. 5). Bottom plot (e) shows heart rate reference obtained from a finger pressure sensor.

the angle towards the VSD radar is changing.

Signal processing is carried out to obtain the phase information of the desired signals. The processing steps are illustrated in Fig. 5. After having located the center frequency, and band-pass filtered the incoming signal, a complex exponential carrier is created and multiplied with the signal to obtain a complex baseband signal (i.e. an I/Q representation). This signal is low pass filtered and resampled to a sampling frequency of 40 Samples/s to ease the requirements to the order of the following filters, and thus computational effort. After resampling, the phase is obtained by use of arc-tangent demodulation and finally filters are applied to separate respiration and heartbeat signals. These signals are plotted in Fig. 4(c) and (d) together with the response from a finger pressure heartbeat sensor (Fig. 4(e)), which was used for reference.

To obtain the heart rate based on the signal from Fig. 4(d) an auto-correlation was carried out on a sliding window of 5 second duration. From this, the frequency of the fundamental periodic signal was extracted. Results show that the heart rate measurement stays within 10% of the reference (finger pressure sensor) at all times. Moving towards coherent data acquisition, it is expected that this deviation can be lowered even further. Work is being carried out to update the instrument capabilities for such measurements.

No reference was recorded for the respiration activity.

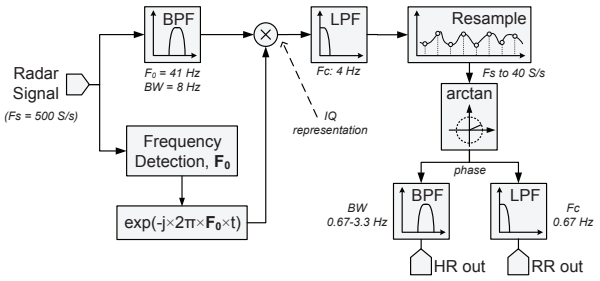

Fig. 5. Block diagram of the signal processing steps done in Matlab.

However, simply counting the number of breaths per minute agreed well with the 12 breaths/minute obtained in Fig. 4(e).

IV. Conclusion

A VSD radar using a heterodyne architecture that samples directly at an IF of 10 MHz is presented. Using this low-IF architecture it is possible to eliminate the normal DC offset and null-detection-point problems encountered in direct-conversion tranceivers. This lowers the complexity of the signal processing when doing arctangent demodulation to obtain change in phase caused by the chest wall displacement during heart- and respiration activity. Through theory and measurements is has been shown that null-detection-points are only eliminated if SSB transmission (or demodulation) is used.

Although present instrument limitations do not allow for coherent data acquisition, results show good agreement with the reference heart rate sensor, and stays within 10%.

Acknowledgment

The authors would like to thank the Danish fond "Radiopartsfonden" for financial support.

References

[1] J. C. Lin, "Noninvasive Microwave Measurement of Respiration," Proceedings of the IEEE, p. 1530, 1975.

[2] Amy D. Droitcour, Olga Boric-Lubecke, Victor M. Lubecke, Jenshan Lin and Gregory T. A. Kovacs, "Range Correlation and I/Q Performance Benefits in Single-Chip Silicon Doppler Radars for Noncontact Cardiopulmonary Monitoring," *IEEE Transactions on Microwave Theory and Techniques*, Vol. 52, No. 3, pp. 838-848, March 2004.

[3] Yanming Xiao, Jenshan Lin, Olga Boric-Lubecke and Victor M. Lubecke, "Frequency-Tuning Technique for Remote Detection of Heartbeat and Respiration Using Low-Power Double-Sideband Transmission in the *Ka*-band," *IEEE Transactions on Microwave Theory and Techniques*, Vol. 54, No. 5, pp. 2023-2032, May 2006.

[4] Enrico M. Staderini, "UWB Radars in Medicine," *IEEE AESS Systems Magazine*, pp. 13-18, January 2002.

[5] Changzhan Gu, Changzhi Li, Jenshan Lin, Jiang Long, Jiangtao Huangfu and Lixin Ran, "Instrument-Based Noncontact Doppler Radar Vital Sign Detection System Using Heterodyne Digital Quadrature Demodulation Architecture," *IEEE Transactions on Instrumentation and Measurement*, Vol. 59, No. 6, pp. 1580-1587, June 2010.

[6] Isar Mostafanezhad, Olga Boric-Lubecke and Victor Lubecke, "A Coherent Low IF Receiver Architecture for Doppler Radar Motion Detector Used in Life Signs Monitoring," *IEEE Radio and Wireless Symposium*, pp. 571-574, 2010.

[7] M. C. Budge and M. P. Burt, "Range Correlation Effects in Radars," *IEEE National Radar Conference*, pp. 212-216, 1993.

[8] Byung-Kwon Park, Olga Boric-Lubecke and Victor M. Lubecke, "Arctangent Demodulation With DC Offset Compensation in Quadrature Doppler Radar Receiver Systems," *IEEE Transactions on Microwave Theory and Techniques*, Vol. 55, No. 5, MAY 2007.

Conference Paper 5 [CP5]

Bondwire array modeling for the design of hybrid high power amplifiers above C-band

Carlos Cilla Hernández, Sævar Þór Jónasson
and Jesper Hanberg

Conference:	Asia-Pacific Microwave Conference, Kaohsiung, Taiwan
Published :	Dec. 2012

Bondwire Array Modeling for the Design of Hybrid High Power Amplifiers above C-band

Carlos Cilla, Sævar Þór Jónasson, Jesper Hanberg

Department of Electrical Engineering, Technical University of Denmark

Oersteds Plads 348, DK-2800, Kgs. Lyngby, Denmark

***Abstract* — This paper presents a bondwire array model obtained using a software based on the finite elements method and validated up to 15 GHz by measurements over a purpose-build array structure. This work addresses the limits of the inductor-based bondwire model when used at frequencies above C-band to simulate the large bondwire arrays that are used in long multi-transistor power bars. The usefulness of an accurate 3D EM model during the amplifier's matching network design process is highlighted using a practical example, and the effect of the insertion loss variations along the different bondwires comprising the array on the hybrid performance is discussed.**

***Index Terms* — High power amplifier, Hybrid integrated circuits, Integrated circuit packaging, Power transistors, Semiconductor device packaging, Wafer bonding.**

I. Introduction

Bondwire arrays are extensively used in electronic packaging and to interconnect microwave components. An example of this is the electrical connection provided between the power bar die, comprising several transistor cells in parallel, and the external matching structures.

Lately, there has been a renewed interest in high power amplifier design thanks, to a large extent, to the development of GaN semiconductor technology that is already having an important impact into the wireless and radar market. At frequencies below 6GHz, it is typical to find hybrid packaged transistor power bars with prematched structures like MOS capacitors and bondwire arrays connecting to the package flange.

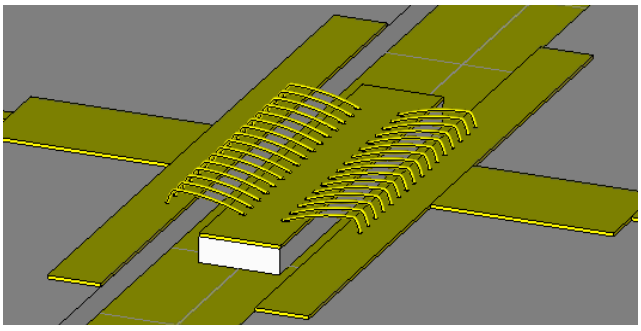

Fig. 1. Drawing of the fabricated bondwire structure using full wave simulation CAD

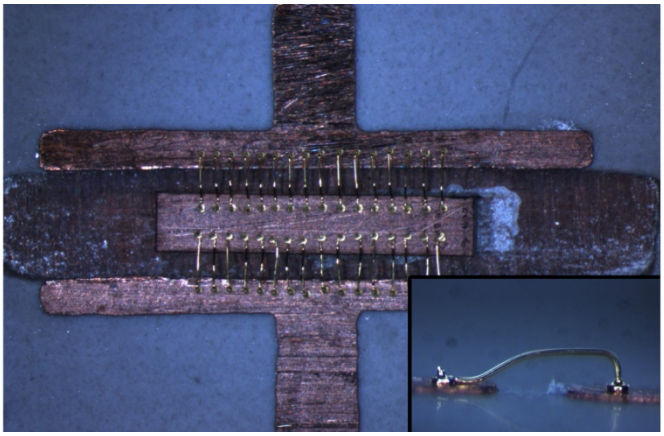

Fig. 2. Fabricated structure with two, 16 bondwire arrays in parallel. A close-up of a bondwire is illustrated in the lower right corner.

At frequencies above 6 GHz, MMIC solutions dominate the market, and it is challenging to find hybrid solutions, since the package and bondwire parasitics become increasingly important at sizes comparable to the operating wavelength.

Hybrid solutions above C-band have two main advantages that make them worth further investigation: the reduction in semiconductor area needed, therefore reducing drastically the final cost, and the possibility of implementing the external matching and biasing networks on very low loss substrates, thus improving output power and efficiency capabilities. Alumina substrate has e.g., 10 times lower loss tangent at 10GHz than SiC semiconductor which is the most commonly used substrate for GaN transistors.

Hybrid design above C-band requires a good model of the bondwires and their transition (see Fig. 1), in order to achieve a proper matching and to avoid the need of tuning after manufacturing, if even possible.

Previous research has focused on closed-form equations used to compute self and mutual inductances of the bondwire arrays [1]-[5]. Full wave software simulations of single and double bondwires have also been published. [6], [7].

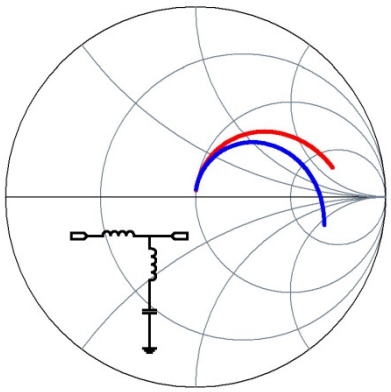

Fig.3. Single bondwire S_{11}-parameter using ADS inductance-based model (Red) and full wave 3D simulation (Blue) from 1 to 32 GHz. Also shown the lumped equivalent model of the bondwire-to-microstrip transition, which added to the ADS model, would make both curves to match.

In this paper we examine the limitation of the inductor-based bondwire model at frequencies above 6 GHz. Section II presents a comparison between measurements of the fabricated array structure, shown in Fig. 2, and data obtained from a full wave simulation up to 15 GHz. Finally, Section III focuses on the importance of having an accurate bondwire model during the design process of hybrid high power amplifiers.

II. Bondwire Model

Traditionally at low frequencies, the bondwire is considered to have an inductive behavior, and it is a good principle to keep it as short as possible. The ADS bondwire array model [3] is based on self and mutual inductance calculations, modeling each bondwire with five segments of a given radius, conductivity, distance from ground plane and separation between adjacent bondwires.

At higher frequencies however, the bondwire-to-microstrip transition becomes significant, and the behavior depends on the permittivity and thickness of the substrate used, the bondwire-to-microstrip connection angle and the distance from the connection point to the substrate edge.

Fig. 3 shows a comparison up to 32 GHz of a single bondwire simulation using the inductor-based ADS model and a simulation using 3D full wave electromagnetic simulation software. Both models match up to around 6GHz, but not at higher frequencies. 3D EM CAD programs like HFSS or CST are efficient with the computers available nowadays, and a good matching between simulation and measurements was verified both for the single bondwire and for more complex structures, as shown in the next section. In Fig.3, a lumped equivalent of the bondwire-to-microstrip transition can be added to the ADS model in order to fit both curves.

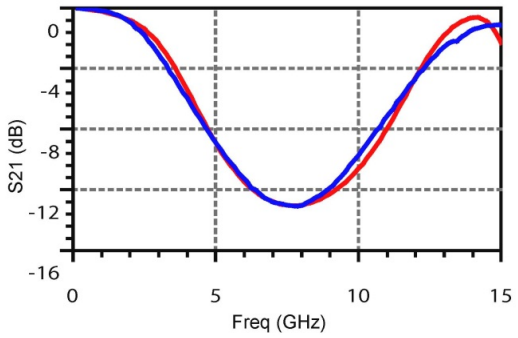

Fig. 4. Comparison between measurement (blue) and full wave electromagnetic simulation (red) of fabricated structure.

III. Bondwire Array: Measurements vs Simulations

Large arrays using many bondwires in paralell are usually found in the large single tabs of the output ports of transistor power bars. The number of bondwires in parallel and the radius are chosen to accommodate properly all the current at the output power stage.

When paralleling bondwires in the same tab as shown in Figs. 1 and 2, the overall parasitic inductance is reduced while the capacitance to ground increases, relative to a single bondwire, due to the paralleling. This makes the full wave 3D modeling even more necessary than in the case of a single bondwire.

Fig 4. shows good agreement between measurements of the structure shown in Fig. 2 and simulations in Fig. 1, using the finite elements method (FEM) up to 15 GHz. The behavior was also validated using software based on the finite-difference time-domain method (FDTD).

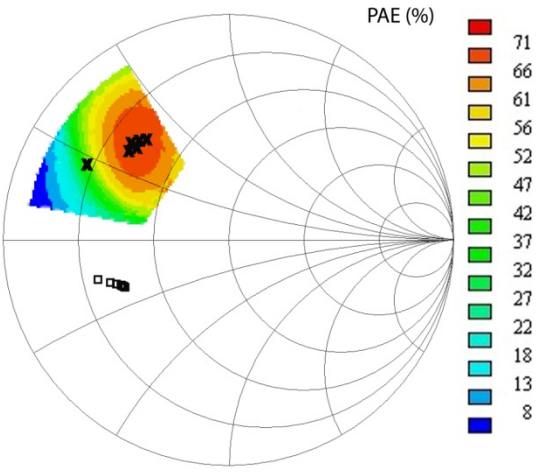

Fig. 5. Load pull data for a single transistor cell showing PAE circles at 9 GHz and synthesized impedances for each one of the 16 cells of a power bar, using the bondwire full wave model (crosses) and the inductor-based model (squares)

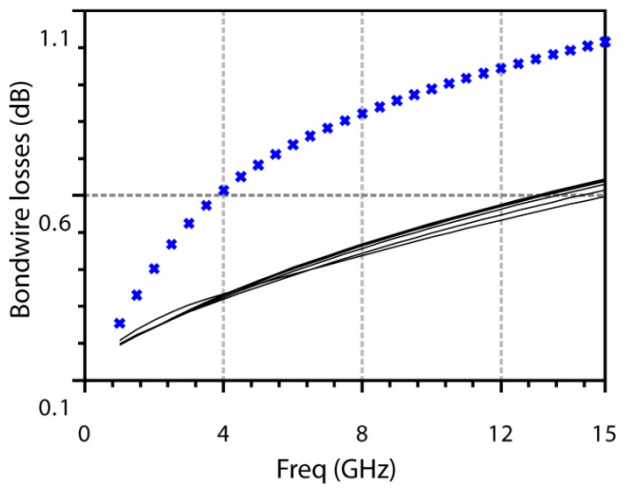

Fig. 6. Losses along the two bondwires at the edges of the array in blue (crosses) and for the other 14 bondwires in black.

IV. How an accurate bondwire model improves the hybrid design process

The process of designing a hybrid power amplifier using multi-transistor power bars can be greatly improved by the use of the accurate models available nowadays both for the active and passive elements. The first step in the design is to find optimal loading conditions for a single cell performing load and source pull. Fig. 5 shows the Power Added Efficiency (PAE) contours for a given transistor cell operating at 9 GHz, where the red area corresponds to the optimal performance in terms of PAE. Next step is to design the matching networks for the power bar containing several cells in parallel, taking into account that the bondwire array is actually part of the matching structure. Using a multiport bondwire array model obtained using a full wave solver makes possible to simulate the impedance that each of the cells of the array is loaded with.

When paralleling many cells in a power bar, the impedances to match are typically very low, therefore only narrowband designs are often possible, and it is therefore necessary to be very careful when designing the matching networks.

The crosses in Fig 5 represent the output impedances seen by the individual transistors of a 16 cells power bar at 9 GHz when using the full-wave array model during the matching network design process, and the squares represent the impedance seen when the full-wave array model is substituted by an inductor based one. When looking at the PAE corresponding to both cases, we can conclude that the use of a non accurate model can completely detune the performance of the hybrid design.

There exist also imbalances in the synthesized impedance along the different ports of the bondwire array, partially due to the fact that the two bondwires on the edges of an array only have one neighboring bondwire instead of two. This modifies the magnetic and electric fields along the array, and therefore the couplings and losses between the different bondwires will also vary along the array. The bondwire losses will also depend on the loading impedance levels when compared with the equivalent characteristic impedance of the bondwire [3].

Fig. 6 corresponds to a simulation showing the variation of the insertion losses along the different bondwires of an array used at the gate of a 16 cells hybrid power transistor. At the gate, these variations in loss-levels will create differences in the operating compression point of each of the individual cells. At the drain, the differences in synthesized impedance for each of the cells will create differences in performance between the cells. These differences in performance between the cells will add to other imbalances created due e.g. to the differences in the temperature of operation along the bar.

V. Conclusion

The usefulness and accuracy of full-wave electromagnetic simulation tools for modeling bondwire arrays has been validated. A 16 bondwire array structure has been fabricated obtaining a good matching between measurements and the full-wave model up to 15 GHz. It has been demonstrated that the accuracy of the inductor-based bondwire model is not always enough above 6GHz, which is especially true in the case of bus bar arrays with many bondwires in parallel. This work has revealed the importance of using an accurate bondwire array model during the design of hybrid power amplifiers above C-band.

References

[1] K. Mouthaan et al., “Microwave modeling and measurement of the self and mutual inductances of coupled bondwires,” in IEEE Bipolar Circuits Technology Meeting, Minneapolis, MN, 1997, pp. 166–169.

[2] A.O. Harm and K. Mouthaan and E. Aziz and M. Versleijen, "Modelling and Simulation of Hybrid RF Circuits Using a Versatile Compact Bondwire Model," Proceedings of the European Microwave Conference, pp. 529-534, Oct. 1998. Amsterdam

[3] K. Mouthaan, “Modelling of RF High Power Bipolar Transistors.” Ph.D. dissertation, ISBN 90-407-2145-9, Delft University of Technology, 2001.

[4] S. March “Simple equations characterize bond wires”, Microwaves & RF, pp. 105-110, Nov. 1991

[5] M. Kamon, M. J. Tsuk, and J. K. White. \FASTHENRY: a multipole-accelerated 3-D inductance extraction program". IEEE Trans. Microwave Theory and Techniques,page 1750, 1994.

[6] F. Alimenti et al., “Modeling and characterization of bonding-wire interconnection”, IEEE Transactions On Microwave Theory and Techniques, vol. 49, No. 1, Jan 2001

[7] C. Schuster et al.,“Electromagnetic Simulation of Bonding Wires and Comparison with Wide Band Measurements”, IEEE Transactions On Advanced Packaging, vol. 23, No. 1, Feb 2000

Conference Paper 6 [CP6]

Cantilever-Based Microwave Biosensors: Analysis, Designs and Optimizations

Chenhui Jiang, Tom Keinicke Johansen,
Sævar Þór Jónasson, Lei Yan and Anja Boisen

Conference:	27th Annual Review of Progress in Applied Computational Electromagnetics, Virginia, USA
Published :	March 2011

Cantilever-based Microwave Biosensors: Analysis, Designs and Optimizations

Chenhui Jiang[1], Tom K. Johansen[1], Sævar Þór Jónasson[1], Lei Yan[1] and Anja Boisen[2]

[1]Department of Electrical Engineering
Technical University of Denmark, Kgs. Lyngby, 2800, Denmark
cj@elektro.dtu.dk

[2]Department of Micro- and Nanotechnology
Technical University of Denmark, Kgs. Lyngby, 2800, Denmark

Abstract: This paper presents a novel microwave readout scheme for measuring deflection of cantilevers in nanometer range. The cantilever deflection can be sensed by the variation of transmission levels or resonant frequencies of microwave signals. The sensitivity of the cantilever biosensor based on LC resonators is at first theoretically analyzed. A LC resonator based biosensor with beams is designed and optimized by using 3D electromagnetic (EM) simulations, where the beam is a typical variation of cantilevers. The sensitivity of the lossless biosensor is predicted as 4.6MHz/nm. The 3-dB bandwidths of the resonances are narrowed for improving the resolution of distinguishing resonances by reducing conductive loss of electrodes. The lossy biosensor can achieve the highest sensitivity as 5.6 MHz/nm and narrowest 3-dB bandwidth as 5 GHz.

Keywords: Cantilevers, beams, microwave biosensors, LC resonators, electromagnetic simulations,

1. Introduction

Biosensors have been widely used in identifying target molecular, recognizing a suitable biological element, monitoring micro-environment parameters, developing drug discovery and targeted drug delivery systems [1-4]. They are attracting numerous research and commercial interests due to these applications. Cantilevers, which are micrometer sized diving boards, can be used as sensitive and versatile label free biosensors [5]. The cantilever based sensors exhibit merits in the aspect of label-free usage, high sensitivity, portability, low cost and highly parallel and fast responsibility. The cantilever may deflect due to changes in temperature, surface stress and mass, which are major concerned parameters for biosensing [5]. The cantilever-based biosensors can measure these parameters due to deflections of cantilevers by several read-out principles. However, current read-out methods always have their limitations. For example, the optical read-out [6, 7] is difficult to apply for large arrays and not suitable for nanometer sized cantilevers. Even though piezoresistive read-out [8, 9] is suitable for large arrays and system integration, a piezoresistive layer needs to be integrated into the cantilever so that it affects the mechanical performance.

In order to overcome these limitations, microwave readout is proposed to detect cantilever deflections. It is feasible to be applied in a single cantilever or a large array of cantilevers. Microwave electrodes are easily integrated with operational cantilevers, and can act as an active layer on cantilevers as well. Moreover microwave read-out scheme provides a possibility to approach lab-on-a-chip due to the full integration sensor implementation and realize wireless sensing manners. Biosensors probed with microwave, millimeter-wave or terahertz signals have been recently proposed by several groups [10-12]. These activities employ either split-ring resonators (SRRs) or Goubau lines (G-lines) [13] as sensing

elements. SRRs may be added in the development of ultra-sensitive cantilever-based biosensors based on resonator arrays. This technique includes solutions of coupled dynamic system arrays as well as appropriate models for resonating structures such as SRRs. A completely new technique could rely on the variation in transmission properties of G-lines due to cantilever excursion or vibration, when G-line structures are integrated with cantilevers. Such sensors should exhibit very high sensitivity, due to the strong EM field localization around the G-line [13]. In addition, one can measure vibrating cantilever resonance frequency variation remotely, due to modulation of the transmitted microwave signal.

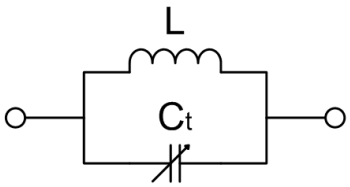

$$f_r = \frac{1}{2\pi\sqrt{LC_t}}$$

Fig. 1. A circuit model of parallel LC resonators and resonant frequency expression.

This paper will firstly theoretically analyze cantilever deflection sensitivity. Afterwards, a microwave biosensor is proposed, on which a parallel LC resonator is integrated with both ends clamped beams [14]. The beam is an important variation of cantilevers, and it has the similar properties as cantilevers have. Fig.1 shows a circuit model of parallel LC resonators. The resonant frequency, f_r, can be derived by the above equation. If the microwave electrodes are deposited on cantilevers and build capacitive coupling between electrodes, the cantilever deflection can result in variation of capacitive coupling, which is consistent with C_t values. Therefore, cantilever's deflection is corresponding to the resonant frequency shift and can be measured by microwave signals. The beam-based microwave biosensors with LC resonators are designed and optimized by using 3D electromagnetic (EM) simulations.

2. Theoretical Sensitivity Analysis on Cantilever-based Microwave Biosensors

Fig. 2. (a) Cross section view illustration of two capacitively coupled electrodes on cantilevers; (b) extracted model for analyzing cantilevers deflection.

Fig. 2 (a) illustrates a cross section view of two capacitively coupled electrodes on cantilevers, which are not shown. Two rectangular blocks represent cross sections of two electrodes. They have horizontal difference as denoted "*h*", and the horizontal gap is denoted as "*g*". The capacitance between electrodes is inversely proportional to the distance, which is denoted as "*d*". The electrodes deflect vertically with cantilevers. The cantilever deflection causes horizontal difference deviation and distance deviation, Δh and Δd as denoted in Fig. 2 (b), respectively. The relationship among these parameters can be expressed as

$$h^2 + g^2 = d^2 \tag{1}$$

$$(h + \Delta h)^2 + g^2 = (d + \Delta d)^2 \tag{2}$$

If $\Delta h << h$ and $\Delta d << d$, the sensitivity of d can be derived by combining equation (1) and (2) as

$$\frac{\Delta d}{d} = \frac{h}{h^2 + g^2}\Delta h \tag{3}$$

From equation (3), the highest sensitivity of d is obtained when $h = g$, if g is treated as a constant. In this case, the maximum sensitivity can be expressed as

$$\frac{\Delta d}{d} = \frac{\Delta h}{2g} \tag{4}$$

This result reveals that the highest deflection sensitivity occurs when cantilevers have initial deflection, which is equal to the designed electrode horizontal gaps. Furthermore, the deflection sensitivity can be improved by reducing the gap between electrodes.

For the purpose of the microwave biosensor based on LC resonator, the deflection sensitivity has to be translated into resonant frequency sensitivity. Since the capacitance in the resonator is inversely proportional to the distance between electrodes, the capacitance can be estimated as

$$C_t = K\frac{1}{d} \tag{5}$$

where K is a constant, which is related to capacitive coupling effect. By using equation (5), the resonant frequency can be expressed as a function of d as following,

$$f_r(d) = \frac{1}{2\pi\sqrt{LK}}\sqrt{d} \tag{6}$$

The resonant frequency deviation with respect to the distance can be derived as

$$\Delta f_r = f_r^{'}(d)\Delta d = \frac{1}{4\pi\sqrt{LK}\sqrt{d}}\Delta d \tag{7}$$

By combining equation (1), (4) and (7), the relationship between the resonant frequency deviation and the small deflection can be written as

$$\Delta f_r = \frac{1}{8\pi\sqrt{LK}}\frac{\sqrt{d}}{g}\Delta h = \frac{\sqrt[4]{2}}{8\pi\sqrt{LK}}\frac{1}{\sqrt{g}}\Delta h \tag{8}$$

Equation (9) shows that smaller L, K and g will result in higher resonant frequency deviation. Therefore, the biosensor is required to operate at very high frequencies. However, the loss of the biosensor will dramatically increase with operation frequencies rising. The loss of the biosensors influences the resolution of the biosensor which is important for distinguish resonance notches.

3. Beam-based Microwave Biosensor Designs and Optimizations

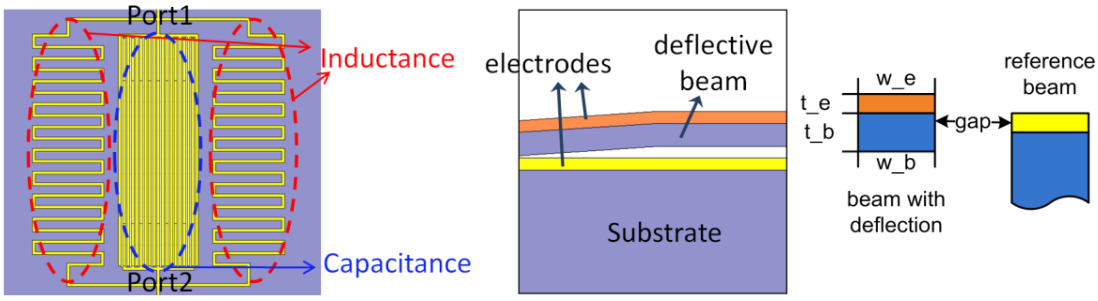

(a) (b) (c)

Fig. 3. (a) Top view of the LC resonator based biosensor; (b) side view of the biosensor with deflection; (c) the cross section of beams and electrodes with parameter indications.

The microwave biosensors based on both ends clamped beams were designed and optimized by using 3D electromagnetic (EM) simulations. The beams have similar deflection properties as cantilevers. Fig. 3

shows a microwave biosensor integrated with a parallel LC-resonator. The inductors are realized by meander lines and the capacitor is built based on interdigital coupling structures. Two inductors are in parallel to keep the device symmetric and decrease the inductance and the loss of the device.

The electrodes for the interdigital structure are deposited on beams. As shown in Fig. 3 (b), some of electrodes are deposited on the beams which are capable of deflecting, and some are deposited on fixed beams or the substrate as reference. When the beams with interdigital electrodes deflect due to temperature or surface stress change, the capacitance will change correspondingly. As shown in Fig. 3 (c), the fixed beam should be much thicker than the deflective one to be a reference beam. The width of electrode and beam, *w_e* and *w_b*, are designed to be 2 μm. The thickness of electrode and beam, *t_e* and *t_b*, are designed to be 0.5 μm and 1 μm, respectively. The *gap* between beams is designed to be 2 μm. Fig. 4 (a) shows the simulated transmissions of lossless biosensors with various deflections from 0 μm to 5 μm by 1 μm step. The notches of the resonances are very sharp due to lossless properties of the device. The resonant frequency shifts upwards with the increased deflection level. Fig. 4 (b) summarizes the resonant frequencies versus deflections. Positive deflection indicates the bi-material beams are higher than the reference electrodes, and vice versa. The lowest resonant frequency is observed when the deflection is 0 μm, because the highest capacitance is obtained when all interdigital electrodes are at the same horizontal level. The lowest sensitivity is also observed around this range, which is consistent to the equation (4) if $h = 0$. The highest sensitivity is observed as 4.6 MHz/nm in the range from 2 μm to 3 μm, which is close to the value of horizontal gap. The EM simulation results prove the conclusions derived by theoretical analysis.

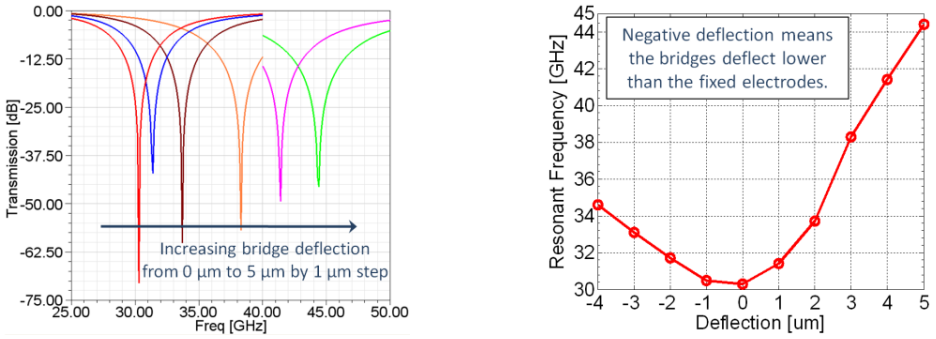

(a) (b)

Fig. 4. (a) Simulated transmission properties of the lossless biosensor; (b) resonant frequency variation versus deflections.

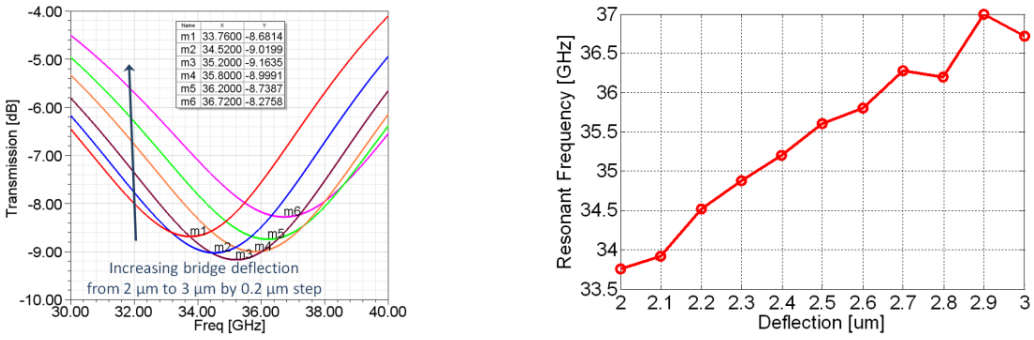

(a) (b)

Fig. 5. (a) Simulated transmission properties of the lossy biosensor; (b) resonant frequency variation versus deflections.

When the lossless materials are replaced by lossy materials, the gold has finite conductivity with 4.1×10^7 S/m and the silicon substrate becomes lossy with 1000 Ω·cm resistivity. The EM simulations on

the lossy biosensor are only performed in the deflection range from 2 μm to 3 μm because it is the highest sensitivity range. Fig. 5 (a) plots the transmissions of the lossy biosensor. The resonant notches shift while the deflection varies. The relationship between the resonant frequency and the deflection is plotted in Fig. 5 (b). It is approximately linear relationship as predicted by equation (8). Since the loss mechanism of the sensor is included in EM simulations, the sensitivity of the sensor degrades to 3 MHz/nm from 4.6 MHz/nm. Simultaneously, as demonstrated in Fig. 5 (a), the blunt notches make them difficult to be distinguished to each other. The resolution of the biosensor is seriously decreased due to the loss of the device.

The optimization on the lossy biosensor will improve both sensitivity and resolution of resonant frequencies by reducing the loss of the device. The electrode loss is more dominant than substrate loss when the high resistive silicon substrate is used, so that the electrodes are optimized in three cases. The simulated transmissions of three cases are summarized in Fig. 6. The inserted arrow indicates that curves are parameterized according to beam deflections from 2 μm to 3 μm by 0.2 μm step. Narrower 3-dB bandwidth of resonance is equivalent to higher resolution for distinguishing shifting resonances.

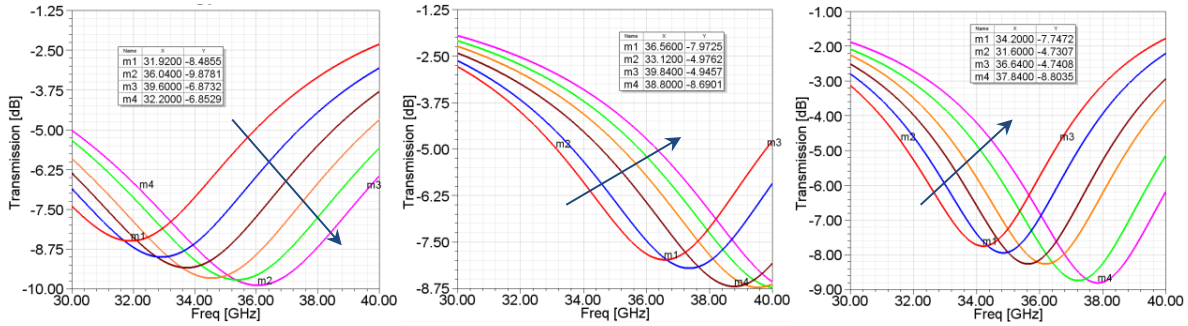

(a) (b) (c)

Fig. 6. Simulated transmission properties of optimized lossy biosensors, the inserted arrow indicating that bridge deflects from 2 μm to 3 μm by 0.2 μm step: (a) case 1; (b) case 2; (c) case 3.

Table 1. Summarization of optimized biosensor performance

Parameters	t_e (μm)	w_e (μm)	sensitivity	3-dB bandwidth
Original Case	0.5	2	3 MHz/nm	9.1 GHz
Opt. Case 1	1	2	4.1 MHz/nm	7.4 GHz
Opt. Case 2	1	4*	5.6 MHz/nm+	6.72 GHz
Opt. Case 3	2	4*	3.64 MHz/nm	5 GHz

*Only the electrodes not on beams are widened; +Calculated in the range from 2 μm to 2.4 μm.

As summarized in Table.1 for all three cases, increasing the thickness and width of electrodes is an effective method for improving the resolution of resonances by alleviating the electrode loss. However, the sensitivity is low to be 3.64 MHz/nm, when the electrodes on beams are too thick to be 2 μm. It is because the coupling effect between electrodes is enhanced by thick electrode. As described in equation (9), higher coupling effect (*K*) results in smaller resonant frequency shifting, which is equivalent to low sensitivity.

4. Conclusions

This paper, for the first time, proposes the methods of using microwave signal to detect tiny deflections in cantilever-based biosensors. The novel microwave read-out method provides a promising perspective of fully integrated lab-on-chip systems with noninvasive detections. The sensitivity of the biosensor is theoretically analyzed as a guideline for designing high sensitive biosensors. A LC-resonator

based microwave biosensor is designed and optimized by using 3D EM simulations. In the sensor, the LC-resonator is integrated on both ends clamped beams. The lossless sensor is predicted to have 4.6 MHz/nm sensitivity, which is very high for the static operation of cantilevers or bridges. The lossy sensor is optimized to obtain higher resolution of resonant frequencies by reducing the conductive loss of electrode. The highest sensitivity can be achieved to be 5.6 MHz/nm, and the narrowest 3-dB bandwidth of resonant notches can be achieved as 5 GHz. The future work will focus on developing a prototype of beam-based microwave biosensor for measuring its performance experimentally. The measurement results should be presented on the conference site.

References

[1] A. Cavalcanti, B. Shirinzadeh, M. Zhang, and L. C. Kretly, "Nanorobot hardware architecture for medical defense," *Sensors*, Vol. 8, Issue 5, pp. 2932-2958, 2008.

[2] P. J. Vikesland and K. R. Wigginton " Nanomaterial Enabled Biosensors for Pathogen Monitoring - A Review," *Environ. Sci. Technol.* Vol. 44, Issue. 10, pp. 3656-3669, 2010

[3] M. Pohanka, D. Jun, and K. Kuca, "Mycotoxin assay using biosensor technology: a review," *Drug Chem. Toxicol.* Vol. 30, No. 3, pp. 253-261, 2007

[4] C. Bunte, O. Prucker, T. König, and J. Rühe "Enzyme containing redox polymer networks for biosensors or biofuel cells: A photochemical approach," *Langmuir*, Vol. 26, Issue. 8, pp. 6019-6027, 2010

[5] C. Ziegler, "Cantilever-based biosensors," *Anal. Bioanal. Chem.*Vol. 379, pp. 946-959, 2004.

[6] H. P. Lang, R. Berger, C. Andreoli, J. Brugger, M. Despont, P. Vettiger, Ch. Gerber, J. K. Gimzewski, J. P. Ramseyer, E. Meyer, and H.-J. Güntherodt, "Sequential position readout from arrays of micromechanical cantilever sensors," *App. Phys. Lett.* Vol. 72, Issue 3, pp. 383-385, 1998

[7] M. Nordströma, D. A. Zauner, M. Calleja, J. Hübner and A. Boisen, "Integrated optical readout for miniaturization of cantilever-based sensor system," *App. Phys. Lett.* Vol. 91, Issue 10, pp. 103512, 2007

[8] J.-H. Park, D. Graf, T. P. Murphy, G. M. Schmiedeshoff, and S. W. Tozer, "High resolution miniature dilatometer based on an atomic force microscope piezocantilever," *Rev. sci. instrum.* Vol. 80, Issue. 11, pp.116101, 2009.

[9] G. Yoshikawa, H-P. Lang, T. Akiyama, L. Aeschimann, U. Staufer, P. Vettiger, M. Aono, T. Sakurai, and C. Gerber, "Sub-ppm detection of vapors using piezoresistive microcantilever array sensors," *Nanotech.* Vol. 20, Issue. 1, pp. 015501, 2009.

[10] A. C. Stevenson, B. Araya-Kleinsteuber, J. Lee, and C. R. Lowe, "Electromagnetic excitation of acoustic biosensors," *Proc. IEEE Int. Freq. Control Symp.* 2007

[11] N-F. Chiu, Y-H. Liang, and C-W. Lin, "Novel biomolecular finger printing with an active dual-band antenna biosensor," *Proc. IEEE Sensors*, 2006

[12] H-J. Lee and J-G. Yook, "Biosensing using split-ring resonators at microwave regime," *App. Phys. Lett.* Vol. 92, Issue 25, pp.245103-1-3, 2008

[13] T. Akalin, A. Treizebre, and B. Bocquet, "Single-wire transmission lines at terahertz frequencies," *IEEE Trans. Microwave Theor. Tech.* Vol. 54, Issue 6, Part2, 2006

[14] A. O. Niskanen, J. Hassel, M. Tikander,P. Maijala, L. Grönberg, and P. Helistö, "Suspended metal wire array as a thermoacoustic sound source," *App. Phys. Lett.* Vol. 95, Issue 16, pp. 163102, 2010

www.elektro.dtu.dk

Department of Electrical Engineering
Electromagnetic Systems Group (EMS)
Technical University of Denmark
Ørsteds Plads
Building 348
DK-2800 Kgs. Lyngby
Denmark
Tel: (+45) 45 25 38 00
Fax: (+45) 45 93 16 34
Email: info@elektro.dtu.dk

ISBN XX-XXXXX-XX-X